Fermilab

Measurement of the W Boson Mass With the Collider Detector at Fermilab

FERMILAB-THESIS-1998-10

A thesis presented

by

Andrew Scott Gordon

to

The Department of Physics

in partial fulfillment of the requirements

for the degree of

Doctor of Philosophy

in the subject of

Physics

Harvard University

Cambridge, Massachusetts

November 1998

©1998 by Andrew Scott Gordon

All rights reserved.

Measurement of the W Boson Mass With the Collider Detector at Fermilab

Andrew Scott Gordon

Thesis Advisor: Melissa Franklin

Abstract

We measure the W boson mass using the $W \to e\nu$ decay channel. We use data collected at the Collider Detector at Fermilab from $p\overline{p}$ collisions at $\sqrt{s} = 1800$ TeV. The data were taken from January 1994 through July 1995 and represent an integrated luminosity of 90.1 pb^{-1}. We determine the W mass to be $80.473 \pm 0.067(stat) \pm 0.097(sys)$ GeV. The dominant contribution to the systematic uncertainty is the uncertainty on the calorimeter energy scale. The energy scale contributes 0.080 GeV to the systematic uncertainty.

Acknowledgements

I would like to thank my advisor Melissa Franklin for her guidance through graduate school; and also Nica, for sharing his toys. I thank the W mass group at CDF for their help—particularly, Young-kee Kim, with whom I first worked on the Run 1B analysis. The W mass group also included Mark Lancaster, Randy Keup, Adam Hardman, Kevin Einsweiler, Bill Ashmanskas, Larry Nodulman and Barry Wicklund, and was a source of many useful discussions, ideas, and results. And I thank my parents, who have been here before, for their encouragement and wise counsel, as well as my brother and sister who were here more recently.

The tragedy of graduate school is sometimes a comedy. For example: Steve Hahn and Larry Nodulman, who regularly dragged me to the Taqueria; Bob Mattingly, to whose attention I called one day that it is forbidden to discuss Ezekiel's vision of the Chariot, and who understood; Rowan Hamilton, with whom I shared an office for a while, and who was my fas-appointed Big Brother advisor; Fotis Ptohos and Maria Spiropulu, who made me many excellent dinners and who it doesn't go without saying put up with me; and David Kestenbaum, who offered me many invitations to parties downtown. And I would like to remember my friend George Michail, if only because one day we had to change 96 fuses on 96 CMX cards, *in situ*.

Maria gets her own paragraph.

I have not yet mentioned Thomas Dignan. He also gets his own paragraph.

Contents

Acknowledgements **iv**

List of Figures **xii**

List of Tables **xviii**

1 Introduction to the W Mass Measurement **1**

1.1 W Events at Fermilab 1

1.2 Theoretical Motivation and Historical Overview 3

1.3 The Jacobian Edge and the Transverse Mass 11

1.4 Measurement Overview 16

2 Fermilab Accelerator and CDF Detector **19**

2.1 The Accelerator 19

2.2 Detector Overview 23

2.3 Tracking 24

2.3.1 Central Tracking Chamber (CTC) 24

2.3.2 Vertex Time Projection Chamber (VTX) 30

2.3.3 Silicon Vertex Detector (SVX) 33

2.4 Calorimetry 34

2.4.1 Central Electromagnetic Calorimeter (CEM) 35
2.4.2 Central and Wall Hadronic Calorimeters (CHA and WHA) . . 37
2.4.3 Plug Calorimeters (PEM and PHA) 39
2.4.4 Forward Calorimeters (FEM and FHA) 40
2.5 Trigger 41
2.5.1 Level 1 42
2.5.2 Level 2 42
2.5.3 Level 3 46

3 Data Reduction and Signal Extraction 50

3.1 Event Variables 51
3.1.1 E_T: Electron Transverse Energy 51
3.1.2 P_T: Track Momentum and Beam Constraint 51
3.1.3 $\vec{U}$: Boson Transverse Momentum 56
3.1.4 $\sum E_T$: Scalar Energy in the Event 61
3.1.5 $\not{E}_T$: Missing Transverse Energy 61
3.1.6 M_T: Transverse Mass 61
3.2 P_T Corrections 62
3.3 Initial CEM Corrections 65
3.3.1 Time Dependent Corrections 65
3.3.2 Mapping Corrections 67
3.3.3 Summary 70
3.4 Underlying Energy CEM Corrections 70
3.5 Default Energy Scale 73
3.6 W Selection Requirements 73

3.7 Z Selection Requirements 78

4 Background Determination **82**

4.1 Lost Z Background 82

4.2 QCD Background 88

4.3 $W \to \tau\nu$ Background 100

4.4 Summary 102

5 Event Generation **104**

5.1 W Production Cross Section 105

5.1.1 Lowest Order Cross Section 107

5.1.2 Higher Order Cross Section 109

5.1.3 Functional Form for Initial State Radiation 110

5.1.4 Summary 113

5.2 Generation of Event Variables 113

5.2.1 x_1 and x_2 Generation 113

5.2.2 Q_T and Δy Generation 114

5.2.3 Breit-Wigner Rejection 115

5.2.4 Flavor Generation 116

5.3 Boson Decay 117

5.3.1 Angular Distribution 117

5.3.2 Radiative Decay 119

5.4 Differences Between Production of W and Z Events 121

5.4.1 Difference In Cross Sections 121

5.4.2 Difference In Boson P_T Distributions 123

5.5 Summary 126

6 Electron Simulation **128**

6.1 CTC Simulation 128

6.1.1 Material Distribution 129

6.1.2 Bremsstrahlung Simulation 136

6.1.3 CTC Measurement 137

6.1.4 Beam Constraint 139

6.2 Calorimeter Simulation 140

6.3 Tower Removal Simulation 141

6.4 Underlying Energy Simulation 147

6.5 N_{tracks} Simulation 147

6.6 Summary 150

7 Boson P_T Determination **153**

8 Calorimeter Response Model **159**

8.1 $\sum E_T$ Fit 160

8.2 Dependence of $\vec{U}$ Resolution on $\sum E_T$ 163

8.3 $\vec{U}$ Model 167

8.3.1 Parameter Definitions 167

8.3.2 Fits to the Z Data 169

8.4 Correcting the Z Fits 177

8.4.1 Correction to $\sum E_T$ Fits 178

8.4.2 Correction to $\vec{U}$ Fits 181

8.5 Summary 183

9 Comparison of W Data and Monte Carlo **185**

9.1 $\vec{U}$ Distributions 186

9.2 E_T, $\not{E}_T$, and M_T 191

9.3 $U_{||}$ as a Function of M_T, $|\vec{U}|$, and E_T 195

9.4 Conclusion 204

10 Energy Scale Determination with M_Z **206**

10.1 Likelihood Fit 207

10.2 Fitting with the Mean of M_Z 210

10.3 Kolmogorov-Smirnov Comparison 212

10.4 Conclusion 218

11 Energy Scale Determination with E/p **219**

11.1 Check on Amount of Material with E/p Tail 221

11.2 Momentum Resolution 227

11.2.1 Very Low E/p Tail 227

11.2.2 Peak of E/p Distribution 232

11.3 Scale Determination With W Events 235

11.4 Scale Determination With Z Events 241

11.5 Conclusion 244

12 Non-Linearity Between W and Z Energy Scales **247**

12.1 Comparison of W and Z E/p Fits 250

12.2 E/p vs E_T for W Events 251

12.3 <E/p> vs $U_{||}$ for W Events 255

12.4 Conclusion 259

13 W Mass Fit **261**

13.1 W Mass and Width Fits Using Inputs Parameters from Z Data, $\vec{\omega}_Z$. 262

13.2 Perturbing the Input Parameters 265

13.3 W Mass Fit Using Perturbed Input Parameters, $\vec{\omega}_W$ 267

13.4 Systematic Uncertainties on the W Mass 268

13.4.1 Energy Scale 268

13.4.2 Energy Scale Non-linearity 271

13.4.3 Monte Carlo Input Parameters 273

13.4.4 Backgrounds 274

13.4.5 Electron Resolution 274

13.4.6 Parton Distribution Functions 275

13.4.7 Monte Carlo Statistical Uncertainty 277

13.5 Checks on the W Mass Fits 278

13.5.1 M_W in Bins of $|\vec{U}|$ and $U_{||}$ 278

13.5.2 M_W Fit Using E_T and $\not{E}_T$ Distributions 282

13.5.3 M_W Fit with Higher E_T and $\not{E}_T$ Cuts 284

13.5.4 M_W Fit for Different M_T Boundaries 284

13.5.5 Check of Bias from the Fitting Procedure 285

13.5.6 Check of Monte Carlo Calculation of Statistical Uncertainty . 286

14 Conclusion **287**

A Summary of Monte Carlo Input Parameter Results **290**

B Discussion of Discrepancy Between E/p and M_Z **293**

B.1 Is the Discrepancy Caused by Tracking? 296

B.2 Is the Problem the E/p Fitting Procedure? 300

B.3 New Physics? 306

B.4 Conclusion 309

Bibliography **310**

List of Figures

1.1 Schematic Diagram of W Production at $p\overline{p}$ Collisions. 2

1.2 Predicted Values for M_W as a Function of M_{TOP}, for Different Values of M_{HIGGS} 6

1.3 Predicted Values for M_W as a Function of the Higgs Mass 7

1.4 Previous Measurements of the W Mass, this Measurement, and the World Average 10

1.5 Jacobian Edge of E_T Distribution 13

2.1 Schematic Diagram of Fermilab Accelerator Complex 20

2.2 Schematic Diagram of CDF 25

2.3 CTC Cross Section 27

2.4 Schematic of Track Parameters 29

2.5 z Distribution of Event Vertices 32

2.6 CEM and CHA Wedges 35

2.7 Level 2 Efficiencies 45

3.1 qD_0 and Z_0 Relative to Event Vertex 54

3.2 Effect of the Beam Constraint 57

3.3 E_T of Neighboring Towers vs X_{strips} 59

3.4 Sinusoidal P_T Correction 63

3.5 Invariant Mass Distribution of $J/\psi \rightarrow \mu\mu$ Events. 64

3.6 CEM Energy Scale Time Dependence 66

3.7 Mean E/p vs X_{strips} 68

3.8 Mean E/p vs Z_{strips} 69

3.9 Electron Corrections and E/p With and Without Corrections 71

3.10 Mean E/p vs $\sum E_T$ 74

3.11 E_T, $\not{E}_T$, and M_T for the $W \rightarrow e\nu$ Sample 79

3.12 M_Z Shape for Signal and Background in the $Z \rightarrow ee$ Sample 81

4.1 Locations of Second Track in $W \rightarrow e\nu$ Events (With No Lost Z Cut) 84

4.2 Invariant Mass of Second Track and Primary Electron (With No Lost Z Cut) 86

4.3 $U_{||}$, $U_{\perp}$, and M_T for the Lost Z Background 89

4.4 M_T Without the $|\vec{U}| < 20$ GeV Cut, and $\Delta\phi$(e,jet) for the Normal $W \rightarrow e\nu$ Sample and for the Very Low M_T Events 91

4.5 E/p and $\frac{E_{had}}{E_{EM}}$ for Very Low M_T Events 92

4.6 M_T vs $|\vec{U}|$ for Data and QCD Background 94

4.7 $\frac{E_{had}}{E_{EM}}$, Isolation, $q\Delta x$, and χ^2_{strips} 96

4.8 Measured QCD Background Fraction 98

4.9 $U_{||}$, $U_{\perp}$, and M_T for the QCD Background 99

4.10 $U_{||}$, $U_{\perp}$, and M_T for the τ Background 101

5.1 Feynman Diagram of W Production 106

5.2 Collins-Soper Frame 118

5.3 Generated Quantities for $W \rightarrow e\nu$ Events: Boson P_T, Lepton P_T, Boson Rapidity, Lepton Pseudorapidities 120

5.4 Internal Bremsstrahlung Distributions 122

5.5 Generated W and Z P_T Distributions and Ratios 125

6.1 Radial Distribution of Bremsstrahlung in the Monte Carlo 134

6.2 E/p Distribution of Data, and X_0 Distribution of Monte Carlo 135

6.3 E_T of Fake Clusters 144

6.4 Mean E_T of Fake Clusters vs $\Delta\phi$, $|\vec{U}|$, and $\sum E_T$ 145

6.5 N_{tracks} Failure Rate vs $\Delta\phi$, $|\vec{U}|$, and $\sum E_T$ 149

6.6 P_T of Photon Conversion Track in Monte Carlo Events That Fail the N_{tracks} Cut 151

7.1 Fitted Z P_T Distribution 156

8.1 $\sum E_T$ shape of W and Z Data 161

8.2 Underlying Event Resolution vs $\sum E_T$ for Minimum Bias Data 166

8.3 Mean of U_1 vs Z P_T With Fit Result Overlaid 171

8.4 Residuals of Final U_1 and U_2 Fits to the Data 173

8.5 U_1/σ_{mb} in Four Z P_T Regions 174

8.6 U_2/σ_{mb} in Four Z P_T Regions 175

8.7 Gaussian Fits for U_1/σ_{mb} and U_2/σ_{mb} vs Z P_T 176

9.1 $|\vec{U}|$ for $W \rightarrow e\nu$ Data and Monte Carlo 187

9.2 $U_{||}$ for $W \rightarrow e\nu$ Data and Monte Carlo 188

9.3 $|U_{\perp}|$ for $W \rightarrow e\nu$ Data and Monte Carlo 189

9.4 E_T for $W \rightarrow e\nu$ Data and Monte Carlo 192

9.5 $\not\!\!E_T$ for $W \to e\nu$ Data and Monte Carlo 193

9.6 M_T for $W \to e\nu$ Data and Monte Carlo 194

9.7 $U_{||}$ for $65 < M_T < 70$ and $70 < M_T < 75$ GeV for Data and Monte Carlo 196

9.8 $U_{||}$ for $75 < M_T < 80$ and $80 < M_T < 85$ GeV for Data and Monte Carlo 197

9.9 $U_{||}$ for $85 < M_T < 90$ and $90 < M_T < 100$ GeV for Data and Monte Carlo 198

9.10 Mean $U_{||}$ between ± 20 GeV vs M_T for Data and Monte Carlo 200

9.11 Mean $U_{||}$ between ± 10 GeV vs M_T for Data and Monte Carlo 201

9.12 $U_{||}$ for $0 < |\vec{U}| < 5$ and $5 < |\vec{U}| < 10$ GeV for Data and Monte Carlo . 202

9.13 $U_{||}$ for $10 < |\vec{U}| < 15$ and $15 < |\vec{U}| < 20$ GeV for Data and Monte Carlo 203

9.14 Mean $U_{||}$ between ± 20 GeV vs E_T for Data and Monte Carlo 205

10.1 $1-$ and $2-\sigma$ Contours for the Energy Scale and κ as Determined from the Z Mass 209

10.2 Best fit for Z mass, Data and Monte Carlo 211

10.3 Mean of M_Z as a Function of Energy Scale 213

10.4 Integrated M_Z Distribution for Data and Monte Carlo 215

10.5 Kolmogorov-Smirnov Statistic vs CEM Scale for M_Z 217

11.1 χ^2_{strips} and L_{share} for Z Data in Two E/p Regions 223

11.2 f_{TAIL} vs f_{BACK} for L_{share} and χ^2_{strips} Regions 225

11.3 f_{TAIL} and Mean E/p vs $< X_0 >$ for $W \to e\nu$ Monte Carlo 226

11.4 E/p Distribution with Gaussian Fit Overlaid, and M_T Distribution for Low and Peak E/p Events 228

11.5 $M_T(track)$ and $\Delta\phi(jet - electron)$ for low E/p and peak E/p events 230

11.6 N_{stereo} and N_{axial} for low E/p and peak E/p events 231

11.7 Fitted Values for $\sigma(1/P_T)$ as a Function of the Monte Carlo Value for κ 234

11.8 Fitted Values for the Energy Scale as a Function of the Monte Carlo Value for κ 236

11.9 Best Fit E/p Distribution with Data Overlaid for W Events 238

11.10 Best Fit E/p Distribution with Data Overlaid for W events on Log Scale, and Residuals 239

11.11 Mean of Monte Carlo E/p vs Monte Carlo Energy Scale 240

11.12 Best Fit E/p Distribution with Data Overlaid for Z Events 243

11.13 Best Fit for Geometric Mean of E/p for $Z \rightarrow ee$ Events with Data Overlaid 245

12.1 Comparison of E_T Distributions for Electrons from W and Z Data . . 248

12.2 <E/p> vs E_T for W and Z Events 252

12.3 <E/p> vs E_T for W and Z Events 254

12.4 $< E_T >$ and <E/p> vs $U_{||}$ for $W \rightarrow e\nu$ Events 256

12.5 <E/p> vs $< E_T >$ for $U_{||}$ Bins for $W \rightarrow e\nu$ Events 258

13.1 Fitted M_W and , $_W$ Using Inputs from Z fits, and Variation from Parameter Uncertainties 264

13.2 Binned Likelihood of M_T Distribution as a Function of M_W 269

13.3 Fitted Results for M_W as a Function of the Energy Scale 270

13.4 Shift in Fitted Mass For Different Parton Distribution Functions . . . 276

13.5 M_T Distributions in Bins of $|\vec{U}|$, for $W \rightarrow e\nu$ Data and Monte Carlo . 280

13.6 M_T Distributions in Bins of $U_{||}$, for $W \rightarrow e\nu$ Data and Monte Carlo . 281

13.7 Fitted results for M_W in Bins of $|\vec{U}|$ and $U_{||}$ 283

B.1 Summary of Measured Values for M_Z with CDF Data. 295

B.2 Measured J/ψ Mass as a Function of Muon P_T. 298

List of Tables

1.1 Previous Measurements of the W Mass 9

1.2 Outline of the Paper 18

3.1 List of Cuts for W Decays 75

3.2 List of Cuts for Z Decays 78

4.1 Summary of Background Rates in $W \to e\nu$ Sample 103

5.1 Flavor Generation Probabilities 116

14.1 Measurement Uncertainties on the W Mass 287

A.1 Summary of Monte Carlo Input Parameters. 290

A.2 Covariance Matrices of Input Parameter Fits to the Z Data. 291

A.3 Covariance Matrix from W and Z Combined Fits. 292

Chapter 1

Introduction to the W Mass Measurement

1.1 W Events at Fermilab

At Fermilab, 900 GeV* beams of protons and anti-protons are collided at a center of mass energy of 1800 GeV. W bosons are produced by hard scatters between the quarks which are inside the protons and anti-protons. Protons and anti-protons are bound states of constituent partons, which are quarks and gluons. A schematic diagram of the W production process is shown in Figure 1.1. The partons are shown as the horizontal lines which are surrounded by ovals, and the ovals represent the protons and anti-protons. In the diagram, the W is produced by the hard scatter of a u quark from the proton with a $\overline{d}$ quark from the anti-proton. The proton and anti-proton remnants consist of the partons which do not participate in the hard scatter. These are spectator particles, and their contribution to the W event is referred to as the

*In this paper, we use units where $\hbar = c = 1$. Energy, momentum, and mass all have the same units.

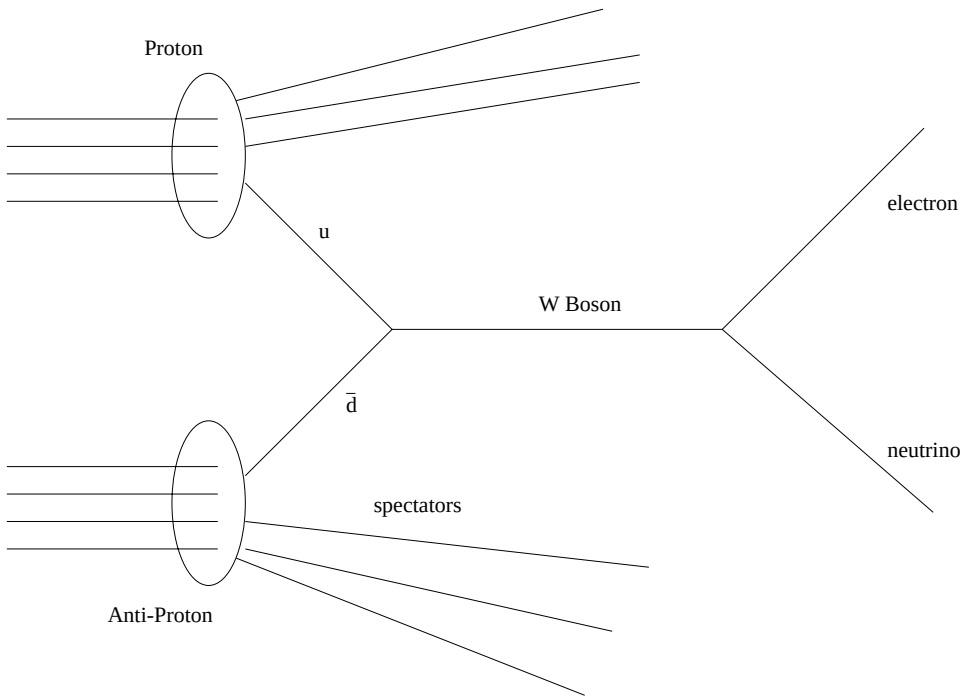

Figure 1.1: Schematic diagram of W production at $p\overline{p}$ collisions. The constituent partons of the protons and anti-protons are shown as the horizontal lines, and the ovals that surround the lines represent protons and anti-protons. A hard scatter between a u quark from the proton and a $\overline{d}$ quark from the anti-proton is shown. These two quarks form a W, and the W is shown subsequently decaying into an electron and a neutrino. The other partons in the proton and anti-proton are spectators to the event, and they form the "underlying event." The protons and anti-protons travel in opposite directions, although this is not indicated in the diagram.

underlying event.

The W is one of the fundamental particles of the current theory of elementary particles, and it is also one of the heaviest. It weighs approximately 80 times the mass of the proton, and roughly 15 times the mass of the next lightest fundamental particle, the b quark. It exists on average for less than 10^{-24} s, before decaying into one of several decay channels.

Because of the short lifetime, there is a natural uncertainty on the mass of the

created W. There is an uncertainty relation of the form

$$\tau \times ,_W = \hbar$$

where $\hbar$ is Planck's constant divided by 2π, τ is the average lifetime of the W, and $,_W$ is a measure of the mass spread of created W events. We refer to $,_W$ as the W width. The masses are produced with a random spread according to a Breit-Wigner distribution. The mean of this distribution is referred to as the W mass, M_W. The width of the distribution is determined by $,_W$ and is roughly 2.5% of M_W.

In approximately 10% of the W events, the W decays into an electron* and a neutrino. We refer to these events as $W \rightarrow e\nu$ decays. These are the events which we use in this paper to measure the W mass. The neutrino is not detected, and passes through the detector without interacting. The electron, on the other hand, leaves a track in the tracking chamber, and also deposits its energy in the calorimeters that surround the interaction region. We use the electron energy, as well as information from other particles associated with the W production, to deduce the W mass.

We use CDF Run 1B data to measure the W mass. The Run 1B data represent a ~ 4 fold increase in statistics over the previous run at Fermilab, Run 1A. We expect the 1B measurement uncertainty to be roughly half the previous CDF measurement.

1.2 Theoretical Motivation and Historical Overview

The current unified theory of electroweak interactions (the "Standard Model") was first developed in the sixties [1, 2, 3, 4]. The theory predicts the existence of three

*We will use the word electron to refer to both the electron and its anti-particle, the positron.

heavy gauge bosons: two charged bosons ($W^{\pm}$) and one neutral (Z), which couple to both leptons and quarks. If we write the coupling strength of the W boson to fermions as g, then the theory connects the electromagnetic coupling to the weak coupling as

$$g = \frac{e}{\sin\theta_W} \tag{1.1}$$

where e is the electric charge of the charged leptons, and $\sin\theta_W$ is an undetermined parameter of the theory. The theory further makes the remarkable prediction that

$$M_W / M_Z = \cos\theta_W \tag{1.2}$$

which relates the masses of the bosons to the strength of the weak coupling. That the masses are related to the coupling strength is a consequence of the boson couplings to the Higgs field. The Higgs field has a non-zero vacuum expectation value, and the masses of the bosons are proportional to their couplings to the Higgs field. The Higgs field is introduced into the theory to allow the bosons to have mass while retaining the renormalizability of the theory.

The theory replaced Fermi's four-point interaction model of muon decay. In the Standard Model, muon decay occurs through the production of an off-shell W and a neutrino, with the W further decaying to an electron and a second neutrino. In Fermi's theory, the muon decay rate is proportional to the Fermi constant, G_F*. At tree-level in the Standard Model, the weak coupling g is related to the Fermi constant through the relation

$$G_F = \frac{\sqrt{2}g^2}{8M_W^2} = \frac{\pi\alpha}{\sqrt{2}M_W^2\sin^2\theta_W} \tag{1.3}$$

*The muon decay rate is well measured, and the Fermi constant is currently known to a part in one hundred thousand [5].

where $\alpha = e^2/4\pi$ is the fine structure constant. This equation puts limits on the allowed size of the W mass. Since $|\sin\theta_W|$ is always less than 1, we have $M_W^2 > \pi\alpha/\sqrt{2}G_F$. Reference [2] predicted $M_W > 40$ GeV, $M_Z > M_W$ and $M_Z > 80$ GeV. The last two predictions use Equation 1.2 and the inequality $|\sin\theta\cos\theta| < 0.5$.

Higher order corrections change the tree-level relations of Equations 1.2 and 1.3. The calculation of the muon decay rate in the Standard Model includes loop corrections to the W propagator, evaluated at low momentum transfer. The loop corrections include tb loops, as well as loops which include the Higgs particle. In the on-shell renormalization scheme, Equation 1.2 is correct at all orders in the coupling constants, while Equation 1.3 is altered to

$$G_F = \frac{\pi\alpha}{\sqrt{2}M_W^2\sin^2\theta_W}\frac{1}{1-\Delta r} \tag{1.4}$$

where Δr accounts for the radiative corrections [6, 7, 8]. This equation relates M_W to the quantities G_F, α, and M_Z. M_Z is included through Equation 1.2. Δr depends on all the masses and couplings in the theory, and also on the masses of the top quark and the Higgs particle.

Figure 1.2 shows the predicted value for M_W as a function of the top quark mass M_{TOP}. The plot is shown for different values of the Higgs mass, M_{HIGGS}. The measurement of the W mass from the current paper is shown at the location of the top quark mass. The world average value for M_W is also shown. Figure 1.3 shows the predicted value for M_W as a function of the Higgs mass. For both plots we use the world average value for the top quark mass.

Figures 1.2 and 1.3 do not rule out any value for the Higgs mass, although a lower value is preferred. Precision measurements of the W mass, in conjunction with

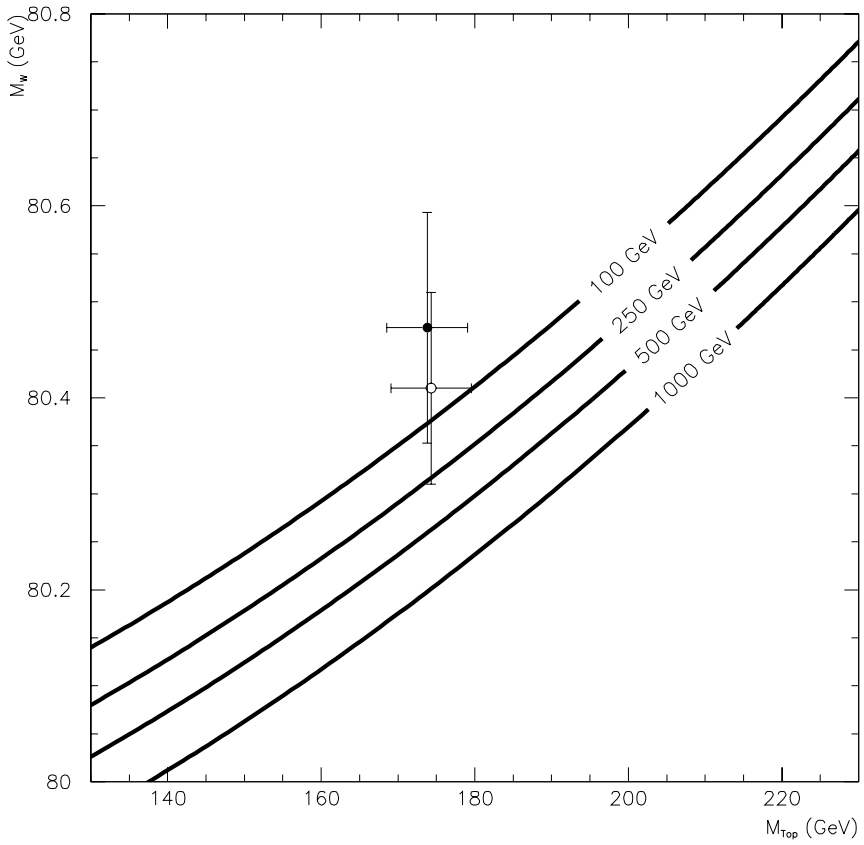

Figure 1.2: Predicted value for M_W as a function of the top quark mass M_{TOP}. The four curves are for a Higgs mass of 100 GeV, 250 GeV, 500 GeV, and 1000 GeV. Two points are shown. The solid circle is the measurement for the W mass from this paper and the open circle is the world average value. Both points are shown at the world average for M_{TOP}, and the open circle is offset slightly to the right to make the error bars easier to see. The world average values are from [5]. The calculation of the curves is from [8].

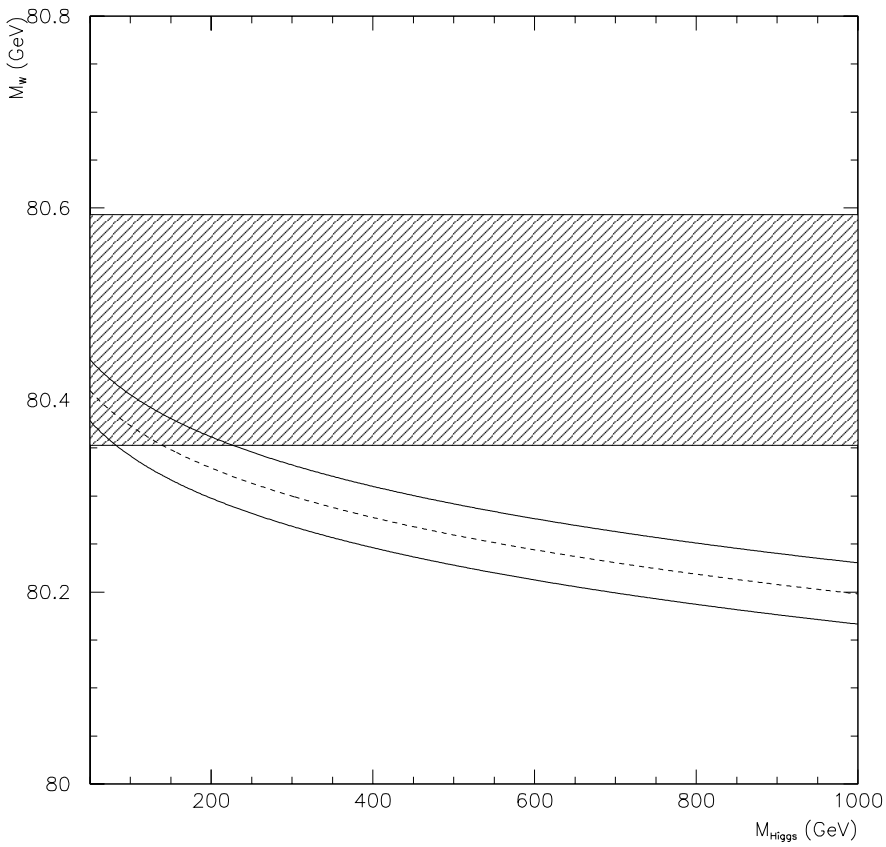

Figure 1.3: Predicted value for M_W as a function of the Higgs mass, M_{HIGGS}. The dashed curve is the predicted value for M_W as a function of M_{HIGGS} for the top quark mass at the world average value of 173.8 ± 5.2 GeV. The solid curves represent the $1-\sigma$ bounds from the uncertainty on the top quark mass. The area filled in with slanted lines represents the $1-\sigma$ uncertainties of the M_W measurement of this paper. The world average values are from [5]. The calculation of the curves is from [8].

precision measurements of the top quark mass, allow tests of the Standard Model at the level of its radiative corrections.

The W and Z bosons were first discovered by UA1 at the CERN $\overline{p}p$ collider in 1983 [9, 10]. Six $W \rightarrow e\nu$ events were observed with the expected signature of a high E_T electron in conjunction with high missing E_T. The W mass was measured to be 81 ± 5 GeV, and the Z mass to be 95 ± 3 GeV. The CERN LEP ring has since produced several million Z events at several center of mass energies around the Z mass. The Z mass is currently known with a precision of roughly one part in ten thousand. The current world average Z mass is 91.187 ± 0.007 GeV [5].

A number of experiments have measured the W mass since 1983, with the goal of improving the precision on the measured mass. The current precision on the W mass is approximately one part in one thousand, roughly ten times worse than the Z mass. Several recent, published measurements are listed in Table 1.1.

Table 1.1 lists measurements from $p\overline{p}$ colliders as well as results from e^+e^- collisions at CERN. At $p\overline{p}$ colliders, the quarks inside the protons produce the W. Since the proton remnants are mostly undetected, the longitudinal momentum of the W is unmeasured; and the longitudinal momentum of the neutrino cannot be reconstructed. The $p\overline{p}$ measurements use transverse quantities to infer the W mass.

At e^+e^- colliders, W's are produced in W^+W^- pairs since charge must be conserved. One can infer the W mass from the measured cross section for W^+W^- pair production. This is the technique used by the CERN experiments with the center of mass energy at 161 GeV, just above the pair production threshold. One can also measure the W mass with its decay products. In e^+e^- collisions, the longitudinal momentum is known, and the full three vector of the neutrino can be reconstructed. The bottom four measurements in the table calculate an invariant mass of each W

W Mass (GeV)	Events	Decay Channel	Experiment-Year	Reference
79.91 ± 0.39	1,722	$p\overline{p}$: $W \to e\nu, \mu\nu$	CDF-1990	[11]
80.36 ± 0.37	2,065	$p\overline{p}$: $W \to e\nu$	UA2-1992	[12]
80.49 ± 0.23	5,718	$p\overline{p}$: $W \to e\nu$	CDF-1995	[13]
80.31 ± 0.24	3,268	$p\overline{p}$: $W \to \mu\nu$	CDF-1995	[13]
80.35 ± 0.27	5,982	$p\overline{p}$: $W \to e\nu$	D0-1996	[14]
80.44 ± 0.12	28,323	$p\overline{p}$: $W \to e\nu$	D0-1997	[15]
80.40 ± 0.44	23	e^+e^-: $\sigma(W^+W^-)$	OPAL-1996	[16]
80.14 ± 0.35	32	e^+e^-: $\sigma(W^+W^-)$	ALEPH-1997	[17]
$80.80^{+0.48}_{-0.42}$	20	e^+e^-: $\sigma(W^+W^-)$	L3-1997	[18]
80.40 ± 0.45	29	e^+e^-: $\sigma(W^+W^-)$	DELPHI-1997	[19]
80.71 ± 0.35	101	e^+e^-: $WW \to l\nu jj, jjjj$	L3-1997	[20]
80.80 ± 0.34	95	e^+e^-: $WW \to l\nu jj, jjjj$	ALEPH-1998	[21]
80.32 ± 0.31	96	e^+e^-: $WW \to l\nu jj, jjjj$	OPAL-1998	[22]
80.22 ± 0.42	72	e^+e^-: $WW \to l\nu jj, jjjj$	DELPHI-1998	[23]

Table 1.1: Some previous measurements of the W Mass. The table is divided into three sections. The top measurements are from $p\overline{p}$ colliders, and the W mass is inferred from the transverse mass distribution. The next four measurements are from e^+e^- collisions at CERN, at a center of mass energy of 161 GeV, which is just above the threshold energy for W^+W^- pair production. The W mass is inferred from the measured pair production cross section. The bottom measurements are from e^+e^- collisions at CERN at a center of mass energy of 172 GeV; and the W mass is measured from the reconstructed mass of the decay products. Only W mass measurements from recent years are shown. Not all the measurements shown are independent.

event with the W decay products.

The results of Table 1.1 are plotted in Figure 1.4, along with the measurement of this paper, and the world average value. As mentioned above, precision measurements of the W mass can be used to test the Standard Model at the level of its radiative corrections. With precision measurements, the Standard Model can make predictions about the Higgs sector of the model. It is hoped that these predictions can be confirmed or proven wrong by experimental searches for the Higgs particle.

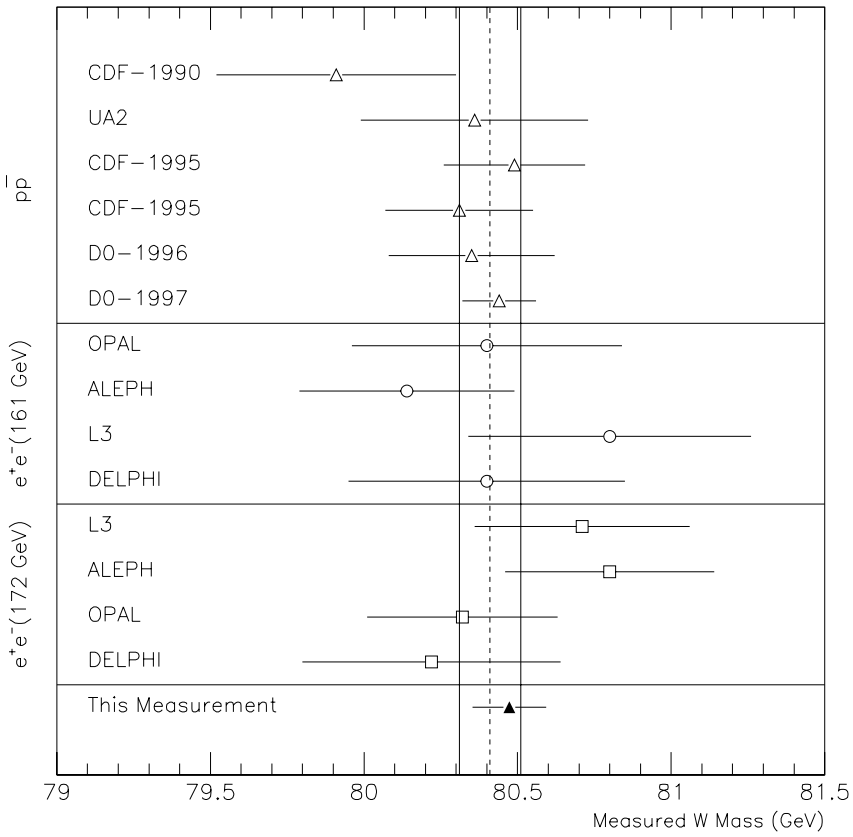

Figure 1.4: Some previous measurements of the W mass, this measurement, and the world average. The top measurements (open triangles) are results from $p\overline{p}$ colliders. The next four (open circles) are results from e^+e^- collisions at CERN, at a center of mass energy of 161 GeV, just above the W^+W^- pair production threshold. These measurements infer the W mass from the pair production cross section. The next four results (open squares) are from CERN with the center of mass energy at 172 GeV. For these results, the W mass is measured by direct reconstruction. All these measurements are summarized in Table 1.1. The bottom result (filled triangle) is the result of this paper. The vertical dashed and solid lines indicate the world average and its $1-\sigma$ uncertainties. This average does not include the D0 − 1997 result. The world average is from [5]. Not all the results shown are independent.

1.3 The Jacobian Edge and the Transverse Mass

In $p\overline{p}$ collisions, quarks inside the protons and anti-protons collide to produce W events. As mentioned above, we cannot measure the longitudinal momentum of the quarks, and therefore we cannot reconstruct the longitudinal momentum of the neutrino. Instead, we rely on transverse quantities to measure the W mass.

In this section we discuss the Jacobian edge of the electron E_T distribution. This edge occurs in the W rest frame but is broadened by the W transverse motion. We also define the transverse mass and show that it provides a correction for the broadening of the Jacobian edge. For this section, we consider the two-body decay $W \to e\nu$. Radiative decays, and the Monte Carlo generator that we use to measure the W mass, are discussed in Chapter 5.

We first consider the case that the W is produced at rest. The differential cross section is

$$\frac{d\sigma}{d(\cos\hat{\theta})} = \sigma_0(\hat{s})(1+\cos^2\hat{\theta}) \tag{1.5}$$

where $\sqrt{\hat{s}}$ is the center of mass energy of the colliding quarks, and where $\hat{\theta}$ is the polar angle of the electron with respect to the proton beamline. The function $\sigma_0(\hat{s})$ is proportional to a Breit-Wigner distribution. This distribution and the cross section are further discussed in Chapter 5.

We define the quantity $E_T \equiv E\sin\theta$. This quantity is useful because it is invariant under longitudinal boosts. In the W rest frame, $E = \sqrt{\hat{s}}/2$ and $E_T = (\sqrt{\hat{s}}/2)\sin\hat{\theta}$. In the rest frame, we can write the cross section which is differential in E_T as

$$\frac{d\sigma}{dE_T} = \frac{2}{\sqrt{\hat{s}}}\frac{d\sigma}{d(\sin\hat{\theta})} \tag{1.6}$$

$$= \frac{2}{\sqrt{\hat{s}}}\frac{d\sigma}{d(\cos\hat{\theta})}\left|\frac{d(\cos\hat{\theta})}{d(\sin\hat{\theta})}\right| \tag{1.7}$$

$$= \frac{2}{\sqrt{\hat{s}}}\sigma_0(\hat{s})(1+\cos^2\hat{\theta})|\tan\hat{\theta}| \tag{1.8}$$

$$= \sigma_0(\hat{s})\frac{4E_T}{\hat{s}}(2-4E_T^2/\hat{s})\frac{1}{\sqrt{1-4E_T^2/\hat{s}}} \tag{1.9}$$

For the transition from Equation 1.7 to 1.8 we use the above formula for $d\sigma/d(\cos\hat{\theta})$, and we also use the formula $|d(\cos\hat{\theta})/d(\sin\hat{\theta})| = |\tan\hat{\theta}|$. For Equation 1.9 we use the formula $\sin\hat{\theta} = E_T/E = 2E_T/\sqrt{\hat{s}}$. Equation 1.9 is independent of the longitudinal momentum of the W since E_T and $\hat{s}$ are invariant under longitudinal boosts.

Equation 1.9 has a singularity at $E_T = \sqrt{\hat{s}}/2$. This is also the maximum value for E_T for a given value of $\sqrt{\hat{s}}$. Thus, for a fixed value of $\sqrt{\hat{s}}$, the E_T distribution has an infinitely sharp edge at $\sqrt{\hat{s}}/2$. This edge is referred to as the Jacobian edge, since it derives from the Jacobian factor $d(\cos\hat{\theta})/d(\sin\hat{\theta})$. If we distribute $\hat{s}$ according to the Breit-Wigner shape, instead of using a fixed value, then the singularity in the E_T distribution is made finite. There is still, however, a sharply falling edge in the distribution, which occurs at half the W mass. The sharpness of the falling edge is determined by the W width. Figure 1.5 shows the rest frame E_T distribution for a fixed value of $\sqrt{\hat{s}}$. It also shows the E_T distribution where $\sqrt{\hat{s}}$ is distributed according to a Breit-Wigner shape.

The transverse motion of the W further reduces the sharpness of the Jacobian edge. In the lab frame, the W is not produced at rest, and the electron E_T is

$$\vec{E}_T \approx \vec{E}_T^{rest} + \frac{1}{2}\vec{P}_T^W \tag{1.10}$$

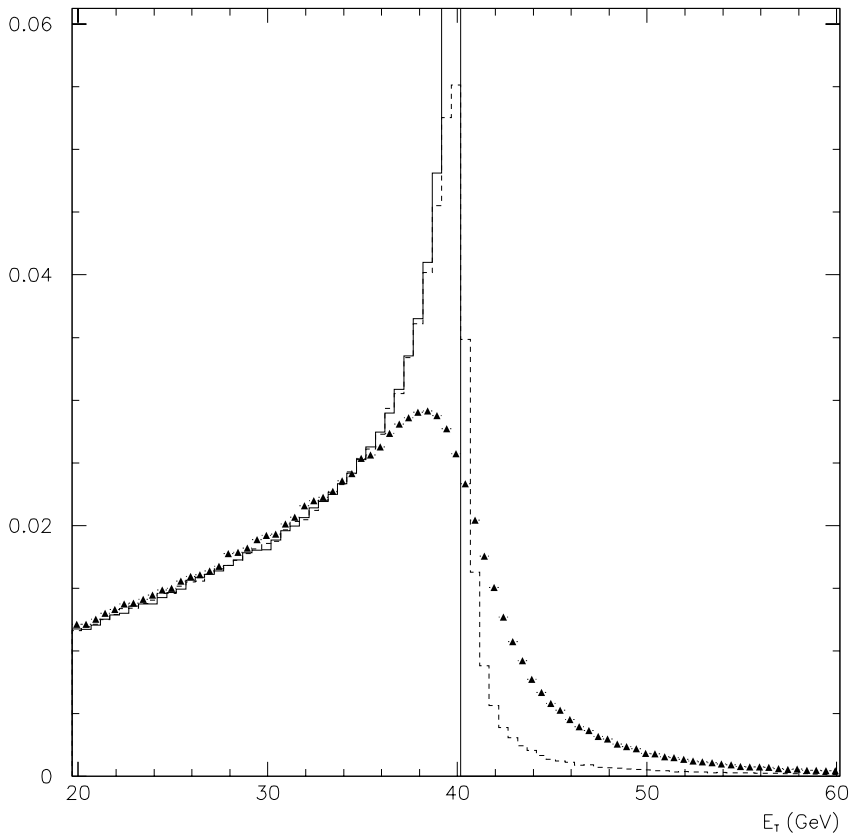

Figure 1.5: The Jacobian edge of the electron E_T distribution, for $W \to e\nu$ decays. The solid curve is for a W with no transverse momentum, and with $\sqrt{\hat{s}}$ fixed at $M_W = 80.35$ GeV. The dashed curve is the same distribution but with $\sqrt{\hat{s}}$ distributed according to a Breit-Wigner shape with mass 80.35 GeV and width 2.09 GeV. The triangles are the electron E_T shape in the lab frame. This shape includes the effect of the W transverse motion, and $\sqrt{\hat{s}}$ is distributed according to the Breit-Wigner distribution.

where $\vec{E}_T^{rest}$ is the electron transverse momentum in the W rest frame, and $\vec{P}_T^W$ is the boson transverse momentum. This equation is accurate to first order in the ratio of the W P_T to the W energy. The magnitude of $\vec{E}_T$ is given by

$$E_T \approx E_T^{rest} + \frac{1}{2} P_{||}^W \tag{1.11}$$

where $P_{||}^W$ is $\vec{P}_T^W$ projected along the electron direction. This equation is accurate to first order in $|\vec{P}_T^W|/E_T^{rest}$.

The W P_T can be large, and the W P_T significantly washes out the Jacobian edge. This is shown in Figure 1.5, which shows the lab frame E_T distribution compared to the rest frame distribution. The falling edge in the lab frame is significantly wider.

From Equation 1.11 we see that the lab frame E_T has a first order dependence on the W P_T. If we use the edge of the E_T distribution to determine the W mass, then we will have a strong dependence on the W P_T distribution. To reduce this dependence we use the transverse mass instead. The transverse mass is defined as [24, 25]

$$M_T \equiv \sqrt{(E_T + E_T^\nu)^2 - |\vec{E}_T + \vec{E}_T^\nu|^2} \tag{1.12}$$

where $\vec{E}_T$ is the electron transverse momentum and $\vec{E}_T^\nu$ is the neutrino transverse momentum. E_T and E_T^ν are the magnitudes of the respective vector quantities. The transverse mass has the form of an invariant mass without any longitudinal information. For the case that the longitudinal momentum of the electron and neutrino are both zero, M_T is identical to the invariant mass.

The variable M_T is useful because it has a second order dependence on the W P_T.

To see this, we use the relation

$$\vec{P}_T^W = \vec{E}_T + \vec{E}_T^\nu \tag{1.13}$$

We can replace $\vec{E}_T^\nu$ by $\vec{P}_T^W - \vec{E}_T$ everywhere in the definition of M_T. Expanding Equation 1.12 to first order in $|\vec{P}_T^W|/E_T$, we get the approximation

$$\frac{1}{2}M_T \approx E_T - \frac{1}{2}P_\parallel^W \tag{1.14}$$

We compare this to Equation 1.11, which is also accurate to first order in $|\vec{P}_T^W|/E_T$. We get the relation

$$\frac{1}{2}M_T \approx E_T^{rest} \tag{1.15}$$

where E_T^{rest} is the electron E_T in the W rest frame. The corrections to this equation are second order in $|\vec{P}_T^W|/E_T$. Thus, to first order in the W P_T, we expect the transverse mass to have the sharp Jacobian edge that is characteristic of the electron E_T distribution in the boson rest frame.

In practice, however, our measurement of the W P_T is biased low. On average the measured W P_T is $\sim 50\%$ of the correct W P_T. We do not scale our measured W P_T since this measurement has a large resolution which we do not want to scale. When we construct the transverse mass distribution with measured quantities, we do not fully recover the Jacobian edge. The definition of M_T using measured quantities is presented in Chapter 3.

In this paper, we use the M_T distribution to measure the W mass. Since the M_T distribution using measured quantities does not fully reconstruct the Jacobian edge, our W mass fit has a residual dependence on the boson P_T shape. This dependence

is weaker than first order but stronger than second.

1.4 Measurement Overview

An outline of the paper is shown in Table 1.2. The paper is divided into five main parts, which are summarized in the table. The five parts are

Introduction Chapter 1.

Data Chapters 2 to 4. In Chapter 2 we discuss the Fermilab accelerator and the CDF detector. We emphasize those parts of the detector which relate to the measurement of the W mass in the electron channel. We also describe the triggers that contribute to the $W \rightarrow e\nu$ sample. In Chapter 3 we define the variables that we use to describe the W event, and we present a number of corrections that are applied to the data. We also discuss the various cuts that are used to extract $W \rightarrow e\nu$ and $Z \rightarrow ee$ samples from the data. In Chapter 4 we measure the fraction of background that remains in the $W \rightarrow e\nu$ data sample.

Simulation Chapters 5 to 9. We use the M_T distribution to measure the W mass. A significant part of the paper is the simulation of the measured M_T distribution. There are several inputs to this simulation.

1. Chapter 5: Event generation. The generation of W and Z events is discussed. The generation includes both the production of the bosons at 1.8 TeV $p\overline{p}$ collisions and the radiative decay of the bosons, $W \rightarrow e\nu\gamma$ and $Z \rightarrow ee\gamma$.

2. Chapter 6: Electron measurement. We simulate the electron energy and momentum measurements. This includes the effects of measurement res-

olution, photon bremsstrahlung, underlying event energy, and cut biases. We leave the determination of the energy scale to a later chapter.

3. Chapter 7: Z P_T determination. The Z P_T distribution is an input to the Monte Carlo. We use the electron simulation to match the Monte Carlo Z P_T shape to the data Z P_T shape.

4. Chapter 8: Underlying event and recoil energy. We simulate the energy from multiple interactions and the proton remnants, and we also simulate the measurement of the energy which recoils against the boson P_T. The measurement of the recoil energy is our only direct measurement of the W P_T.

5. Chapter 9: Comparison of data and Monte Carlo. We use the simulation of the preceding chapters to compare various distributions of the Monte Carlo with the $W \rightarrow e\nu$ data.

Energy Scale Chapters 10 to 12. We have not yet determined an absolute energy scale for the electron measurement. We determine the energy scale with the invariant mass of $Z \rightarrow ee$ events. We also determine the energy scale with the E/p distribution. The E/p distribution compares the calorimeter measurement of the electron energy with the tracking chamber measurement. We use E/p to tie the calorimeter energy scale to the CTC energy scale. The E/p result for the energy scale differs significantly from the Z mass result. This discrepancy is not understood, and it is discussed in Appendix B. We use the Z mass to set the energy scale for the final W mass measurement. In this way, our energy scale determination is separated from potential complications in the tracking measurement. The E/p distribution is also used to measure a non-linearity in

Introduction	
	Chapter 1: Introduction
Data	
	Chapter 2: The accelerator and the CDF detector
	Chapter 3: W and Z data samples
	Chapter 4: Background rates
Simulation	
	Chapter 5: Event generation
	Chapter 6: Simulation of electron measurement
	Chapter 7: Boson P_T distribution, fit to the Z data
	Chapter 8: Underlying event and recoil energy
	Chapter 9: Comparison of data and Monte Carlo
Energy Scale	
	Chapter 10: Energy scale with M_Z
	Chapter 11: Energy scale with E/p
	Chapter 12: Non-linearity in Energy Scale
W Mass Fit	
	Chapter 13: Fits for M_W
	Chapter 14: Conclusion

Table 1.2: Outline of the paper.

the CEM energy scale, which is the subject of Chapter 12.

W Mass Fit Chapters 13 and 14. We use the M_T distribution to fit for the W mass. We also determine the magnitude of various systematic uncertainties and perform a number of checks on the fit. We summarize the paper in Chapter 14.

Chapter 2

Fermilab Accelerator and CDF Detector

The Collider Detector at Fermilab (CDF) surrounds an interaction region where 900 GeV beams of protons and anti-protons collide head-on, with a resulting center of mass energy of $\sqrt{s} = 1800$ GeV. In Section 2.1 we briefly describe the accelerator; and in Sections 2.2, 2.3, and 2.4 we describe the detector, with emphasis on the components which are used in the W mass measurement with electrons. The trigger system and the triggers which contribute to the signal sample are discussed in Section 2.5.

2.1 The Accelerator

The accelerator complex is shown schematically in Figure 2.1. We can use this diagram to follow the protons and anti-protons from their production to their final collision in the center of the CDF detector.

The protons begin as H^- ions, produced from a bottle of hydrogen gas. The ions are accelerated through a 145 m linear accelerator (the Linac) to an energy of 400

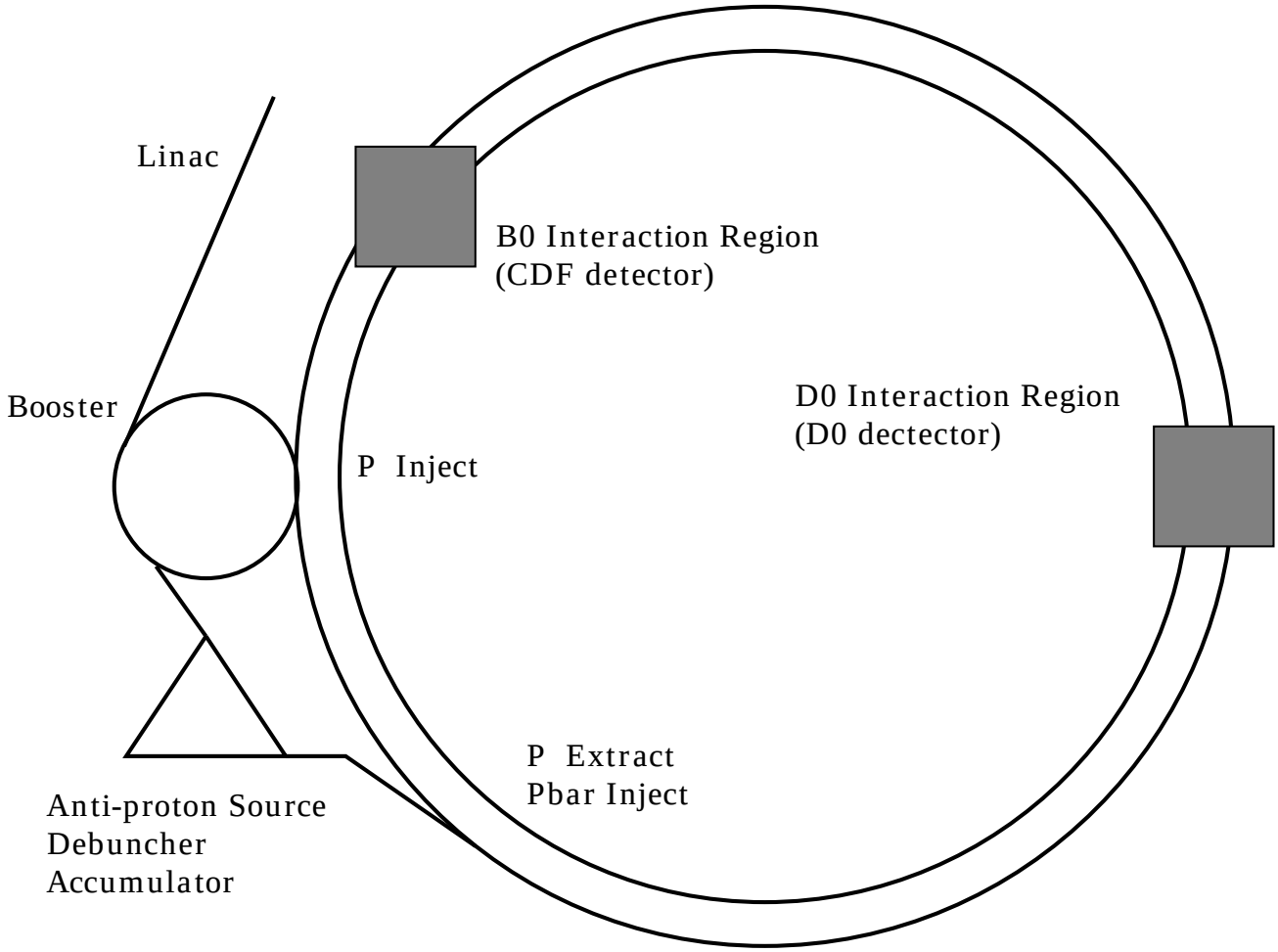

Figure 2.1: Schematic Diagram of Fermilab Accelerator Complex. The largest two circles represent the Tevatron and the Main Ring. The Main Ring lies directly above the Tevatron, and both have a radius of 1 km.

MeV. At the end of the Linac, the electrons from the H^- ions are stripped off by copper foil, and the resulting protons are passed into the Booster ring. The Booster ring is a synchrotron with a 23 m radius, and it takes the protons up to an energy of 8 GeV and also forms them into bunches. The 8 GeV proton bunches are then injected into the 1 km radius Main Ring synchrotron.

The Main Ring is represented schematically in Figure 2.1 by the large circle which lies tangential to the Booster ring. The protons are accelerated by the Main Ring to an energy of 150 GeV, stepping up in energy by 0.5 MeV per turn. To keep the 150 GeV protons travelling in a circle, the Main Ring magnets must generate fields up to 0.7 Tesla.

The 150 GeV proton bunches are formed into one bunch and injected into the evacuated beam pipe of the Tevatron ring. The Tevatron is represented schematically in Figure 2.1 by the circle just inside the Main Ring. In reality, the Tevatron has the same radius as the Main Ring and is located physically just below it. Before the Tevatron further accelerates the protons, six equally spaced proton bunches and also six equally spaced anti-proton bunches are injected. The anti-protons travel in a direction opposite to the protons.

The production of the anti-protons begins with 120 GeV protons which are stripped off the Main Ring and smashed into a tungsten target. Anti-protons are selected from the resulting particles, and they are then passed into the Debuncher. The anti-protons are produced with a spread of momenta, and the Debuncher tightens up the spread of energies through a process known as "stochastic cooling." They are then stored in the Accumulator ring to form a "stack" of anti-protons. Under typical conditions the stack of anti-protons can be built at a rate of $\sim 4 \times 10^{10}$ anti-protons per hour.

When the stack is large enough, six bunches of anti-protons are transferred into

the Tevatron ring. Typical bunch sizes in the Tevatron are 5.5×10^{10} anti-protons per bunch. By comparison, the proton bunches are typically around 2×10^{11} per bunch. The counter-rotating bunches of protons and anti-protons in the Tevatron are then accelerated to 900 GeV.

There are two instrumented collision points along the ring. One is labelled D0 and the other B0. The CDF detector is located at B0. Before the bunches of protons and anti-protons enter the collision points, they are focused by quadrupole magnets. Typical starting luminosities for Run 1B were $1.6 \times 10^{31} cm^{-2} s^{-1}$.

The bunches are spaced so that collisions occur every 3.5 μs, and the dimensions of each bunch are $\sim$ 30 cm along the direction of motion, and $\sim$ 40 μm in the transverse direction.

The bunches continue to cycle around the ring until the luminosity gets too small due to beam spreading, collisions, and beam losses. The bunches typically remain in the ring for $\sim$ 12 hours.

The production of more anti-protons continues even while the bunches cycle around the Tevatron and collide at the interaction point. The goal is to build the Accumulator stack so that when the proton and anti-proton beams are dumped, the stack is large enough to create more anti-proton bunches. The result of this is that even while data is being recorded at CDF and D0, the Main Ring continues to run. The Main Ring lies directly above the Tevatron ring, and at the CDF interaction point would pass straight through the upper half of the detector, if it were not bent upwards and then downwards to pass over the detector. Even though the Main Ring beam does not pass directly through the detector, Main Ring activity can create a spray of undesired energy in the upper parts of the CDF detector, and the trigger includes a veto to avoid part of the Main Ring cycle.

2.2 Detector Overview

The CDF detector is a multi-purpose device designed to detect many of the particles produced in $p\overline{p}$ collisions.

The detector is designed with an overall cylindrical symmetry. The axis of symmetry is labelled the z-axis and points along the direction of the incoming proton beams. The physical location of CDF is such that the z-axis points east. We then define a right handed coordinate system such that the x- and y-axes point north and up, respectively. We define the polar angle θ with respect to the z-axis, and we define "detector pseudorapidity" according to

$$\eta_{detector} = -\log[\tan(\theta/2)] \tag{2.1}$$

We will often use $\eta_{detector}$ to label the physical location of a particular part of the detector. The origin of coordinates is the physical center of the detector, which is the nominal interaction point.

Figure 2.2 shows a schematic of the rz-view of the detector, for $x = 0$. In the diagram the nominal interaction point is along the beamline in the bottom right hand corner. The detector has an overall forward-backward symmetry, and only the forward part of the detector is shown.

A particle which is produced at the origin and which has high enough transverse momentum will pass through three separate central tracking devices, which are labelled in the diagram as the Silicon Vertex Detector, the Vertex TPC, and the Central Tracking Chamber. These are discussed in Section 2.3. The trackers are immersed in a 1.4 Tesla magnetic field which is produced by a superconducting solenoidal magnet.

Outside the solenoid is the Central Electromagnetic Calorimeter. This is the

device that is used to measure the energy of the primary electrons produced in the $W \rightarrow e\nu$ decay. Other calorimeters also surround the interaction region, and all the calorimeters are used in the $\not{E}_T$ measurement. The calorimeters are discussed in Section 2.4.

The detector also contains muon chambers. These devices allow CDF to identify muons out to $\eta \approx 1.0$, and the forward muon toroids can be used to do measurements with non-central muons. The beam-beam counters, also shown in the diagram, are scintillators located close to the beam line, and they are used to measure the luminosity at the interaction point. For the W mass measurement with $W \rightarrow e\nu$ decays, we will not make use of the muon chambers.

2.3 Tracking

There are 3 primary tracking detectors, and they are used for various purposes at CDF. The SVX, for example, can be used to search for displaced vertices near the beamline. For the W mass measurement, however, we do not need the SVX for that purpose. We use the outermost tracker (the CTC) for the measurement of the primary electron track, and the VTX and SVX are used to provide vertex information. The CTC track is "beam constrained" to point at this vertex, and this produces a significant improvement in the CTC resolution. All three of these trackers are discussed immediately below.

2.3.1 Central Tracking Chamber (CTC)

The Central Tracking Chamber (CTC) is a cylindrically symmetric, open-wire drift chamber that lies just inside the solenoidal magnet, and provides tracking out to

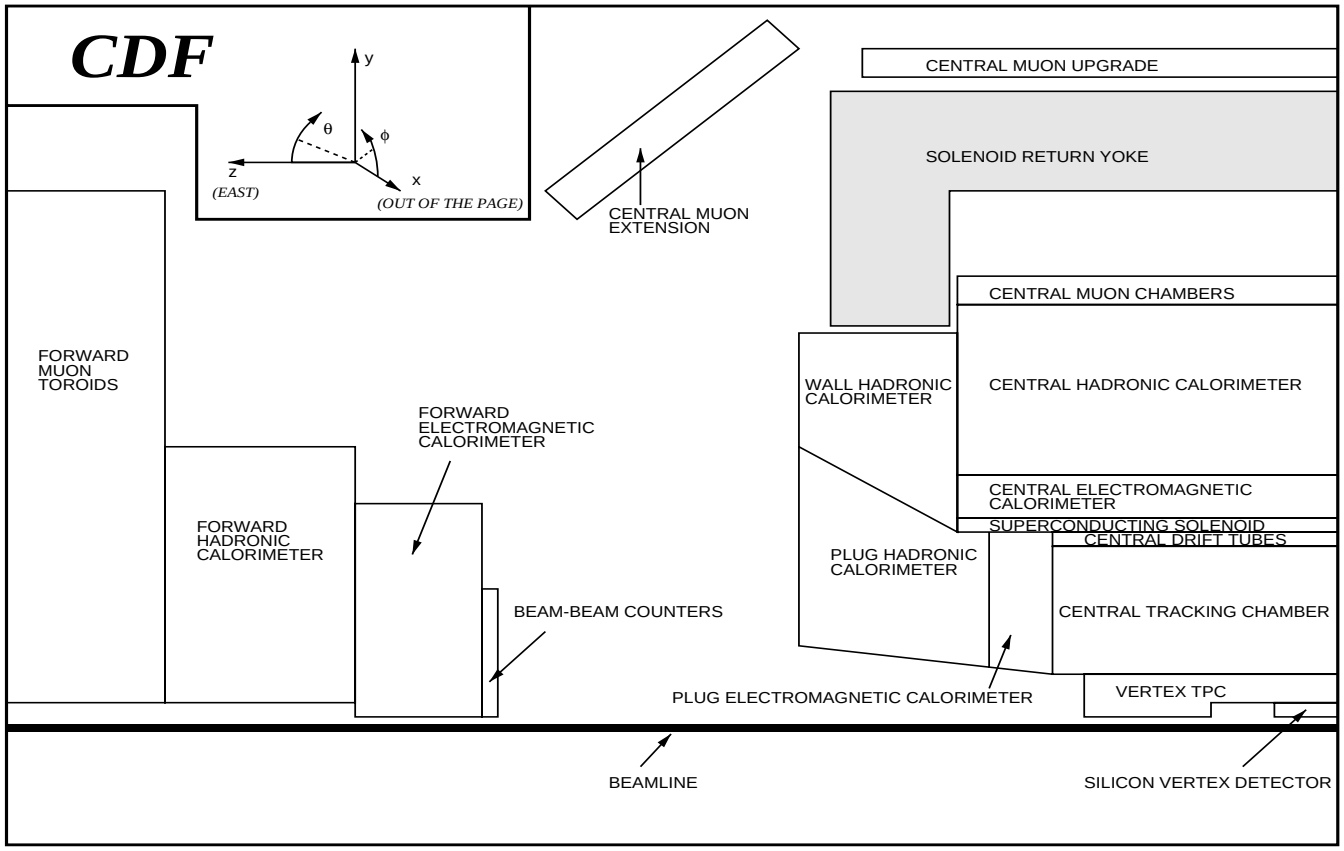

Figure 2.2: Schematic Diagram of CDF. The nominal interaction point is located along the beamline in the bottom right hand corner. There is an overall forward-backward symmetry, and only the forward part of the detector is shown. The coordinate system which CDF uses is shown inset in the diagram.

$\eta_{detector} \sim 1$. It extends 3.2 m in the z-direction, and in the radial direction it covers the region between $r = 28$ and $r = 138$ cm. Wires are stretched along the z-direction between endplates at $z = \pm 1.6$ m.

The chamber consists of 84 layers of sense wires, formed into 9 "superlayers." These are shown schematically in Figure 2.3. The superlayers are numbered from 0 to 8 going from inner to outer radius. The superlayers are sub-divided into cells which contain series of sense wires, field wires, and field-shaping wires. The sense wires in each cell are aligned along a 45° angle with the radial direction. The drift field in each cell is ~ 1350 V/cm, and the field also makes a $\approx 45°$ angle with respect to the radial direction. This angle is chosen so that the crossed electric and magnetic fields produce an azimuthal drift direction. The cells in each superlayer are evenly spaced in azimuth, and going from superlayer 0 to 8, the superlayers contain 30, 42, 48, 60, 72, 84, 96, 108, and 120 cells, respectively.

The 4 odd numbered superlayers are "stereo" superlayers. Each cell in these superlayers contains 6 sense wires, for a total of 24 stereo sense wires, and the wires form an angle with respect to the z-axis of $\pm 3°$. The sign of this angle alternates among the 4 stereo superlayers. The 3° stereo angle provides information about the motion of charged particles in the z-direction, which information would otherwise not be available.

The 5 even numbered superlayers are "axial" superlayers, and each wire in these superlayers is aligned with the z-axis. There are 12 sense wires per cell, for a total of 60 axial wires.

Charged particles pass through the 1.4 Tesla magnetic field along a helical trajectory, making a circle in the xy-plane. The helix is described by 5 "helix parameters,"

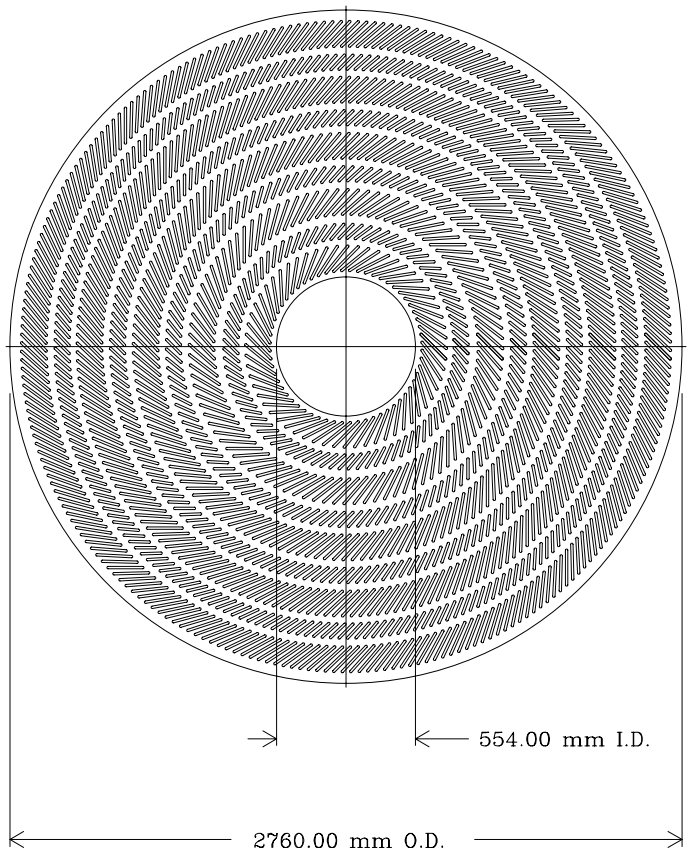

Figure 2.3: xy-view of the CTC. Starting at 0 radius and moving outwards, one crosses the 9 superlayers, starting with superlayer 0. Superlayers 0, 2, 4, 6, and 8 are the "axial" superlayers, and the superlayers 1, 3, 5, and 7 are the "stereo" superlayers. In the azimuthal direction, the wires are grouped into cells of 12 sense wires each for the axial superlayers, and 6 for the stereo. The cells are shown in the diagram and lie at an angle of 45° with respect to the radial direction. The inner diameter (I.D.) and outer diameter (O.D.) are shown on the plot.

namely

$$\{crv, D_0, \phi_0, \cot\theta, Z_0\}$$

The first three parameters describe the circle that the charged particles make in the xy-plane. $|crv|$ is the inverse of the diameter of the circle; $|D_0|$ is the shortest distance from the origin to the circle; and ϕ_0 is the angle of the line tangent to the circle at its point of closest approach to the origin. These three parameters uniquely determine a circle. The definitions of ϕ_0 and D_0 are shown schematically in Figure 2.4

Positive and negative tracks will curve in opposite directions, and crv is signed so that positive tracks have crv positive, and negative tracks have crv negative. The sign convention for D_0 is such that qD_0 is positive if the origin lies outside the circle, and negative otherwise, where q is the charge of the track.

The P_T of the track is proportional to the product of crv^{-1} and the magnetic field. Specifically, for the magnetic field at CDF, it is calculated according to the equation

$$P_T = \frac{2.998 \times 10^{-4} B_z}{2|crv|} = \frac{.002116}{|crv|} \tag{2.2}$$

where B_z is the z-component of the solenoidal field measured in kGauss; and P_T is in GeV and crv is in cm^{-1}. The magnetic field is $B_z = 14.116$ kGauss.

The measured P_T resolution is $\sigma(P_T)/P_T \approx .002 \times P_T$, where P_T is in GeV. This resolution is improved to $\sigma(P_T)/P_T \approx .001 \times P_T$ after the beam constraint, which is discussed in Section 3.1.2 below.

$\cot\theta$ and Z_0 determine the motion of the track in the rz-view. Z_0 is the z-coordinate at the point of closest approach to the z-axis, and θ is the polar angle of the track at that point.

There are $6,156$ sense wires in the CTC, and each is read out by a multi-hit TDC.

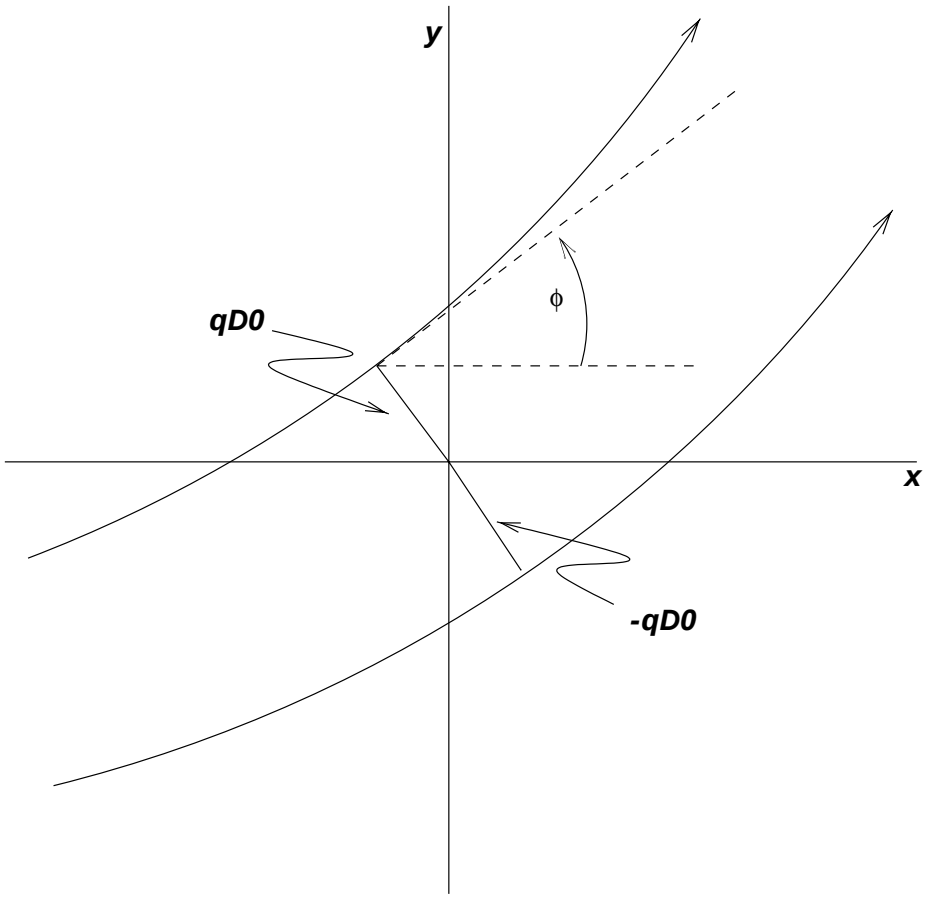

Figure 2.4: Schematic of track parameters. An extrapolation of two sample tracks in the region near the origin are shown. The actual CTC hits occur farther out along the track paths. The tracks trace out an arc of a circle. The diameter of the arc is crv^{-1}. The smallest distance between the origin and the circle is the impact parameter D_0. The sign convention for the impact parameter is such that $q \times D_0$ is positive if the origin lies outside the circle and negative otherwise, where q is the charge of the track. ϕ_0 is the angle of the line tangent to the circle at the distance of closest approach and is shown schematically in the diagram by ϕ.

The TDC data is searched for line segments in each of the 9 superlayers, and these line segments are subsequently combined into tracks. It is not required that all 84 layers be used for a track fit, and the fitting program removes hits with residuals which are too large.

$Z \rightarrow ee$ data has been used to measure the efficiency for finding a CTC track for electrons that pass through all 9 superlayers. This efficiency has been measured to be above 99.5%. Charged particles which are produced in the forward or backward directions may not pass through all 9 superlayers, and the probability of finding these tracks is significantly lower. For example, the probability to find tracks which exit the CTC in the middle of superlayer 4 is $\sim 50\%$. We only use central electrons for the W mass measurement, and we require that the electron tracks geometrically pass through all 9 superlayers. We also use the CTC to search for $Z \rightarrow ee$ background in the $W \rightarrow e\nu$ sample, and for this purpose we consider tracking out to $\eta_{detector} \sim 1.2$.

2.3.2 Vertex Time Projection Chamber (VTX)

The Vertex Time Projection chamber (VTX), which is labelled in Figure 2.2 as "Vertex TPC," is used primarily to reconstruct the z position of primary interactions. The VTX lies just inside the CTC and covers the region in z between $z = \pm 1.4$ m. The active volume of the detector extends approximately from a radius of 7 to a radius of 21 cm.

The VTX is divided in the z direction into 8 separate chambers, each of which forms an octagon centered on the beamline. Each chamber has a central high voltage grid that divides the chamber into two oppositely directed drift regions. The drift direction is along the z-axis, and the 50/50 argon-ethane gas used in the chambers, in conjunction with the 320 V/cm longitudinal electric field produced by the high

voltage grid, produces a drift velocity of 46 μm/ns. The maximum drift distance in the chambers is 15.25 cm, and this is such that the maximum drift time is always less than the 3.5 μs timing between $p\overline{p}$ bunch crossings.

The ionization electrons drift to the endcaps of each chamber, where they encounter rows of sense wires. The endcaps are divided into octants, and each octant contains 24 sense wires which lie in the xy-plane and run parallel to the lines which define the outer boundaries of the octagon. The sense wires cover the region from $r \approx 7$ to $r \approx 21$ cm. The drift is in the $\pm z$ direction, and the timing of the hits and the radial position of the wires give information on the location of the hits in the rz-view.

The rz-view of many reconstructed tracks are combined to determine an event vertex with a resolution of $\sim$ 1 mm. Multiple vertices are often found, and these correspond to multiple interactions occurring during a given bunch crossing. The number of vertices correlates well with luminosity, and for the Run 1B $W \rightarrow e\nu$ sample, the average number of vertices found is 1.8.

For the W mass analysis, we use the VTX only to determine the z location of the event vertex. If the VTX identifies a vertex within ± 5 cm of the Z_0 of the primary electron track, then we use the VTX vertex for the event vertex, and otherwise the event vertex is identified with the Z_0 of the track. If no track is associated with the electron cluster, then the vertex position is taken to be $z = 0$.

The vertex position associated with the primary electron track is referred to by the variable Z_{vertex}. Figure 2.5 shows the z distribution of the event vertices for the $W \rightarrow e\nu$ sample. The longitudinal extent of the proton and anti-proton bunches creates the spread in the vertex positions.

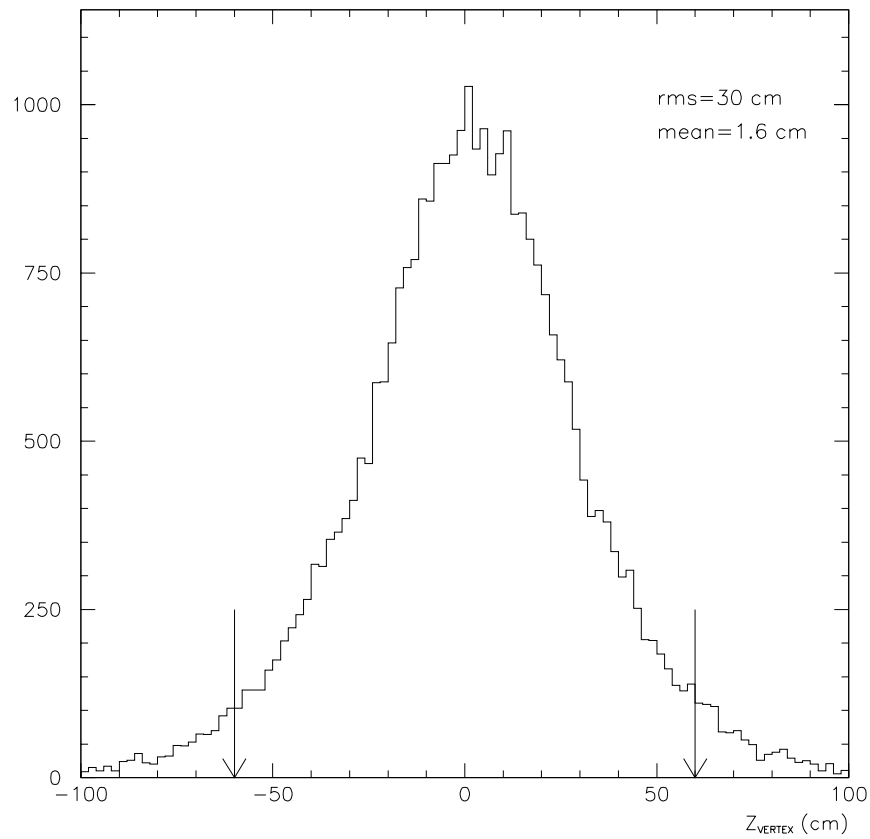

Figure 2.5: z distribution of event vertices for $W \to e\nu$ sample, without the event vertex cut applied. The $W \to e\nu$ sample is described in Chapter 3. The mean and rms of the distribution are shown on the plot. The arrows indicate the cut which is applied in Chapter 3.

2.3.3 Silicon Vertex Detector (SVX)

The Silicon Vertex Detector* (SVX) provides tracking in the $r\phi$ view in the region outside the beampipe. The beampipe has a radius of ≈ 1.5 cm, and the SVX covers a region in radius from 2.86 to 7.87 cm. It is divided into two identical "barrels" which surround the beampipe on opposite sides of the $z = 0$ plane. There is a 2.15 cm gap between the barrels at $z = 0$, which space is needed for read-out cables, and each barrel has an active length in the z direction of 25.5 cm.

The barrels consist of four radial layers of silicon strip detectors, and each layer is divided in azimuth into 30° wedges. The radii of the four layers are 2.86, 4.26, 5.69, and 7.87 cm. The strips extend along the z direction, providing $r\phi$ information only. For each of the 30° wedges, and going from the inner radial layer to the outer, there are 256, 384, 512, and 768 strips, respectively. This results in an intrinsic hit resolution in the $r\phi$ direction of ~ 15 μm.

The proton and anti-proton bunches have longitudinal extents of ~ 30 cm, and the event vertex is roughly distributed as a gaussian distribution of width ~ 30 cm. The SVX extends to ≈ 26 cm, and approximately one third of the data will be produced outside the physical volume of the SVX. For this reason, we do not require SVX information for the reconstructed primary electron tracks in the W mass measurement. We still use the SVX information, but we use it on a run-averaged basis, to determine the position of the beamline.

The nominal beamline is aligned with the z-axis, but in practice the beamline may be offset in radius by ~ 0.2 cm, and the beamline may have a slope such that

*The SVX used in Run 1B is sometimes referred to as SVX′ since it has replaced the silicon vertex detector that was used in Run 1A. The configuration of the detector was largely unchanged, and the major differences are that the 1B SVX has a radiation-hard read-out chip and that the innermost radial layer has been extended to complete azimuthal coverage. We are only using the 1B data, and we only consider the Run 1B implementation of the silicon vertex detector.

the offset radius changes by several microns per cm in the z direction. The SVX is used to calculate these offsets and slopes on a run by run basis. Since many tracks and many events are used for these calculations, the beamlines can be determined with negligible statistical uncertainties.

The run by run SVX determination of the beamline, in conjunction with event by event vertex information from the VTX, is used to calculate a three dimensional origin for each $W \rightarrow e\nu$ event. This information is used to perform a beam constraint on the CTC track associated with the primary electron. While the run-averaged beamlines can be determined with negligible statistical uncertainty, the $r\phi$ determination of the origin for any given event has an intrinsic uncertainty from the ~ 40 μm transverse spread of the proton and anti-proton bunches.

2.4 Calorimetry

There are four different calorimeter systems at CDF, and these provide nearly contiguous coverage out to $|\eta_{detector}| = 4.2$. They are labelled in Figure 2.2 as "central," "wall," "plug," and "forward" calorimeters. Three of the four systems have both electromagnetic and hadronic calorimetry, and all the calorimeters are segmented into towers which point back to the nominal interaction point. We discuss all the calorimeters immediately below. All are used in the $\not\!\!E_T$ measurement, and the central electromagnetic calorimeter provides the energy measurement for the primary electrons in our $W \rightarrow e\nu$ events.

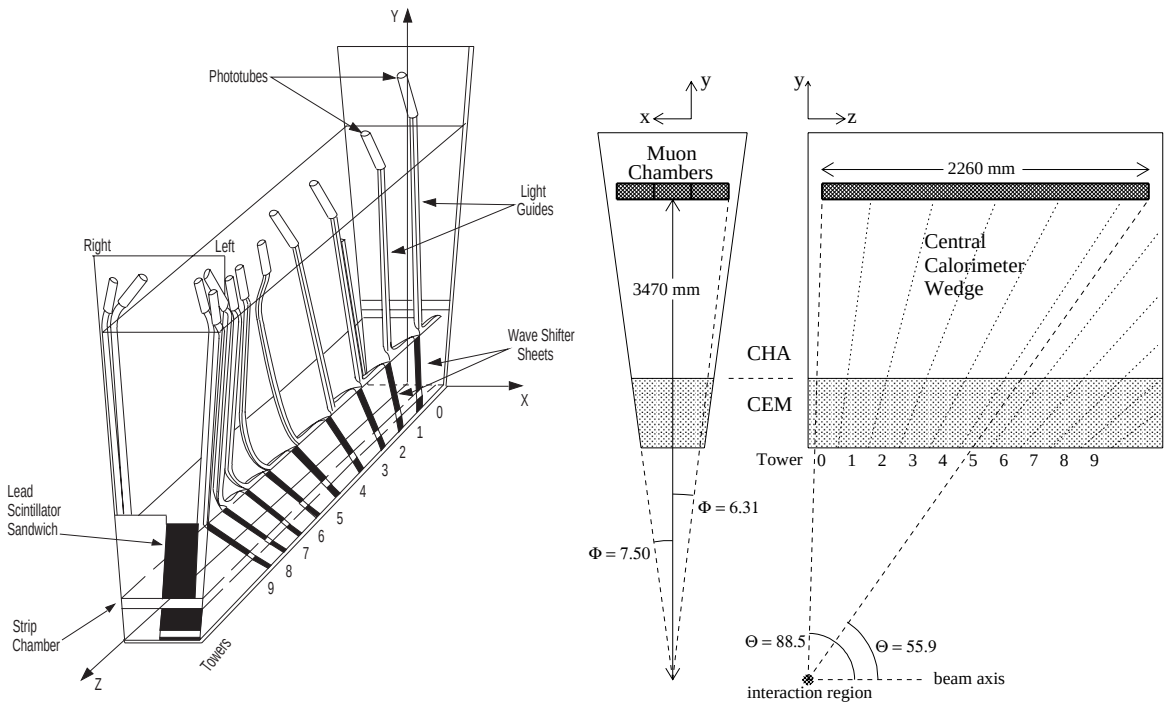

Figure 2.6: Central calorimeter wedges. Both CEM and CHA are shown, as well as the location of the central muon chambers. The left diagram shows the structure of the wave shifters and light guides that collect the scintillator light for the CEM, as well as the phototubes that convert the light to electric signals. The y-axis in the diagrams corresponds to the radial direction, and the x-axis to the azimuthal direction.

2.4.1 Central Electromagnetic Calorimeter (CEM)

The Central Electromagnetic Calorimeter (CEM) is physically separated into two halves, one covering positive $\eta_{detector}$ (east) and one covering negative $\eta_{detector}$ (west). Both halves are divided in azimuth into 24 wedges, subtending 15° each. Each wedge extends along the z-axis for 246 cm and is divided into 10 projective towers of $\approx .1$ units in $\eta_{detector}$. The active volume of both the east and west halves begins at $|z| \approx 4$ cm. The two halves are pushed against each other at $z = 0$, but a dead region remains between them of approximately $\Delta z = 8$ cm. This is known as the 90° crack.

The CEM begins outside the solenoidal magnet, at a radius of 173 cm. It has a

radial thickness of 32 cm and consists of 31 layers of 5 mm thick plastic scintillator interleaved with 30 layers of $\frac{1}{8}$ inch lead sheets. The scintillators are cut into projective towers which are viewed on both sides in azimuth by wave shifter sheets. The light is then collected by light guides and converted to electrical signals by photomultiplier tubes. There are two phototubes per tower, one on either side in azimuth, and the energy deposited by an electromagnetic shower is proportional to the pulse heights. The default calibration is determined from the test beam.

Figure 2.6 shows several views of a 15° wedge. Each wedge also contains hadronic calorimetry and muon chambers. The location of the muon chambers are shown in the figure, but we will not make use of these devices for the W mass measurement with electrons.

The CEM is located lowest in radius in each wedge and is the shaded region in the right and middle drawings of Figure 2.6. The right and left drawings show the tower structure along the z direction. The towers are labelled 0 through 9, and each covers $\Delta\eta_{detector} \approx 0.1$. The diagram shows that tower 9 does not contain as many scintillators as the other towers, and the lead sheets present $\sim 60\%$ of the number of radiation lengths that the other towers present to incoming particles. The light guides and phototubes which read out the towers are pictured in the left diagram, and the location of strip chambers is also visible.

In each wedge, a proportional strip chamber is inserted between the eighth lead layer and the ninth scintillator layer, at a radius of 184 cm. The proportional chamber is composed of a 95%/5% mixture of argon and carbon dioxide. Cathode strips and wires provide information about the electromagnetic shower location and its transverse development. The strips and wires are arranged perpendicular to each other so that one measures the position and development in the z direction, and the

other in the ϕ direction.

Acrylic sheets are substituted for lead sheets at some locations so that the strip chamber always occurs at the shower maximum position of 5.9 radiation lengths, including the solenoid, independent of polar angle. The solenoid presents 1 radiation length to particles travelling in the radial direction. The lead sheets are also adjusted so that each tower presents a total of 18 radiation lengths to electromagnetic particles, independent of the polar angle. The 18 radiation lengths do not include the solenoid, and the number of radiation lengths before the CEM increases as $\sim 1/\sin(\theta)$.

One of the wedges is constructed to allow cryogenic access to the solenoid. This is referred to as the "chimney" module, and we only have towers 0 through 6 of Figure 2.6 for this wedge.

The CEM response was initially measured in the test beam. It was found that the energy resolution is well described by $\sigma(E)/E = 13.5\%/\sqrt{E\sin\theta}$, where E is measured in GeV. We account for tower to tower variations and the uneven effects of aging by introducing a constant term, κ, to the resolution. The energy resolution is then given by

$$(\frac{\sigma}{E})^2 = (\frac{13.5\%}{\sqrt{E\sin\theta}})^2 + \kappa^2 \tag{2.3}$$

We determine κ from the Z data in Chapter 10, and the best fit is $\kappa = (1.6 \pm 0.3)\%$.

2.4.2 Central and Wall Hadronic Calorimeters (CHA and WHA)

The Central Hadronic Calorimeter (CHA) is located directly behind the CEM and is contained in the same physical wedges as the CEM. It has the same tower structure, and it is also shown in the diagrams of Figure 2.6. The right diagram shows that

towers 5 through 9 do not pass entirely through the CHA and that tower 9 misses it altogether. The Wall Hadronic Calorimeter (WHA) makes up for some of this coverage, and the location of the WHA is shown in Figure 2.2. Towers 6 through 9 are continued in the WHA, and two further towers, 10 and 11, have hadronic coverage in the WHA only. Together, the CHA and WHA provide hadronic coverage to $|\eta_{detector}| \approx 1.3$.

The significant difference with the CEM is that instead of lead-scintillator sandwiches, the CHA and WHA are composed of steel-scintillator sandwiches. The CHA is composed of a stack of 32 layers of alternating 2.5 cm steel absorber and 1.0 cm plastic scintillator. The WHA is similarly constructed, but with 15 layers of 5 cm steel and 1 cm scintillator. The CHA layers are stacked in the radial direction, but the WHA layers are stacked in the z direction. As with the CEM, the scintillation light is collected by wave shifters and light guides and is converted to electric pulses by phototubes.

The CHA and WHA stacks contain 4.7 and 4.5 absorption lengths of material respectively. There is a significant amount of material before the CHA. The solenoid and the CEM present ~ 1.2 absorption lengths.

The resolution for central isolated pions is

$$(\frac{\sigma}{E})^2 \approx (\frac{50\%}{\sqrt{E \sin\theta}})^2 + (3\%)^2 \tag{2.4}$$

where E is measured in GeV.

2.4.3 Plug Calorimeters (PEM and PHA)

The Plug Electromagnetic Calorimeter (PEM) covers the region in $|\eta_{detector}|$ between approximately 1.1 and 2.4, and the Plug Hadronic Calorimeter (PHA) covers the region between 1.3 and 2.4. In polar angle, the plug covers the region from roughly 30° down to 10° relative to the beamline. The electromagnetic calorimeter coverage is continuous between the central and plug regions. The towers near the boundaries, however, are not complete towers, and a region of reduced response results. The boundary occurs at a polar angle of $\sim 30°$, and we refer to this region as the 30° crack.

The PEM is composed of two identical modules, one on the east and one on the west, and each module is composed of four quadrants, each of which subtends an azimuthal angle of $\Delta\phi = 90°$. Each quadrant contains 34 layers of proportional tube arrays interleaved with 2.7 mm thick sheets of lead. The sandwiching of the proportional tube arrays and the lead sheets occurs along the z direction, and the arrays and the lead sheets lie in planes of constant z. The lead sheets form ≈ 18 radiation lengths.

The proportional tubes are constructed from conductive plastic and use a 50/50 mixture of argon-ethane gas. Each array of tubes is sandwiched by 1.6 mm thick $G-10$ panels. Pads are etched out of copper plating which is attached to one of the $G-10$ panels on one side of every array, and the pads are etched to form projective towers which have dimensions $\Delta\eta_{detector} \times \Delta\phi = 0.1 \times 15°$.

The pads provide the primary read-out of the energy of the shower. When a shower develops in the calorimeter, charged particles ionize the gas in the proportional tubes. The electrons from the ionization drift towards the wire in the center of the tube, while the positive ions induce a charge on the copper pads. The charge is

amplified and integrated. The magnitude of the collected charge is a measure of the deposited energy from the electromagnetic shower. The pads are ganged together to form three depth measurements, and for the total energy of a shower, all three depth measurements are summed.

$Z \rightarrow ee$ events are used to maintain the PEM calibration, and its resolution has been determined from test beam electrons to be

$$(\frac{\sigma}{E})^2 \approx (\frac{22\%}{\sqrt{E \sin\theta}})^2 + (2\%)^2 \tag{2.5}$$

where E is measured in GeV.

The PHA contains 20 layers of proportional tube arrays interleaved with 5 cm thick steel plates. The PHA also uses a pad read-out, and the pads have the same dimensions as for the PEM. The PHA resolution has been determined from test beam pions to be

$$(\frac{\sigma}{E})^2 \approx (\frac{90\%}{\sqrt{E \sin\theta}})^2 + (4\%)^2 \tag{2.6}$$

where E is measured in GeV.

2.4.4 Forward Calorimeters (FEM and FHA)

The Forward Electromagnetic Calorimeter (FEM) and Forward Hadronic Calorimeter (FHA) are physically separated from the rest of the detector, with the FEM beginning at a location of $|z| = 6.4$ m. They both cover the region in $|\eta_{detector}|$ between 2.4 and 4.2. In polar angle, they cover the region between 10° and 2° relative to the beamline.

The construction of the two detectors is similar to the construction of the plug detectors. Both the FEM and FHA are split into two identical modules, one for the east and one for the west, and the modules are divided into four quadrants of 90°

each. 30 layers of phototube arrays are interleaved with 4.5 mm thick lead sheets for the PEM; and for the PHA, 27 layers are interleaved with 5 cm steel plates. Pads provide the primary read-out, and the pads have been etched to form a projective tower structure with the same dimensions as in the PEM and PHA.

The pads are ganged together to provide two measurements in depth. The energy deposited in a projective tower is the sum of the two depth measurements.

The energy resolutions have been measured with test beam electrons and pions and have been found to be

$$(\frac{\sigma}{E})^2 \approx (\frac{26\%}{\sqrt{E \sin\theta}})^2 + (2\%)^2 \tag{2.7}$$

for the FEM, and approximately

$$(\frac{\sigma}{E})^2 \approx (\frac{137\%}{\sqrt{E \sin\theta}})^2 + (4\%)^2 \tag{2.8}$$

for the FHA, where E is measured in GeV.

2.5 Trigger

The CDF trigger system consists of three levels. Each level is successively more sophisticated and takes a longer time to reach a decision. If all three trigger levels are passed, the event is written out to tape. Each of the levels consists of a logical OR of a number of triggers which are designed to find many types of events, but we will only discuss the triggers which are most likely to find $W \rightarrow e\nu$ and $Z \rightarrow ee$ events.

2.5.1 Level 1

The general requirement of Level 1 is that it make a decision before the next bunch crossing. The bunch crossings occur every 3.5 μs, and a decision of pass or fail should be made within that time period. There are several Level 1 triggers, and the trigger which our central $W \rightarrow e\nu$ events are likely to pass is a requirement placed on the energy of central calorimeter clusters. It is required that a single "trigger tower" have E_T above 8 GeV for the CEM. A trigger tower is the combination of two adjacent towers, where only neighboring towers in the z direction are combined. In Level 1 E_T is defined as $E \sin\theta$ where $\sin\theta$ is a hardware-encoded value for each trigger tower, and the energy measurement is based on "fast-outs." The fast-outs are analog signals from the detector which are only used for making trigger decisions. The values for $\sin\theta$ are calculated using the center of the detector as the origin of coordinates.

If Level 1 is failed, then the electronics which read out the detector are reset in preparation for the next beam crossing. If passed, the read-out electronics hold their current values, and any activity inside the detector is ignored until Level 2 makes a decision.

2.5.2 Level 2

Level 2 takes $\sim$ 20 μs to make a decision, and the next $\sim$ 6 bunch crossings are ignored by the detector. At Level 2, the calorimeter fast-outs are combined by a hardware cluster-finder to form clusters. There are two clustering algorithms. In the first algorithm, a trigger tower which has $E_T > 5$ GeV initiates the formation of a cluster, and this tower is the "seed" tower. Neighboring towers are added to the cluster if they have $E_T > 4$ GeV. In the second algorithm, the seed tower has $E_T > 8$

GeV, and the shoulder towers must have $E_T > 7$ GeV. A list is made of E_T, $\eta_{detector}$, and ϕ of all the clusters.

Level 2 also searches for tracks using fast timing signals from the CTC and a hardware track processor called the Central Fast Tracker (CFT). The CFT has no stereo information available, and it uses hit pattern masks to search for tracks of different momenta. The CFT resolution is $\sim \sigma(P_T)/P_T \approx .035 \times P_T$.

The $W \rightarrow e\nu$ sample relies on two Level 2 triggers, which are labelled *

CEM_16_CFT_12

and

CEM_16_MET_20_XCES

Both require a CEM cluster with E_T above 16 GeV. The first additionally requires that a CFT track with $P_T > 12$ GeV be found at the same ϕ as the cluster, and the second requires $\not\!\!E_T > 20$ GeV. $\not\!\!E_T$ is defined in Level 2 as the vector sum in the xy-plane of all the calorimeter trigger-towers. The "XCES" label on the second trigger is to indicate the additional requirement that hits be found in the strip chamber which is associated with the cluster seed tower.

We can examine the subset of the $W \rightarrow e\nu$ sample which passes one of these triggers, and then measure the probability of passing the other trigger. This allows us to measure the efficiency of the "CFT_12" part of the first trigger, and the "MET_20_XCES" part of the second. For example, an event that passes the second trigger but fails the first, could only have failed because it failed the CFT_12 requirement.

*The E_T for the CEM_16_CFT_12 trigger comes from the second clustering algorithm discussed above, and for CEM_16_MET_20_XCES, the E_T comes from the first.

The efficiencies for the events in our $W \rightarrow e\nu$ sample to pass the CFT_12 and the MET_20_XCES parts of the triggers are shown in Figure 2.7. The top plot shows the MET_20_XCES efficiency as a function of $\not\!\!E_T$, and the bottom plot shows the CFT_12 efficiency as a function of P_T, where $\not\!\!E_T$ and P_T are the "offline" values. The definitions of these variables, and the cuts which define the $W \rightarrow e\nu$ sample are discussed in Chapter 3.

The average efficiency of the CFT_12 part of the trigger is $(92.8 \pm 0.2)\%$, and the average efficiency for the MET_20_XCES part is $(96.2 \pm 0.1)\%$. If either of these triggers is passed, Level 2 will be passed, and our combined efficiency to pass Level 2 is $1 - (1 - .928)(1 - .962) = 99.7\%$. This is high enough that we do not expect to see any significant effects on the W mass.

The CFT_12 efficiency is higher at the beginning of Run 1B and drops off to $\sim 85\%$ near the end. This drop in efficiency is attributed to CTC aging. The "MET_20_XCES" efficiency is largely unchanged over the course of Run 1B.

There may also be an inefficiency in the "CEM_16" part of the trigger, but we are placing E_T cuts of 25 GeV on the final sample, and such events are expected always to pass the Level 2 E_T cut of 16 GeV. For both triggers above there is also a requirement that the Level 2 hadronic energy lying behind the seed tower be less than 12.5% of the cluster E_T. The efficiency of these two requirements is checked with $Z \rightarrow ee$ data where one of the legs is in the plug and a Level 2 plug trigger is passed. No significant inefficiency is found.

The $Z \rightarrow ee$ sample described in Chapter 3 is fed primarily by the CEM_16_CFT_-12 trigger. The inefficiency of the CFT_12 part of the trigger, however, is reduced since the sample consists of two central electrons, and either electron can cause the trigger to pass. For the $W \rightarrow e\nu$ sample, the second trigger above provides a backup

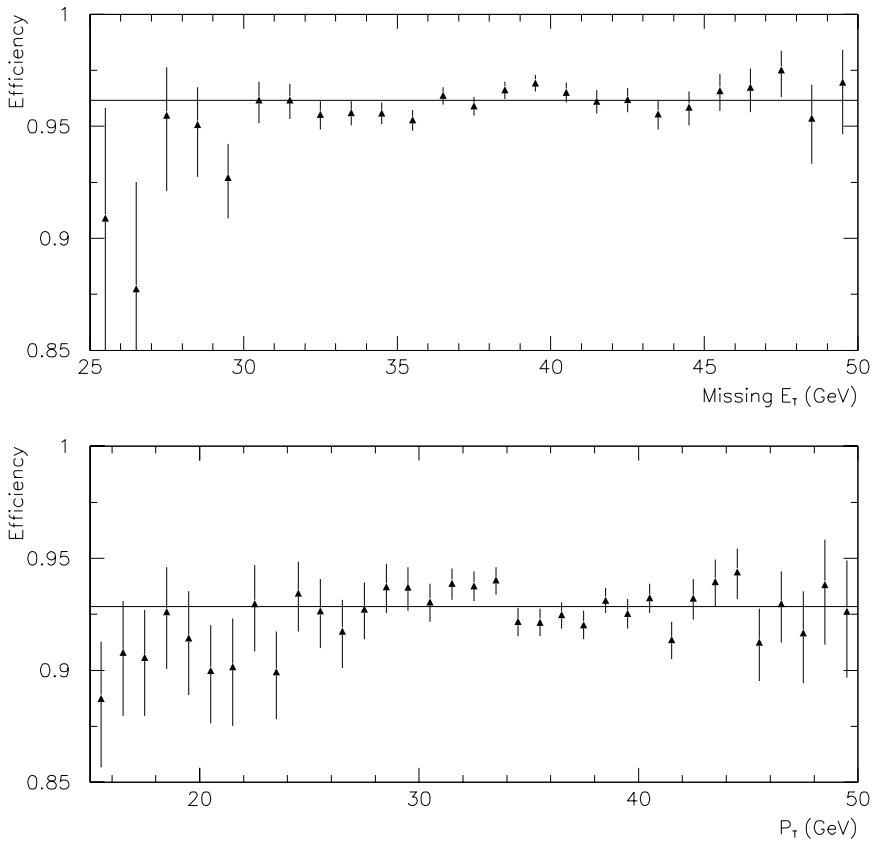

Figure 2.7: Level 2 Efficiencies. Top: MET_20_XCES efficiency as a function of offline $\not\!\!E_T$. Bottom: CFT_12 efficiency as a function of offline P_T. For the top plot we use the subset of the $W \rightarrow e\nu$ sample that passes the CEM_16_CFT_12 trigger, and we plot the fraction that also pass the CEM_16_MET_20_XCES trigger. For the bottom, we use the subset that pass the CEM_16_MET_20_XCES trigger and plot the fraction that also pass the CEM_16_CFT_12 trigger. The horizontal lines are the average efficiencies.

to the CEM_16_CFT_12 trigger; but no backup is needed for the $Z \rightarrow ee$ sample since both electrons are examined by the trigger.

If Level 2 is failed, then the electronics which read out the detector are reset in preparation for the next beam crossing. If passed, all the calorimeter signals are read out, and this includes digitizing and reading out the calorimeter signals. This process takes $\sim 3,000\ \mu s$, during which time all bunch crossings are ignored. Level 2 passes events at a rate of $\sim 20 - 35\ Hz$.

2.5.3 Level 3

The information from the event which has been read out is passed on to a farm of Silicon Graphics processors which run a scaled down version of the full reconstruction code. Events can be written to tape at a rate of $\sim 10\ Hz$, and Level 3 must reject enough events to achieve this rate.

There is significantly more information available at Level 3 than at Level 2. For the calorimeters, the fast-out information is dropped in favor of digitization of all calorimeter channels, and the trigger towers are replaced by the actual physical tower segmentation. Moreover, the CFT information is dropped, and a Level 3 version of the full CTC tracking code is run. The main difference between Level 3 tracking and the "offline" tracking are differences in calibration constants for the CTC chamber.

An electromagnetic cluster is defined in Level 3 in the same way that it is defined in the offline code. The clustering is discussed in Chapter 3 below. E_T is defined as $E \sin\theta$ where E is the energy of the cluster, and θ is the polar angle of a line pointing from the nominal event vertex to the cluster location. The vertexing is discussed in Section 2.3.2 above.

All the tracks are searched, and a list is made of tracks that extrapolate to any

of the towers in the electromagnetic cluster. No beam constraint is applied, and the highest P_T track is considered to be associated with the cluster. The P_T of this track is used in the triggers discussed below.

At Level 3, $\vec{\not{E}}_T$ is the vector sum of all calorimeter towers, both electromagnetic and hadronic, and is defined as

$$\vec{\not{E}}_T = \sum_{towers} (E_i \sin\theta_i)\hat{n}_i \tag{2.9}$$

where E_i is the energy of the ith tower, and $\hat{n}_i$ is a transverse unit vector pointing to the center of each tower. θ_i is the polar angle of the line pointing from $z = 0$ to the ith tower. The sum extends only to $|\eta_{detector}| < 3.6$, and this avoids the region of the forward calorimeters that have been designed to make room for the quadrupole focusing magnets.

Tower energy thresholds are applied to each tower in the sum. The thresholds are set to be significantly higher than fluctuations in the pedestals. The thresholds are 0.1 GeV for the central electromagnetic and hadronic towers, 0.3 and 0.5 GeV for the PEM and PHA, respectively, and 0.5 and 0.8 GeV for the FEM and FHA respectively.

There are two Level 3 triggers that contribute to the $W \to e\nu$ sample, one which requires a track and one which does not. They are labelled

CEM_22_W

and

CEM_22_W_NO_TRACK

We require that one of these Level 3 triggers be passed. Above, we did not require that any particular Level 2 trigger be passed, but we do make a trigger requirement

at Level 3. These Level 3 triggers define our initial event sample.

The CEM_22_W trigger requires

$$P_T > 13 \text{ GeV}$$

$$E_T > 22 \text{ GeV}$$

$$\not{E}_T > 22 \text{ GeV}$$

It also requires $\frac{E_{had}}{E_{EM}} < .125$, where $\frac{E_{had}}{E_{EM}}$ is ratio of hadronic to electromagnetic energy for the towers in the cluster.

The CEM_22_W_NO_TRACK trigger requires $E_T > 25$ GeV and $\not{E}_T > 25$ GeV, but it does not make a track requirement of any kind. This trigger also makes a series of "quality" requirements on the electron cluster, including the requirement that $\frac{E_{had}}{E_{EM}} < .05$. It serves as a backup trigger to the CEM_22_W, and it is used to measure the efficiency of the $P_T > 13$ GeV cut.

We examine the subset of our final $W \rightarrow e\nu$ sample that passes CEM_22_W_NO_-TRACK. All the requirements of this trigger are more stringent than for CEM_22_W, with the exception of the P_T cut. Therefore, events from this subset can only fail CEM_22_W if they fail the P_T cut, and the fraction of events that fail is a measure of the efficiency of the P_T cut. We find that the efficiency for events in our final sample to pass the $P_T > 13$ GeV trigger requirement is $(99.28 \pm 0.05)\%$. The CEM_22_W_-NO_TRACK trigger should make up most of this tiny inefficiency, but the inefficiency is small enough that we can ignore the effect of the backup trigger.

There is also an "inclusive electron" trigger that just looks for CEM clusters with $E_T > 18$ GeV and $P_T > 13$ GeV, and that also makes a series of quality cuts on the cluster. We use this trigger to check the efficiency of the $\not{E}_T > 22$ GeV part of CEM_-22_W. We make a sample of events that pass the inclusive electron trigger and that also pass all our final selection cuts, with the exception of the trigger requirements.

These can only fail CEM_22_W if they fail the $\not\!\!E_T$ requirement. We find that the efficiency of the $\not\!\!E_T > 22$ GeV trigger requirement is higher than 99.9%, and this is high enough that we do not need to consider systematic uncertainties associated with the Level 3 efficiency.

The Level 3 trigger that defines the initial $Z \rightarrow ee$ sample is labelled

CEM_22_Z

This trigger searches for events with one cluster in the CEM and with a second cluster in the CEM, PEM, or FEM. The trigger requires that there be one CEM cluster with $E_T > 22$ GeV and $P_T > 13$ GeV, and the second cluster is required to have $E_T > 20$ (CEM), 15 (PEM), or 10 (FEM) GeV. Our final $Z \rightarrow ee$ sample has both legs in the CEM, and the PEM and FEM requirements do not effect it.

Chapter 3

Data Reduction and Signal Extraction

There are several types of requirements that we put on the data to extract W and Z samples. The first are the requirements that occur in the trigger, which define the initial samples. The trigger is discussed in Chapter 2.

After the initial selection, we require that the electrons be in a region of the detector that allows a good measurement of their energy and momentum. We refer to these as "fiducial" cuts. There are also a series of kinematic requirements, whose primary purpose is to isolate a clean signal. And for the W events, we also apply a few cuts whose purpose is to reduce backgrounds. It is important that we are able to simulate all the cuts we apply since cuts can alter various distributions and possibly bias the measured W mass. There are a number of "quality" cuts which we could place on the electron that reduce the QCD backgrounds, but our simulation does not simulate these cuts well.

In Section 3.1, we define the variables that are used in the event selection and data

analysis. In Sections 3.2 and 3.3 we discuss corrections when are made to the track P_T and to the electron energy. In Sections 3.6 and 3.7, we present the requirements that we use to define both the $W \rightarrow e\nu$ sample and the $Z \rightarrow ee$ sample.

3.1 Event Variables

In this section we define the kinematic variables used in the W mass analysis.

3.1.1 E_T: Electron Transverse Energy

The electron E_T is defined as $E \times \sin\theta$ where E is the energy of the electromagnetic cluster, and $\sin\theta = 1/\sqrt{1+\cot\theta^2}$. $\cot\theta$ is calculated for the beam constrained track, which is discussed immediately below. The cluster energy is the sum of the electromagnetic energies of a CEM seed tower, which is any tower with energy above 5 GeV, and its two neighboring towers in the z direction. If the seed tower borders the 90° crack, then only one neighboring tower is used, so that the cluster is not allowed to cross the 90° crack. The cluster is always 1 tower wide in azimuth.

3.1.2 P_T: Track Momentum and Beam Constraint

The highest P_T track which extrapolates to any of the towers in the cluster is considered to be associated with the cluster. The five track parameters are discussed in Chapter 2. The five parameters are determined from a fit to the CTC hit data where the final CTC calibration is used. The CTC alignment is done with an iterative procedure that uses the E/p distribution of the W data [26]. The track parameters are then adjusted according to a beam constraint, which improves the track resolution by including the beam spot as additional information.

One way to do the beam constraint would be to re-fit the track with the beam spot added as an additional point. In practice, however, we use the wire hit pattern of the track to calculate a covariance matrix, $\widetilde{C}$, for the five track parameters. The beam spot is then included in the fit by minimizing the following function with respect to a new set of track parameters:

$$\chi^2 = (\Delta\vec{\alpha} \cdot \widetilde{C}^{-1} \cdot \Delta\vec{\alpha}) + \frac{(Z_0 - Z_{vertex})^2}{\sigma^2_{VERTEX}} + \frac{D_0^2}{\sigma^2_{xy}} \tag{3.1}$$

where $\Delta\vec{\alpha}$ is the change in the track parameters from the original fit, Z_0 is the z-position at closest approach to the origin, and D_0 is the impact parameter measured relative to the beam spot. The beam spot is determined from the VTX determination of Z_{vertex} and from the SVX beam lines, as discussed in Chapter 2. σ_{VERTEX} and σ_{xy} are the uncertainties in the z direction and transverse directions, respectively, of the determination of the beam spot. These values are fixed at 0.1 cm and 60 μm respectively. The uncertainty on D_0 in the original fit ($\sim$ 370 μm) is so much larger than σ_{xy} that the result is insensitive to the exact value of σ_{xy}.

The first term in Equation 3.1 keeps the track parameters near the original track, while the second and third terms move the Z_0 and D_0 parameters towards the position of the beam spot. The relative weights of the three terms determine to what extent the beam constrained track differs from the original track. The weights are given by the inverse of the covariance matrix and by the inverses of σ_{VERTEX} and σ_{xy}.

The beam constraint improves the track P_T resolution since the beam spot is determined with better resolution than the impact parameter of a given track. The beam constraint forces the impact parameter relative to the beam spot to be very close to zero. If $D_0 = 0$ is the correct value, then we will improve the P_T resolution since

the curvature and D_0 are highly correlated measurements. To a good approximation, the beam constraint can be thought of as altering the curvature according to

$$crv \rightarrow crv - w \times D_0 \tag{3.2}$$

where w is determined by the covariance matrix. For the data, the average value of w is observed to be 0.000127 cm^{-2}.

The top plots of Figure 3.1 show the distribution of impact parameters relative to the event vertex. The spread in the distribution is dominated by the CTC resolution. A Gaussian fit to the peak shows that the D_0 resolution is ≈ 380 μm. Using Equation 3.2, we calculate that a 380 μm spread in D_0 should cause the beam constraint to produce a fractional change in P_T of order 9%. Moreover, the large tails in the D_0 distribution will lead to fractional changes $\sim 50\%$.

The difference between the z position of the vertex and the track Z_0 is shown in the bottom plot of Figure 3.1. The spread in this distribution is dominated by the CTC resolution, and a Gaussian fit to the peak shows that the Z_0 resolution is ≈ 1 cm.

Occasionally, we beam constrain to the wrong vertex z position. In $\approx 1\%$ of the W events, there is no VTX vertex within ± 5 cm of the track Z_0. In these cases, Z_0 is used for Z_{vertex}. There is also the possibility that there is another VTX vertex in the event that has its z position closer to the track Z_0 than the correct vertex. A simple Monte Carlo study shows that this happens $\approx 1.3\%$ of the time. For both these cases, the z position used by the beam constraint is wrong by ~ 1 cm. To see the effect this has on P_T, we generate 40 GeV tracks and vary the position we beam constrain to. We find that if Z_{vertex} is wrong by ± 1 cm, the beam constrained P_T will

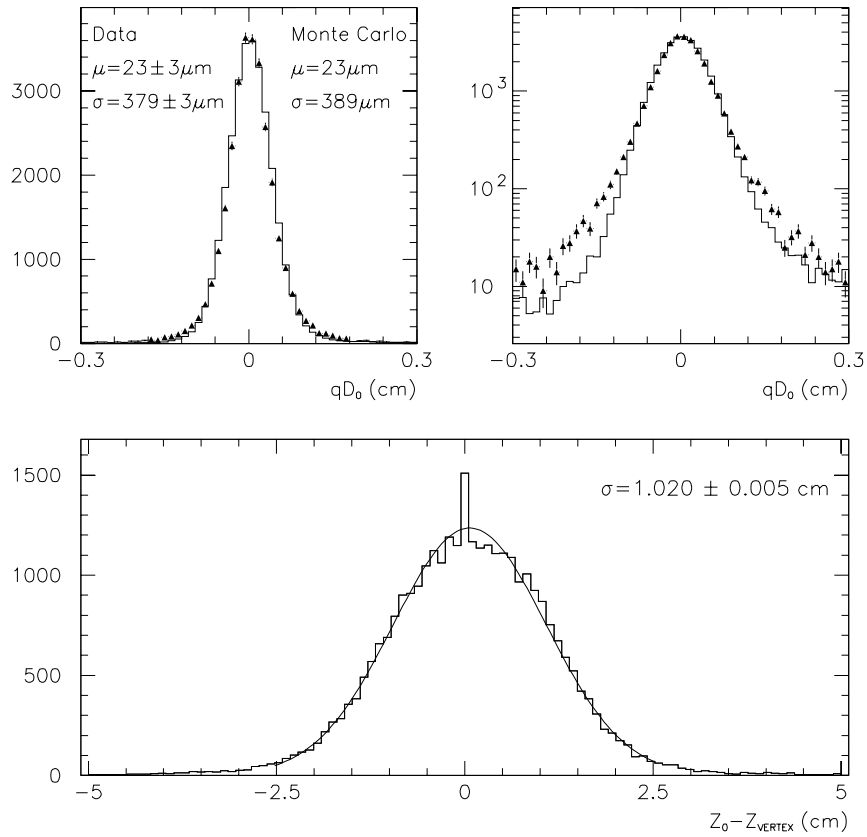

Figure 3.1: Top: qD_0 relative to the event vertex on a linear scale (top left) and a log scale (top right), where q is the charge of the track. The data are the triangles, and the histogram is the Monte Carlo. The Monte Carlo is described in later chapters. Gaussian fit means (μ) and widths (σ) are shown on the top left plot. The fits are only done to the peak position, between $\pm 750\mu$m. Bottom: Z_0 relative to the event vertex. The spike at zero in the bottom plot corresponds to events where no VTX vertex is found, and the z position of the vertex is identified with the track Z_0. A Gaussian fit to the peak position is shown on the plots. The top plot uses tracks with the final CTC alignment and calibration while the bottom plot uses the default alignment and calibration. The default calibration is used when we search for a VTX vertex close the track Z_0, and we maintain the default calibration for the bottom plot so that the spike at zero remains prominent. All plots are for the $W \rightarrow e\nu$ sample.

be altered by $\pm 0.3\%$ of itself. This is negligible compared to the beam constrained fractional P_T resolution of $\approx 4\%$. Moreover, for a 1 cm change in Z_{vertex}, the value for the beam constrained $\cot\theta$ is altered by ≈ 0.01. This value is roughly the same as the resolution on $\cot\theta$, but it is negligible since only a few percent of the events use the wrong Z_{vertex} position.

Electrons which undergo bremsstrahlung have a non-zero impact parameter. For example, the impact parameter after the first brem is

$$D_0 = crv \times r^2 \times y \tag{3.3}$$

where crv is the curvature after the brem, r is the radius at which the brem occurred, and y is the photon energy fraction. Since this D_0 is proportional to curvature, Equation 3.2 will produce a bias that will look like a curvature scaling, which is a bias on P_T. This bias is included in the event simulation, as discussed in Chapter 6.

Since crv is signed according to the charge of the track, the bias on D_0 from Equation 3.3 is opposite for oppositely charged tracks. Equation 3.3 should create a positive bias in the quantity qD_0. qD_0 is plotted in the top plots of Figure 3.1 for the data and Monte Carlo. The Monte Carlo is described in later chapters. Gaussian fits to the peak are shown. The mean of the Monte Carlo peak agrees with the data, although the Monte Carlo has a slightly larger width. The peak of the distribution contains the bulk of the data. The agreement of the means of the peaks indicates that we are correctly simulating the bias in qD_0, at least for the bulk of the data. We will be concerned with the bulk of the distribution when we compare the E/p distribution of the data and Monte Carlo in Chapter 11.

The resolution on the Monte Carlo is fixed so that the E/p distribution has the

correct width. This is discussed in Chapter 11.

The data have significantly larger tails than the Monte Carlo. These tails correspond to non-Gaussian resolutions on the data, which are not reproduced in the Monte Carlo. The tails do not correspond to an excess of bremsstrahlung in the data, since bremsstrahlung only contributes to the right hand side of the plot. If qD_0 is measured significantly wrong, then crv will be also, and the beam constraint uses the correlation between these two quantities to correct crv. We do not necessarily expect the beam constrained P_T to have large tails, but we will see in Chapter 11 that the E/p distribution also has significant non-Gaussian tails which are not predicted by the Monte Carlo.

The effect of the beam constraint is shown in Figure 3.2. The top plot shows the fractional change in $1/P_T$ before and after the beam constraint. The spread in this distribution is expected from the spread in qD_0 shown in Figure 3.1, and Equation 3.2. The negative mean reflects the bias introduced by bremsstrahlung, which is discussed above. The bottom plot shows E/p for tracks before and after the beam constraint. The resolution is significantly improved from $\sigma(1/P_T) \approx 0.0024$ to $\sigma(1/P_T) \approx 0.001$ GeV^{-1}.

By default, we will always assume that the track has been beam constrained, and we will refer to the beam constrained transverse momentum as P_T.

3.1.3 $\vec{U}$: Boson Transverse Momentum

The total transverse momentum in the event is conserved, and the transverse momentum of the boson can be measured from the energy that recoils against it. Our measure of the recoil energy is the variable $\vec{U}$. $\vec{U}$ is the vector sum over all the calorimeter towers, both electromagnetic and hadronic, except for the towers associated with the

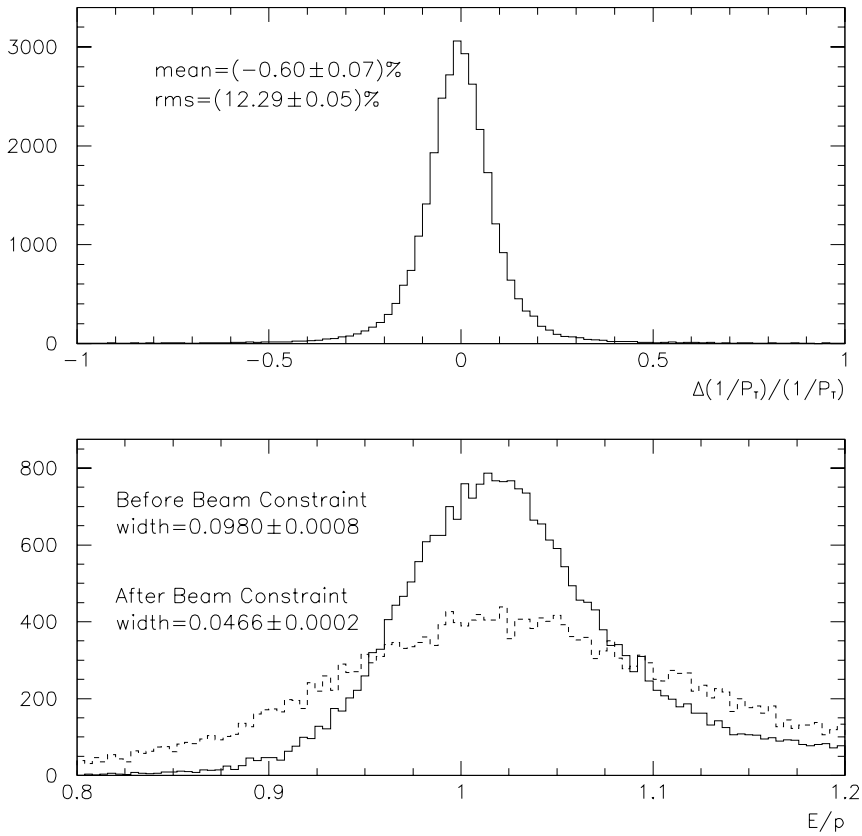

Figure 3.2: Top: $1/P_T$(after)-$1/P_T$(before) divided by $1/P_T$(after), where P_T(before) is value of P_T before the beam constraint, and P_T(after) is the value after the beam constraint. The mean and rms of the distribution is shown on the plot. Bottom: E/p using P_T after the beam constraint (solid) and P_T before the beam constraint (dashed). The widths of Gaussian fits to the peak regions are shown on the plot. The fits used the data between $0.9 < E/p < 1.06$ for the solid histogram, and $0.8 < E/p < 1.2$ for the dashed. All plots are for W events which pass the W cuts listed in Table 3.1.

electromagnetic cluster. We define

$$\vec{U} \equiv \sum_{not\ e^{\pm}} (E_i \sin\theta_i)\hat{n}_i \tag{3.4}$$

where E_i is the energy of the ith tower, and $\hat{n}_i$ is a transverse unit vector pointing to the center of each tower. θ_i is the polar angle of the line pointing from Z_{vertex} to the ith tower. As in Equation 2.9, the sum only extends to $|\eta_{detector}| < 3.6$.

Only towers with energy above a threshold are included in the sum. The thresholds are different than the Level 3 thresholds of Equation 2.9. The thresholds are set to be $5 - \sigma$ above the fluctuations in the pedestal energies. The thresholds are 0.1, 0.15, and 0.2 GeV for the central, plug, and forward electromagnetic calorimeters, respectively; and the thresholds are 0.185, 0.445, and 0.730 for the central, plug, and forward hadronic calorimeters, respectively.

The sum excludes the electromagnetic towers which are included in the primary electron cluster and also the hadronic towers behind them. The towers associated with the primary cluster are removed since we want $\vec{U}$ to be a measure of the recoil energy, and we do not want it to be contaminated with energy from the decay electron. We always remove the three towers associated with the primary cluster, and for some events, depending on the position of the track, the three towers which neighbor the primary cluster in azimuth are also removed. We extrapolate the track to the strip chambers which are inside the CEM. We define X_{strips} to be the extrapolated location in the azimuthal direction, relative to the center of the intercepted tower. If $X_{strips} > 6$ cm, we remove the neighboring three towers which are higher in azimuth, and if $X_{strips} < -6$, we remove the three towers which are lower in azimuth. We use Figure 3.3 to justify this criterion.

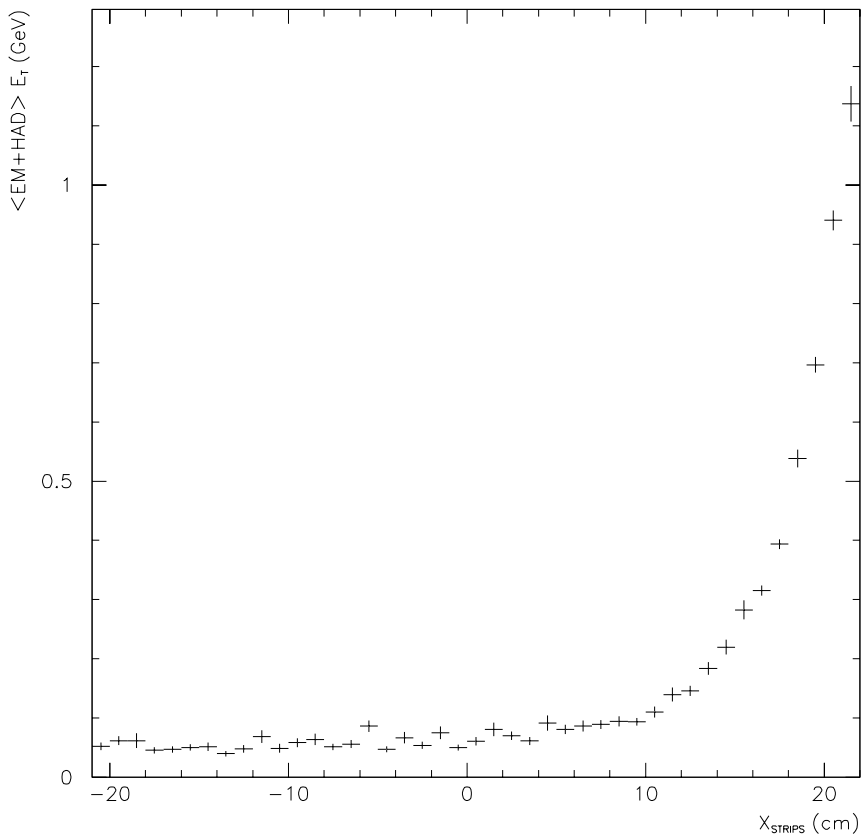

Figure 3.3: Average electromagnetic plus hadronic E_T in the tower which neighbors the seed tower and is one tower higher in azimuth, as a function of X_{strips}. X_{strips} is the extrapolated track position for the primary electron cluster. In this plot, as X_{strips} becomes more and more positive, it corresponds to tracks that extrapolate to positions closer and closer to the neighboring tower. The y-values are ≈ 55 MeV on the left side of the plot.

Figure 3.3 shows the average transverse energy in the tower which neighbors the seed tower and is one tower higher in azimuth. The average is plotted as a function of X_{strips}. When X_{strips} is more and more positive, the extrapolated track is closer and closer to the neighboring tower. When X_{strips} is higher than ~ 6 cm, a clear increase in the neighboring energy is visible. We attribute this to leakage from the electron shower, and large angle bremsstrahlung. We can also plot the average transverse energy of the tower which is one tower lower in azimuth. The plot looks the same, except the peak appears on the left side.

We define the two projections of $\vec{U}$, $U_{||}$ and $U_{\perp}$. $U_{||}$ is $\vec{U}$ projected along the electron track direction, and $U_{\perp}$ is the perpendicular projection. These are calculated as

$$U_{||} = \frac{\vec{U} \cdot \vec{E}_T}{E_T} \tag{3.5}$$

and

$$U_{\perp} = \frac{\vec{U} \times \vec{E}_T}{E_T} \tag{3.6}$$

Since the removed towers lie largely along the track direction, the tower removal procedure produces a bias in the variable $U_{||}$. This translates into a bias on M_T since

$$M_T \approx 2E_T + U_{||} \tag{3.7}$$

where the approximation is accurate to first order in the quantity $|\vec{U}|/E_T$, and M_T is defined below. Since we use M_T to fit for the W mass, it is important to simulate this bias. The simulation of the bias is discussed in Chapter 6.

3.1.4 $\sum E_T$: Scalar Energy in the Event

We define the variable $\sum E_T$ as the scalar sum of the energy in the event. The same towers are summed, and the same thresholds applied, as in Equation 3.4. The definition of $\sum E_T$ is identical to the definition of $\vec{U}$ in this equation, except that we exclude the vector part of the sum, $\hat{n}_i$.

$\sum E_T$ is a measure of the total energy in the event from all sources, including multiple interactions.

3.1.5 $\not{E}_T$: Missing Transverse Energy

We define $\vec{\not{E}}_T$ to be

$$\vec{\not{E}}_T \equiv -(\vec{U} + \vec{E}_T) \tag{3.8}$$

where $\vec{U}$ is defined above. The magnitude of $\vec{E}_T$ is the E_T of the primary electron, and its direction is determined by the beam constrained track. The E_T of the primary electron is defined above, and the E_T includes all the corrections which are discussed below. We will write $\not{E}_T$ for the magnitude of $\vec{\not{E}}_T$.

3.1.6 M_T: Transverse Mass

Our measured value for the transverse mass is defined as

$$\begin{aligned} M_T &= \sqrt{(\not{E}_T + E_T)^2 - (\vec{\not{E}}_T + \vec{E}_T)^2} \\ &= \sqrt{(\not{E}_T + E_T)^2 - |\vec{U}|^2} \end{aligned} \tag{3.9}$$

where $\not{E}_T$, E_T, and $\vec{U}$ are defined above.

3.2 P_T Corrections

The final CTC calibration uses the E/p distribution of positive and negative W decay electrons. Since the E measurement is independent of charge, any significant difference between positive and negative tracks is attributed to errors in the CTC calibration. The calibration forces the positive and negative tracks to have the same mean, and it also forces them to have the same mean as a function of $\cot\theta$.

The CTC calibration, however, does not produce an overall alignment with the position of the SVX. If the center of the SVX is offset with respect to the CTC, then the assumed beamspot will be systematically offset relative to the correct position. Such an offset will show up as a splitting in P_T between positive and negative tracks as a function of azimuth, after we do the beam constraint.

Figure 3.4 shows the difference in <E/p> for positive and negative tracks as a function of azimuth. A sinusoidal fit is also shown on the plot. We determine a correction to $1/P_T$ by dividing the sinusoidal fit by the average value of E_T. We further divide by two since we will correct the positive and negative tracks separately, and each should correct for half the sinusoidal variation. The correction is

$$q/P_T \rightarrow q/P_T - 0.00020 \times \sin(\phi - 2.95) \tag{3.10}$$

where q is the charge of the track, P_T is the beam constrained P_T, measured in GeV, and the argument of the sine function is in radians. The difference between positive and negative tracks after this correction is also shown on the plot. The plot is significantly flatter after the correction.

This correction does not alter the position of the mean of E/p, but only the splitting in the mean between positive and negative tracks.

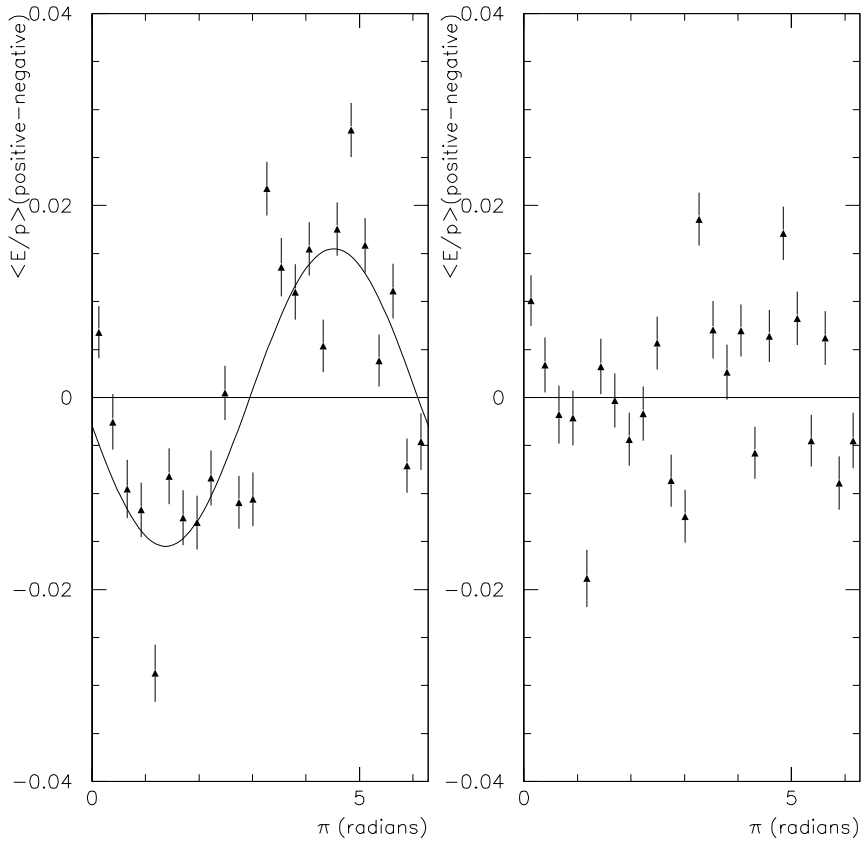

Figure 3.4: Top: The difference in mean E/p for positive and negative tracks, as a function of the azimuth of the track. The mean is between .9 and 1.1. The left plot is before the correction of Equation 3.10, and the right plot is after. A sinusoidal fit is shown on the left plot. The fit is $(0.01551 \pm 0.0008) \times \sin(\phi - 2.95 \pm 0.05)$ for ϕ in radians. The straight line through zero is shown to guide the eye.

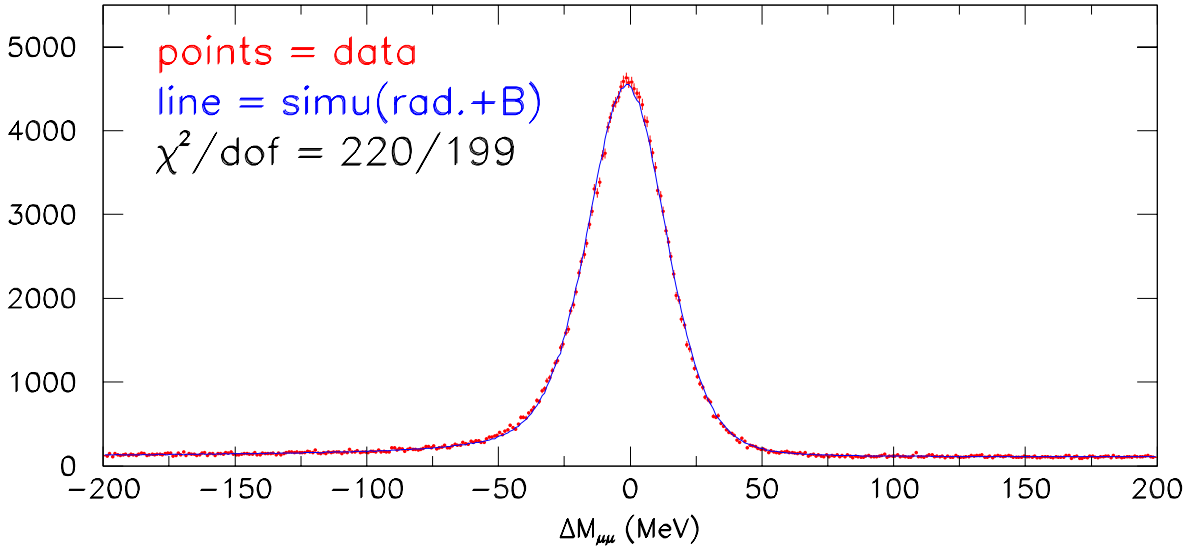

Figure 3.5: The invariant mass distribution of $\sim 250,000$ $J/\psi \rightarrow \mu\mu$ events. The points are the data and the line is the simulation. The variable shown is ΔM which is the difference between the measured invariant mass and the world average for the J/ψ. The simulation includes both radiative corrections and backgrounds. This plot is taken from Reference [27].

We also correct P_T for variations in the magnetic field over the course of Run 1B. NMR probes were used to track the magnetic field, and the correction that is applied varies between 0 and 0.1%.

The P_T scale is determined from $J/\psi \rightarrow \mu\mu$ events. Figure 3.5 shows the invariant mass of $\sim 250,000$ $J/\psi \rightarrow \mu\mu$ events, with a simulation superimposed.

From the $J\psi$ events it is determined that the measured beam constrained P_T should be increased by a factor of 1.00023 ± 0.00048 [27]. The statistical uncertainty from the J/ψ mass peak is negligible, and the uncertainty on this P_T scale is dominated by an unexpected variation in the measured mass as a function of the amount of material the muons pass through, and also by our ability to extrapolate a scale from the relatively low P_T muons of J/ψ events ($\sim$ 3.5 GeV) to the high P_T tracks of W and Z events ($\sim$ 40 GeV).

The P_T scale correction is applied to the data.

3.3 Initial CEM Corrections

In this section we describe various corrections which are applied to the energy measurement.

3.3.1 Time Dependent Corrections

Figure 3.6 shows the mean E/p for W events as a function of run number.* The left side of the plot corresponds to the beginning of Run 1B in January 1994, and the right side is the end of the Run, July 1995. Over the $\sim$ 18 months of the run, the energy scale is observed to drop by $\approx 4\%$.

The aging of the detector may account for this decline in gain. Both the east and west halves of the CEM are further divided into two physical masses, the north halves and the south. This forms four "arches." The decline in gain is observed to occur at different rates over the four arches [28].

Data is used that passes a low P_T inclusive electron trigger, which produces electron candidates with P_T down to 8 GeV. This data is used to provide a high statistics sample. The data is divided according to the four arches, and it is also divided according to different run ranges. Linear fits are made to the E/p distribution for each division of data, as a function of run number [28]. These fits are then used to correct the CEM response.

Figure 3.6 shows mean E/p vs run number after these corrections, for the W data.

*The Run 1B data is divided into many smaller "runs," where each run consists of data taken over a time period typically lasting several hours.

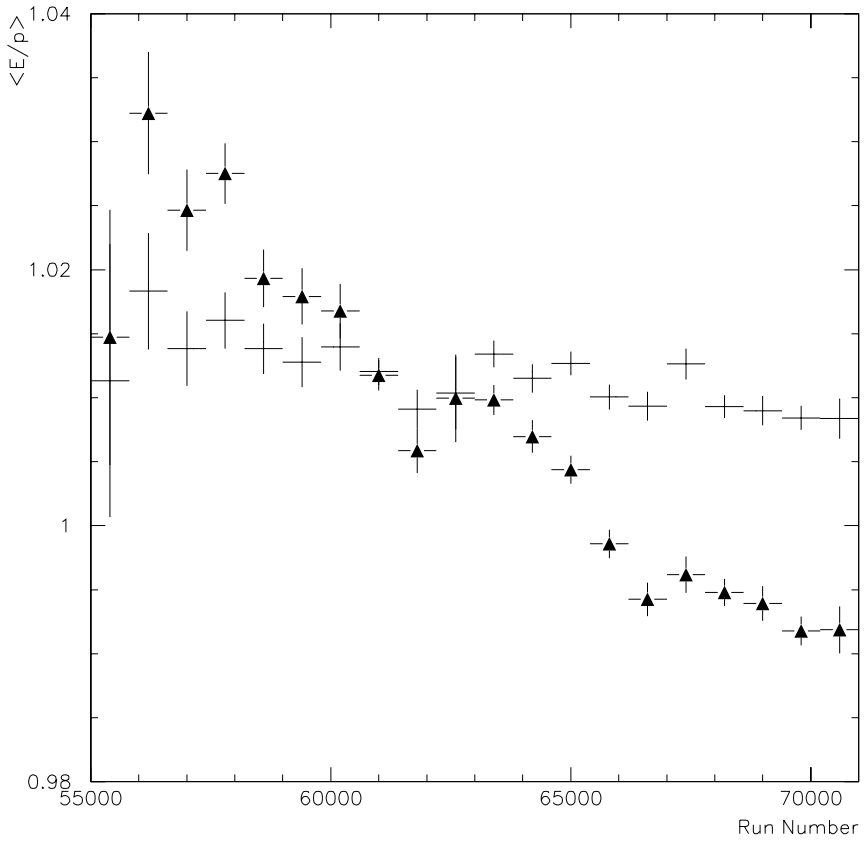

Figure 3.6: <E/p> as a function of run number for W data, for the runs which make up Run 1B. The mean is between .9 and 1.1. The triangles are before any energy corrections, and the dashes are after the corrections of Sections 3.3.1 and 3.3.2. The left side of the plot corresponds to January 1994 and the right side to July 1995.

The curve is significantly flatter after the corrections, although the data still decline by $\approx 0.7\%$ over the course of Run 1B. An explanation for the residual decline in gain is that as Run 1B progressed the luminosity delivered by the accelerator steadily increased. At higher luminosity the average number of multiple interactions increases. This overlapping energy is included in E/p, and is a larger percentage effect for the lower E_T inclusive sample than for the W events.

The energy from multiple interactions is discussed in Section 3.4 below.

3.3.2 Mapping Corrections

A "mapping" correction, which depends on the position of the electron in the tower, was determined using test beam data [29]. This correction is applied to the data, and the W data is used to make small adjustments to this correction [28]. Figure 3.7 shows the mean E/p as a function of extrapolated track position at the strip chambers. The clear reduction in response near the center of the towers is the result of the attenuation of the scintillator light. Light produced near the center of the towers travels over a longer path to the wavelength shifters on either side of the tower. After the correction, the mean is significantly flatter. There appear to be dips in the mean around $X_{strips} = \pm 10$ cm after the correction. This may indicate a small modulation in the P_T measurement with azimuth.

Two corrections are made as a function of Z_{strips} where Z_{strips} is the z coordinate of extrapolated track position. The first is to correct for variations in response near the z-boundaries of the towers. The second is to correct for variations among the towers along the z-direction.

Figure 3.8 shows the mean E/p as a function of Z_{strips} before and after the corrections are applied. The left plot is before the corrections are applied and shows

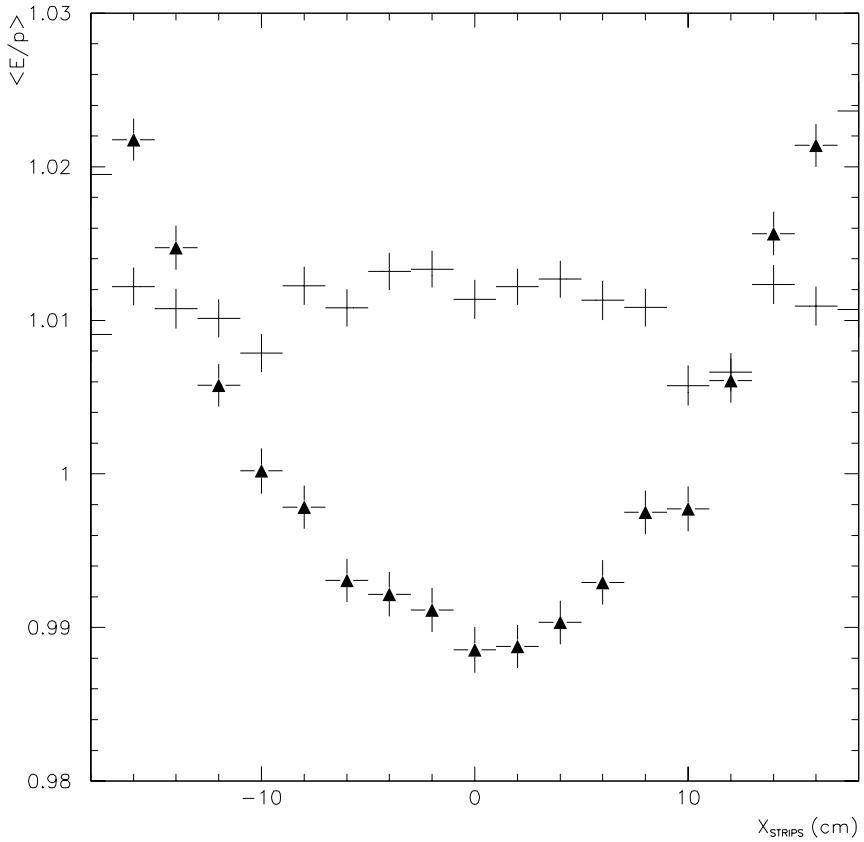

Figure 3.7: <E/p> as a function of X_{strips} for W data. The mean is between .9 and 1.1. The triangles are before any energy corrections, and the dashes are after the corrections of Sections 3.3.1 and 3.3.2.

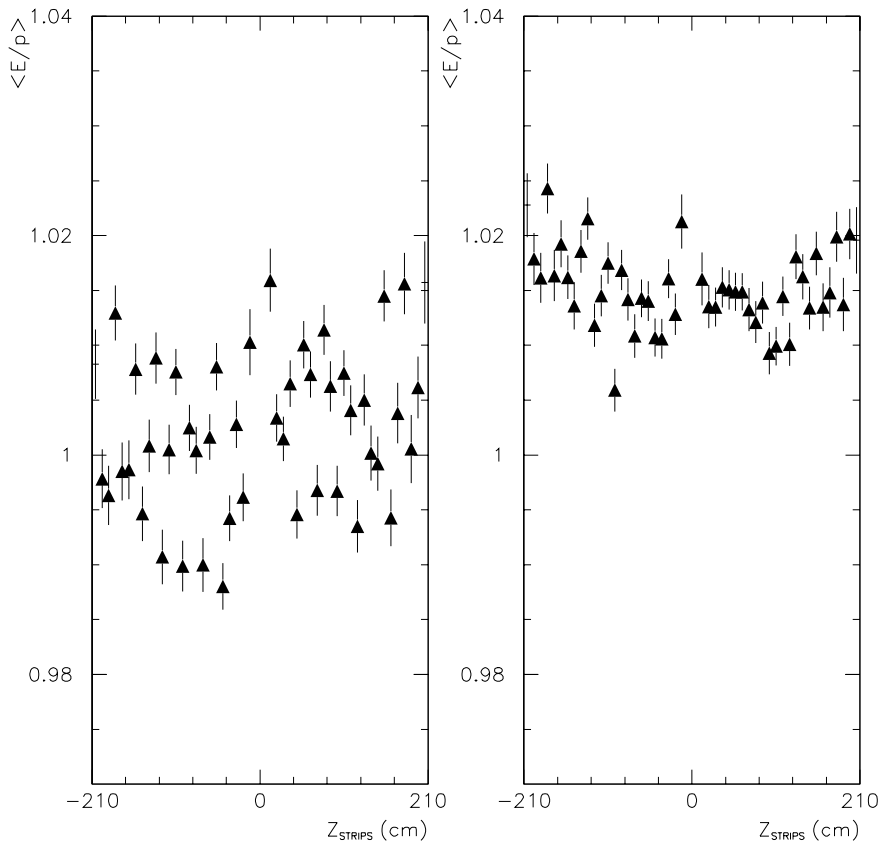

Figure 3.8: <E/p> as a function of Z_{strips} for W data. The mean is between .9 and 1.1. The left plot is before any corrections, and the right plot is after the corrections of Sections 3.3.1 and 3.3.2.

large variations in the mean of E/p. The right plot is after the corrections and is significantly smoother. The right plot shows a slight rise at higher values of $|Z_{strips}|$. This rise is put into the corrections explicitly. Electrons with higher values for $|Z_{strips}|$ pass through more material on average than electrons at lower $|Z_{strips}|$, and the mean E/p increases slightly with $|Z_{strips}|$. The data is corrected to include the expected increase.

There is also a small correction applied which is based on the angle of incidence

into the towers [30].

3.3.3 Summary

The magnitude of the above corrections for the $W \rightarrow e\nu$ data are shown in the top plot of Figure 3.9. The solid curve shows the time dependent corrections and the mapping corrections combined, while the dashed and dotted curves show the two corrections separately. The mean and rms of the different distributions are shown on the plot. The time dependent corrections adjust E by 4.6% upwards on average, while the mapping corrections adjust E by 2.5% downwards on average. An overall adjustment is included with the time dependent corrections so that a preliminary measurement of the $Z \rightarrow ee$ mass agrees with the world average. The distribution of the combined corrections has a 4% spread.

The bottom plot of Figure 3.9 shows the E/p distribution with the different corrections applied. The results of Gaussian fits to the peak of E/p are also shown. The E corrections improve the width of the E/p peak by $\approx 14\%$.

The time dependent corrections and the mapping corrections are applied as a default to all electromagnetic clusters at CDF. In addition, for the W mass analysis, we apply the small corrections of the next section.

3.4 Underlying Energy CEM Corrections

Energy from sources other than the primary electron is included in the CEM cluster. Multiple $p\overline{p}$ interactions, which are unassociated with the W event, as well as the recoil energy from the W P_T, can add energy to the electron cluster.

The energy of the multiple interactions is uncorrelated to the W event. This

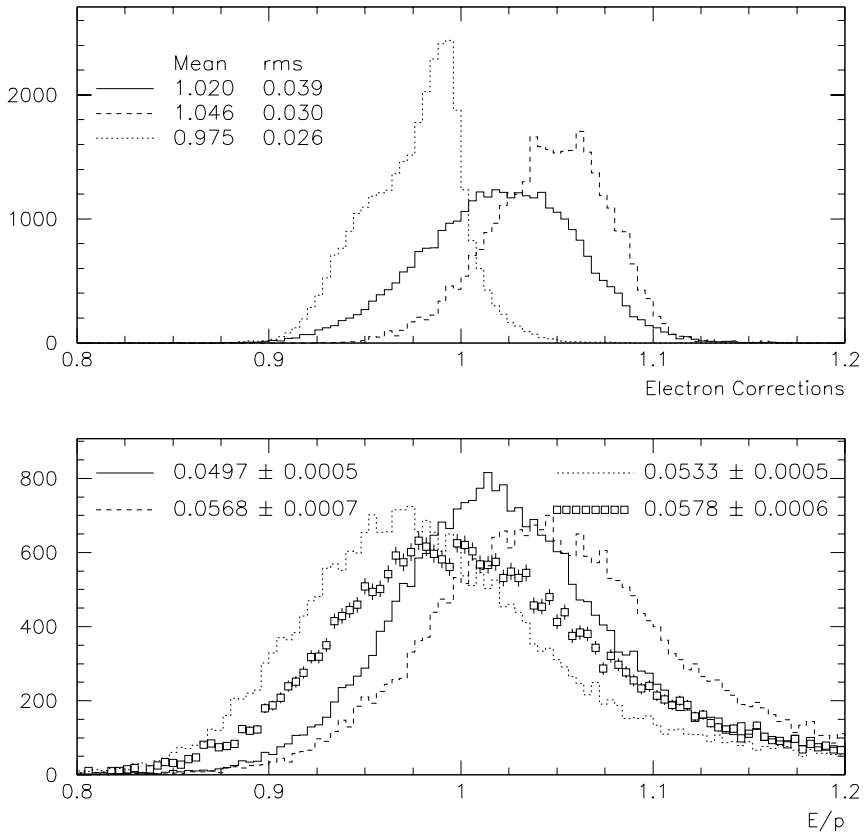

Figure 3.9: Top: Distribution of CEM corrections for $W \rightarrow e\nu$ data. The time dependent corrections (dashed) and the mapping corrections (dotted) are shown individually, and the product of the two corrections is shown in the solid curve. The means and rms of the distributions are also shown on the plot. The CEM energy is multiplied by the corrections. Bottom: The E/p distribution with and without the corrections for $W \rightarrow e\nu$ data. We have applied both corrections (solid), time dependent corrections only (dashed), and mapping corrections only (dotted). The squares are the distribution with no E corrections. The rms of Gaussian fits to the peaks of the distributions are shown. The rms of the case with no corrections is larger than the distributions with the corrections, and the combined corrections produce the smallest rms.

energy creates an effective CEM non-linearity since it does not scale with E_T: the percentage effect of the extra energy is reduced as E_T increases.

The recoil energy, however, is correlated with the electron E_T. If the W P_T is directed along the electron direction, then the recoil energy will tend to be directed opposite the electron. Such events have higher electron E_T since the W motion adds to the electron E_T. If the W is directed opposite the electron direction, then the recoil energy will tend to lie along the electron. Such events have lower electron E_T since the W motion will subtract from the electron E_T.

The recoil energy and the multiple interaction energy which lies on top of the CEM cluster is included in the Monte Carlo simulation. Real W events are used for this simulation, and it is discussed in Chapter 6. This is shown in Figure 3.10, which shows the mean of E/p as a function of $\sum E_T$. The Monte Carlo shows a rise with $\sum E_T$, as expected. The slope of the rise in mean E/p is 2.2×10^{-5} GeV$^{-1} \times \sum E_T$.

The data in Figure 3.10 are flat, although we expect a rise with $\sum E_T$. Events at higher $\sum E_T$ tend to occur later Run 1B, since the average instantaneous luminosity, and hence the average $\sum E_T$, increased as Run 1B progressed. The corrections of Section 3.3 tried to flatten the average of E/p as a function of run number, when we really expect <E/p> to rise slightly with run number because of the increased average $\sum E_T$.

We apply a $\sum E_T$ dependent correction to the data to account for the expect rise in $\sum E_T$. We apply the correction

$$E \rightarrow E \times [1.0 + 3.14 \times 10^{-5}(\sum E_T - 68.17)] \tag{3.11}$$

where $\sum E_T$ is measured in GeV. With this correction, the rise in <E/p> as a function

of $\sum E_T$ for the data agrees with the Monte Carlo. The quantity 68.17 GeV, which is subtracted from $\sum E_T$ in Equation 3.11, is the average $\sum E_T$ for $W \rightarrow e\nu$ events. We subtract this value so that the average correction is 1.0.

3.5 Default Energy Scale

In addition to the corrections discussed above, there is an overall CEM energy scale which is applied to the data. A preliminary scale was determined so that a preliminary measurement of the Z mass with $Z \rightarrow ee$ events produces the world average value [5] of 91.187 GeV. When this scale was determined, the underlying event energy was not included in the simulation. Our simulation adds $\approx$ 90 MeV on average to the electron E_T from the underlying event. This is discussed in Chapter 6. 90 MeV is roughly 0.2% of the average electron E_T of $Z \rightarrow ee$ events. To account for this change, we correct the preliminary CEM energy according to

$$E \rightarrow E \times (1.002) \tag{3.12}$$

This is the default scale that we apply to the CEM energy for both $W \rightarrow e\nu$ and $Z \rightarrow ee$ events. We use this energy scale as a default, and in Chapters 10 and 11, we discuss the final determination of the CEM energy scale.

3.6 W Selection Requirements

The W cuts are listed in Table 3.1, as well as the number of events remaining after each cut. A line-by-line description of this table follows.

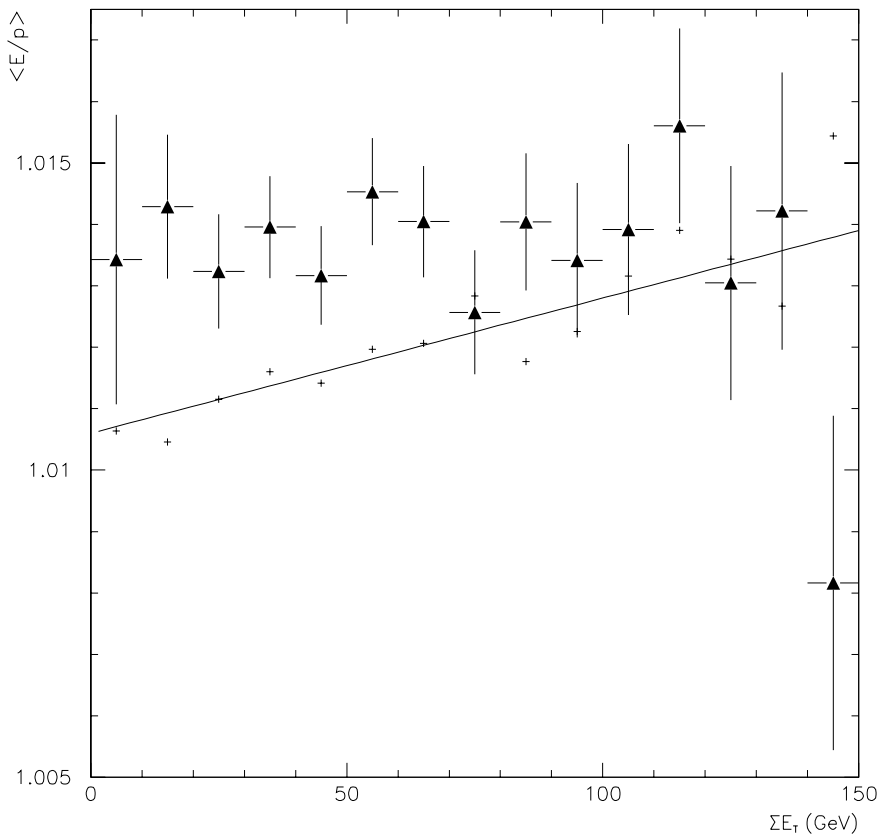

Figure 3.10: <E/p> as a function of $\sum E_T$ for W data and Monte Carlo. The mean is between .9 and 1.1. The triangles are the data, and the squares are the Monte Carlo. The data includes the corrections of Sections 3.3.1 and 3.3.2. A linear fit to the Monte Carlo is shown. The slope of the fit is 2.2×10^{-5} GeV^{-1}. The data have the default energy scale applied. This energy scale produces a value for <E/p> which is significantly higher than the Monte Carlo.

Cut	Events Remaining After Cut
Initial W Selection	108,455
$\lvert Z_{vertex}\rvert < 60$ cm	101,103
Fiducial Requirements	74,475
Track Passes Through all CTC Superlayers	71,877
$E_T > 25$ GeV	67,007
$\not{E}_T > 25$ GeV	55,960
$\lvert\vec{U}\rvert < 20$ GeV	46,910
$P_T > 15$ GeV	45,962
$N_{tracks} \equiv 1$	43,219
$M_{ep} > 1$ GeV	43,198
Not a Z Candidate	42,558
M_T Fit Region: $65 < M_T < 100$ GeV	30,115
(E/p Fit Region: $.9 < E/p < 1.1$)	21,843

Table 3.1: Cuts used to extract W decays from the data. Cuts are described in more detail in the text.

Initial W Selection. We require that the event pass one of the two level 3 W triggers described in Section 2.5. We also require that there be an electromagnetic cluster that has uncorrected $E_T > 20$ GeV and also has an associated track with $P_T > 13$ GeV. The track is fit with the final CTC alignment and calibration constants, but it is not yet beam constrained. A cluster is considered electromagnetic if it has $\frac{E_{had}}{E_{EM}} < .125$.

$|Z_{vertex}| < 60$ cm. The nominal vertex must be within ± 60 cm of the center of the detector. This requirement ensures a good measurement of the electron by the calorimeter.

Fiducial Requirements. We require that the cluster be in a region of the detector that has good energy response. This requirement primarily removes clusters near cracks. First we require that the cluster be in the CEM, excluding the outer-eta towers, which have reduced response. We then extrapolate the electron track to the strip chambers located inside the calorimeter. We define X_{strips}

to be the extrapolated position in the azimuthal direction, starting from the center of the tower the electron hits; and Z_{strips} is the extrapolated longitudinal position from the center of the detector. To avoid the azimuthal boundaries between the towers, we require $|X_{strips}| < 18$ cm, and to avoid the crack between the east and west halves of the detector we require $|Z_{strips}| > 12$ cm. We also require that the track does not point at the "chimney module," which is a tower that has been removed to allow cryogenic access to the solenoid.

Track Passes Through all CTC Superlayers. We require that the reconstructed track describe a path which passes through all 8 superlayers of the CTC. This cut helps remove badly measured tracks.

$\boldsymbol{E_T}$ **>25 GeV.** This cut is made after all offline corrections.

$\boldsymbol{\not{E}_T}$ **>25 GeV.** This cut and the E_T cut are the primary selection cuts for isolating a $W \rightarrow e\nu$ signal.

$|\vec{\boldsymbol{U}}|$ **<20 GeV.** $|\vec{U}|$ is our measure of the W P_T, and this cut limits us to the low P_T region. It also helps to remove backgrounds since non-W backgrounds are concentrated at high $|\vec{U}|$.

$\boldsymbol{P_T}$ **>15 GeV.** The track which is associated with the electron cluster is beam constrained and then corrected according Section 3.2. It is then required to have P_T above 15 GeV. Requiring a high P_T track will remove some backgrounds. It also has the effect of limiting the maximum size of photon bremsstrahlung.

$\boldsymbol{N_{tracks}}$ **≡1.** We make a list of all the tracks in an event that originate within ±5 cm of the nominal event vertex and have $P_T > 1$ GeV. We require that only one of these tracks (the electron track) point to any of the towers contained

in the electron calorimeter cluster. This helps to reduce the QCD dijet background, since jets are more likely than the W decay electrons to have several tracks associated with them. W electrons can also have several tracks associated with them, either through an overlap with unassociated tracks in the event, or through the conversion $\gamma \rightarrow ee$ of a bremsstrahlung photon. The simulation of both these effects is discussed below.

M_{ep} >1. We remove the event if the invariant mass of the electron cluster with the next highest track in the event is less than 1 GeV. In such events, the second track is nearly parallel to the primary electron track, and this can happen in the case of the conversion of hard photon brems. The Z_0 of the second track may be mismeasured enough that we fail to remove the event with the N_{tracks} cut.

Not a Z Candidate. $Z \rightarrow ee$ events can fake $W \rightarrow e\nu$ events if one of the Z decay electrons passes through a crack in the calorimeter. The requirements for an event to be called a Z candidate are motivated and defined in Section 4.1. We also refer to this cut as the "lost Z" cut.

M_T Fit Region: 65< M_T <100 GeV. This region contains the most information on the W mass, and we will ignore the lower M_T region for the final fit. Removing the low M_T region also has the effect of reducing the backgrounds, since the backgrounds tend to occur at low M_T.

E/p Fit Region: 0.9< E/p <1.1. Below we will use the peak of the E/p distribution to compare the calorimeter energy scale to the tracking chamber energy scale. We will use the peak region for this fit. Unless otherwise stated, however, this cut is not applied.

Figure 3.11 shows the E_T, $\not\!\!E_T$, and M_T distributions of the final sample. E_T and $\not\!\!E_T$ are shown both with and without the requirement that M_T be in the M_T fitting region. This requirement has a strong effect on the low end of the E_T and $\not\!\!E_T$ shapes. Below, when we refer to the W sample, we are referring to the sample before the requirement that the event fall in the M_T or E/p fitting regions, unless otherwise stated.

3.7 Z Selection Requirements

The Z sample is used to model the calorimeter response to the boson P_T, and it is also used to set the calorimeter energy scale.

The Z cuts are listed in Table 3.2, as well as the number of events remaining after each cut. The cuts labelled as "both" are applied to both electrons. Most of the cuts are identical to the description in Section 3.6. Those which are different we describe below.

Cut	Events Remaining After Cut
Initial Z Selection	19,527
Same Z_{vertex}	18,461
Both $\|Z_{vertex}\| < 60$ cm	16,724
Both Fiducial Requirements	9,493
Both Tracks Pass Through all CTC Superlayers	8,613
Both $E_T > 25$ GeV	6,687
Both $P_T > 15$ GeV	5,257
Both $N_{tracks} \equiv 1$	1,670
$70 < M_Z < 110$ GeV	1,559
Opposite Sign Tracks	1,541

Table 3.2: Cuts used to extract Z decays from the data. Cuts are described in more detail in the text.

Initial Z Selection. We require that the event pass one of the two level 3 Z triggers

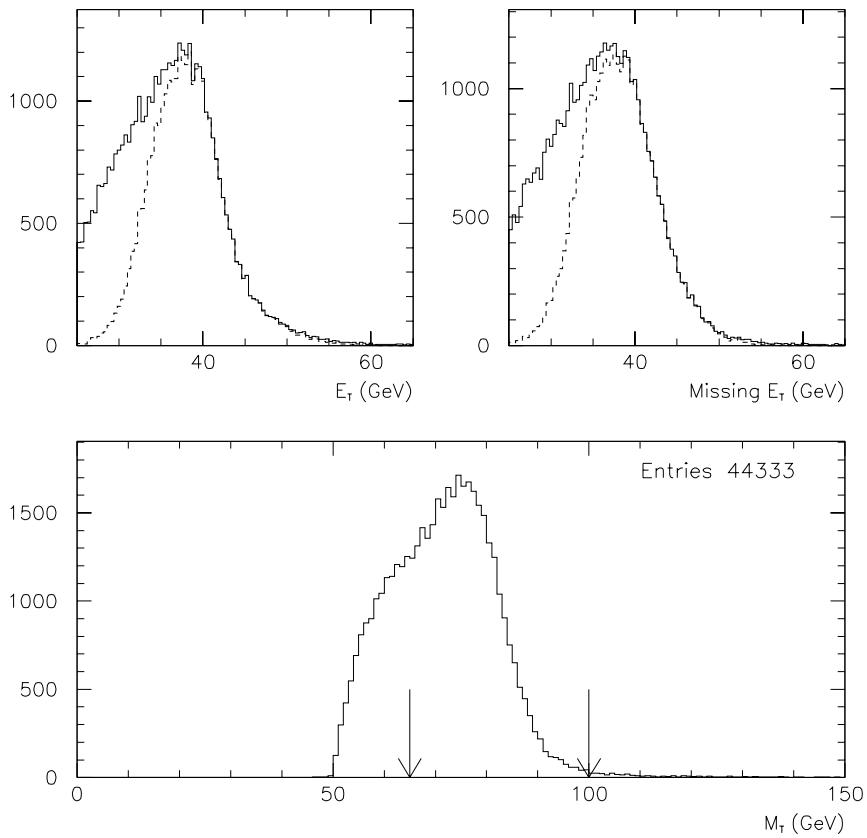

Figure 3.11: Top left: E_T, and top right: $\not{E}_T$ for the final sample. The solid histogram is for all cuts up to the requirement that M_T be in the fitting region, and dashed is for the M_T fitting region. Bottom: M_T distribution. The arrows indicate the M_T fitting region. The number of entries printed on the bottom plot includes events that fall outside the plot boundaries.

described in Section 2.5. We also require that there be two electromagnetic clusters, both with uncorrected $E_T > 20$ GeV and both with an associated track with $P_T > 13$ GeV. For this cut, P_T is not yet beam constrained. In addition, for the Z events, part of the initial selection is that both clusters be central and that they be more than one tower away from each other.

Same Z_{vertex}. Each of the two tracks has an event vertex associated with it. We require that these vertices be within 5 cm of each other.

70< M_Z <110 GeV. This is a loose region around the known Z mass. M_Z is calculated using the corrected calorimeter measurement for the electron energies, and using the beam constrained tracks for the directions.

Opposite Sign Tracks. We require that the two electrons have opposite charges.

To measure how much QCD background remains in the Z sample, we require that the two tracks have the same sign instead of opposite sign. There are 18 such events that pass all other cuts. We assume that the number of opposite sign QCD events is the same as the number of like sign, and we predict that 18 QCD events remain in the Z sample. This amounts to $1.2 \pm 0.3\%$ background. We will use the distributions of these 18 events for various background shapes.

The top plot of Figure 3.12 shows the M_Z shape for the signal events, and the bottom plot for the QCD background.

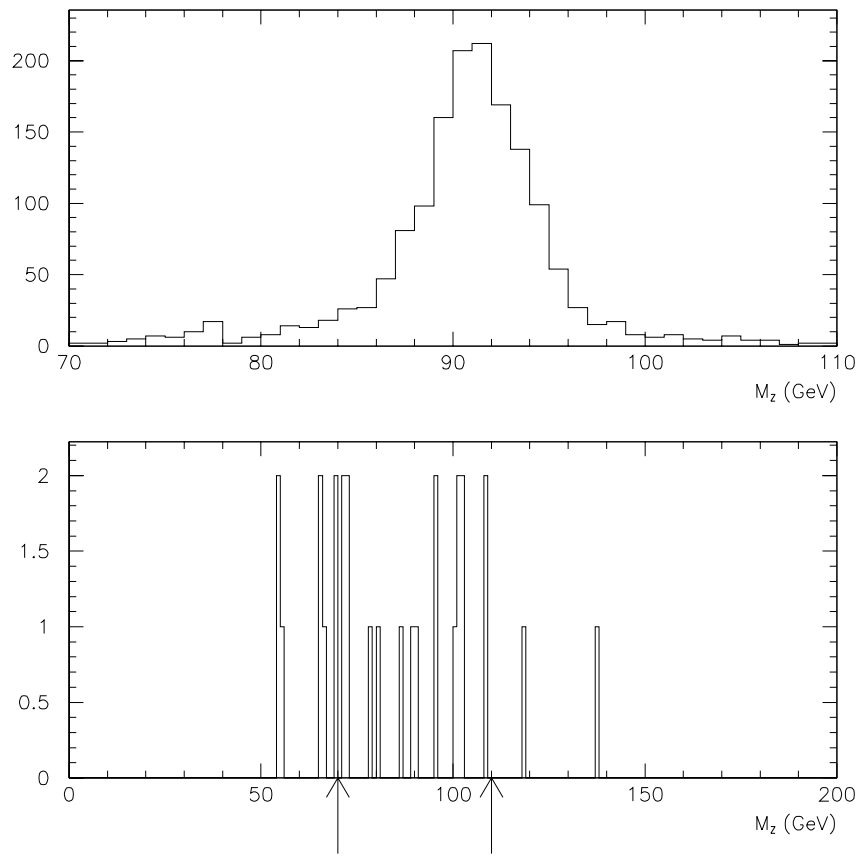

Figure 3.12: M_Z shape for signal (top) and like sign events (bottom). The like sign events pass all other Z selection cuts except the two tracks have the same sign instead of the opposite sign. We have also removed the Z mass cut for the like sign events. The arrows in the bottom plot indicate the M_Z cut region $70 < M_Z < 110$ GeV. There are 30 like sign events for all values of M_Z, and 18 like sign events in the region $70 < M_Z < 110$.

Chapter 4

Background Determination

There are three major sources of background events that remain in the W sample after the requirements of Section 3.6. A $Z \rightarrow ee$ event will pass our W selection cuts if one of the electrons is lost or badly measured by the detector, and this background is discussed in Section 4.1. Dijet events can pass the cuts if one jet looks like an electron and the other is mismeasured, and we discuss this in Section 4.2. And Section 4.3 discusses the case of $W \rightarrow \tau\nu$ decays where the τ subsequently decays to an electron and neutrinos.

4.1 Lost Z Background

A $Z \rightarrow ee$ decay can mimic a $W \rightarrow e\nu$ decay if one of the electrons is badly measured and is mistaken for a neutrino. This can happen if the electron lands in or near cracks between towers, or passes through regions between detectors. There are three main regions where electrons are likely to be mismeasured. The first is the crack between the east and west halves of the central calorimeter ("90° crack"); the second comprises the cracks at the azimuthal boundaries between central towers ("ϕ cracks");

and the third is the region between the central and plug calorimeter ("30° crack"). We still have tracking coverage in all three of these regions, and we can use the track information to reduce the background.

We start by finding the highest P_T track in the event other than the primary electron track, and we only consider tracks with $P_T > 10$ GeV. The top plot of Figure 4.1 shows the extrapolated Z_{strips} position of this track, for both same sign and opposite sign events, where the sign is the charge of the track relative to the primary electron. All the W selection cuts are applied in this figure except of course the lost Z removal cuts. The opposite sign events show peaks at $Z_{strips} < 9$ cm and $Z_{strips} \approx 250$ cm, which is what we expect for lost Z events with the second track pointing at the 90° or 30° cracks. We consider the 90° crack to be $Z_{strips} < 9$ cm, and the 30° crack is defined to include all tracks which have Z_{strips} higher than the middle of the last central EM tower (231.7 cm), and which extrapolate to a detector position more central than the first fiducial annulus of the PEM. The first fiducial annulus of the PEM occurs at $|\eta_{detector}| < 1.2$, and for extrapolating the track we assume the PEM has a Z position of 190 cm.

Between the 90° and 30° crack regions, the ϕ cracks are significant. The bottom plot of Figure 4.1 shows the X_{strips} position of events between the two regions, and spikes corresponding to the edge of the towers are prominent for the opposite sign events.

Following Figure 4.1, we consider an event a lost Z if there is a second track in the event with $P_T > 10$ GeV, which has opposite sign to the primary electron track, and which points at either the 90° crack, the 30° crack, or is before the 30° crack but has $|X_{strips}| > 21$ cm. The crack regions are defined above. In addition, if the track points at the chimney module, we also consider it a lost Z event. This defines the

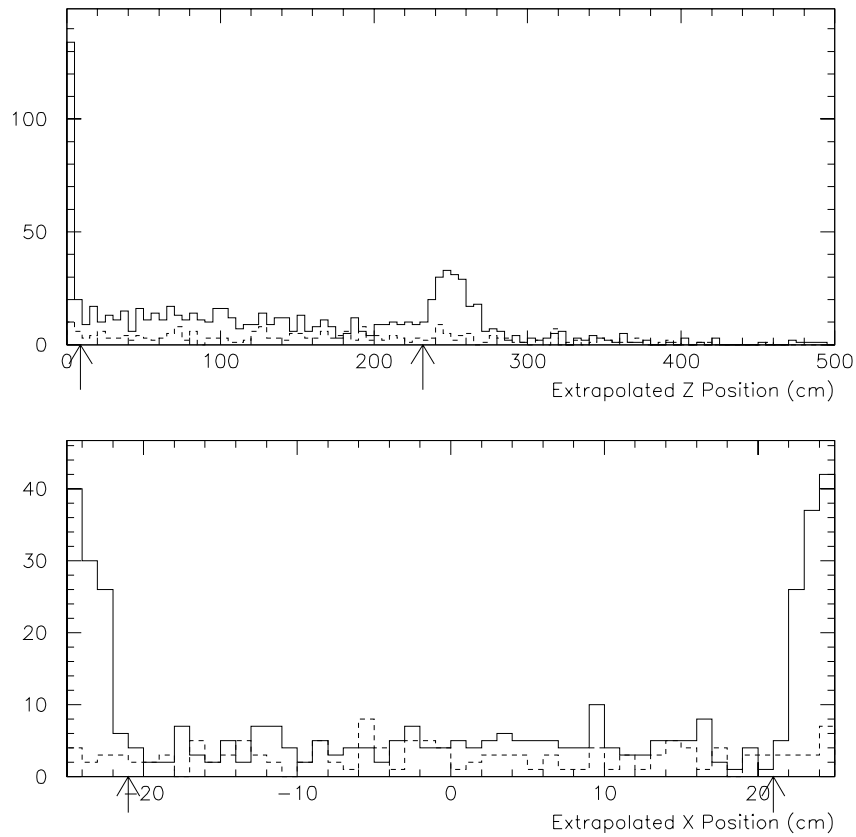

Figure 4.1: Lost Z events in the $W \rightarrow e\nu$ sample. The plots are the locations of second tracks in $W \rightarrow e\nu$ events. Solid histograms are for tracks with opposite sign to the primary electron, and dashed are for the same sign. Top: $|Z_{strips}|$ position of the track. (This variable is defined to be simply the Z position of the track at a radius of 185 cm, which is why it extends beyond the physical Z boundary of the strip chambers.) The arrows shown are at 9 cm and 231.7 cm. Bottom: The X_{strips} position for the tracks with $|Z_{strips}|$ between 9 and 231.7 cm. The arrows are at ± 21 cm and define the ϕ cracks of the central calorimeter. All the W cuts of Table 3.1 up to but not including the lost Z cuts are applied.

"Not a Z Candidate" cut of Section 3.6.

Figure 4.2 shows the invariant mass of the events we are removing as lost Z events. The invariant mass is formed with the primary electron and the second track. The primary electron is taken to point along its track direction, and its energy is taken to be the calorimeter energy. We do the same with the second track, except we use the magnitude of the track momentum for its energy. The top plot shows the lost Z events with the track pointing at the 30° crack, and the bottom plot shows the remaining, central, lost Z events. Both plots show clear Z mass peaks. Also shown are the same sign events, and these show us the size and shape of non-Z events which are being removed as lost Z events. The bottom plot also shows the invariant mass for the second track pointing at a fiducial part of the calorimeter. No mass peak is seen, as expected, since good Z events should fail the $\not\!\!E_T$ cuts.

There are 106 events that would fail the cuts if we replaced the opposite sign requirement with a same sign requirement. This is a measure of the number of events which are mistakenly removed as lost Z events. The azimuthal angle between the second track and the primary electron track for the same sign events has an enhancement around π, indicating that some amount of these events are QCD background. The lost Z cut removes some QCD background. This is expected since the QCD background has a large contribution from jets that point at cracks. When we measure the QCD background below, we only consider the QCD background that remains after the lost Z cut.

The QCD background has a large contribution from jets which point at cracks, and that background is discussed below.

Lost Z events will remain in the sample if the second track is below 10 GeV or is not found by the tracking chamber. Taking the energy distribution of central

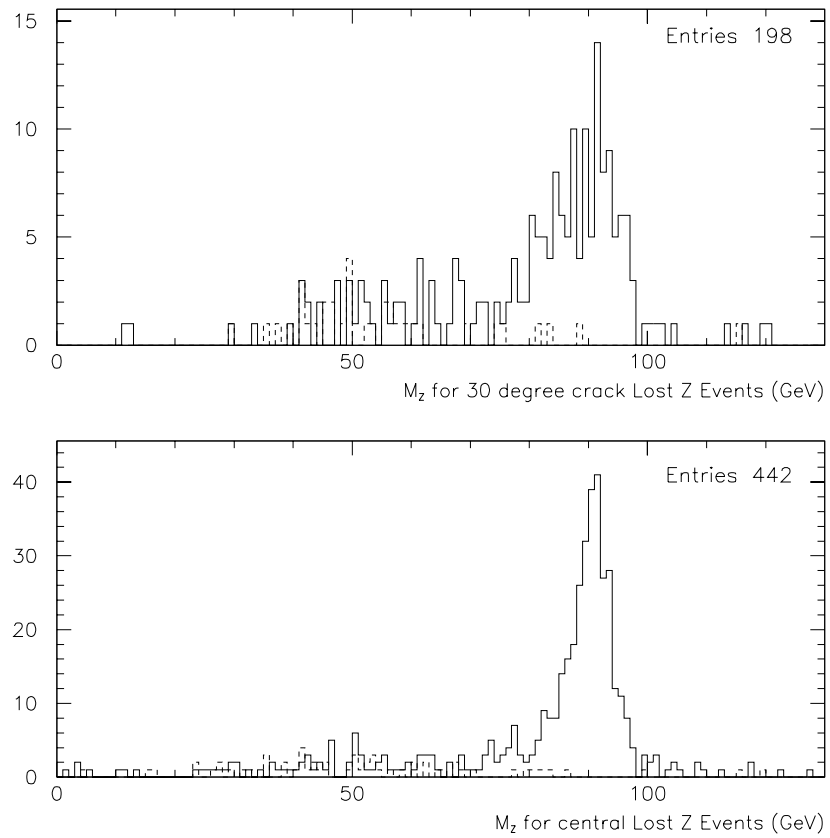

Figure 4.2: Invariant mass of second track and primary electron cluster. The solid histogram are for opposite sign events, and dashed are same sign. Top: events with second track pointing at 30° degree crack, and bottom: events with second track pointing at 90° crack, ϕ cracks, or chimney module. The tracks in the top plot show a worse resolution than the bottom plot since the tracks in the top plot are less likely to pass through all 9 superlayers of the CTC. The number of entries shown are for the solid histograms and include events that fall outside the plot boundaries.

$Z \rightarrow ee$ decays, and assuming that the tracks go through 8.5% of a radiation length, we calculate that each track has a 2.5% probability of emitting a hard enough photon that the track fails the 10 GeV P_T cut above. In addition, the tracking efficiency drops off from 100% in the central region to $\approx 93\%$ at $\eta_{detector} = 1.2$, which defines the outer part of our 30° degree crack region. This inefficiency arises from tracks that fail to pass through all the CTC layers. We take the worst case of 7% inefficiency in the 30° crack region. The top plot of Figure 4.2 has 198 opposite sign entries, and the bottom plot 442 opposite sign entries. The number not removed because of hard brems is 2.5% of the total number of entries in both plots; and the number not removed because of the tracking inefficiency is 7% of the top plot. Thus we expect 30 lost Z events to remain in the W sample because of the P_T cut on the second track or the tracking inefficiency. This is a small background, and, therefore, the worst case tracking inefficiency is an adequate approximation.

We only look for lost Z events in the regions where we have good tracking. Above $\eta_{detector} = 1.2$, we do not make any attempt to remove lost Z events. There are, however, very few low response regions above $\eta_{detector} = 1.2$. The plug calorimeter is expected to have some small azimuthal cracks every 90°, but looking at second tracks in this region, we see no evidence of azimuthal cracks. A toy simulation of all the calorimeters and cracks predicts that 8 $Z \rightarrow ee$ events, in addition to the 30 above, will not be removed by our lost Z cuts. The total number of lost Z events in our sample is therefore predicted to be 38 ± 6 events, where we only consider a statistical uncertainty. There are 42,558 W events which pass our cuts. The lost Z background thus accounts for $(0.090 \pm 0.014)\%$ of the W sample.

We use the events in Figure 4.2 to calculate kinematic shapes for the background. To get the shapes, we combine the results from the different crack regions according

to the expected rate from each region, ignoring the 8 events in the plug and forward regions. Figure 4.3 shows the expected shape for both $U_{||}$ and $U_{\perp}$ as well as M_T for the lost Z background. The $U_{||}$ plot shows a significant negative bias from events where the second electron leaves energy in the calorimeters. The M_T shape of the full $W \rightarrow e\nu$ sample is overlaid on the bottom plot for comparison. The M_T shape of the lost Z background is as high as real W events, and 81% of the lost Z events have M_T in the fitting region. Combining with the above number for the total lost Z background, we measure that the fitting region contains

$$(0.073 \pm 0.011)\% \tag{4.1}$$

lost Z background.

4.2 QCD Background

Dijet events can pass the W selection cuts if one of the jets looks like an electron, and one of them is mismeasured, creating $\not\!\!E_T$. We refer to such events as "QCD" background. A jet looks like an electron if it has $\frac{E_{had}}{E_{EM}} < 0.125$ and passes the other requirements of Section 3.6 These are relatively loose quality requirements, and as mentioned above, we do not wish to apply any quality cuts which may bias our mass measurement and be difficult to simulate. On the other hand, the $|\vec{U}| < 20$ GeV cut is an implicit anti-QCD cut since it is calculated with the electron cluster removed. The high $\not\!\!E_T$ cut also works to reduce the background. The lost Z removal cuts also remove some QCD background, as mentioned above.

A method to measure the QCD background is to release some of the kinematic cuts and to find a region of some variable which is 100% QCD background. We can

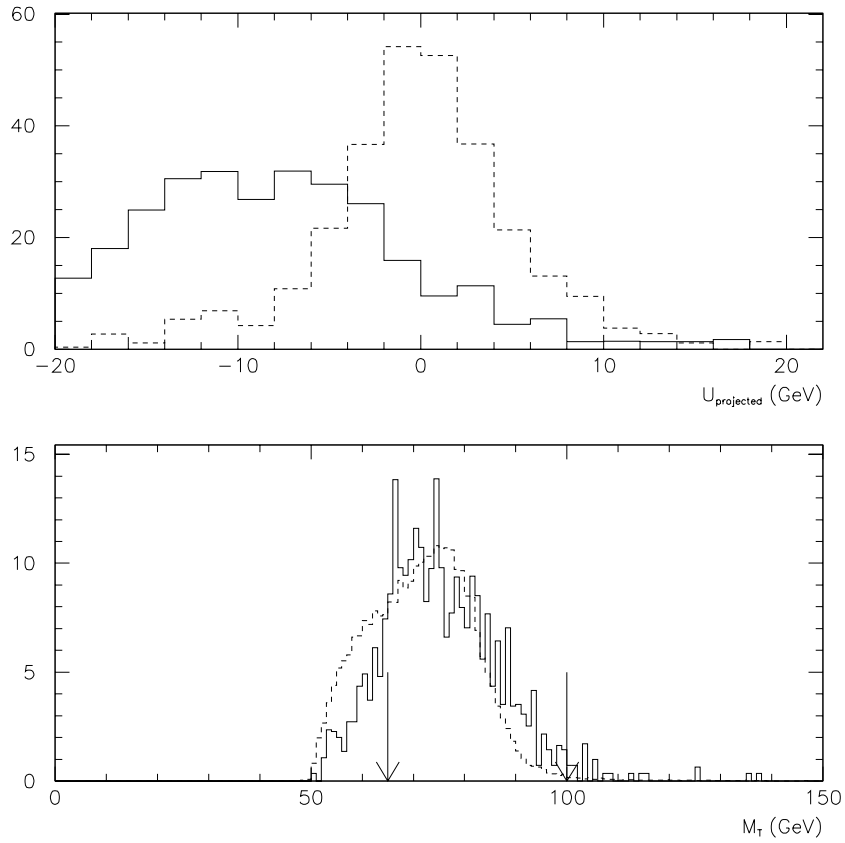

Figure 4.3: Predicted kinematic shapes for the lost Z background events which remain in the W sample. Top: $U_{||}$ (solid) and $U_{\perp}$ (dashed). The mean of the $U_{||}$ shape is -7.5 GeV, and the RMS of $U_{||}$ and $U_{\perp}$ are 7.2 and 5.6 GeV respectively. Bottom: M_T shape for the lost Z background (solid), and for the full $W \rightarrow e\nu$ sample (dashed). The arrows in the bottom plot indicate the M_T fitting region. The normalization in all the plots is the number of events used to calculate the lost Z shapes and does not indicate the total number of events expected in the W sample.

then normalize a QCD shape to this region and extrapolate into the signal region. The $\not{E}_T$ cut is a straightforward choice of a kinematic variable to examine, but there is a $\not{E}_T$ cut in the trigger, which means we cannot release the cut. Instead we look at the data with no $|\vec{U}|$ cut.

The top plot of Figure 4.4 shows the M_T distribution after removing the $|\vec{U}| < 20$ GeV cut. Note the pileup of events in the M_T region below 20 GeV. To explain these events, we note that the transverse mass can be calculated as

$$M_T = 2\sqrt{E_T \not{E}_T} sin(\Delta\phi/2) \tag{4.2}$$

where $\Delta\phi$ is the azimuthal angle between the electron and the direction of the $\not{E}_T$. Since we are retaining the $E_T > 25$ and $\not{E}_T > 25$ GeV cuts, the only way M_T can be small is if $\Delta\phi$ is small. For example, the events with $M_T < 20$ GeV have $\Delta\phi$ peaked near 0, although the distribution extends out to $\approx 45°$. For QCD events the $\not{E}_T$ should point either along the electron direction or opposite to it, depending on which leg is mismeasured and which is called an electron. Thus for the QCD background, we expect both high and low values of $\Delta\phi$. However, for real $W \rightarrow e\nu$ decays we do not expect small $\Delta\phi$, and so we predict that the low M_T events are a pure background sample. The bottom plot of Figure 4.4 shows the azimuthal angle between the electron and the highest E_T jet in the event, for all events and for the low M_T events. The peak around π for the low M_T events is consistent with dijet events. We can also verify that the low M_T events are QCD events by looking at the E/p and $\frac{E_{had}}{E_{EM}}$ shapes of the electron cluster. These are shown in Figure 4.5. Neither of the distributions shows the peaks characteristic of real electrons.

The top plot of Figure 4.6 shows M_T vs $|\vec{U}|$ for the W data with the $|\vec{U}|$ cut

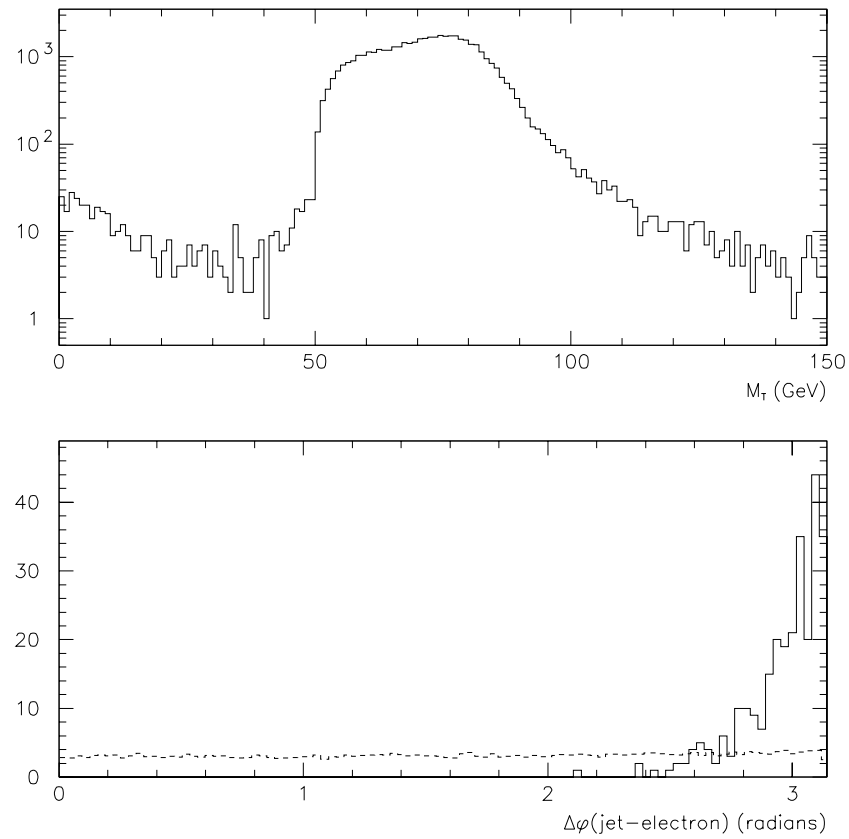

Figure 4.4: Top: M_T distribution of W data without the $|\vec{U}| < 20$ GeV requirement. Bottom: Azimuthal angle between the electron and the highest E_T jet in the event. The solid histogram is the $M_T < 20$ GeV events from the top plot, and the dashed is the full W sample, with the $|\vec{U}|$ cut and with the requirement that M_T be in the fitting region. The dashed plot is normalized to the same area as the solid plot. The dashed plot is flat since most W events do not have significant jet activity. We are considering any jet cluster with $E_T > 1$ GeV to be a jet.

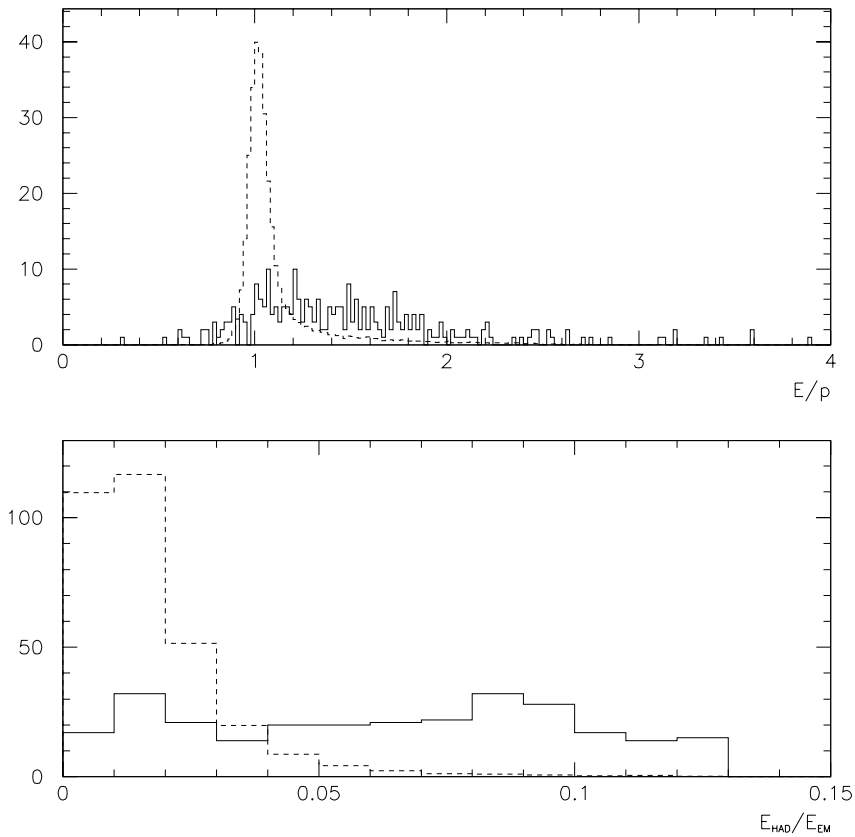

Figure 4.5: Distributions for events with $M_T < 20$ GeV after releasing the $|\vec{U}|$ cut (solid), and for M_T in fitting region with $|\vec{U}|$ cut applied (dashed). Top plot is E/p, and the bottom plot is $\frac{E_{had}}{E_{EM}}$. The cutoff in the $\frac{E_{had}}{E_{EM}}$ plot at 0.125 is from the implicit $\frac{E_{had}}{E_{EM}}$ requirement to consider a cluster electromagnetic.

released. We refer to the region with $|\vec{U}| < 20$ and $M_T > 20$ GeV as "Region A." This region is marked off by the vertical line shown in the plot. "Region B" is defined by $M_T < 20$, and this is marked off by the horizontal line. Only QCD events fall in Region B, and if we know the ratio of A to B for QCD events, we can determine how many QCD events are in Region A. The bottom plot shows M_T vs $|\vec{U}|$ for the QCD events, where the method to extract the QCD shape from the data is described immediately below.

To find a QCD background shape, we use a series of quality cuts on the electron cluster to reject real electrons. We use the following four quality variables:

- $\frac{E_{had}}{E_{EM}}$. This is defined above and is the hadronic energy associated with the cluster divided by the cluster energy.

- Iso. This is the "isolation" of the electron, and is defined as the energy, excluding the electron cluster, located in calorimeter towers within a cone of $\Delta R \equiv \sqrt{(\Delta\phi)^2 + (\Delta\eta)^2} < 0.4$ around the electron cluster, divided by the energy of the electron cluster.

- $q\Delta x$. Δx is defined as the difference between the actual measured strip chamber x-position and the extrapolated position of the associated track. Real electrons may have a non-zero Δx from resolutions, and also from photon bremsstrahlung. The photon will show up in the strip cluster, and the extrapolated track position will be off-center relative to the cluster. It will be on one side for positive tracks and the other side for negative, and for this reason we use the signed quantity $q\Delta x$, where q is the sign of the electron track.

- χ^2_{strips}. This variable compares the longitudinal profile of the energy in the strip chambers with a shape measured with test beam data.

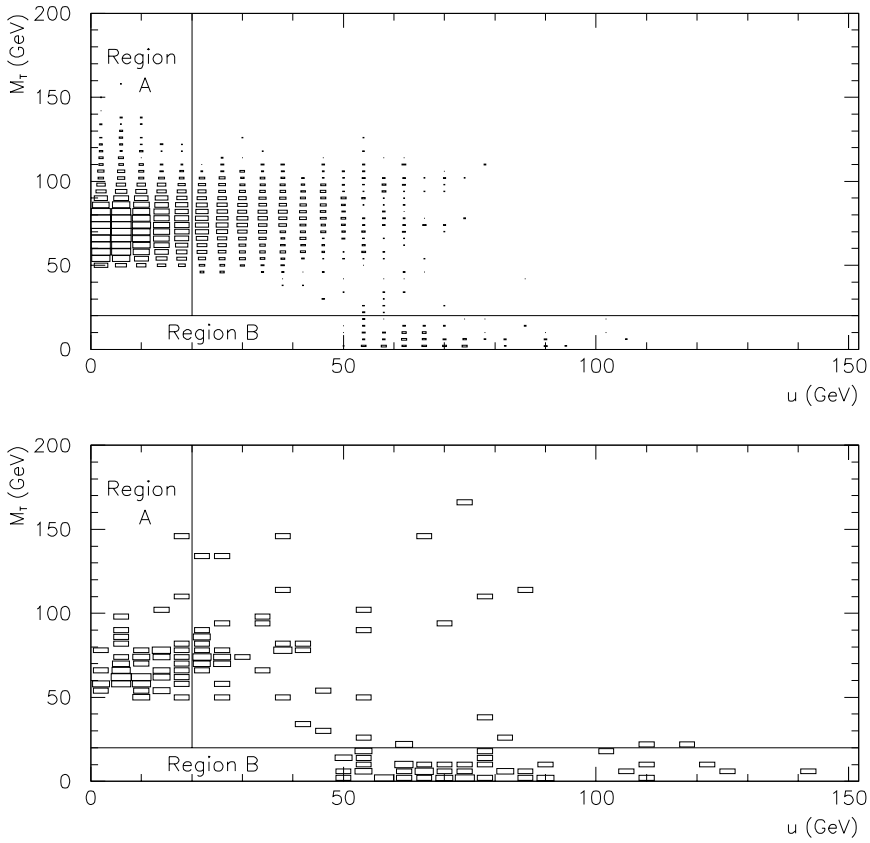

Figure 4.6: M_T vs $|\vec{U}|$ with the $|\vec{U}|$ cut released. Top: All W data, and bottom: the subset of the W data that passes any combination of three of the anti-selection cuts. These cuts are described in the text and are used to find a pure QCD subset of the W data. The horizontal and vertical lines define Regions A and B. In the plots the area of the boxes is proportional to the log of the number of events at each point. If we did not use a log scale, the low M_T region of the top plot would not be visible.

All four variables are shown in Figure 4.7 for the M_T fitting region of the full W sample.

We use the Z sample to determine cuts that will reject electrons and retain QCD events with good efficiency. These cuts are $\frac{E_{had}}{E_{EM}} > 0.08$, Iso$> 0.25$, $q\Delta x < -1.5$, and $\chi^2_{strips} > 20$. The Z sample shows that none of these cuts is 100% efficient to reject electrons, but that combinations of them should be very close to 100%.

To illustrate the background calculation method, we look at the subset of the W sample that passes the $\frac{E_{had}}{E_{EM}} > 0.08$ and Iso> 0.25 "anti-selection" cuts. We find 67 events in Region B, and 62 events in Region A. For the full W sample, without the anti-selection cuts, we find 278 events in Region B. The number of QCD events predicted to be in the signal region (Region A) is then

$$\frac{62}{67} \times 278 = 257 \pm 48.$$

Dividing by the $42,558$ W events of the signal region, we find

$$(0.60 \pm 0.11)\% \tag{4.3}$$

QCD background. The uncertainty on this result is calculated assuming all the numbers are independent. This is not actually the case since the 67 events are a subset of the 278, and the 62 are a subset of the $42,558$. However, a more careful determination of the uncertainty gives a similar answer.

Figure 4.8 shows the calculated percent background for different combinations of anti-selection cuts. The first six points anti-select on two of the quality variables, and the next four on three of the variables. Note that the point that uses $q\Delta x$ and χ^2_{strips} to define the QCD shape is anomalously high, and this perhaps indicates that some

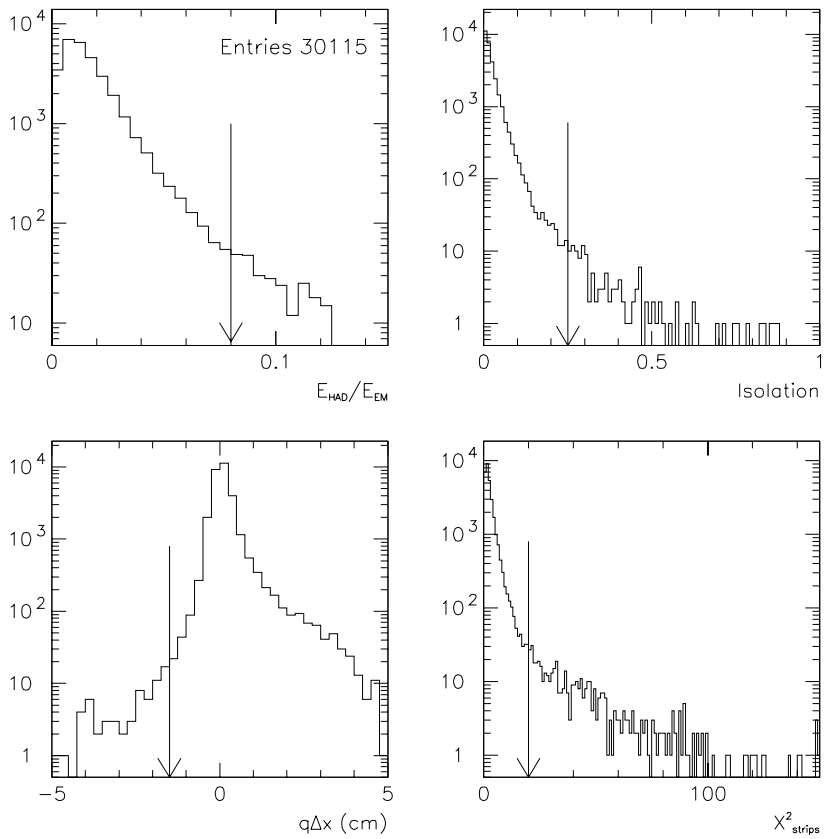

Figure 4.7: Some electron quality variables for the full W sample, in the M_T fitting region. Top left: $\frac{E_{had}}{E_{EM}}$, top right: Iso, bottom left: $q\Delta x$, and bottom right: χ^2_{strips}. The enhancement on the right side of the $q\Delta x$ plot is a result of photon bremsstrahlung. The arrows shown indicate the location of the "anti-selection" cuts. To select QCD events we require that the variables be to the right of the arrows, except for $q\Delta x$ which is required to be to the left.

real W electrons remain in Region B for those cuts. The last point defines Region B with events that pass any combination of three of the anti-selection cuts. This point is labeled "OR" on the axis and is the number we will use for the assumed QCD background rate. Since the points are not statistically independent, we include the error-weighted RMS of the first ten points as a systematic uncertainty on the final value. This value is 0.0029, and the final value for the QCD background fraction in the W sample is

$$(0.76 \pm 0.15(stat) \pm 0.29(sys))\% = (0.76 \pm 0.33)\%. \tag{4.4}$$

To determine the $U_{||}$, $U_{\perp}$, and M_T shapes, we use the events that pass any combination of three of the four anti-selection cuts. There are 167 such events before we apply the $|\vec{U}|$ cut, and 62 after. To increase the statistics, we remove the N_{tracks} cut and we end up with 249 events after the $|\vec{U}|$ cut. The distributions of these 249 events are shown in Figure 4.9. The negative bias on the $U_{||}$ shape is from residual energy left in the detector from the lost jet. The M_T shape is lower than for the real W electrons, and we count that 119 of the 249 events have M_T in the fitting region. Combining this with the above number for the fraction QCD background before the M_T cut, we calculate that the QCD events comprise

$$(0.36 \pm 0.17)\% \tag{4.5}$$

of the W events in the M_T fitting region.

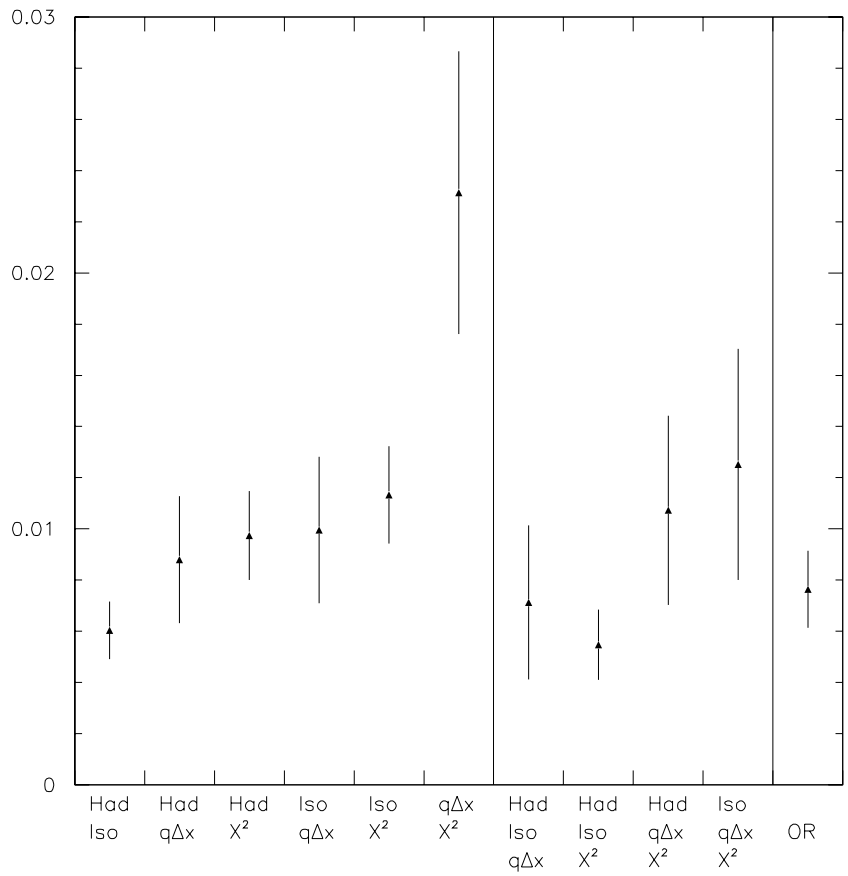

Figure 4.8: The background fraction as a function of the combination of anti-selection cuts used to define Region B. "Had" refers to the $\frac{E_{had}}{E_{EM}}$ cut and χ^2 to the χ^2_{strips} cut. The last point labelled "OR" uses all combinations of three of the cuts. The text has more details.

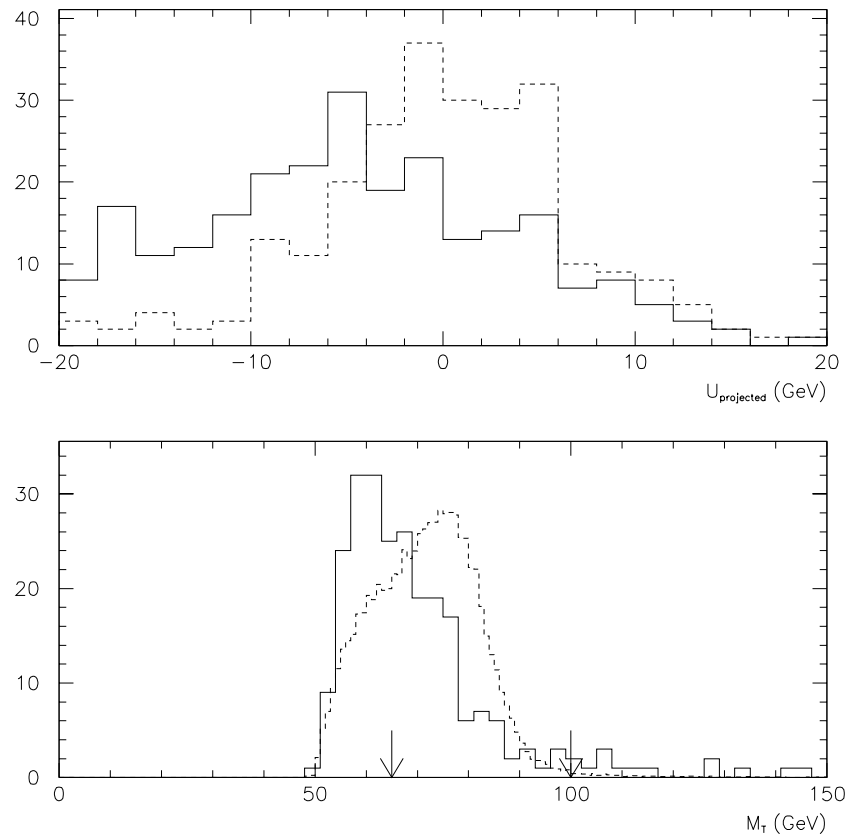

Figure 4.9: Kinematic shapes for the QCD background events. Top: $U_{||}$ (solid) and $U_{\perp}$ (dashed). Bottom: M_T for the QCD background events (solid), and for the full $W \to e\nu$ sample (dashed), which is shown for comparison. The mean of the $U_{||}$ histogram is -4.5 GeV, and the RMS of $U_{||}$ and $U_{\perp}$ are 8.1 and 6.6 GeV respectively. The arrows in the bottom plot indicate the M_T fitting region.

4.3 $W \rightarrow \tau\nu$ Background

The decay $W \rightarrow \tau\nu \rightarrow e\nu\nu\nu$ results in a relatively high E_T electron and $\not{E}_T$, and so can fake a $W \rightarrow e\nu$ decay. Since there are four decay products, the electron will have substantially lower energy then in a $W \rightarrow e\nu$ decay, and this background is reduced by the E_T cut. It is further reduced by the requirement that M_T appear in the fitting region. Besides the kinematic cuts, we make no other attempt to reduce this background, and instead we include it in the simulation.

We simulate the decay by starting with a $W \rightarrow e\nu$ decay, and then calling the electron a τ. We then decay the τ into an electron and two neutrinos, and add the new neutrino 4-vectors to the original neutrino 4-vector. The simulation then proceeds as if a $W \rightarrow e\nu$ decay had been generated to start with. We randomly choose 15.132% of the Monte Carlo events to change into τ decays in this way. The number 15.132% is derived by assuming that the W decays with equal rates into $e\nu$ and $\tau\nu$. With 15.132%, the number of $W \rightarrow \tau\nu \rightarrow e\nu\nu\nu$ events we will generate divided by the number of $W \rightarrow e\nu$ events is then $0.15132/(1 - 0.15132) = 0.1783$. This is the value of the branching ratio , $(\tau \rightarrow e\nu\nu)/$, (τ), as desired.

Figure 4.10 shows the distributions of $U_{||}$, $U_{\perp}$, and M_T for the simulated $\tau \rightarrow e\nu\nu$ background. The events shown pass all the W selection cuts. For the $U_{||}$ and $U_{\perp}$ plots, M_T is required to be in the fitting region, but this requirement is released for the M_T plot. The M_T plot is clearly peaked at lower transverse mass than the full $W \rightarrow e\nu$ data sample. This reduces the effect of this background on the fitted W mass.

We count the total number of generated events that pass all the cuts. We find that the simulation predicts the $\tau \rightarrow e\nu\nu$ background to be 2.8% of the events without

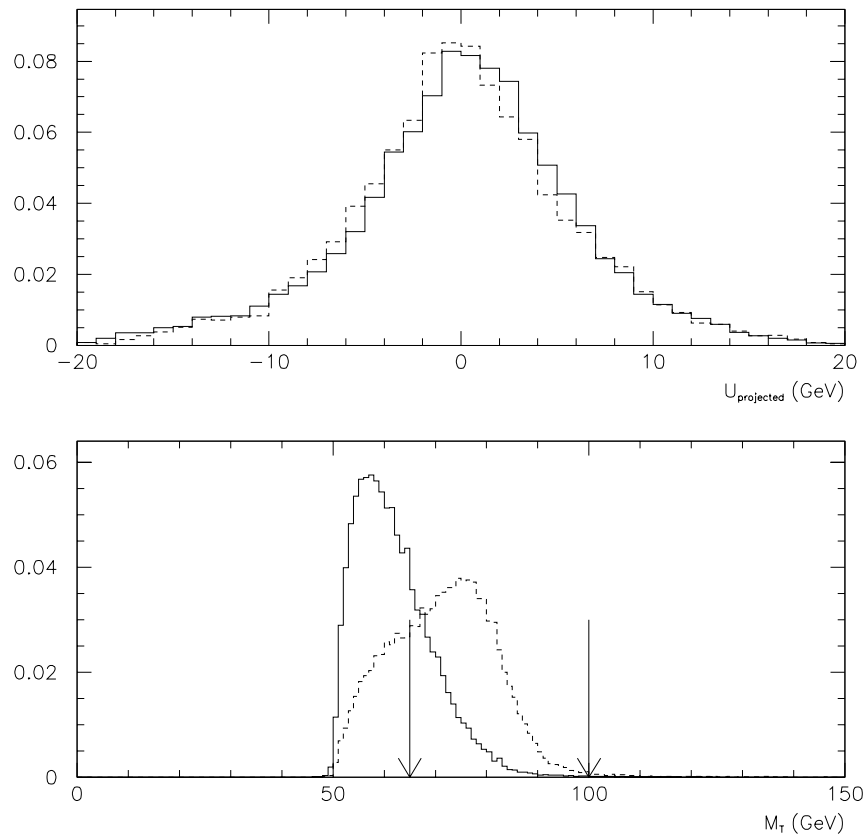

Figure 4.10: Kinematic shapes for the τ background events. Top: $U_{||}$ (solid) and $U_{\perp}$ (dashed). Bottom: M_T for the τ background events (solid), and also for the full $W \rightarrow e\nu$ data sample (dashed). The full data sample is shown for comparison. For the $U_{||}$ and $U_{\perp}$ plots, M_T is required to be in the fitting region. The mean of the $U_{||}$ histogram is 0.1 GeV, and the RMS of $U_{||}$ and $U_{\perp}$ are 5.9 and 5.8 GeV respectively. The arrows in the bottom plot indicate the M_T fitting region.

the M_T requirement, and 0.8% if M_T is required to be in the fitting region.

We have also studied the $W \to \tau\nu$ background where the τ decays hadronically. We generate $1,000,000$ PYTHIA events. We find that 586 of these events will form an electromagnetic cluster and will pass all our $W \to e\nu$ selection requirements. Using a production cross section times branching ratio of $\sigma(p\overline{p} \to WX)Br(W \to \tau\nu) = 2.2 \pm 0.2$ nb, we expect $\approx 200,000 \pm 20,000$ $W \to \tau\nu$ events in the 90 pb^{-1} Run 1B data sample. $\approx 80\%$ of the τ's decay hadronically, and the total number of hadronic τ decays in our $W \to e\nu$ sample is predicted to be $(586/1,000,000) \times (200,000 \pm 20,000) \times 0.8 = 94 \pm 9$ events. Of the 586 Monte Carlo events, only 101 have $65 < M_T < 100$ GeV, and we expect 16 ± 2 events in the fitting region. This is a 0.05% background in the fitting region.

4.4 Summary

We have discussed the three main sources of background: Z events where one leg is lost, QCD events where the jets are mismeasured and one is identified as an electron, and $W \to \tau\nu$ events. For the lost Z and QCD backgrounds, we used the data to calculate the background rates and distributions. The electron decays of the τ are included directly in the simulation, while the hadronic τ decays, the lost Z, and the QCD background are included after the simulation. Histograms of the shapes of these last three backgrounds are added to the Monte Carlo when we do fits of the data to the Monte Carlo. This is true when we compare the $\vec{U}$ distributions of data and Monte Carlo and also when we compare the E/p and M_T distributions of data and Monte Carlo.

Table 4.1 summarizes the rates for the three different backgrounds.

	M_T in Fitting Region	No M_T Requirement
QCD	$(0.36 \pm 0.17)\%$	$(0.76 \pm 0.33)\%$
Lost Z	$(0.073 \pm 0.011)\%$	$(0.090 \pm 0.014)\%$
$W \to \tau\nu \to e\nu\nu\nu$	0.8%	2.8%
$W \to \tau\nu \to$hadrons ν	$(0.054 \pm 0.005)\%$	$(0.31 \pm 0.03)\%$

Table 4.1: Background rates for the four largest sources of background in the W sample. The four backgrounds considered are lost Z events, QCD events, and $W \to \tau\nu$ events where τ decays to electrons and hadrons are considered separately. The rates are for the W sample after all cuts, and we also show the rates without the requirement that M_T is in the fitting region.

Chapter 5

Event Generation

The simulation of the scattering process

$$p\overline{p} \rightarrow W + X \rightarrow e\nu\gamma + X$$

proceeds in two steps. The 4-momenta of the decay products e, ν, and γ are written out to disk, along with associated weights and other event information, and later a detector simulation is applied to these events. In this chapter we discuss the production of the event, and in later chapters we discuss the detector simulation.

In Section 5.1 we discuss the cross section for W production, and in Section 5.2 we discuss the details of the generation of the Monte Carlo variables. In Section 5.3 we discuss the decay of the boson, and in Section 5.4 we discuss differences in the Monte Carlo between W production and Z production. We summarize in Section 5.5.

5.1 W Production Cross Section

We consider a parton model in which the quarks involved in the hard scatter are treated as free particles, and their momentum distributions are determined by the parton distribution functions. The distribution functions account for initial state radiation in the longitudinal direction only, and we will need to consider the possibility of transverse radiation.

A Feynman diagram of the production process is shown in Figure 5.1. The initial state consists of two quarks with momenta q_1 and q_2. The momentum fractions x_1 and x_2 are defined as $q_1 = x_1 P_1$ and $q_2 = x_2 P_2$, where P_1 and P_2 are the momenta of the colliding proton and anti-proton, respectively.

The center of mass energy of the two-quark system is $\sqrt{\hat{s}}$ where

$$\hat{s} = (q_1 + q_2)^2 = x_1 x_2 s \tag{5.1}$$

and $\sqrt{s} = 1800$ GeV is the center of mass energy of the proton collision. We have neglected the mass of the quarks and protons relative to the center of mass of the system.

In Section 5.1.1 we present the lowest order cross section for W production, which corresponds to the top diagram of Figure 5.1. At higher orders, the W acquires transverse momentum. In previous W mass analyses at CDF, the lowest order cross section was used to generate the event, and afterwards the center of mass was boosted according to a W P_T distribution. There was an ambiguity, however, in whether to perform the transverse boost in the W rest frame, or in the lab frame. The two frames are potentially different if $x_1 \neq x_2$. Our method of producing an event with W P_T is discussed in Sections 5.1.2 and 5.1.3.

Figure 5.1: Feynman diagrams of the event production. The initial state consists of two quarks with 4-vectors q_1 and q_2 which have momentum fractions x_1 and x_2. The boson 4-vector, Q, has associated mass squared, transverse momentum, and rapidity Q^2, Q_T, and y_W respectively. The top plot is the lowest order diagram, where only longitudinal gluon radiation is considered. The longitudinal radiation is subsumed in the x_1 and x_2 distributions. The bottom plot represents higher order diagrams, where one or more gluons with non-zero P_T may be radiated from the initial quarks.

In general, any 4-momentum can be written as

$$\begin{pmatrix} Q_0 \\ Q_1 \\ Q_2 \\ Q_3 \end{pmatrix} = \begin{pmatrix} \sqrt{Q_T^2 + Q^2}\cosh y_W \\ Q_T \cos\phi \\ Q_T \sin\phi \\ \sqrt{Q_T^2 + Q^2}\sinh y_W \end{pmatrix} \tag{5.2}$$

where Q_0 is the energy, and Q_1, Q_2, and Q_3 are the x-, y-, and z-components of the 3-momentum respectively; and where Q_T and ϕ are the transverse component and azimuthal angle of the 3-momentum respectively, and Q^2 is the invariant square of the 4-vector. The rapidity of the 4-vector, y_W, is given by

$$y_W = \frac{1}{2}\log(\frac{Q_0 + Q_3}{Q_0 - Q_3}) \tag{5.3}$$

We use these variables below to describe the W boson.

5.1.1 Lowest Order Cross Section

The boson is determined by its mass $\sqrt{Q^2}$, transverse momentum Q_T, and rapidity y_W. At lowest order in the strong coupling constant, α_s, there is no transverse radiation, and the W kinematics are completely determined by x_1 and x_2. Energy and momentum conservation require

$$Q^2 = \hat{s}, \quad Q_T = 0, \quad y_W = y_0 \equiv \tfrac{1}{2}\log\frac{x_1}{x_2} \tag{5.4}$$

We are ignoring the intrinsic K_T of the quarks in the protons.

The total cross section σ_{total} is calculated by an integral over x_1 and x_2

$$\sigma_{total} = \int\int dx_1 dx_2 p(x_1, x_2, Q^2)\sigma_0(Q^2) \tag{5.5}$$

where

$$\sigma_0(Q^2) = \frac{1}{Q^2} \times \frac{1}{(1 - M_W^2/Q^2)^2 + (, _W/M_W)^2} \tag{5.6}$$

This is a relativistic Breit-Wigner distribution with an "s-dependent width," scaled by $1/Q^2$. The parameter , $_W$ is the total width of the W, and M_W is the W mass. This cross section is correct only up to overall constants, but since we are not concerned with the absolute rate of W production, there is no need to include these constants.

The function $p(x_1, x_2, Q^2)$ in Equation 5.5 represents the contribution to the integral from quarks with momentum fractions x_1 in the proton and x_2 in the anti-proton. In terms of the parton distribution functions we have

$$p(x_1, x_2, Q^2) = \sum_{ij} |V_{ij}|^2 f_i(x_1, Q^2)\bar{f}_j(x_2, Q^2) \tag{5.7}$$

were $f_i(x_1, Q^2)$ is the differential probability that a quark in the proton of type i with momentum fraction x_1 will contribute to an interaction at an energy scale of Q^2. $\bar{f}_j(x_2, Q^2)$ is the analogous function for the anti-proton. Our default choice for the parton distribution functions are the MRS-R2 distribution functions, and in a later chapter we will consider the systematic uncertainty on the fitted W mass due to the choice of distribution functions. The sum is over all quark types, and V_{ij} are the corresponding CKM matrix elements. We only consider contributions from the first two quark generations, ignoring top and bottom quarks. Both sea quark and valence quark contributions are considered. For the CKM matrix elements, we use

$|V_{ud}|^2 = .95$, $|V_{us}|^2 = |V_{cd}|^2 = .0484$, and $|V_{cs}|^2 = .903$.

5.1.2 Higher Order Cross Section

At higher orders in α_s, the initial quarks can radiate gluons, and the W can acquire transverse momentum. The rapidity of the W, y_W, is in general different from $y_0 = \frac{1}{2}\log\frac{x_1}{x_2}$.

The initial state radiation is dominated by strong processes and should factor from the electroweak part of the diagrams. We consider the production of a real, stable W with a fixed mass M. Below we will integrate the cross section with respect to a Breit-Wigner distribution.

First we consider the cross section for the emission of a single gluon. Since we are treating the W as a real, stable particle, we have a two-body final state. The parton level cross section is

$$\hat{\sigma} = \int |\tilde{M}|^2 \frac{d^3g}{g_0}\frac{d^3Q}{Q_0}\delta^4(q_1 + q_2 - Q - g) \tag{5.8}$$

where we are ignoring overall constants. $\tilde{M}$ is the matrix element for the first order diagram, and the term d^3g/g_0 is the phase space for the gluon, where g_0 is the gluon energy. The phase space for the W is d^3Q/Q_0. The overall δ^4-function enforces energy and momentum conservation, where we have written the gluon and W 4-momenta as g and Q respectively.

The finite W lifetime is included below by integrating this cross section with respect to the generated mass M, weighted by the Breit-Wigner function $\sigma_0(M^2)$. To simplify that calculation, we rewrite the W phase space term according to the identity $d^3Q/Q_0 = d^4Q\delta(Q^2 - M^2)$. We further use the identity $d^4Q = d^3Q dQ_0 =$

$(Q_0 \times dQ_T^2 dy_W) dQ_0$ where y_W is the rapidity of the W and Q_0 is its energy. Integrating the δ^4-function of Equation 5.8 over d^3g and dQ_0 gives

$$\hat{\sigma} = \int\int R(Q_T, \Delta y) dQ_T^2 d(\Delta y) \delta(Q^2 - M^2) \tag{5.9}$$

where $R(Q_T, \Delta y) \equiv |\tilde{M}|^2 Q_0/g_0$. Here we have written $\Delta y \equiv y_W - y_0$, where y_W is the rapidity of the W, and $d(\Delta y) = dy_W$. We will use the Monte Carlo to integrate this equation by generating random points in Q_T and Δy space. This is discussed in Section 5.2.

The function $R(Q_T, \Delta y)$ describes the distribution of the initial state radiation, and we will discuss the form of R in the next section.

Energy and momentum conservation requires $g = q_1 + q_2 - Q$. Evaluating g^2 in the lab frame, and requiring that the gluon be massless, we get the following relation between $\hat{s}$, Q_T, Q^2, and Δy

$$g^2 = \hat{s} - 2\cosh(\Delta y)\sqrt{\hat{s}(Q^2 + Q_T^2)} + Q^2 = 0 \tag{5.10}$$

This relation is only correct to first order. At higher orders in α_s, g is replaced by the 4-vector sum of all emitted gluons, and in that case g^2 is potentially non-zero. Nevertheless, we will use this relation below to connect Q^2 to $\hat{s}$, Q_T, and Δy.

5.1.3 Functional Form for Initial State Radiation

The function $R(Q_T, \Delta y)$, which describes the distribution of the initial state radiation, is a function of $\hat{s}$, Q_T, and Δy. It also depends on Q^2, but Q^2 is determined by $\hat{s}$, Q_T, and Δy through Equation 5.10. We separate $R(Q_T, \Delta y)$ into a function that depends

only on Q_T and a function that describes the rapidity distribution of the initial state radiation. We write the identity

$$R(Q_T, \Delta y) = \bar{R}(Q_T)\Upsilon(Q_T, \Delta y) \tag{5.11}$$

where $\bar{R} \equiv \int R(Q_T, \Delta y) d(\Delta y)$, and $\Upsilon \equiv R/\bar{R}$.

$\bar{R}$ has dimensions of E^{-2}, and therefore the quantity $\hat{s}\bar{R}$ is dimensionless. The argument of a dimensionless function must also be dimensionless, and we can express $\hat{s}\bar{R}$ as some function of the quantity $Q_T/\sqrt{\hat{s}}$. We define the function

$$\frac{\sqrt{\hat{s}}}{Q_T}\Psi(Q_T/\sqrt{\hat{s}}) \equiv \hat{s}\bar{R}(Q_T) \tag{5.12}$$

We have defined Ψ with the extra factor of $\sqrt{\hat{s}}/Q_T$ in front because in the Monte Carlo we will integrate Equation 5.9 with respect to dQ_T instead of dQ_T^2. We will fit for Ψ using the data, and this fit is the subject of Chapter 7. We have divided Q_T by the $\sqrt{\hat{s}}$ to produce the dimensionless quantity $Q_T/\sqrt{\hat{s}}$. However, there is another significant energy in the event which we could have used to produce a dimensionless quantity. This energy is Λ_{QCD}. We could also consider it to be the energy below which the non-perturbative effects in the boson P_T calculation become significant. Thus, for Q_T below or around this cut-off energy, we do not expect the Q_T distribution to scale with the boson mass. We make a correction for this effect in Section 5.4.2 below.

For the distribution Υ, we start with the relation that $R(Q_T, \Delta y) = |\tilde{M}|^2 Q_0/g_0$. The parton distribution functions are evolved to an energy scale of Q^2, as opposed to $\hat{s}$, and therefore the forward part of the gluon radiation is already accounted for. We approximate this effect by adjusting R such that the forward part is subtracted out. We define the forward part as the region where $Q_0 \sim |Q_3|$, where Q_3 is the

longitudinal part of the W momentum. We get

$$\Upsilon = \frac{|\tilde{M}|^2(Q_0 - |Q_3|)/g_0}{\int(\cdots)d(\Delta y)} \tag{5.13}$$

$$= \frac{\{1 + (Q^2/\hat{s})^2 - 2Q_T^2/\hat{s}\}(Q_0 - |Q_3|)/g_0}{\int(\cdots)d(\Delta y)} \tag{5.14}$$

where the symbol "$\int(\cdots)d(\Delta y)$" corresponds to the integral of the numerator with respect to $d(\Delta y)$. The term in squiggly brackets is calculated from the first order matrix element [31].

Since we will determine the function $\Psi(Q_T/\sqrt{\hat{s}})$ from the data, we are effectively including all Feynman diagrams at all orders in α_s. However, for the Δy distribution, we are only calculating Υ at first order in α_s. Moreover, Equation 5.10 is only correct when g^2 is zero, which is not necessarily true when multiple gluons are emitted. g^2 will not always be zero, but we can still use Equation 5.10 as long as we perturb the distribution of Δy appropriately. Therefore, our assumed distribution Υ is only approximate. We expect it to be an adequate approximation however. The first order calculation begins to fail at low values of Q_T. At low Q_T, the Δy distribution we are using is strongly peaked at small values of Δy, and has a pole at $Q_T = 0, \Delta y = 0$. We can assume that purely longitudinal gluon radiation is already accounted for by the parton distribution functions, and we expect the correct distribution also to be strongly peaked at low values of Δy for small Q_T. Since Δy is mostly small, we are not sensitive to the exact shape of its distribution. At higher values of Q_T, the Δy distribution has a larger tail, but there we expect the first order calculation to be a good approximation.

5.1.4 Summary

Equation 5.9 is the parton level cross section to produce a real, stable W with a mass M. The total parton level cross section will be an integral over all masses, weighted by the W propagator squared. The W propagator squared is exactly the function $\sigma_0(M^2)$ which we have defined in Equation 5.6. The $\delta(Q^2 - M^2)$ term makes the integral with respect to M^2 trivial, and embedding $\hat{\sigma}$ in an integral over the parton distribution functions, we get

$$\sigma_{total} = \int \frac{1}{\sqrt{\hat{s}}} \Psi(Q_T/\sqrt{\hat{s}}) \Upsilon(Q_T, \Delta y) \sigma_0(Q^2) p(x_1, x_2, Q^2) \times dx_1 dx_2 dQ_T d(\Delta y) \quad (5.15)$$

where Ψ and Υ are discussed in Section 5.1.3, and Q^2 is a function of Q_T and Δy through Equation 5.10.

5.2 Generation of Event Variables

We use the Monte Carlo to perform a numerical integral over the 4 integration variables of Equation 5.15, dx_1, dx_2, dQ_T, and $d(\Delta y)$. The integral is calculated by generating non-uniform distributions and then adjusting an event weight so that the weighted density of points is uniform. Before the generation the event weight starts with a value of one.

5.2.1 x_1 and x_2 Generation

We generate x_1 and x_2 independently according to the exponential distribution $\exp(-9x)$, and we divide the event weight by $\exp(-9x_1 - 9x_2)$ so that the weighted distributions are uniform. The exponential is an approximation to the parton distribution

functions, and this will improve the generation efficiency.

The center of mass energy squared is $\hat{s} = sx_1x_2$, and $y_0 = \frac{1}{2}\log\frac{x_1}{x_2}$.

5.2.2 Q_T and Δy Generation

The lower bound on Q_T is zero, and the upper bound is the kinematic limit $\sqrt{\hat{s}}/2$. The upper limit corresponds to the case of the $Q^2 = 0$.

We generate the variable $Q_T/\sqrt{\hat{s}}$ according to a histogram between 0 and 0.5 which peaks a low values, and we divide the weight by the value of the histogram at the generated point. In this way the weighted density of points is flat in the variable $Q_T/\sqrt{\hat{s}}$, and we also attain a higher efficiency of generation since most of the cross section is at low Q_T. We then multiply the event weight by $\sqrt{\hat{s}}$ to make the weighted density of points flat in Q_T.

We can include the function $\Upsilon(Q_T, \Delta y)$ in the numerical integral of Equation 5.15 by generating Δy according to a flat distribution and multiplying the weights by $\Upsilon(Q_T, \Delta y)$. To calculate $\Upsilon(Q_T, \Delta y)$, we need to integrate the numerator of Equation 5.14 with respect to Δy, but this is not a simple function to integrate. However, the effect of this normalizing integral is that the Q_T distribution is identical before and after the choice of Δy. Thus, we account for the normalizing integral by generating values for Δy according to the numerator of Equation 5.14, between the allowed boundaries for Δy. We do not need to calculate the normalizing integral of Equation 5.14.

For the given value of Q_T, the upper bound on Δy is determined from Equation 5.10 with Q^2 evaluated at 0. The upper bound is the solution to

$$\cosh(\Delta y) = \sqrt{\hat{s}}/(2Q_T) \quad (\textit{upper bound}) \tag{5.16}$$

and the lower bound is 0. We are assuming that Δy is positive, since all our equations are symmetric in Δy, and later we will choose its sign randomly. As $Q_T \rightarrow 0$, the upper bound on Δy becomes arbitrarily large. At the same time, the Δy distribution becomes more and more peaked at 0, becoming a pole for $Q_T = 0$. To account for this, we adjust the Δy distribution to be $\delta(\Delta y)$ for $Q_T/(\sqrt{\hat{s}}) < 0.1\%$. The integral of this distribution is 1, and for those values of Q_T, we simply choose $\Delta y = 0$.

5.2.3 Breit-Wigner Rejection

When we multiply the event weight by the Breit-Wigner function of Equation 5.6, many of our generated events will be given small weights. To reduce the number of small weight events that we will run a detector simulation on, we reject events at this point according to a Breit-Wigner shape. We calculate a Breit-Wigner with $M_W = 80.35$ GeV and a width which is twice the expected W width. We double the width because we will vary the mass in our final fits, and we want to generate events over a wide enough range in Q^2.

Normalizing the function so that the maximum is 1, we choose a random number and reject the event according to the size of the function. If the event is not rejected, we divide the event weight by the value of the Breit-Wigner. In this way, we produce fewer events in the Breit-Wigner tails, but we increase their weights so the weighted distributions remain uniform.

For Z production we apply the same rejection technique, except that the Breit-Wigner is evaluated at the expected values for the Z mass and width of 91.187 and 2.49 GeV respectively.

5.2.4 Flavor Generation

The relative probabilities of the different quark flavors are determined by the distribution functions through Equation 5.7. Rather than choose a quark type uniformly among the different possibilities, it is more efficient to choose according to the expected distribution, and then to adjust the event weight. We evaluate the product of the parton distribution functions at values of x_1 and x_2 which will give $\sqrt{\hat{s}}$ near the W mass. We choose $x_1 = x_2 = 80.35/1800$, and we then multiply by the appropriate CKM matrix elements.

These numbers give us a measure of the relative probabilities for the different flavor combinations, and they are shown to three significant digits in Table 5.1. The table shows that $\approx 75\%$ of W^+ events are produced by a u quark from the proton and a $\overline{d}$ from the anti-proton.

	u	c	$\overline{d}$	$\overline{s}$
u	0	0	.756	.124
c	0	0	.00678	.0461
$\overline{d}$	.125	.00359	0	0
$\overline{s}$	.00388	.0461	0	0

Table 5.1: Relative probabilities for the generation of different quark flavors for W^+ production. The rows label the quark type in the proton, and the columns in the anti-proton. We generate the event according to these probabilities to make the generation efficient, but subsequent weighting will alter the actual contributions to the final event. The numbers are normalized so that they sum to 1. MRS-R2 distribution functions were used for the calculation.

After choosing a flavor type, we divide the event weight by the probability of choosing that type. The weighted distribution of quark types will then be uniform. We generate W^+ events according to the probabilities in Table 5.1, and a similar procedure is followed for W^- and Z production.

5.3 Boson Decay

5.3.1 Angular Distribution

In the lab frame, the 4-momentum of the boson is

$$(\sqrt{Q_T^2 + Q^2}\cosh y_W, Q_T \cos\phi, Q_T \sin\phi, \sqrt{Q_T^2 + Q^2}\sinh y_W)$$

where ϕ is chosen randomly and the generation of Q_T, $y_W = \Delta y + y_0$, and Q^2 is described above. The first component is the energy, and the last three are the $x-$, $y-$, and $z-$components of the 3-momentum. This 4-vector defines a Lorentz transformation which we use to boost into the rest frame.

We consider the two-body decay $W \rightarrow e\nu$ in the boson rest frame. The electron and neutrino are back to back, and the energy of each is half the generated W mass. The electron angular distribution is $(1 - \lambda \cos\theta)^2$, where $\lambda = \pm 1$ and is determined from the charge of the W and which of the two quarks involved in the hard scatter comes from the proton. If the quark that comes from the proton is a quark, as opposed to an anti-quark, then λ is equal to the W charge, and otherwise it is the opposite of the W charge.

The polar angle θ is defined with respect to the "Collins-Soper" z-axis. This axis is given by [32]

$$\hat{z} \propto \hat{P}_+ - \hat{P}_- \tag{5.17}$$

where $\hat{z}$ is normalized to be a unit vector, and $\hat{P}_+$ and $\hat{P}_-$ are unit vectors pointing along the proton and anti-proton directions, respectively, in the boson rest frame. A schematic drawing of the definition of this axis is shown in Figure 5.2. In the case that the W has no transverse momentum, this z-axis will coincide with the proton

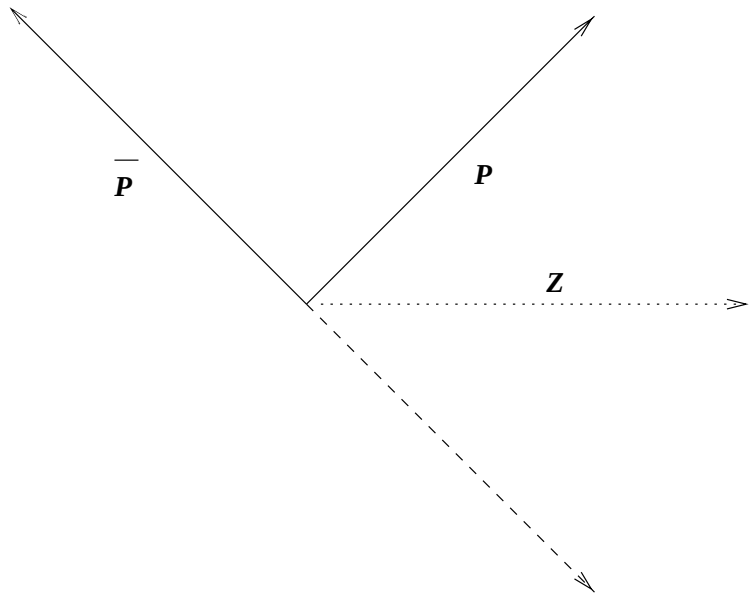

Figure 5.2: Schematic of Collins-Soper axis. The W rest frame is shown. The directions of proton and anti-proton are labelled p and $\bar{p}$ respectively. The dashed line is the negative of the anti-proton direction. The Collins-Soper z-axis is the dotted line labelled z, and it bisects the proton direction and the negative of the anti-proton direction.

direction. To calculate $\hat{z}$, we boost the proton and anti-proton from the lab frame into the W rest frame. In the lab frame, their 4-momenta are $\sqrt{s}/2(1,0,0,\pm 1)$.

To generate the $(1-\lambda\cos\theta)^2$ distribution, we produce the electron isotropically. We then calculate $\cos\theta$ as the dot product of $\hat{z}$ and the unit vector parallel to the electron, and the event weight is then scaled by $(1-\lambda\cos\theta)^2$.

The electron and neutrino are then boosted into the lab frame.

The top plots of Figure 5.3 show the generated P_T distributions for the W boson and the decay leptons in simulated $W \to e\nu$ events. The bottom left plot show the generated rapidity distribution of the W boson. The bottom right plots shows the pseudorapidity distribution of the decay leptons after all the cuts have been applied. All the plots are for the generated quantities before any cuts, except for the bottom right plot, which has all the cuts applied. The electron P_T distribution is softer

than the neutrino as a result of internal bremsstrahlung. Internal bremsstrahlung is discussed in the next section. The effect of the fiducial cuts can be seen in the bottom right plot. Electrons with pseudorapidity of ~ 1.2 can still land in the CEM if $|Z_{vertex}|$ is large enough. Z_{vertex} is generated according to a Gaussian distribution of width 30 cm. The fiducial cuts deplete the region around zero rapidity because they remove events that point at the 90° crack.

5.3.2 Radiative Decay

We allow the electron to produce up to two "internal" photons, using the PHOTOS generator. For Z decays both electrons are allowed to radiate. We only produce photons above 0.1% of the electron energy. We refer to these photons as "internal" photons. "External" photons are those which are produced by bremsstrahlung emission in the material of the detector. The internal photons are significant since they are often produced at wide enough angles to the electrons that they are not clustered with the electron. Failure to simulate any internal photons at all would shift the measured boson masses by $\approx$ 150 MeV. We have checked that the PHOTOS generator and the 1985 single photon calculation by Berends and Kleiss give the same result for the energy which is not clustered with the electron, and also the same result for the mean of E/p.

The top plot of Figure 5.4 shows the angular difference between the electron and the vector sum of all generated photons. The difference in azimuth ($\Delta\phi$), as well as the difference in pseudorapidity ($\Delta\eta$) are shown. The bottom plot shows the fraction of the electron energy taken up by the internal photons. This plot shows the quantity $y \equiv \frac{E_\gamma}{E_\gamma + E_e}$ where E_γ is the sum of the energies of all the internal photons, and E_e is the generated electron energy, after the internal photons are produced. The bottom

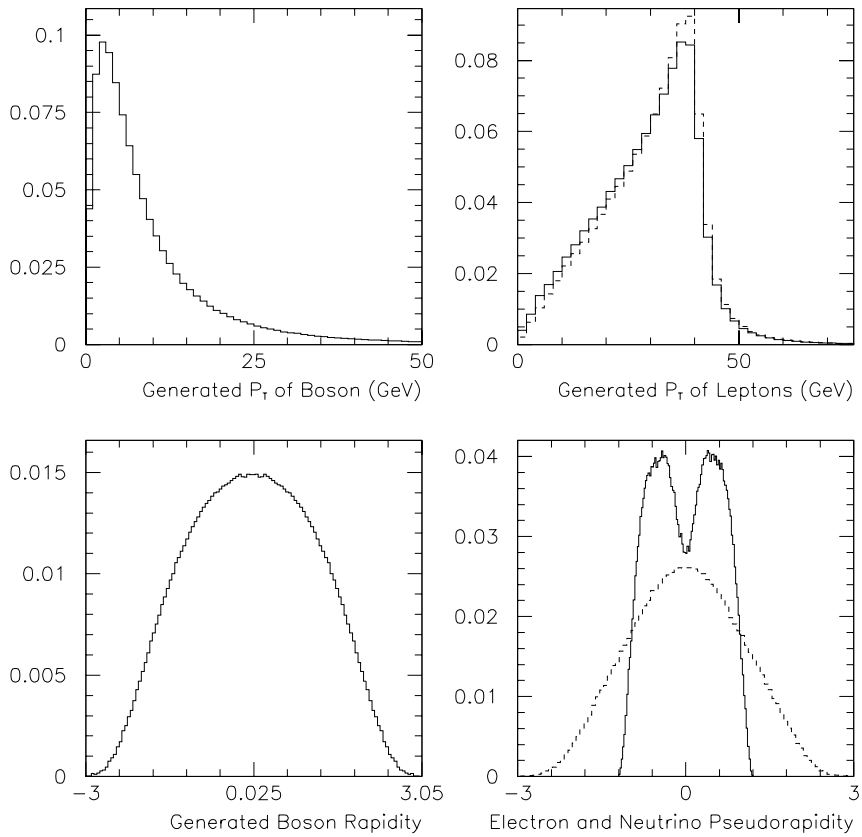

Figure 5.3: Generated quantities for Monte Carlo $W \rightarrow e\nu$ events. Top left: Boson P_T. Top right: Electron P_T (solid) and neutrino P_T (dashed). Bottom left: Boson rapidity. Bottom right: Electron (solid) and neutrino (dashed) pseudorapidities after all cuts. All the plots are generated quantities with no cuts applied, except for the bottom right dashed plot which has all cuts applied. All the plots are normalized to unit area.

plot also shows the distribution of y for events with $\Delta\phi > 15°$ or $\Delta\eta > 0.2$. The internal photons for these events are less likely to be clustered with the electron. 19% of events with internal photons have $\Delta\phi > 15°$ or $\Delta\eta > 0.2$, but these events have a harder y distribution. Internal photons are generated for 26% of the events.

5.4 Differences Between Production of W and Z Events

One significant difference between W and Z events is that different quark types are involved in Z decays. To choose the quark types for Z events, we follow a procedure analogous to one presented in Section 5.2.4. The difference in cross section is discussed in Sections 5.4.1 below, and the boson P_T distributions in Section 5.4.2 below.

5.4.1 Difference In Cross Sections

The Z boson has both axial and vector couplings, and so the angular distribution of electrons from Z decays is different than in W decays. Moreover, we must consider the contribution and interference from diagrams where the Z propagator is replaced by a photon propagator. The zeroth order cross section for $q\bar{q} \to e^+e^-$, up to overall constants, is

$$\begin{aligned}\sigma(q\bar{q} \to e^+e^-) = \; & \frac{e_q^2}{Q^2}(1+\cos^2\theta) + \sigma_0(Q^2) \times \\ & \Big[(g_V^{e\,2} + g_A^{e\,2})(g_V^{q\,2} + g_A^{q\,2})(1+\cos^2\theta) + 8 g_V^e g_A^e g_V^q g_A^q \cos\theta \\ & -2e_q(1 - M_Z^2/Q^2)(g_V^e g_V^q(1+\cos^2\theta) + 2 g_A^e g_A^q \cos\theta)\Big]\end{aligned} \tag{5.18}$$

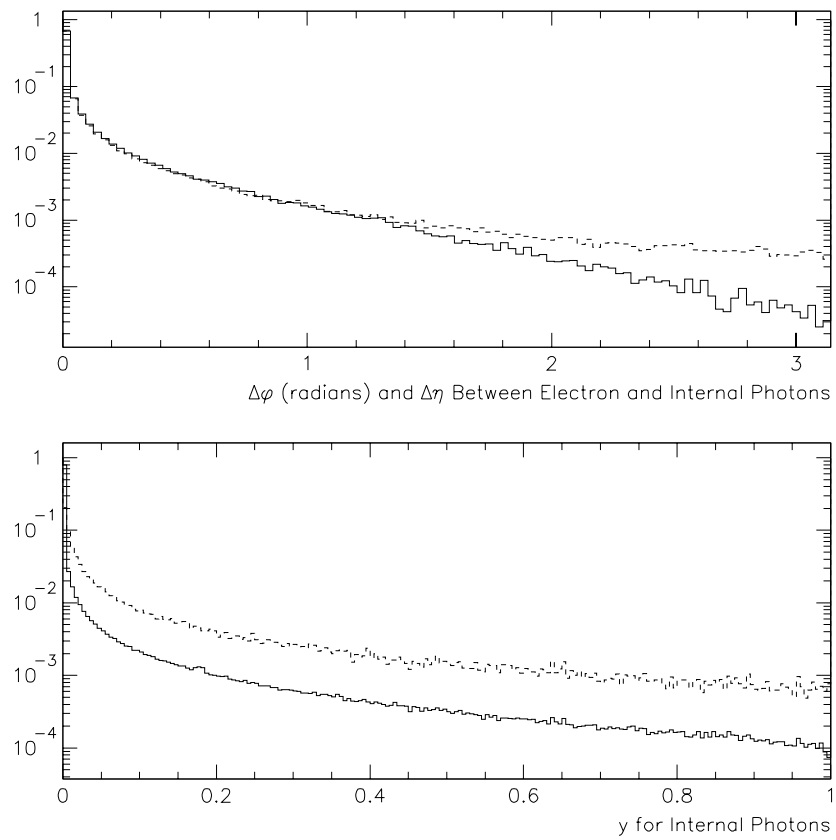

Figure 5.4: Generated quantities for internal bremsstrahlung in Monte Carlo $W \rightarrow e\nu$ events, before all cuts. Top: Difference in azimuth ($\Delta\phi$) (solid) and difference in pseudorapidity ($\Delta\eta$) (dashed) between the electron and the vector sum of all generated internal photons. Bottom: y for all internal photons (solid) and for events with $\Delta\phi > 15°$ or $\Delta\eta > 0.2$ (dashed); where y is the fraction of the electron energy in the photons. For this plot y is defined as the internal photon energy divided by the sum of the electron energy and the internal photon energy. For the dashed curve, the internal photons are less likely to be clustered with the electron. 19% of the events with internal photons fall in the dashed curve of the bottom plot. All plots are normalized to unit area.

where g_V and g_A are the vector and axial couplings of the fermion-Z vertex, $\cos\theta$ is the polar angle of the electron in the boson rest frame as defined in Section 5.3.1, and e_q is the charge of the quark. Here we have written Q^2 for the 4-momentum squared of the propagator, and σ_0 is defined above in Equation 5.6. The first term represents the contribution from the photon propagator, while the first term in the square brackets is the contribution from the Z propagator. The second term in the square brackets is the photon-Z interference term.

For Z decays we use this equation in place of σ_0 in Equation 5.15. To generate the angular distribution of the decay electrons, we simply generate a flat distribution in $\cos\theta$, and the weighted distribution will be correct since we are now including the $\cos\theta$ term in the cross section.

5.4.2 Difference In Boson P_T Distributions

The function $\bar{R}(Q_T)$ describes the boson P_T distribution, as discussed in Section 5.1.3. In that section, we argued that a dimensionless function can only depend on dimensionless arguments. We divided Q_T by $\sqrt{\hat{s}}$, and we defined the function $\Psi(Q_T/\sqrt{\hat{s}})$ in Equation 5.12. There are only two kinematic variables with units of energy other than Q_T: $\sqrt{Q^2}$ and $\sqrt{\hat{s}}$. Q^2 and $\hat{s}$ are related through Equation 5.10, and it does not matter which we choose to divide Q_T by in the argument.

In the Q_T region where the calculation of Section 5.1.2 is valid, we expect the boson P_T distribution to depend only on the ratio $Q_T/\sqrt{\hat{s}}$ [33, 34]. The Z P_T distribution will be higher than the W P_T distribution, and the average is higher by $\sim M_Z/M_W$. This difference is included in the Monte Carlo because we generate the events according to the function $\Psi(Q_T/\sqrt{\hat{s}})$, which only depends on the ratio. By fitting to the Z P_T distribution of the data, we should be able to determine a functional form for

$\Psi(Q_T/\sqrt{\hat{s}})$ which also describes the W data. The top plot of Figure 5.5 shows the generated W and Z P_T distributions. The average of the Z distribution is higher by $\sim 10\%$, as expected from the ratio of the boson masses.

The low Q_T region corresponds to the "non-perturbative" region where we cannot do an expansion in α_s. For the Monte Carlo Z events, since we fit $\Psi(Q_T/\sqrt{\hat{s}})$ with Z data and do not rely on a perturbative calculation, we are generating events in the non-perturbative region correctly.

However, above we stated that $\sqrt{\hat{s}}$ and $\sqrt{Q^2}$ are the only available quantities to divide Q_T by in the argument of $\Psi(Q_T/\sqrt{\hat{s}})$. This is not correct in the low Q_T region since there is another energy scale: the "QCD confinement" scale. For low Q_T, the function Ψ may depend on Q_T only, as opposed to the ratio $Q_T/\sqrt{\hat{s}}$. Therefore, we do not necessarily expect the boson P_T distribution for the low Q_T events to scale with the boson masses. By fitting $\Psi(Q_T/\sqrt{\hat{s}})$ with Z data, we get the correct distribution for Z events; but since we assume that Ψ only depends on the ratio $Q_T/\sqrt{\hat{s}}$, the distribution for low Q_T W events may be generated incorrectly.

To correct the W P_T distribution, we use a calculation by Ladinsky and Yuan [35]. The Ladinsky and Yuan calculation includes a rough cut-off energy in the region of $Q_T \sim 2.0$ GeV, below which non-perturbative effects become significant. The cut-off energy thus defines a rough threshold region, above which we expect the W and Z P_T distributions to scale with the boson mass, and below which we expect them to have roughly the same P_T distribution. We use the ratio of W to Z P_T distributions from the Ladinsky and Yuan calculation to correct our generated W P_T shape. Without this correction, the E_T shape of the $W \rightarrow e\nu$ data does not agree well with the Monte Carlo. The E_T shape of the data and Monte Carlo are shown in Chapter 9.

For the non-perturbative region, Ladinsky and Yuan use a parameterization which

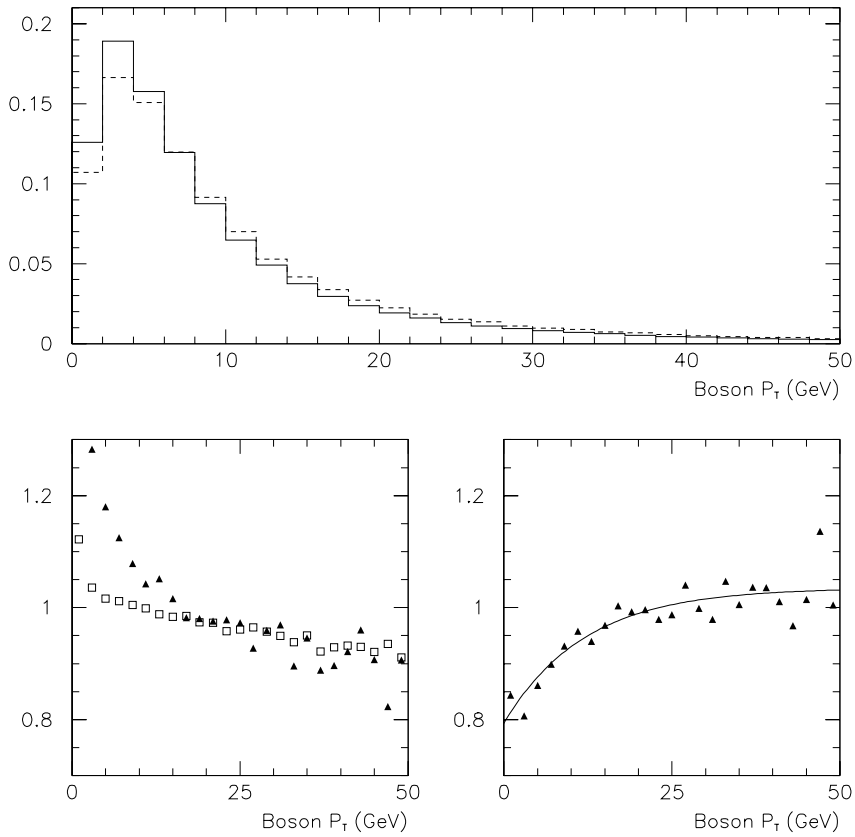

Figure 5.5: Top: Generated boson P_T distributions for W events (solid) and Z events (dashed). For the W distribution, the mean and rms are 9.42 and 9.03 GeV respectively. For the Z events, they are 10.36 and 9.56 GeV respectively. Bottom plots: Left plot is the ratio of the W P_T distribution to the Z P_T distribution. The triangles are for our Monte Carlo, and the squares are the Ladinsky-Yuan calculation. The normalization is arbitrary. The right plot is the ratio of points in the left plot: the squares of the left plot divided by the triangles of the left plot. The fit curve is $1.0 - 0.233\exp(-x/12.0)$ where x is the boson P_T in GeV.

they fit to different data sets. We expect that uncertainties in the W and Z P_T distributions will largely cancel in the ratio of the two distributions [36].

We generate W and Z events using the Ladinsky and Yuan calculation, and we also generate W and Z events with our Monte Carlo, where we use a Z P_T distribution which is close to the fitted function of Chapter 7. For the Ladinsky and Yuan calculation we use the MRS-R2 parton distribution functions. The bottom left plot of Figure 5.5 shows the ratio of the generated W and Z P_T distributions for our Monte Carlo and for the Ladinsky-Yuan calculation. The Ladinsky-Yuan calculation is significantly flatter in the low P_T region, where the above scaling arguments may fail. The two curves are significantly different for P_T below $\sim$ 15 GeV. The bottom right plots shows the ratio of the ratios. The points are the Ladinsky-Yuan calculation of the W and Z P_T ratio, divided by our calculation. We correct the Monte Carlo according to this plot. A fit curve is shown on the bottom right plot, and we adjust the event weight by this function.

5.5 Summary

We have discussed the generation of the variables which determine W and Z production. The events are weighted in such a way that the weighted distribution of the variables is uniform. The 4-vectors of the decay products and associated weight and other information are then written out to disk. A detector simulation will later be applied to the quantities written out to disk. We will multiply the event weight by the value of the integrand of Equation 5.15, and in this way each event will be weighted according to its contribution to the total cross section. When we weight by the integrand, we do not include the contribution from Υ since that function was

accounted for in the generation of the Δy.

We evaluate the distribution functions before we write out the event, but for the W simulation, we do not evaluate either the zeroth order cross section, σ_0, or the boson P_T function, Ψ, until after the detector simulation. We do this so that we can vary the parameters of those functions while fitting the output of the Monte Carlo to the data. For the Z events, Ψ is the only part of the integrand that we leave unevaluated until after the detector simulation.

Chapter 6

Electron Simulation

We have two independent measurements of the electron energy: the CTC measurement of p and the calorimeter measurement of E. The CTC simulation is presented in Section 6.1, and the calorimeter simulation in Section 6.2. In Sections 6.3 and 6.4, we describe a method for simulating the removal of the electron towers for the calculation of $\vec{U}$, and for the simulation of the extra energy included in the electron cluster. In Section 6.5, we discuss how the N_{tracks} cut is simulated.

6.1 CTC Simulation

It is necessary to simulate the CTC measurement of the electron track, $\vec{P}$, for several reasons. We cut on P_T, requiring $P_T > 15$ GeV. Moreover, we use the simulation in Chapter 11, where we attempt to tie the calorimeter scale to the CTC scale by using the E/p distribution. Finally, the track parameter $\cot\theta$ is used in the data to define E_T since we use $E_T \equiv E \times \sin\theta$, and so it is desirable to have a simulation of the $\cot\theta$ measurement.

In Section 6.1.1, we discuss the material before and in the CTC; and in Sec-

tion 6.1.2, we discuss photon bremsstrahlung before and in the CTC. Section 6.1.3 discusses the simulation of the CTC measurement, and in Section 6.1.4 we discuss the altering of the track parameters through the beam constraint.

6.1.1 Material Distribution

For the simulation of bremsstrahlung, discussed below, we need to know the location and quantity of the material in the detector, in radiation lengths. We use a sample of photon conversion events $\gamma \rightarrow ee$ [37] to determine these quantities. The photon conversion sample is defined in [37], and the results of this section are derived from the results and methods of [37].

The conversion events are selected from a sample of low E_T inclusive electrons. The conversions are identified by searching for two oppositely signed electron tracks whose helices pass near each other and which are roughly parallel at their point of closest approach. The requirements on the helices are

$$\begin{aligned} |Sep| &< 0.3\ cm \\ \Delta \cot\theta &< 0.03 \end{aligned} \tag{6.1}$$

where Sep is the separation of the two helices in the xy-plane, and $\Delta \cot\theta$ is the difference between the $\cot\theta$ parameters of the two tracks. In the xy-plane the tracks trace out arcs of circles, and Sep is the distance between the two circles along a line connecting the centers of the circles.

The position at which the tracks overlap marks the location of the photon conversion. The resolution of the radial position of the conversion is improved by adjusting the helix parameters so that Sep is forced to be zero, and so that the photon momen-

tum vector is forced to point back to the beam spot. The momentum of the photon is reconstructed from the two decay electron tracks. After this improvement, the radial position of the conversions is determined with a resolution of 4.14 mm.

More than 200,000 photon conversion events are identified [37]. The conversion events are from Run 1A data. The only differences between the 1A and 1B detectors are changes in the SVX. The 1B SVX has slightly more material than the 1A, but the difference is small. To account for this difference, the total number of observed conversions should be increased by $\approx 0.5\%$.

We partition the detector into volumes which correspond to the different components of the detector, and we determine how many conversions, N, are found in each volume. For a photon passing through a given volume, the probability of conversion is

$$\frac{7}{9}\Delta x \cdot \rho / x_0 \tag{6.2}$$

where Δx is the distance travelled by the photon in the volume, ρ is the mass density of the material, and x_0 is the radiation length of the material in units of mass per area. The total number of conversions in a given volume is then

$$N = \frac{7}{9}\frac{\rho}{x_0}\sum_{photons}\Delta x_i \tag{6.3}$$

where the sum is over all incident photons. To calculate the sum, we use the conversions which occur in the inner wall of the CTC. For each of these conversions, we form a line from the event vertex to the conversion point. For every volume that the line passes through, we calculate the length of the line segment that occurs in that volume. We weight each line segment by $\sin\theta$, where θ is the polar angle of the photon. This weight corrects for the bias in the CTC inner wall $sin\theta$ distribution

which occurs because particles incident at smaller angles pass through more material.

We repeat this calculation for all the conversions found in the CTC inner wall. For each volume, we sum the length of all the line segments in that volume. We write the sum of the segments as $\mathcal{L}$. For each volume, $\mathcal{L}$ is proportional to the sum in Equation 6.3. Equation 6.3 then gives

$$\frac{\rho}{x_0} \propto N/\mathcal{L} \tag{6.4}$$

The variable $\mathcal{L}$ allows us to correct the conversion data for the uneven flux of initial photons through the different volumes. The uneven flux results from the event vertex distribution, as well as the angular distribution of the photons.

The quantity ρ/x_0 is the number of radiation lengths per distance of material. If a particle makes a step ΔX through material with a given value for ρ/x_0, it will pass through $(\Delta X) \times (\rho/x_0)$ radiation lengths.

We make a correction for a selection bias in the conversion pairs. The selection bias occurs because the initial conversion sample has a minimum CEM E_T cut, and this cut is more likely to be passed if both tracks land in the same tower. For conversions at high radius, the resulting tracks will have separated less when they reach the CEM than conversions at lower radius. The efficiency to find conversion pairs is found to increase with radius at a rate of 0.0077 per cm in radius. We correct for this efficiency by decreasing the value for ρ/x_0 for each volume, depending on the radial position of the volume.

We also make a small correction for the attenuation of the initial photon flux as the photons pass through the material.

Equation 6.4 only determines the distribution of ρ/x_0 to an overall constant of

proportionality. The material of the inner wall of the CTC is used for the normalization. This material has been determined to present $(1.26 \pm 0.06)\%$ of a radiation length to particles traveling at $\theta = 90°$ [38]. To determine a constant of proportionality in Equation 6.4, we first calculate the number of conversion events that occur in the CTC inner wall and also the number of conversion events before the CTC. Each event is weighted by the efficiency correction and a photon attenuation correction.

We write the weighted number of events in the CTC inner wall as N_{INNER}, and the number before the inner wall as N_{BEFORE}. On average the photons pass through

$$\frac{N_{INNER} + N_{BEFORE}}{N_{INNER}} \times < 1/\sin\theta > \times 1.26 = 7.34 \pm 0.05(stat) \pm 0.39(sys) \quad (6.5)$$

percent of a radiation length before the CTC active volume. The quantity $< 1/\sin\theta >$ is the average value of $\sin\theta$ for events in the CTC inner wall. This number is necessary since 0.0126 is the number of radiation lengths in the CTC inner wall for particles incident at 90°. Away from 90°, the particles pass through $1/\sin\theta \times 0.0126$ radiation lengths. The statistical uncertainty on Equation 6.5 is negligible compared to the calibration uncertainty. The calibration uncertainty is dominated by the uncertainty on the material of the CTC inner wall.

To determine the constant of proportionality of Equation 6.4, we use all the conversion photons found in the CTC. We step the photons through our simulation, counting the total number of radiation lengths they pass through. As in the calculation of $\mathcal{L}$, we include a weight factor of $1/\sin\theta$ to account for the biased θ distribution of the CTC inner wall. We adjust our constant of proportionality so that the average number of radiation lengths that the photons pass through in our simulation is the same as Equation 6.5.

When we step simulated $W \rightarrow e\nu$ electrons through the simulation, after all the $W \rightarrow e\nu$ cuts are applied, we calculate the electrons pass through 7.20% of a radiation length on average. The similarity between this number and Equation 6.5 indicates that the W decay electrons have a similar angular distribution to the photons of the $\gamma \rightarrow ee$ sample.

The photon conversions only determine the amount of material before the CTC active volume. For the material inside the CTC active volume, the simulation averages the CTC gas and wires to form a homogeneous substance with $\rho/x_0 = 0.0001865/\text{cm}$. Averaging the gas and wires together to form a homogenous material in the Monte Carlo does not effect the total rate of bremsstrahlung. Also, it will not significantly alter the radial distribution of bremsstrahlung because the wire planes in the CTC are relatively close together, with a radial separation ~ 1 cm.

Figure 6.1 shows the radial position of bremsstrahlung events in simulated $W \rightarrow e\nu$ events. The bremsstrahlung simulation is discussed in the next section. The events below ~ 14 cm correspond to the SVX material, and the peak at ~ 27 cm is the CTC inner wall. The material of the VTX is also visible between the CTC inner wall and the SVX. The flat region above the CTC inner wall corresponds to the material of the active volume of the CTC.

The bottom plots of Figure 6.2 show the amount of material used in the simulation. The plots show the distribution of the number of radiation lengths traversed by the primary electrons in Monte Carlo $W \rightarrow e\nu$ events. The left plot only includes the material before the CTC active volume, and the right plot only includes the CTC active volume. The average amount of material traversed by the electrons before the CTC active volume for these plots is 7.2% of a radiation length.

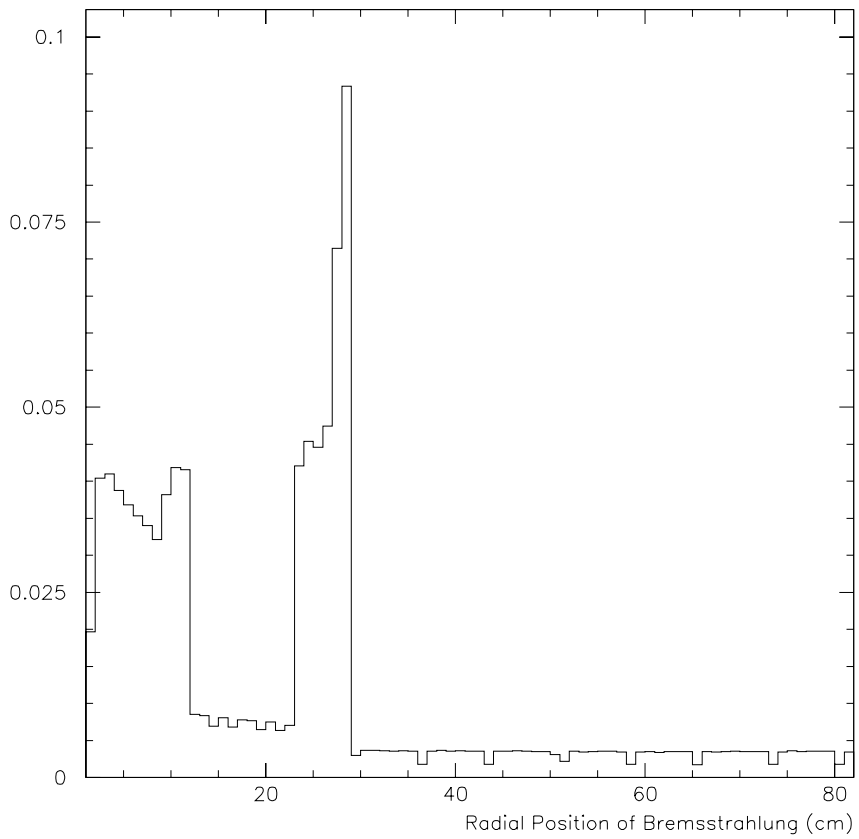

Figure 6.1: The radial distribution of bremsstrahlung in Monte Carlo $W \rightarrow e\nu$ events. The distribution is only shown to the middle of the CTC, but bremsstrahlung is allowed to occur in the Monte Carlo in the entire CTC. The average radius of bremsstrahlung for the Monte Carlo is 22.9 cm, where only the inner half of the CTC is included in the average. The normalization of the plot is arbitrary.

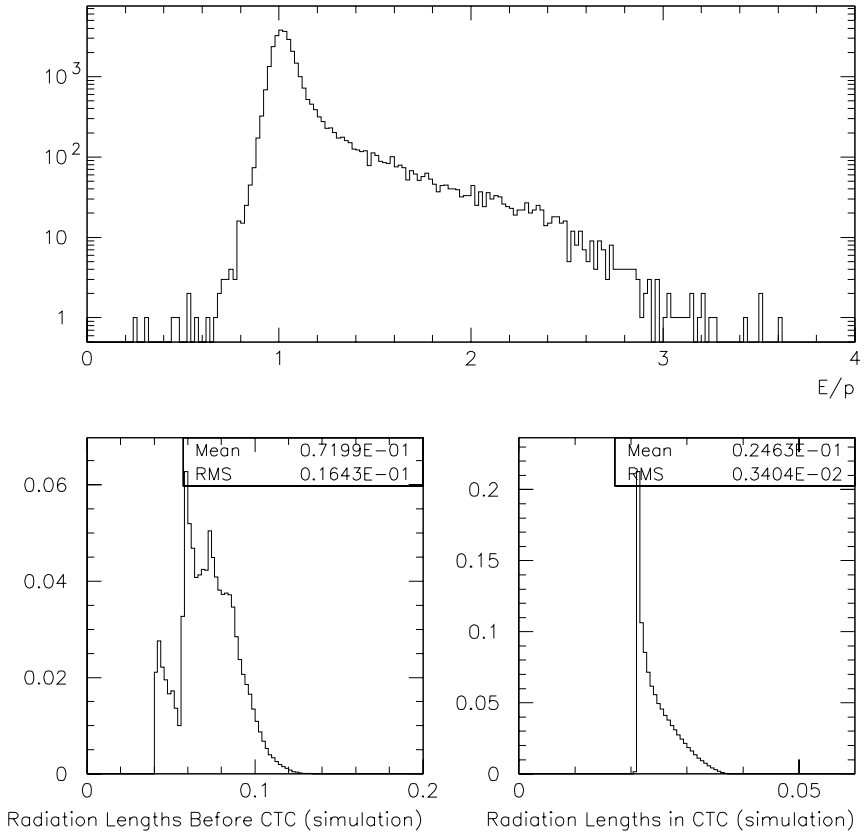

Figure 6.2: Top: E/p distribution of data for events in the M_T fitting region. Bottom: Number of radiation lengths traversed by primary electrons in simulated $W \rightarrow e\nu$ events, before the CTC active volume (left), and in the CTC active volume (right). The bottom distributions are normalized to unit area.

6.1.2 Bremsstrahlung Simulation

We start the simulation of the CTC measurement with the generated electron 4-vector, which was written out to disk, and we convert the 4-vector to track parameters $\vec{\alpha}$, which have no measurement error. The electron undergoes photon bremsstrahlung in the material before the CTC and also inside the CTC. These photons will be included in the calorimeter measurement but never in the CTC measurement. This is a significant bias in the CTC track measurement which we simulate. The top plot of Figure 6.2 shows the E/p distribution for the data. The high-end tail is a result of hard bremsstrahlung events where the photon is included in the E_T measurement, but not the P_T measurement.

We step the simulated track through the material and decide at each step whether a brem occurred or not. The distribution of material is described in the previous section. If we step through dt radiation lengths, then the probability of creating a bremsstrahlung photon is [39]

$$dt \times \int_{y_{min}=.001}^{1} p(y)dy \tag{6.6}$$

where y is the fraction of the electron energy given up to the photon, and y_{min} is the minimum value of y we choose to simulate. $p(y)$ is the distribution of y and is given by [39]

$$p(y) = \frac{1}{y}[(1-y)(\frac{4}{3}+k)+y^2] \tag{6.7}$$

The constant k is a small correction, on the order of 3%, which depends on the assumed material type in the detector. If we decide that a photon brem occurred, then we generate a photon which takes away a fraction of the electron energy given by y, where y is generated according to Equation 6.7. We then adjust the electron

track parameters and continue stepping through the material.

At every step, we allow any photon which has been generated to convert to e^+e^- pairs, and conversion occurs with a probability given by $\frac{7}{9}dt$. This includes the internal photons produced at the initial generation. These pairs are used to check if the event fails the $N_{tracks} = 1$ cut.

6.1.3 CTC Measurement

If there are no bremsstrahlung photons created in the CTC, then we assume that the final track parameters describe the track which enters the CTC. We calculate a covariance matrix $\tilde{C}$ for the 5 track parameters. The calculated covariance matrix depends on which CTC layers are used in the track reconstruction, and we randomly choose a layer pattern from real electrons in $W \rightarrow e\nu$ events.

It is a well known problem at CDF that the calculated covariance matrix needs to be scaled by a factor ~ 2 to correctly describe the data. The need for this scale factor is not well understood. We use the E/p distribution to calculate a covariance scale factor, and this is one of the subjects of Chapter 11. We vary the scale factor until the E/p distribution of data and Monte Carlo agree.

The E/p distribution is useful for determining the P_T resolution since the E/p width is dominated by the P_T resolution. The fractional E resolution for W decay electrons is $\approx 2.7\%$, while the fractional P_T resolution is $\approx 4\%$. Since $E_T = E \sin\theta$ and E/p=E_T/P_T, it is possible that the $\sin\theta$ resolution also contributes significantly. We calculate the $\sin\theta$ resolution by varying $\cot\theta$ according to the $\sigma^2_{\cot\theta}$ term of the scaled covariance matrix. We find the resolution varies from $\sigma(\sin\theta) = 0.001$ for $\theta \sim 80°$ to $\sigma(\sin\theta) = 0.002$ for $\theta \sim 30°$. These values are negligible compared to the E and P_T resolutions.

After we scale the covariance matrix, we "smear" the track parameters according to

$$\vec{\alpha} \rightarrow \vec{\alpha} + \delta(\vec{\alpha}) \tag{6.8}$$

where $\delta(\vec{\alpha})$ is a random variable drawn according to $\tilde{C}$.

If there are brems in the CTC, then we have several different track segments which connect inside the CTC, but which have different track parameters. We assume that the CTC measurement produces a linear combination of the different track segments. For example, if there is exactly one brem in the CTC, then we have a track segment before the brem described by the track parameters $\vec{\alpha}_{before}$, and we also have a track segment after the brem described by $\vec{\alpha}_{after}$. To combine these two segments, we calculate two covariance matrices, $\tilde{C}_{before}$ which only uses CTC layers before the brem, and $\tilde{C}_{after}$ which only uses layers located after the brem. We take the combined track to be

$$\vec{\alpha} = \tilde{C}(\tilde{C}^{-1}_{before}\vec{\alpha}_{before} + \tilde{C}^{-1}_{after}\vec{\alpha}_{after}) \tag{6.9}$$

where $\tilde{C} = (\tilde{C}^{-1}_{before} + \tilde{C}^{-1}_{after})^{-1}$ is the assumed covariance matrix for the measured track. An analogous procedure is performed for the case of more than one brem inside the CTC. As above, we scale $\tilde{C}$ and smear the track parameters.

This procedure of combining the different track segments to form $\vec{\alpha}$ gives shorter segments a smaller weight than longer segments. The shorter segments go through fewer CTC layers and have a worse resolution, and this is reflected in their covariance matrix. They then contribute to Equation 6.9 with a smaller weight.

Track segments which begin near the outer radius of the CTC will be shorter on average than segments which begin near the inner radius; and for this reason, brems which occur near the outer radius have a smaller effect on $\vec{\alpha}$ than brems which occur

near the inner radius. As a rule of thumb, one can consider that the CTC presents an effective number of radiation lengths to electrons that is $\sim \frac{1}{2}$ of what is shown in Figure 6.2.

6.1.4 Beam Constraint

In Chapter 3 in Section 3.1.2 we discussed the beam constraint and the bias introduced by beam constraining tracks which have undergone significant bremsstrahlung.

To account for this bias, we apply the beam constraint to the Monte Carlo as well as to the data. Any bias introduced by the beam constraint in the data should be reproduced in the simulation. The simulated beam spot is distributed in the xy-plane around the origin according to a Gaussian distribution of width 60μ in each direction. This number is the assumed resolution for the beam spot in the data. By beam constraining to the origin, we are placing the Monte Carlo beam spot at the origin. This is in contrast to the data where the beam spots are offset from the origin by several millimeters. For the beam constraint calculation, we use the covariance matrices calculated above, and we use the same beam constraint code as is used for the data.

In Chapter 3 we plot qD_0 for the data and the Monte Carlo, in Figure 3.1. The peak position of the Monte Carlo in this plot agrees well with the data, which indicates that we are correctly simulating the bias in qD_0 from bremsstrahlung. The bias on qD_0 will result in a bias on the beam constrained P_T. We can use the average of the peak of qD_0 and Equation 3.2 to calculate the average bias from the beam constraint. The average fractional change in P_T is $\sim 0.55\%$ for a 40 GeV track. This is not a negligible shift; but the average offset for qD_0 in the data agrees with the Monte Carlo, and since we calculate the track covariance matrices in the Monte Carlo using

$W \rightarrow e\nu$ data, the bias will be the same for the data and Monte Carlo.

6.2 Calorimeter Simulation

The calorimeter simulation begins with the electron after it has undergone the photon bremsstrahlung of Section 6.1.2. We extrapolate this track to the position of the calorimeter, and we apply the same fiducial cuts as we applied to the data.

We determine which calorimeter tower the electron extrapolates to, and we define a cluster region around this tower. As in the data, this region is defined as ± 1 towers in the z direction except that we do not allow clusters to extend across the $90°$ crack. We examine all electrons and photons which have been produced by the simulation, and we sum the energies of all those which extrapolate to the cluster towers. The particles we examine include the primary electron, as well as internal and external bremsstrahlung photons, and also electrons from photon conversions.

By adding the energies of all the electrons and photons which land in the cluster, we are assuming that the calorimeter response is linear over a wide range of energies, from $\sim$ 40MeV to $\sim$ 40 GeV. The lower number, $\sim$ 40 MeV, is determined from the minimum allowed photon bremsstrahlung, which is 0.1% of the electron energy. In Chapter 11, we will examine the extent to which this assumption effects the measured W mass.

When we determine which towers are part of the electron cluster, we also determine which towers are removed for the $\vec{U}$ calculation. The towers of the electron cluster are removed; and if $X_{strips} < -6$ cm, then the towers which border the cluster and are lower in azimuth are removed; and if $X_{strips} > 6$ cm, then the border towers which are higher in azimuth are removed. These are the same criteria that are applied to

the data in Section 3.1.3. Any simulated electrons or photons which do not land in the removed towers are added to $\vec{U}$.

We simulate the calorimeter resolution with a simple Gaussian smearing function. If the summed cluster energy is E, then we adjust the energy to its "measured" value as $E \rightarrow E + \delta_E$, where δ_E is a Gaussian distributed random variable with zero mean and width σ_E. The width σ_E is given by

$$\frac{\sigma_E}{E} = \sqrt{(13.5\%/\sqrt{E_T})^2 + \kappa^2} \tag{6.10}$$

The 13.5% stochastic term is determined from test beam data, and for that term E_T is assumed to be measured in GeV. The constant term κ is included to account for additional sources of resolution such as tower-to-tower variations and variations with time. We fit for κ with the Z data, and this is the subject of Chapter 10. The default value is $\kappa = 1.6\%$.

6.3 Tower Removal Simulation

When we calculate $\vec{U}$ in the data, we remove towers which are in the electron cluster or near it. The towers that make up the electron cluster are removed; if $X_{strips} < -6$ cm, then the towers which border the cluster and are lower in azimuth are removed; and if $X_{strips} > 6$ cm, then the border towers which are higher in azimuth are removed. Depending on the position of the electron, up to 6 towers may be removed. This procedure creates a hole in the calorimeter at the position of the primary electron. The hole biases $U_{||}$ since $U_{||}$ is $\vec{U}$ projected along the electron direction. A bias in $U_{||}$ can bias M_T, and it is important to simulate the removed energy.

To model the removed energy, we use real $W \rightarrow e\nu$ events and examine the

calorimeter in regions which are not near the primary electron. For each event in the $W \rightarrow e\nu$ sample, we make fake electron clusters whose seed towers have the same value for $\eta_{detector}$ as the primary electron. The fake clusters contain the same number of towers as the primary electron cluster (± 1 towers in the z direction except not crossing the 90° crack). For each tower in the cluster, we apply a 100 MeV energy threshold for the electromagnetic and hadronic energies separately, since this is what we do for the $\vec{U}$ calculation in the data; and for each cluster, both the electromagnetic and hadronic E_T are recorded.

For each fake cluster, we also record how many tracks extrapolate to the cluster, where only tracks which originate within ± 5 cm of the event vertex and which have $P_T > 1$ GeV are considered. We refer to the number of tracks as N_{other}. This variable is used to simulate the $N_{tracks} \equiv 1$ cut, which is applied to the data. The simulation of this cut is further discussed in Section 6.5. Only fake clusters with $N_{other} = 0$ are used to make corrections in the Monte Carlo.

We do not want the fake clusters to be contaminated with energy associated with the primary electron, and so we do not use the 3 fake clusters that are within ± 1 towers of the primary electron, in the azimuthal direction. The CEM is divided in azimuth into 24 wedges, and 3 of the wedges are not used. This leaves 21 fake clusters for each real $W \rightarrow e\nu$ event.

The E_T of the fake clusters is shown in Figure 6.3. Both electromagnetic E_T as well as the sum of electromagnetic and hadronic E_T are shown. Only fake clusters with $N_{other} = 0$ are included in the plots, and the plots otherwise include all 21 fake clusters for all real $W \rightarrow e\nu$ events. The average electromagnetic E_T of the fake clusters is 82 MeV, which is $\sim 0.2\%$ of the primary electron E_T. The average of the sum of the electromagnetic and hadronic E_T is 110 MeV. Since we sometimes remove

the neighboring clusters in the calculation of $\vec{U}$, removing 1.67 clusters on average, the average energy removed is predicted to be $\sim$ 180 MeV.

We expect the energy in the fake clusters to be correlated not only to $|\vec{U}|$ and $\sum E_T$, but also to the azimuthal position relative to the direction of $\vec{U}$. Figure 6.4 shows the average E_T of the fake clusters as a function of the three variables $\Delta\phi$, $|\vec{U}|$, and $\sum E_T$, where $\Delta\phi$ is the difference in azimuth between the fake cluster and the direction of $\vec{U}$. $\vec{U}$ is a measure of the jet energy that balances the W P_T, and a correlation is expected with $\Delta\phi$ since if $\vec{U}$ is directed at a given tower, that tower will have more energy; and if it is directed away from a tower, that tower will have less energy. Similarly, if $|\vec{U}|$ or $\sum E_T$ is higher, there will be more energy in the event, and we expect the average fake cluster energy to be higher. The plots show clear correlations with all three variables.

It is important to include these correlations in the simulation. For example, $\Delta\phi$ is directly correlated to the E_T of the primary electron. The boson P_T can add to or subtract from the E_T of the electron in the W rest frame. If it adds, the recoil energy will tend to be directed opposite the electron direction; and if it subtracts, the recoil energy will tend to be along the electron direction. Thus, larger E_T events will tend to have $\Delta\phi$ around 180°, and the towers associated with the electron will include less recoil energy.

The correlations with all three of the variables are included in the simulation by partitioning the list of fake clusters according to $\sum E_T$, $|\vec{U}|$, and the angle each cluster makes with respect to $\vec{U}$.

For a given Monte Carlo event, we decide how much energy to associate with the removed towers as follows. We divide up the W events according to $|\vec{U}|$ and $\sum E_T$. We then take our simulated values for $|\vec{U}|$ and $\sum E_T$ and choose a real event

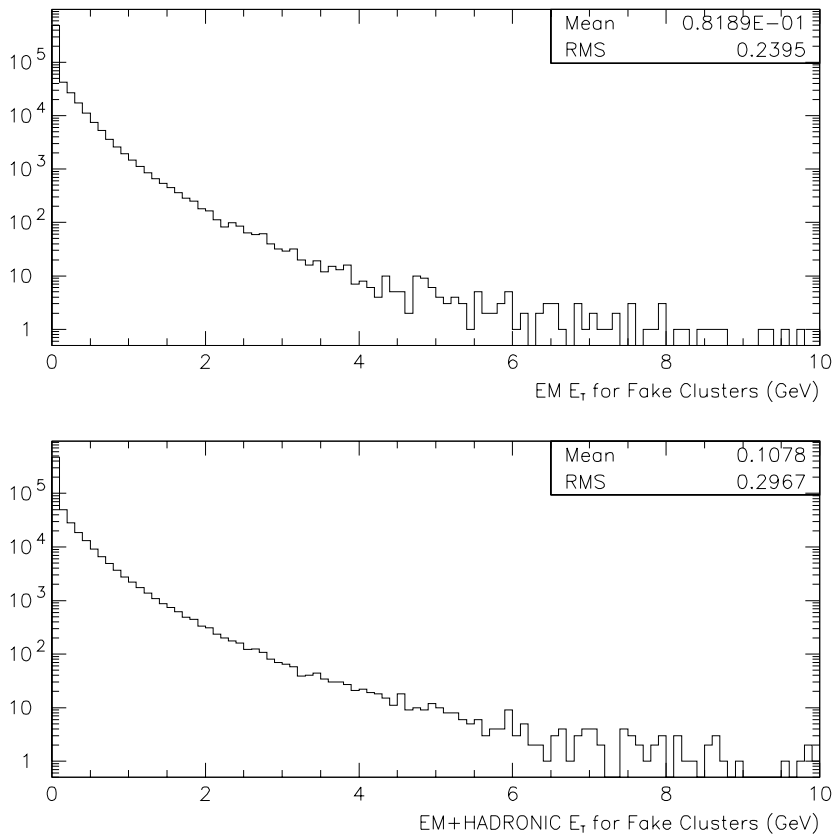

Figure 6.3: Average E_T of fake cluster for real $W \rightarrow e\nu$ events. The top plot is the electromagnetic E_T only, and the bottom plot is the electromagnetic plus hadronic E_T. The means and rms of the distributions are shown on the plot. 1.67 clusters are removed on average in the calculation of $\vec{U}$, and the bottom plot predicts that the average energy of these clusters should be $\sim 1.67 \times 110$ MeV $= 180$ MeV. All fake clusters which have $N_{other} = 0$ are included in the plots.

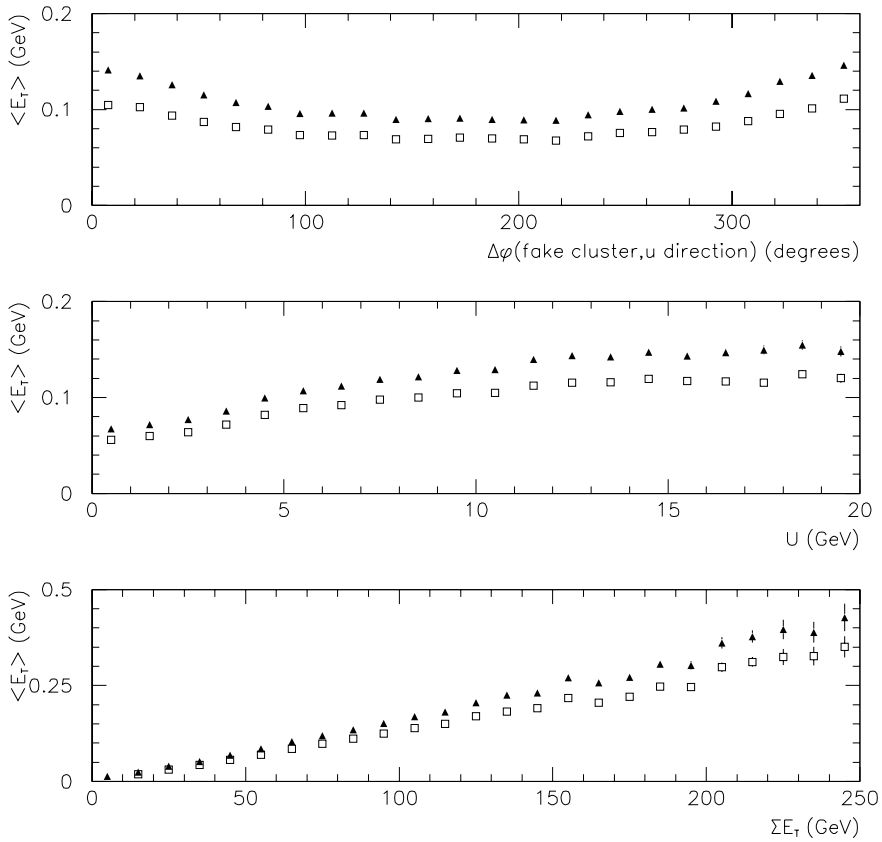

Figure 6.4: Average E_T of fake clusters as a function of event model variables, for real $W \rightarrow e\nu$ events. The triangles are electromagnetic plus hadronic E_T, and the squares are electromagnetic only. The top plot is the average vs $\Delta\phi$ between the fake cluster position and the direction of $\vec{U}$. The middle plot is vs $|\vec{U}|$, and the bottom plot is vs $\sum E_T$. Only fake clusters with $N_{other} = 0$ are used in the averages.

at random that has similar values. The simulation of $|\vec{U}|$ and $\sum E_T$ are the subjects of later chapters. We then calculate $\Delta\phi$, where $\Delta\phi$ is the azimuthal angle between the simulated electron position and the simulated value for $\vec{U}$. We choose the fake cluster which occurs at the same angle $\Delta\phi$, except that $\Delta\phi$ for the fake cluster is calculated relative to the real value of $\vec{U}$ in the real chosen W event. In this way, we include the dependencies on $\Delta\phi$, $|\vec{U}|$, and $\sum E_T$. If the fake cluster we want is unusable because it is too close to the real electron in the W event, then we choose another event.

For Monte Carlo events where the simulated X_{strips} position is outside of ± 6 cm, we also remove a cluster which neighbors the electron cluster. For these events, we repeat the above procedure, but with $\Delta\phi$ offset by one tower in azimuth. The same real W event that was used to choose the first fake cluster is used again if possible.

We correct $\vec{U}$ for the removal of the towers as

$$\vec{U} \rightarrow \vec{U} - \delta_U \hat{e} \tag{6.11}$$

where δ_U is the E_T of the fake clusters that we found, and $\hat{e}$ is the direction of the electron track in the xy-plane. The average for δ_U is 190 MeV. Thus, the Monte Carlo makes a 190 MeV correction on average to $U_{||}$ to simulate the bias that occurs from removing towers in the calculation of $\vec{U}$. This average is slightly different than the prediction from the bottom plot of Figure 6.3, which is discussed above. Figure 6.3 includes all clusters of every real W event, while the calculation of δ_U uses the W events and fake clusters based on the simulated values of $|\vec{U}|$, $\sum E_T$, and $\Delta\phi$.

6.4 Underlying Energy Simulation

As discussed in Section 3.4, energy unassociated with the W decay electron can sometimes fall on top of the CEM cluster. This is included in the simulation using the same method of Section 6.3. Up to two fake clusters were chosen in Section 6.3 to account for the energy removed in the calculation of $\vec{U}$: one which is associated with the simulated primary electron, and one which is associated with a neighboring cluster if $|X_{strips}| > 6$ cm. We use the same fake clusters, but only consider the cluster associated with the simulated primary electron.

The electromagnetic energy in this fake cluster is added to the electron E_T in the simulation. We make the correction

$$E_T \rightarrow E_T + \delta_E \tag{6.12}$$

where δ_E is the electromagnetic E_T of the chosen fake cluster. The average value for δ_E is 90 MeV. This is an average correction of $\approx 0.23\%$ on the electron E_T. This average correction is slightly different than the prediction from the top plot of Figure 6.3. Some difference is expected as mentioned at the end of the previous section.

In Section 6.3 we apply 100 MeV threshold for electromagnetic and hadronic energy in each tower. For the electromagnetic energy added to E_T, we do not apply any thresholds.

6.5 N_{tracks} Simulation

The data includes the cut that $N_{tracks} \equiv 1$. This cut produces a small bias on the $\sum E_T$ and $\vec{U}$ distributions, since it prefers events that have fewer unassociated tracks.

If we look at fake clusters without requiring that $N_{other} = 0$ we find that the average electromagnetic plus hadronic E_T per cluster is 130 MeV. The variable N_{other} is defined in the previous section, and it is the number of tracks that point at a cluster which have Z_0 within ± 5 cm of the event vertex and which have $P_T > 1$ GeV. 1.6% of the fake clusters have $N_{other} \geq 1$. If the primary electron had pointed at one of those clusters, the event would have failed the N_{tracks} cut. This small subset of the fake clusters, however, has an average E_T of 1360 MeV, which is significantly higher than the clusters without the tracks. Because of the N_{tracks} cut, the data does not include a contribution from this subset, and removing these towers reduces the overall average from 130 to 110 MeV. This corresponds to a shift in $U_{||}$ of 20 MeV.

This effect is easily accounted for however, and we do so by recording the value of N_{other} for each fake cluster. When we choose a fake cluster to associate with the simulated electron, we check how many tracks point at that cluster. If the number is not zero, then we consider the simulated event to have failed the N_{tracks} cut, and we throw the simulated event away.

Figure 6.5 shows the probability of failing the N_{tracks} cut as a function of the same variables as in Figure 6.4. Explicitly, we are plotting the fraction of the fake clusters which have 1 or more tracks pointing at them, as a function of the different variables. We consider all the fake clusters in all $W \rightarrow e\nu$ events, except for the clusters within ± 1 tower in azimuth of the primary electron.

The top plot of Figure 6.5 shows that the failure probability is lower for $\Delta\phi \sim 180°$ than for $\Delta\phi \sim 0°$ and $360°$. The fake clusters with $\Delta\phi \sim 180°$ have the recoil energy directed opposite the clusters, and there are fewer tracks pointing at these clusters. Similarly, the bottom two plots show that the probability of having a track associated with a fake cluster is proportional to the amount of energy in the event. The amount

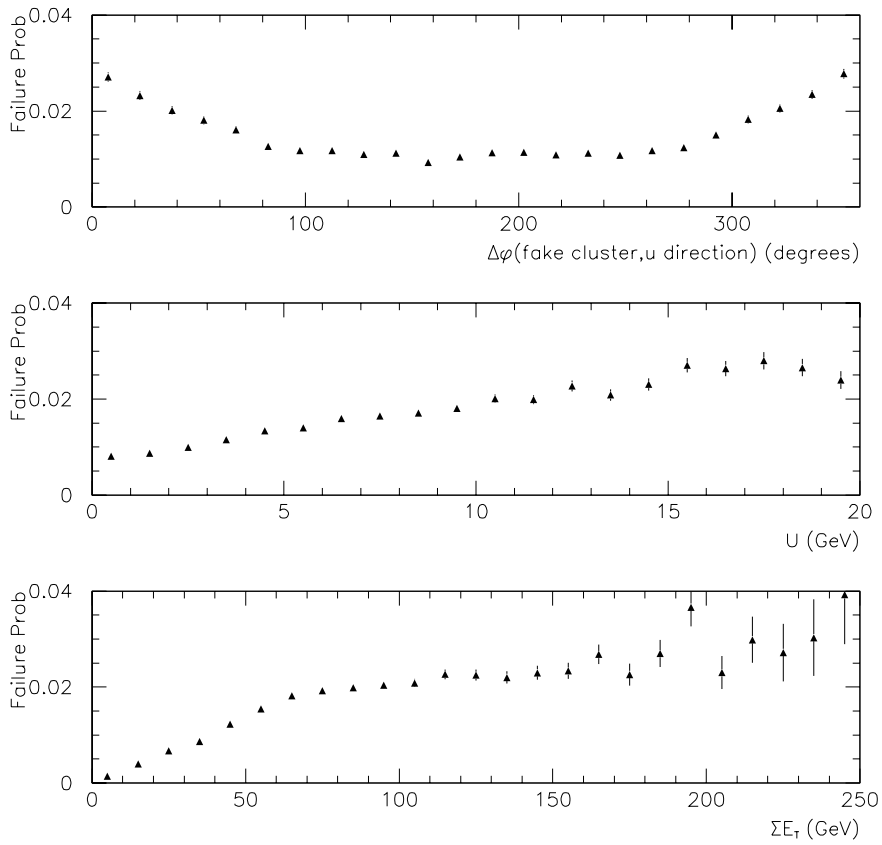

Figure 6.5: Probability of failing N_{tracks} cut for the fake clusters. The probability is the fraction of fake clusters which have 1 or more tracks pointing at them. The top plot is the probability vs $\Delta\phi$ between the fake cluster position and the direction of $\vec{U}$. The middle plot is vs $|\vec{U}|$, and the bottom plot is vs $\sum E_T$.

of energy increases with the recoil energy $|\vec{U}|$ (middle plot), and also $\sum E_T$ (bottom plot).

Our simulation of the $N_{tracks} \equiv 1$ cut also includes electrons from the conversion, $\gamma \rightarrow ee$, of both external and internal photons. The photon conversions are discussed in Section 6.1.2 above. Electrons from photon conversions can cause the event to fail the $N_{tracks} \equiv 1$ cut. We examine the conversion electrons that extrapolate to the simulated cluster. If any of those electrons were produced in the first half of the CTC (at a radius of less than 81.45 cm), then we assume that the real CTC would reconstruct the track. If the P_T of such a track is above 1 GeV then we consider the event to fail the $N_{tracks} \equiv 1$ cut, and we throw the event away. Figure 6.6 shows the P_T of the conversion electron for Monte Carlo events that fail the N_{tracks} cut because of the conversion electron. 0.4% of the simulated $W \rightarrow e\nu$ events fail for this reason, and Figure 6.6 is normalized to 0.4% of the real W data. The plot drops off around 1 GeV because the conversion electron must have P_T high enough to extrapolate to the electron cluster.

6.6 Summary

We have presented the basics of the P_T simulation, which includes photon bremsstrahlung as well as a simulation of the CTC resolution and the beam constraint. This is most significant for trying to tie the calorimeter energy scale to the CTC scale, and we will do this in a later chapter. We have also discussed the calorimeter simulation. The simulation sums the energies of the primary electron and associated particles and applies a gaussian resolution. By excluding energy which does not point at the cluster, we allow the possibility of some of the radiated energy being lost. In this way

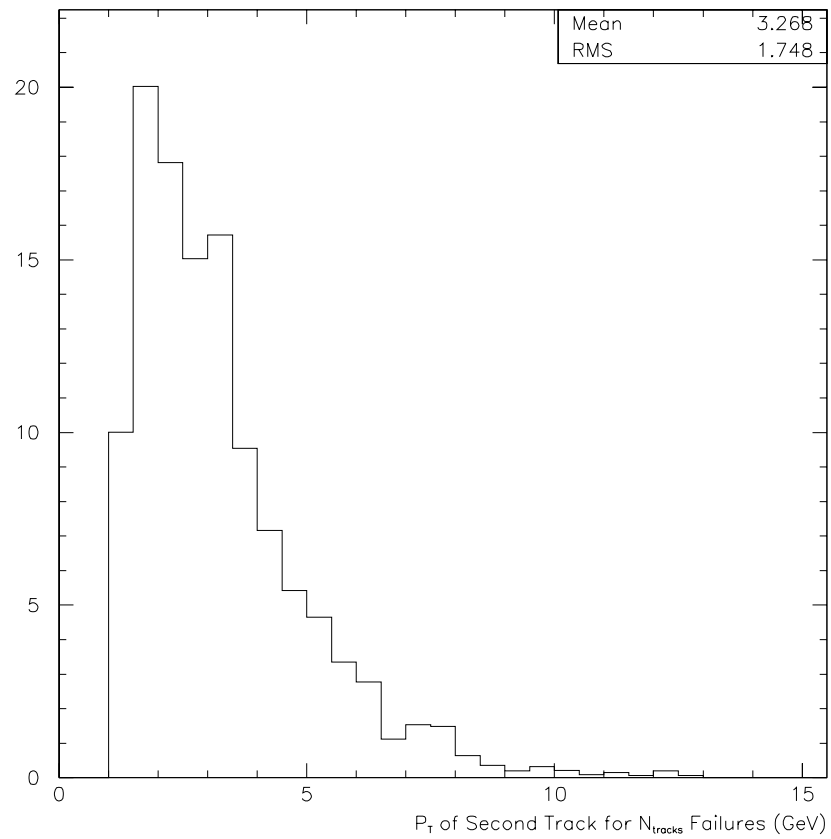

Figure 6.6: P_T of the photon conversion electron that lands in the primary electron cluster, for Monte Carlo events that fail the N_{tracks} cut because of the conversion track. 0.4% of the Monte Carlo events fail because of the conversion track, and the plot is normalized to the predicted distribution for real $W \rightarrow e\nu$ events.

a radiative correction is included in the simulation.

We have also presented a technique to embed the simulated events in real W events in such a way as to account for the bias introduced by our lepton removal procedure. This technique also allows us to simulate the N_{tracks} cut by looking for secondary tracks in the real event. An event can also fail the N_{tracks} cut because of photon conversions, and this possibility is considered in the simulation.

Another potential bias on $U_{||}$ arises if the photons or their conversion electrons do not get included with the electron cluster. If they point at the neighboring towers and those towers are removed in the $\vec{U}$ calculation, then there is no bias, but otherwise they will end up in the calculation of $\vec{U}$ and can bias $U_{||}$. We consider these possibilities, and such particles are added to our simulated value of $\vec{U}$.

Chapter 7

Boson P_T Determination

In this chapter we fit the Z data to find a P_T^{boson} distribution to use in the event generator. The Monte Carlo input P_T^{boson} distribution is determined by the weighting function Ψ, as discussed in Chapter 5. We vary the Monte Carlo event weights by varying the function Ψ, and in this way, we alter the input P_T^{boson} distribution. To fit to the Z data, we use the output of the Monte Carlo. We form the Z P_T distribution using the simulated, measured values for the two decay electrons, and we compare this distribution to the Z P_T distribution of the data. The weighting function, Ψ, is varied until the two distributions agree.

The function Ψ is a function of the variable X_{Pt}, as discussed in Chapter 5, where X_{Pt} is defined as the ratio $Q_T/\sqrt{\hat{s}}$. The quantity X_{Pt} is written out to disk in the event generation, along with the event weights and decay particle 4-momenta. The functional form for Ψ is chosen to be

$$\Psi(x) = x^p[(1-f)\exp(-ax)a^{p+1} \ + \ f\exp(-bx)b^{p+1}]\frac{1}{,(p+1)} \tag{7.1}$$

where a, b, f and p are parameters that we will fit for by comparing the Monte Carlo Z

P_T distribution to the data. The factor x^p forces the function to go to zero as $x \to 0$, as long as $p > 0$. The terms in the square brackets are the sum of two exponentials. The terms a^{p+1}, b^{p+1}, and $1/, (p+1)$ are normalization terms that force the function to integrate to 1.

For the Z data and Monte Carlo, we do not cut on $|\vec{U}|$ or on variables which are derived from $\vec{U}$. Thus, our P_T^{boson} fit is mostly independent of the model parameters for $\vec{U}$, which are discussed in the next chapter. There is a small dependence on the $\vec{U}$ model, however, since we run the Monte Carlo Z events through the electron simulation described in Chapter 6, and that simulation has a dependence on $\sum E_T$ and $\vec{U}$ because of the N_{tracks} cut. This does not present a problem since we have iterated the fitting procedure several times, and the Z P_T fit has only a small dependence on the details of the $\sum E_T$ and $\vec{U}$ shapes.

We do a binned likelihood fit to the data. We histogram the Z P_T distribution of the data in 45 bins from 0 to 45 GeV, and we do the same for the Monte Carlo except that the Monte Carlo histogram is weighted. For each Monte Carlo event, the event weight is multiplied by Ψ, and the resulting weight is used in the histogram. We vary the three input parameters to find a minimum of the function

$$L = -2 \times \sum_{bins} [-\lambda_i T + n_i \log(\lambda_i T)] \tag{7.2}$$

where n_i is the number of data points in bin i, and λ_i is the sum of the weights of the Monte Carlo events in bin i. The quantity T normalizes the Monte Carlo to the data and is the number of data points divided by the sum of all the Monte Carlo weights.

We will refer to the final fit parameters as $\vec{\Pi}_x$. After fitting with slightly more

than 975,000 Monte Carlo events, the fit gives

$$\vec{\Pi}_x \equiv \begin{pmatrix} a \\ b \\ f \\ p \end{pmatrix} = \begin{pmatrix} 54.8 \\ 18.2 \\ 0.642 \\ 1.40 \end{pmatrix} \tag{7.3}$$

The covariance matrix returned by the fit is

$$\tilde{C}_x = \begin{pmatrix} \sigma^2(aa) & \sigma^2(ab) & \sigma^2(af) & \sigma^2(ap) \\ & \sigma^2(bb) & \sigma^2(bf) & \sigma^2(bp) \\ & & \sigma^2(ff) & \sigma^2(fp) \\ & & & \sigma^2(pp) \end{pmatrix} = \begin{pmatrix} 279 & 56.9 & 0.324 & 6.26 \\ & 12.5 & 7.63 \times 10^{-2} & 1.29 \\ & & 4.65 \times 10^{-3} & -2.15 \times 10^{-3} \\ & & & 0.166 \end{pmatrix} \tag{7.4}$$

where we have only listed the upper triangular part of the matrix and have rounded off the numbers to three significant digits.

The top plot of Figure 7.1 shows the Z P_T distribution for data with the best Monte Carlo fit superimposed. The mean and rms of the data agree well with the mean and rms of the Monte Carlo. We sum the squares of the difference between data and Monte Carlo, bin by bin, divided by the squares of the uncertainties on each point. This quantity should be a χ^2-distribution for 41 degrees of freedom (45 bins less the 4 parameters of the fit). We get the value $\chi^2/dof = 0.90$. This indicates good agreement between data and Monte Carlo, and indicates that we have introduced enough degrees of freedom into the form of Ψ to get a good fit. The bottom plot of Figure 7.1 shows Ψ for the final fit parameters $\vec{\Pi}_x$.

To determine the uncertainty associated with the 975,000 Monte Carlo events,

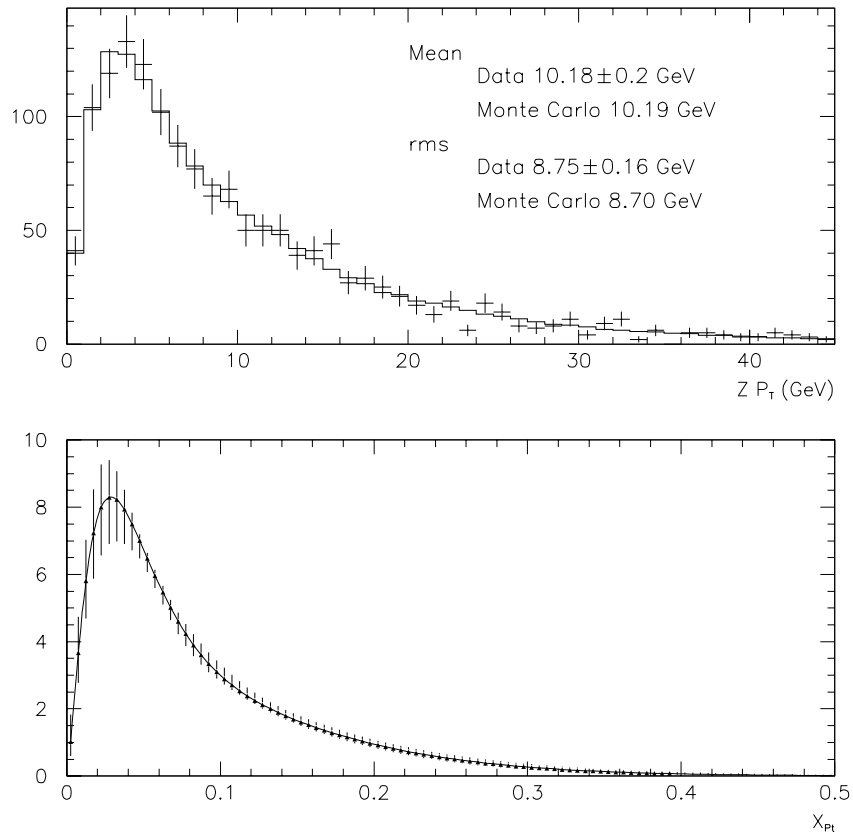

Figure 7.1: Top: Z P_T distribution of Z data (points) and Z Monte Carlo (histogram). The Monte Carlo uses the final fitted values for $\vec{\Pi}_x$. The mean and rms of the data and Monte Carlo are shown on the plot. Bottom: The function Ψ for the final fitted values for $\vec{\Pi}_x$. The error bars at each point in the bottom plot indicate the range of values consistent with the statistical uncertainty of the fit. The y-axis scale on the bottom plot is arbitrary.

we split the Monte Carlo into 10 independent subsamples of 97,000 events each. We refit with each subsample, and we label the set of fit parameters from the ith subsample as $\vec{\Pi}_x^{\,i}$. To measure of the variation of the fits, we calculate the quantity $\Delta \equiv (\vec{\Pi}_x^{\,i} - \vec{\Pi}_x) \cdot \tilde{C}_x^{-1} \cdot (\vec{\Pi}_x^{\,i} - \vec{\Pi}_x)$, where $\tilde{C}_x$ is the covariance matrix that is derived from the full Monte Carlo fit. $\tilde{C}_x$ represents the statistical uncertainty associated with the real data, and Δ is a measure of how the fits are varying relative to the statistical error on the data.

If the covariance matrix $\tilde{C}_x$ correctly describes the statistics of the 10 subsamples, then the 10 values for Δ should be distributed as a χ^2-distribution for 4 degrees of freedom. The distribution should have a mean of 4. The distribution of the 10 values has a smaller mean. The 10 values for Δ are distributed with a mean of 0.2 and an rms of 0.12. Therefore, for $\tilde{C}_x$ to correctly describe the statistics of the 10 subsamples, we need to scale it by the measured mean of 0.2 divided by the expected mean of 4. Since the full Monte Carlo has ten times the statistics of each of the subsamples, we need an additional factor of 1/10 to describe the full Monte Carlo. Thus, the contribution to the covariance matrix from the Monte Carlo is a factor of $(0.2/4) \times (1/10) = 1/200$ smaller than the contribution from the data. We conclude that the Monte Carlo sample is adequately large, and that we can neglect its contribution to the statistical uncertainty.

The measured Z P_T depends on the E_T of the two electrons, but we have not yet determined an energy scale. As a check that the fit is not sensitive to the assumed energy scale, we scale the energy in the data by $\pm 1\%$, which is a large variation. We scale the E_T in the data of both electrons before applying the cuts, and we recalculate Z P_T. We check how the fit results vary relative to the statistical error on the fits. We form the quantity $\Delta \equiv (\vec{\Pi}_x^{\,\pm 1\%} - \vec{\Pi}_x) \cdot \tilde{C}_x^{-1} \cdot (\vec{\Pi}_x^{\,\pm 1\%} - \vec{\Pi}_x)$, where $\vec{\Pi}_x^{\,\pm 1\%}$ are the fit

results after scaling the energy by $\pm 1\%$, and $\vec{\Pi}_x$ are the original fit values. As above, $\tilde{C}_x$ is the covariance matrix that describes the statistical uncertainty of the original fit.

We get the values $\Delta = 0.2$ for the fit which had the energy increased by 1%, and $\Delta = 0.3$ for the decrease of 1%. These are small values for a 4−parameter fit, and they indicate that the changes in the fit parameters from varying the energy scale are small compared to the statistical uncertainty on the parameters. We conclude that the systematic uncertainty in $\vec{\Pi}_x$ from the energy scale is negligible compared to the statistical uncertainty.

Chapter 8

Calorimeter Response Model

The neutrino from $W \rightarrow e\nu$ decays leaves no energy in the detector, and we infer its transverse energy from the $\not\!\!E_T$. Since $\not\!\!E_T = |\vec{E}_T + \vec{U}|$, the $\not\!\!E_T$ simulation depends strongly on the $\vec{U}$ simulation. There are two contributions to $\vec{U}$. The first is the energy related to the hard scatter. This energy is composed mostly of the initial state radiation from the quarks involved in the $q\overline{q}$ collision that creates the W or Z boson. This energy balances the P_T of the boson, and we refer to it as the recoil energy. The second contribution is the energy associated with multiple interactions and also with the remnants of the protons and anti-protons that are involved in the hard scatter. The remnants are related to the "spectator" quarks that did not take part in the hard scatter. We refer to the multiple interactions and the proton remnants as the underlying event.

The contributions of the underlying event and recoil energy to the $\vec{U}$ resolution are included in the Monte Carlo by assuming that the resolution depend on $\sum E_T$. In Section 8.1 we fit the data for a $\sum E_T$ shape, and in Section 8.2 we discuss how the resolutions depend on $\sum E_T$. We also allow the mean of $\vec{U}$ along the boson direction

to vary with P_T^{boson}, and the full $\vec{U}$ model is discussed in Section 8.3. In Section 8.4, we correct for biases associated with the fits.

We use the Z data to fit for the various parameters of the model. None of the cuts that define our Z sample depend directly on the variable $\vec{U}$, and this simplifies our fits.

8.1 $\sum E_T$ Fit

Figure 8.1 shows the $\sum E_T$ distribution for the W and Z data. Also shown are the results of two-parameter fits to a , -distribution. The , -distribution is

$$\gamma(x) = \frac{b}{,(a)}(bx)^{a-1} exp(-bx) \tag{8.1}$$

where a and b are the fit parameters, , is the gamma-function, and the variable x is $\sum E_T$ for this case. The term $b/,(a)$ normalizes the distribution. For the fits in Figure 8.1, we normalized the , -distribution to match the total amount of W or Z data. The fits are good, with a χ^2/dof of 1.0 for the Z case and 1.1 for the W case. We will use a , -distribution for the $\sum E_T$ shape of the Monte Carlo.

The fits in Figure 8.1 are different for W and Z data. The reason for this is that in the W data, we cut on $|\vec{U}|$, $\not{E}_T$, and M_T, all of which depend on $\vec{U}$; and the resolution on $\vec{U}$ depends on $\sum E_T$. In the W Monte Carlo, we find that the $\sum E_T$ distribution which is used as an input to the Monte Carlo has an average that is ~ 3 GeV higher than the $\sum E_T$ distribution of Monte Carlo events that pass all the W cuts. Since this effect is included in the Monte Carlo, we want the Monte Carlo to use an input $\sum E_T$ shape that has been corrected for the effect. Rather than correct the W data, we use the Z data to determine a $\sum E_T$ shape.

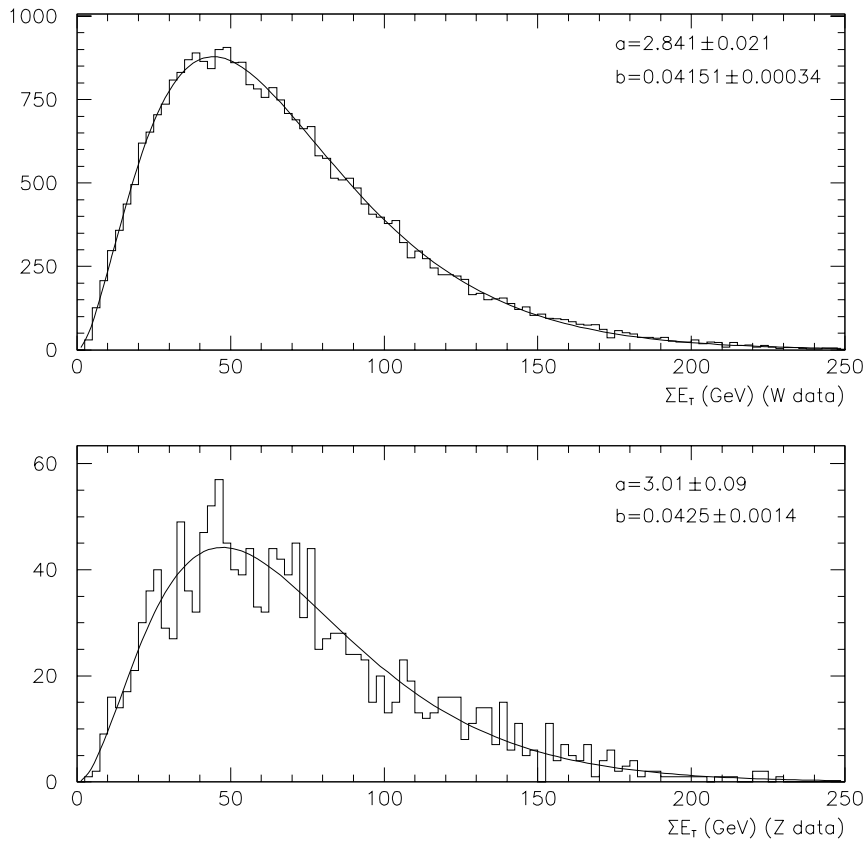

Figure 8.1: $\sum E_T$ distribution of W data (top) and Z data (bottom). The curves shown are fits to gamma-distributions, as discussed in the text. The fit parameters, a and b, are printed on the plots.

The $\sum E_T$ shape has a dependence on the boson P_T since $\sum E_T$ includes the recoil energy. To include this in the simulation, we allow the parameter a of Equation 8.1 to have a linear dependence on the boson P_T. We define three parameters $\vec{\Pi}_\Sigma \equiv (\alpha_0, \alpha_1, \beta_0)$ as

$$\begin{aligned} a &= \alpha_0 + \alpha_1 \times P_T^{boson} \\ b &= \beta_0 \end{aligned} \tag{8.2}$$

and we will fit the Z data for these parameters.

Since the W data has a $|\vec{U}| < 20$ GeV cut, we are not interested in events with large values for the boson P_T. When we fit for the above $\sum E_T$ parameters, we only use $Z \to ee$ data with $P_T^{boson} < 45$ GeV.

We use the two electrons from the Z decay to calculate a value for the measured Z P_T. For a given set of the three parameters $\vec{\Pi}_\Sigma$, we then calculate a and b based on the measured Z P_T and Equation 8.2. The probability for a given event is $\gamma(\sum E_T)$, where γ is defined in Equation 8.1. We do an unbinned likelihood fit and minimize the function

$$L = -2 \times \sum_{Z\ data} \log \gamma(\sum E_T) \tag{8.3}$$

where the sum is over all the Z data.

The best fit results are

$$\vec{\Pi}_\Sigma^{data} \equiv \begin{pmatrix} \alpha_0 \\ \alpha_1 \\ \beta_0 \end{pmatrix} = \begin{pmatrix} 2.74 \\ 0.0447 \\ 0.0462 \end{pmatrix} \tag{8.4}$$

where we write $\vec{\Pi}_\Sigma$ with the superscript "data" to indicate that the fit was done to the data without any corrections. We correct these results below in Section 8.4.

The covariance matrix returned by the fitter represents the uncertainty on the fits associated with the Z statistics. The covariance matrix is

$$\tilde{C}_\Sigma = \begin{pmatrix} \sigma^2(\alpha_0\alpha_0) & \sigma^2(\alpha_0\alpha_1) & \sigma^2(\alpha_0\beta_0) \\ & \sigma^2(\alpha_1\alpha_1) & \sigma^2(\alpha_1\beta_0) \\ & & \sigma^2(\beta_0\beta_0) \end{pmatrix} = \begin{pmatrix} 1.16\times10^{-2} & -1.14\times10^{-4} & 1.50\times10^{-4} \\ & 3.12\times10^{-5} & 2.94\times10^{-6} \\ & & 3.05\times10^{-6} \end{pmatrix} \tag{8.5}$$

where we have only listed the upper triangular part of the matrix and have rounded off the numbers to three significant digits. We have not labelled any numbers with units, but for all these fits we are measuring $\sum E_T$ and P_T^{boson} in units of GeV.

8.2 Dependence of $\vec{U}$ Resolution on ΣE_T

In this section, we discuss our parameterization of the $\vec{U}$ resolution in terms of the quantity $\sum E_T$. First we discuss why we expect the resolution to depend on $\sum E_T$, and then we discuss the functional form for the dependence, as fit from minimum bias data.

The explicit form for our calculation of $\vec{U}$ is

$$\vec{U} = \sum_{calorimeter} E_i \sin\theta_i \begin{pmatrix} \cos\phi_i \\ \sin\phi_i \end{pmatrix} \equiv \begin{pmatrix} <\cos\phi> \\ <\sin\phi> \end{pmatrix} \sum E_T \tag{8.6}$$

where E_i is the energy of the ith calorimeter tower, θ_i is the polar angle of a line pointing from the event vertex to the ith tower, and ϕ_i is the azimuthal position of the center of calorimeter tower i. The sum includes both electromagnetic and hadronic towers. The brackets, $<>$, denote the E_T weighted average, which is defined by this equation.

There are two contributions to the resolution on $\vec{U}$. The first is the variation in the energy that misses the calorimeters and lands in cracks, and the second is the energy resolution of each calorimeter tower. In general, the energy resolution on a calorimeter tower is proportional to the square root of the energy in the tower so that $\sigma^2(E_i) \propto E_i$. However, for the central calorimeters, particles that enter towers which have higher values for $\eta_{detector}$ pass through the absorber layers at more oblique angles. The effective absorber thickness increases as $1/\sin\theta$. We expect the energy resolution in these towers to be $\sigma^2(E_i) \propto E_i/\sin\theta_i$. In the plug and forward regions, the absorber is vertical, and the effective absorber thickness increases as $1/\cos\theta$. For these regions, we expect $\sigma^2(E_i) \propto E_i/\cos\theta_i$.

From Equation 8.6, the contribution to the resolution on $\vec{U}$ from the calorimeter resolution is $(\sigma^2_{Ux}, \sigma^2_{Uy})$, where

$$\begin{pmatrix} \sigma^2_{Ux} \\ \sigma^2_{Uy} \end{pmatrix} = \sum_{calorimeter} \sigma^2(E_i)\sin^2\theta_i \begin{pmatrix} \cos^2\phi_i \\ \sin^2\phi_i \end{pmatrix} \tag{8.7}$$

The contribution to this quantity from the central calorimeters is

$$\propto \sum E_{Ti} \begin{pmatrix} \cos^2\phi_i \\ \sin^2\phi_i \end{pmatrix} \tag{8.8}$$

and the contribution from the plug and forward calorimeters is

$$\propto \sum E_{Ti} \begin{pmatrix} \cos^2\phi_i \\ \sin^2\phi_i \end{pmatrix} \tan\theta_i \tag{8.9}$$

where we assume that $\sigma^2(E_i) \propto E_i/\sin\theta_i$ for the central calorimeters and $\sigma^2(E_i) \propto$

$E_i/\cos\theta_i$ for the plug and forward. The proportionality constant of Equation 8.8 is smaller than Equation 8.9 since the plug and forward calorimeters have worse resolutions than the central. The $\tan\theta_i$ term in Equation 8.9, however, reduces the contribution of the plug and forward calorimeters, compared to the central. As a rough approximation, we drop the $\tan\theta_i$ term and assume that the proportionality constants of Equations 8.8 and 8.9 are the same.

Our rough approximation for the $\vec{U}$ resolution is then

$$\begin{pmatrix} \sigma^2_{Ux} \\ \sigma^2_{Uy} \end{pmatrix} \propto \sum E_{Ti} \begin{pmatrix} \cos^2\phi_i \\ \sin^2\phi_i \end{pmatrix} = \begin{pmatrix} <\cos^2\phi_i> \\ <\sin^2\phi_i> \end{pmatrix} \sum E_T \tag{8.10}$$

where the sum is over all calorimeters. If the energy has an azimuthally flat distribution, as we expect from minimum bias events, then the expected value for $<\cos^2\phi>$ and $<\sin^2\phi>$ is $\frac{1}{2}$.

Equation 8.10 is a rough approximation for the reasons stated above, and also because we are assuming that the hadronic and electromagnetic calorimeters contribute equally to the resolution. Moreover the equation does not consider the contribution to the variance in $\vec{U}$ from lost energy in cracks. The equation is not exact, but it indicates that we should expect the resolutions to be approximately proportional to $\sqrt{\sum E_T}$.

We use the minimum bias data to determine a functional form for the dependence of the $\vec{U}$ resolution on $\sum E_T$. The expected value for $\vec{U}$ in minimum bias data is zero, and any non-zero value is a result of measurement resolutions. The widths of the U_x and U_y distributions will then give us the resolutions $(\sigma_{Ux}, \sigma_{Uy})$ for this data. We can also calculate $\sum E_T$ in the minimum bias data, and we make plots of σ_{Ux} and σ_{Uy} as a function of $\sum E_T$. The widths of the Gaussian fits to U_x and U_y in bins of $\sum E_T$ for

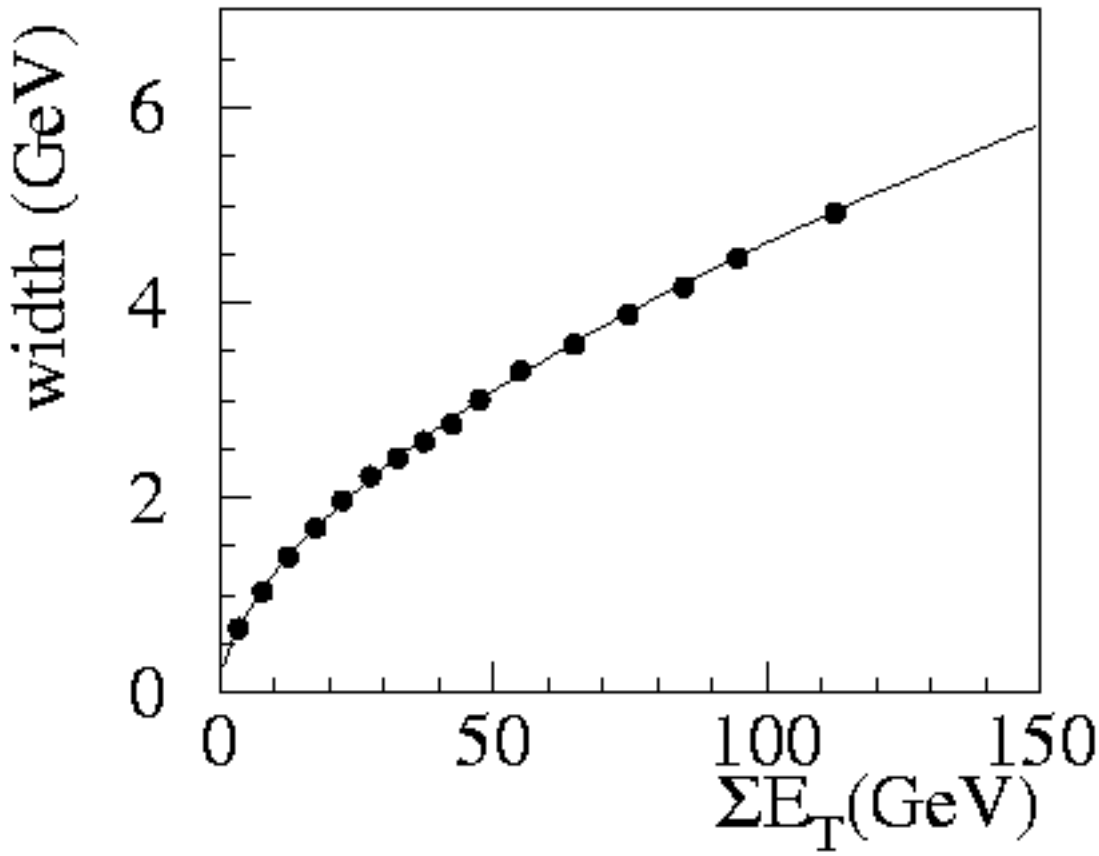

Figure 8.2: Widths of Gaussian fits to U_x and U_y as a function of $\sum E_T$, for minimum bias data. The curve shown is $0.324 \times (\sum E_T)^{0.577}$. This figure is taken from [40].

the minimum bias data are shown in Figure 8.2. A good fit to the data is [40]

$$\sigma_{Ux} = \sigma_{Uy} = 0.324 \times (\sum E_T)^{.577} \tag{8.11}$$

where $\vec{U}$ and $\sum E_T$ are calculated in GeV. Some deviation from the $\sqrt{\sum E_T}$ form is expected since Equation 8.10 is only approximate.

The minimum bias data was taken during all of Run 1B, and the distribution in luminosity is roughly the same for the minimum bias data as for the W and Z data. The luminosity, however, does not appear explicitly in the $\vec{U}$ model below, but it

is included through the $\sum E_T$ variable. Changes in luminosity cause changes in the $\sum E_T$ distribution, and the $\sum E_T$ distribution is used to determine the $\vec{U}$ resolutions. The use of Equation 8.11 in the $\vec{U}$ model, and the details of the model, are the subjects of the next section

8.3 $\vec{U}$ Model

We begin by defining the parameters of the model, and then we discuss how these parameters are fit from the Z data. In Section 8.4 we discuss biases on the fit and how we correct for those biases.

8.3.1 Parameter Definitions

Since $\vec{U}$ is a measure of the boson P_T, a natural axis to use for the $\vec{U}$ simulation is the boson P_T direction. Knowledge of this axis is not available in the W data, but it is available in the Z data since the Z P_T can be measured with the two decay electrons; and it is also available in the simulation. We define U_1 to be $\vec{U}$ projected parallel to the boson direction and U_2 to be the perpendicular projection. These variables should not be confused with $U_{||}$ and $U_{\perp}$ which are $\vec{U}$ projected parallel and perpendicular to the primary electron in the W data.

For the simulation of the variables U_1 and U_2, we use the formula

$$\begin{pmatrix} U_1 \\ U_2 \end{pmatrix} = \begin{pmatrix} \mu(P_T^{boson}) \\ 0 \end{pmatrix} + \begin{pmatrix} g_1(\sigma_1) \\ g_2(\sigma_2) \end{pmatrix} \tag{8.12}$$

where $g_1(\sigma_1)$ and $g_2(\sigma_2)$ are Gaussian distributed random variables of mean zero and widths σ_1 and σ_2 respectively, and the function μ will be determined from the data.

The strongest justification for using Gaussian distributions is that they fit the Z data well. This will be shown below. The widths have the form

$$\begin{pmatrix} \sigma_1 \\ \sigma_2 \end{pmatrix} = \sigma_{mb}(\sum E_T) \times \begin{pmatrix} 1 + s_1 \times (P_T^{boson})^2 \\ 1 + s_2 \times (P_T^{boson})^2 \end{pmatrix} \tag{8.13}$$

where σ_{mb} is the resolution which is predicted from the value of $\sum E_T$. This resolution is given by the minimum bias fit of Equation 8.11, $\sigma_{mb} = 0.324 \times (\sum E_T)^{.577}$. In the Monte Carlo, $\sum E_T$ is drawn randomly from the gamma-distributions of Section 8.1. P_T^{boson} is the value that the simulation generates for the boson P_T, and s_1 and s_2 are parameters which we will fit for. The underlying event energy is expected to have the same dependence on $\sum E_T$ as the minimum bias data, but the recoil energy contains low energy jets that balance the boson P_T. This energy may contribute to the resolution differently than the underlying event energy. The parameters s_1 and s_2 allow us to account for this difference. Even if s_1 and s_2 were zero, however, the resolutions still have some dependence on P_T^{boson}, since $\sum E_T$ varies with P_T^{boson} through Equation 8.2.

The average of U_2 is zero since neither side of the boson direction is preferred. On the other hand, the average of U_1 is the response to the boson P_T, and the function $\mu(P_T^{boson})$ determines how the mean varies in the simulation. We find that a good fit to the Z data is given by a "quadratic spline." The explicit equation is

$$\mu(x) = \begin{cases} a_0 + b_0 x + c_0 x^2, & 0 < x < 2.5 \\ a_1 + b_1 x + c_1 x^2, & 2.5 < x < 5 \\ a_2 + b_2 x + c_2 x^2, & 5 < x < 15 \\ a_3 + b_3 x + c_3 x^2, & 15 < x \end{cases} \tag{8.14}$$

where the given quadratic is used for the indicated region, and the numbers shown are in GeV. We reduce the number of free parameters by requiring that μ be smooth and continuous at the boundaries between the regions. There are three boundary points and two conditions at each point, and this reduces the number of free parameters by six. We also require that μ is 0 at 0, and so we set $a_0 \equiv 0$. Five free parameters remain, and we choose them to be $\{b_0, c_0, c_1, c_2, c_3\}$.

8.3.2 Fits to the Z Data

We fit for the model parameters with the Z data. We use an unbinned likelihood function. There are seven parameters, two from the P_T^{boson} dependence of the resolutions from Equation 8.13, and five from the functional form for μ of Equation 8.14. For every event in the Z data we use U_1, U_2, and $\sum E_T$; and for P_T^{boson} we use the Z P_T as measured from the two decay electrons. For each event we calculate the probability

$$P_i = \frac{1}{\sqrt{2\pi}\sigma_1} exp(-\frac{(U_1 - \mu)^2}{2{\sigma_1}^2}) \times \frac{1}{\sqrt{2\pi}\sigma_2} exp(-\frac{{U_2}^2}{2{\sigma_2}^2}) \tag{8.15}$$

where σ_1, σ_2, and μ are determined from Equations 8.13 and 8.14. We use MINUIT to minimize the function

$$L = -2 \times \sum_{Z\ data} \log P_i \tag{8.16}$$

As for the $\sum E_T$ fits above, we only use Z events with $P_T^{boson} < 45$ GeV. We do this since the W data has a $|\vec{U}| < 20$ GeV cut, and so we are not interested in the fit results for large values of the boson P_T.

We label the results of the fit as $\vec{\Pi}_U^{data}$. As in the $\sum E_T$ fits, we append the superscript "data" to indicate that we have not yet corrected these results for biases

associated with fitting directly to the data. The results are

$$\vec{\Pi}_U^{data} \equiv \begin{pmatrix} s_1 \\ s_2 \\ b_0 \\ c_0 \\ c_1 \\ c_2 \\ c_3 \end{pmatrix} = \begin{pmatrix} (5.02 \pm 0.77) \times 10^{-4} \\ (1.77 \pm 0.60) \times 10^{-4} \\ (-2.94 \pm 26.0) \times 10^{-2} \\ (-1.07 \pm .87) \times 10^{-1} \\ (-9.13 \pm 46.1) \times 10^{-3} \\ (-5.47 \pm 5.4) \times 10^{-3} \\ (-1.44 \pm 3.2) \times 10^{-3} \end{pmatrix} \tag{8.17}$$

where the data quantities are measured in GeV. The errors shown are the square roots of the diagonal parts of the covariance matrix. Since the μ terms are highly correlated, the full covariance matrix is more meaningful than the errors shown here. Whenever we consider the statistical error on this fit, we always use the full covariance matrix.

The solid line in Figure 8.3 is μ vs Z P_T using the parameters of Equation 8.17. Also shown are the results of Gaussian fits to the U_1 distribution in bins of Z P_T. The Gaussian fits agree well with the fitted result for μ. The dashed line in Figure 8.3 is the function μ after the corrections of the next section.

The top plot of Figure 8.4 shows the distribution of $(U_1 - \mu)/\sigma_1$ for all the Z data, where the fit parameters $\vec{\Pi}_U^{data}$ are used to calculate μ and σ_1 according to Equations 8.14 and 8.13. For this figure, we require that $ZP_T < 45$ GeV, as was done for the fit. The bottom plot shows the distribution of U_2/σ_2. If the model accurately describes the data, then these plots should look like Gaussian distributions with mean 0 and width 1. Gaussian fits are shown on both plots. The fitted means are consistent with 0, and both widths are consistent with 1. The goodness of the Gaussian fits and

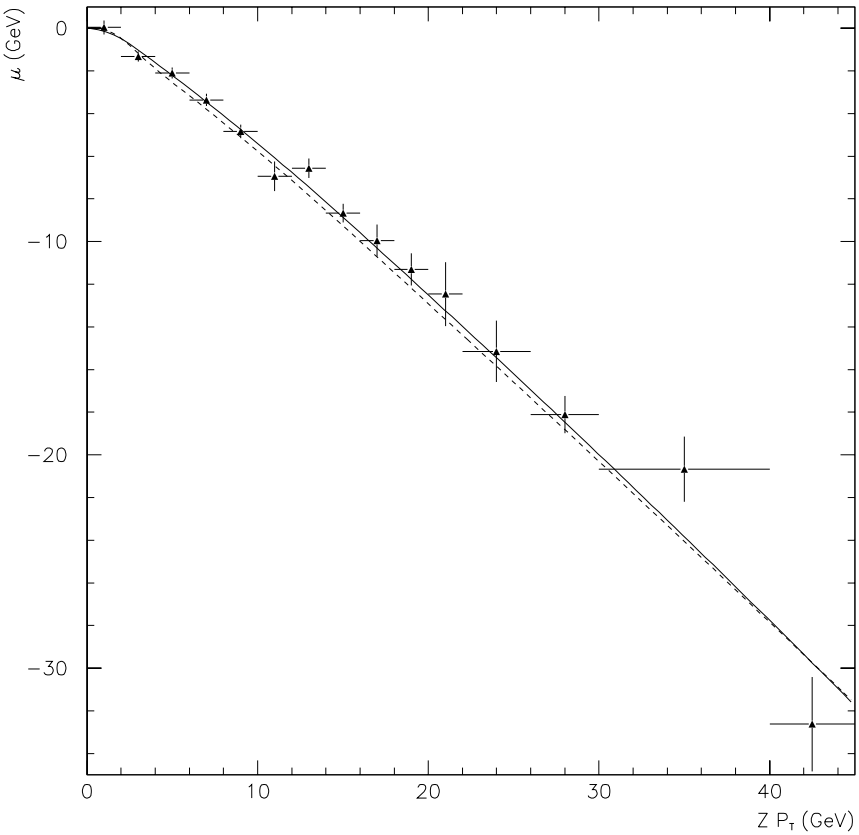

Figure 8.3: Triangles: Results of Gaussian fits to the U_1 distribution in regions of Z P_T. The x-axis defines the Z P_T regions, with the points placed in the middle, and the x-error bars indicate the extent of the regions. Solid line: μ vs P_T^{boson}, where μ is defined by Equation 8.14. The fit parameters from the Z data fit are used. Dashed line: μ vs P_T^{boson}, using the final, corrected values for the parameters.

the lack of large tails in the data indicate that the resolutions are understood and that it is reasonable to use Gaussian distributions in the simulation.

We also check that Gaussian distributions give good descriptions of the Z data in different regions of Z P_T. Figure 8.5 shows plots of U_1/σ_{mb} for different regions of Z P_T, where Z P_T is measured with the two decay electrons. The variable σ_{mb} is $0.324 \times (\sum E_T)^{.577}$, following Equation 8.11. Similarly, Figure 8.6 shows plots of U_2/σ_{mb} for the same regions. Gaussian fits to the histograms are overlaid on both sets of plots. The fits are good, and there are no non-Gaussian tails in the plots.

Only four Z P_T regions are shown in Figures 8.5 and 8.6. In addition we partition all the Z data into Z P_T regions, and all the regions show good Gaussian fits. Figure 8.7 shows the means and widths of the Gaussian fits in all the regions. The mean of U_1/σ_{mb} has a clear dependence on the Z P_T, as we expect since U_1 is a measure of the recoil response to the boson P_T. The mean of U_2/σ_{mb} is flat and distributed around zero.

Equation 8.11 describes the dependence of the $\vec{U}$ resolutions on $\sum E_T$. This dependence was fit with minimum bias data. To check that Equation 8.11 is also appropriate for $Z \rightarrow ee$ data, we use the bottom plots of Figure 8.7. These plots show the widths of the Gaussian fits to the distributions of U_1/σ_{mb} and U_2/σ_{mb}. As Z $P_T \rightarrow 0$, the recoil energy becomes small, and only the underlying event energy contributes to $\vec{U}$. For low Z P_T, the widths of both U_1/σ_{mb} and U_2/σ_{mb} approach 1, as expected if correctly describes the resolutions.

The widths of U_1/σ_{mb} show some increase with Z P_T, but no clear increase is evident in the U_2/σ_{mb} fits. The recoil energy changes the resolution of U_1 more than the resolution of U_2. The model is able to account for increases in the resolution through the parameters s_1 and s_2, which are defined in Equation 8.13. The curves

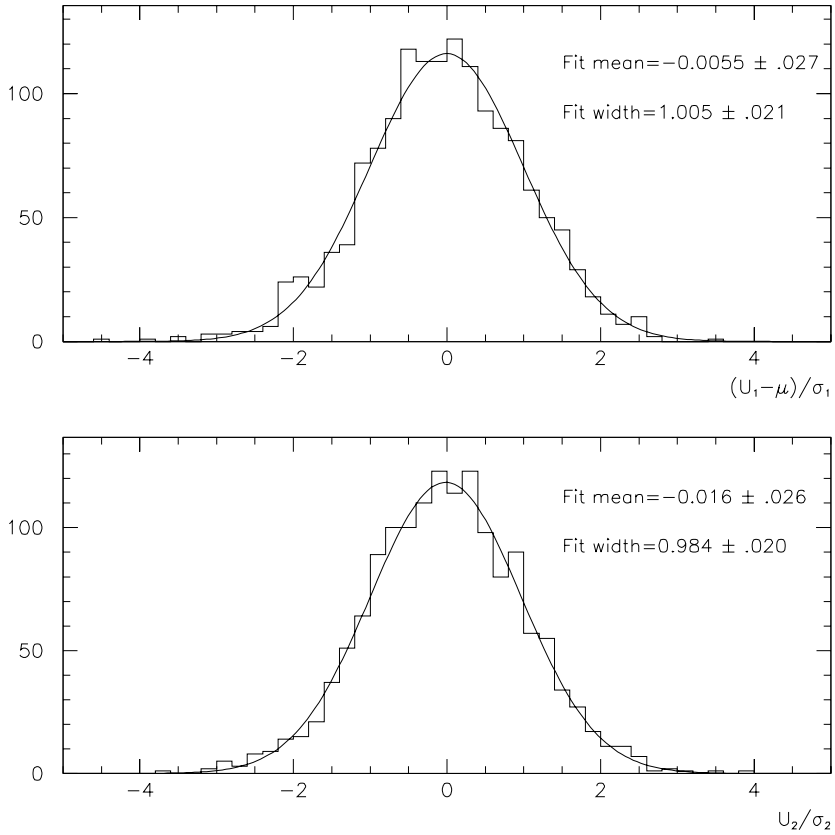

Figure 8.4: The distribution of $(U_1 - \mu)/\sigma_1$ (top) and U_2/σ_2 (bottom) for Z data with $ZP_T < 45$ GeV, where the Z data fit parameters are used to calculate μ, σ_1, and σ_2. Gaussian fits to the histograms are overlaid, and the means and widths of the fits are printed on the plots. $\chi^2/dof = 0.92$ for the fit in the top plot and 0.72 for the fit in the bottom plot.

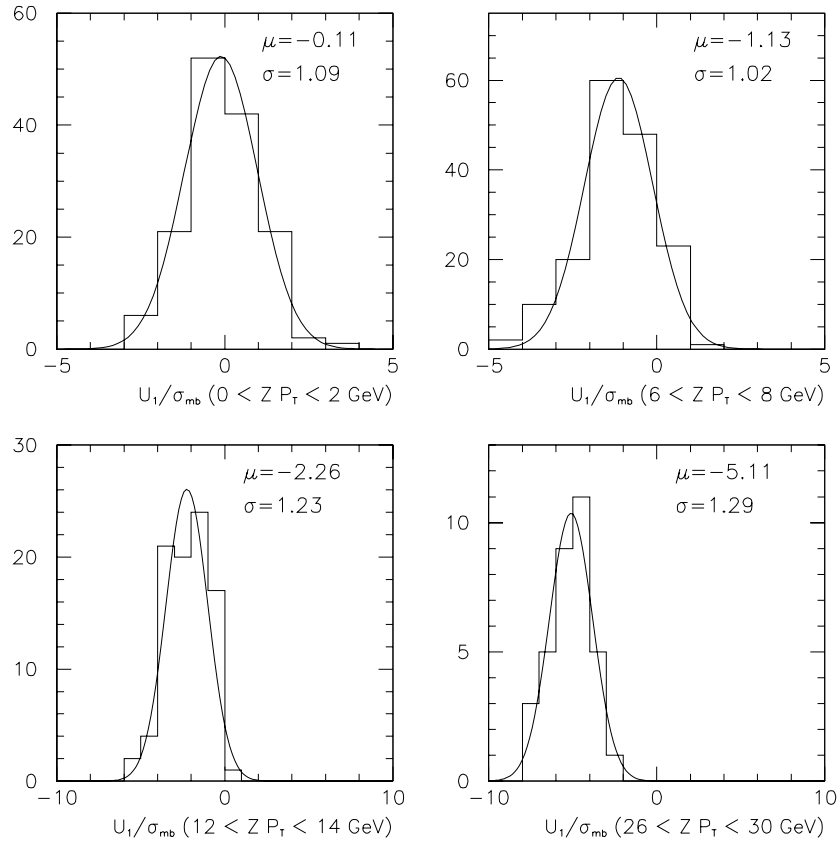

Figure 8.5: Distributions of U_1/σ_{mb} for $Z \rightarrow ee$ data, where $\sigma_{mb} = 0.324 \times (\sum E_T)^{.577}$, in four regions of Z P_T. The upper left plot is for $0 < ZP_T < 2$, the upper right is for 6 to 8, the bottom left for 12 to 14, and the bottom right for 26 to 30 GeV. Gaussian fits to each plot are overlaid. The means (μ) and widths (σ) of the fits are shown on each plot. The means and widths and their uncertainties are plotted in Figure 8.7 below. The y-axes are the number of events. The bottom two plots have different x-axis scales than the top two plots.

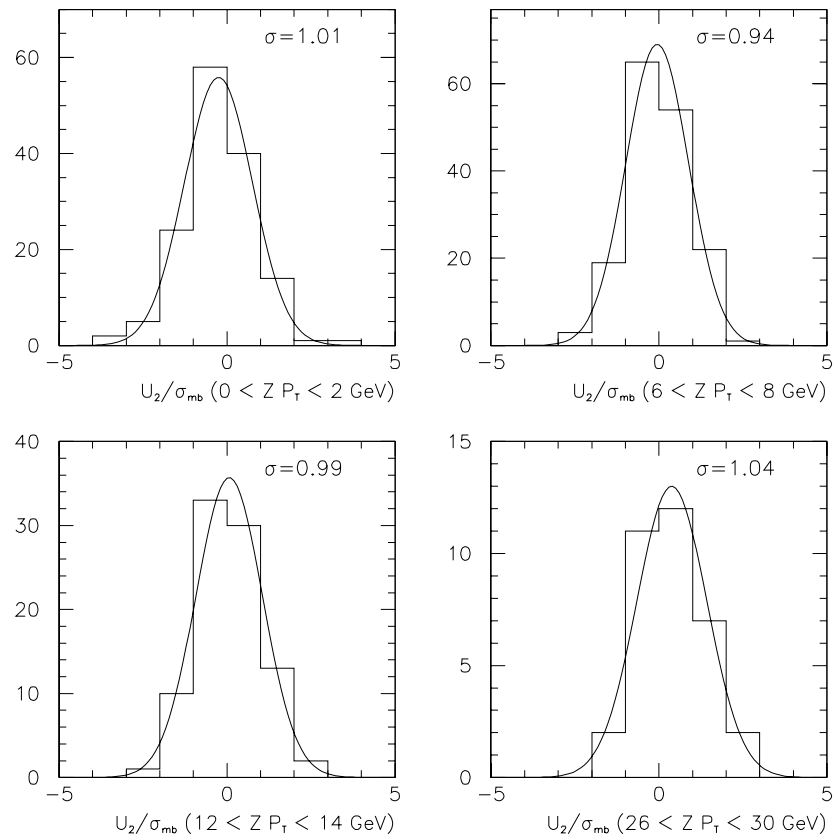

Figure 8.6: Distributions of U_2/σ_{mb} for $Z \rightarrow ee$ data, where $\sigma_{mb} = 0.324 \times (\sum E_T)^{.577}$, in four regions of Z P_T. The Z P_T regions are labelled on the plots and are the same Z P_T regions as in Figure 8.5. Gaussian fits to each plot are overlaid. The widths (σ) of the fits are shown on each plot. The means and widths and their uncertainties are plotted in Figure 8.7 below. The y-axes are the number of events.

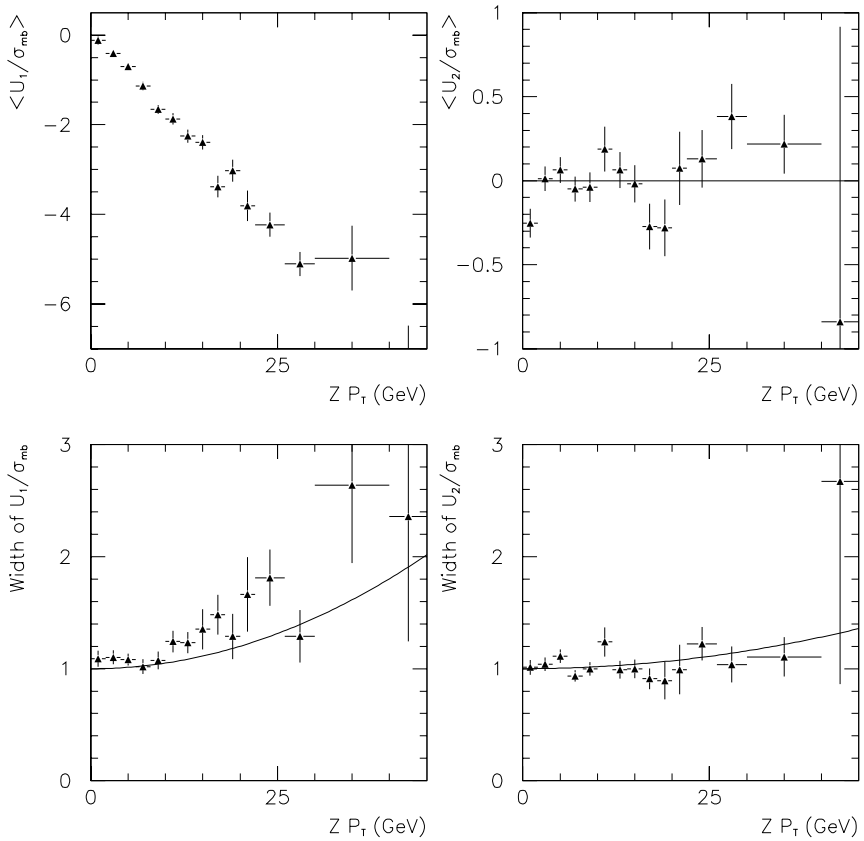

Figure 8.7: Results of Gaussian fits to the histograms of U_1/σ_{mb} and U_2/σ_{mb} in different regions of Z P_T. The x-axes define the Z P_T regions, with the points placed in the middle, and the x-error bars indicate the extent of the regions. The plots show the fitted mean of U_1/σ_{mb} (upper left), the fitted mean of U_2/σ_{mb} (upper right), and the fitted widths of U_1/σ_{mb} (bottom left) and U_2/σ_{mb} (bottom right) as functions of the Z P_T regions. A straight line at zero is shown in the upper right plot to indicate the expected value for the mean of U_2/σ_{mb}. The curves shown on the bottom two plots are $1 + s_1 \times (ZP_T)^2$ and $1 + s_2 \times (ZP_T)^2$, where s_1 and s_2 are the fitted values of Equation 8.17.

$1 + s_1 \times (P_T^{boson})^2$ and $1 + s_2 \times (P_T^{boson})^2$ are shown on the bottom plots of Figure 8.7, where s_1 and s_2 are the fitted values of Equation 8.17. The plot of the width of U_1/σ_{mb} vs Z P_T is not perfectly described by the function $1 + s_1 \times (P_T^{boson})^2$. s_1 was determined using an unbinned fit, and it is possible that the binned Gaussian fits of Figure 8.17 give slightly different results for the widths.

The Z data and Monte Carlo only include "central-central" $Z \rightarrow ee$ events, where both decay electrons land in the central electromagnetic calorimeter. Our $W \rightarrow e\nu$ Monte Carlo predicts that in $\sim \frac{1}{3}$ of the final $W \rightarrow e\nu$ sample, the neutrino passes through the plug or forward calorimeters. If the "central-plug" events are significantly different than the central-central, we may be introducing a bias into the model by only using central-central $Z \rightarrow ee$ events. We find, however, that the "central-plug" $Z \rightarrow ee$ events are not significantly different than the central-central. For example the mean of U_1 as a function of Z P_T is less negative for the central-plug events, but this is accounted for by the worse resolution of the central-plug events. In the next section we discuss how resolution effects can bias the results. We do not use the central-plug events because of the increased difficulty of correcting the results.

8.4 Correcting the Z Fits

We want to use the model to generate values for U_1 and U_2 as a function of P_T^{boson}. The above fit parameters $\vec{\Pi}_{\Sigma}^{data}$ and $\vec{\Pi}_{U}^{data}$, which determine the $\sum E_T$ shape and $\vec{U}$ model respectively, are not the correct parameters to use. For example, some of the parameters describe the mean of U_1 as a function of the measured P_T^{boson}, and not the actual P_T^{boson}. In a given region of measured Z P_T, there will be events whose true Z P_T was higher than the measured Z P_T and also events whose true Z P_T was lower.

Where the Z P_T is a falling distribution, we will have more events from lower true Z P_T. In that region $< U_1 >$ will be systematically less negative. Where the Z P_T is a rising distribution, we will get the opposite effect.

The direction of the Z P_T also has a measurement error, and this will cause the measured U_1 and U_2 to be rotated into each other. Since U_2 has zero mean, this will cause $< U_1 >$ to be less negative. Other effects include the N_{tracks} cut sculpting the $\sum E_T$ and $\vec{U}$ distributions; and to lesser extents, the bremsstrahlung photons potentially being included in $\vec{U}$, and the removal of the electron towers potentially biasing $\vec{U}$. These last two are not expected to be significant since the two electrons in Z events are largely back to back in azimuth. The additional or removed energy associated with one electron should cancel with the other on average since they are back to back.

The simulation includes the measurement error on the Z P_T, as well as the other effects mentioned above, and we can use the simulation to correct for any biases in the fits. In the next sections we discuss how we correct both sets of parameters $\vec{\Pi}_{\Sigma}^{data}$ and $\vec{\Pi}_{U}^{data}$.

8.4.1 Correction to $\sum E_T$ Fits

In this Section we correct the $\sum E_T$ fits of Section 8.1. The $\sum E_T$ fits define the parameters of the , -distribution which we use to generate $\sum E_T$ in the Monte Carlo. The three parameters of the fits are defined in Equation 8.4, and we label them as $\vec{\Pi}_{\Sigma}$.

We want to find parameters $\vec{\Pi}_{\Sigma}^{in}$ which we can use as the input to the Monte Carlo, and which are such that the Monte Carlo output looks like the data. To see how close the output is to the data, we fit the output as if it were real data. This gives us a set

of fit parameters which we label $\vec{\Pi}_{\Sigma}^{out}$. The Monte Carlo input parameters are correct when $\vec{\Pi}_{\Sigma}^{out}$ is close to the original fits, $\vec{\Pi}_{\Sigma}^{data}$.

We define the variable $\vec{\delta} \equiv \vec{\Pi}_{\Sigma}^{data} - \vec{\Pi}_{\Sigma}^{out}$. The output of the Monte Carlo looks like the data when $\vec{\delta}$ is small. To measure the size of $\vec{\delta}$, we form the quantity

$$\Delta \equiv \vec{\delta} \cdot \tilde{C}_{\Sigma}^{-1} \cdot \vec{\delta} \tag{8.18}$$

where $\tilde{C}_{\Sigma}$ is the covariance matrix from the original fit to the data and is printed in Equation 8.5. The quantity Δ is a measure of how large $\vec{\delta}$ is relative to the statistical uncertainty on the original fit. When Δ is small, the difference between $\vec{\Pi}_{\Sigma}^{out}$ and $\vec{\Pi}_{\Sigma}^{data}$ is small compared to the statistical uncertainty on $\vec{\Pi}_{\Sigma}^{data}$.

In the $\sum E_T$ fits of Section 8.1, we did an unbinned likelihood fit using the two variables $\sum E_T$ and Z P_T. We run the $Z \rightarrow ee$ Monte Carlo with a first guess at $\vec{\Pi}_{\Sigma}^{in}$, and we write out the two variables $\sum E_T$ and Z P_T, where the Z P_T is formed from the simulated values of the two decay electrons. The output of the Monte Carlo has all the $Z \rightarrow ee$ cuts applied. We fit the Monte Carlo output using the same method as Section 8.1.

The only difference between this fit and the original fit of Section 8.1 is that instead of minimizing Equation 8.3, we minimize a weighted unbinned likelihood function

$$L = -2 \times \sum w_i \log \gamma(\sum E_T) \tag{8.19}$$

where the sum is over all the Monte Carlo data, w_i is the event weight, and γ is the , -distribution of Equation 8.1. The weighted likelihood function is necessary since the Monte Carlo produces weighted events. The output of the fitting procedure is the set of parameters $\vec{\Pi}_{\Sigma}^{out}$.

We calculate the quantities $\vec{\delta}$ and Δ described above. If Δ is greater than 0.0001, then we iterate $\vec{\Pi}_{\Sigma}^{in}$ as

$$\vec{\Pi}_{\Sigma}^{in} \rightarrow \vec{\Pi}_{\Sigma}^{in} + \vec{\delta} \tag{8.20}$$

We then repeat the fitting procedure, using the new $\vec{\Pi}_{\Sigma}^{in}$ in the Monte Carlo. When we iterate the procedure, we do not regenerate the Monte Carlo. Instead, we adjust the event weights. For every Monte Carlo event, we use the generated value of $\sum E_T$, and we re-weight the event according to the $\sum E_T$ parameters $\vec{\Pi}_{\Sigma}^{in}$ and the , -distribution of Equation 8.1.

If $\Delta < 0.0001$, then $\vec{\Pi}_{\Sigma}^{in}$ are the final, corrected fit parameters. We will refer to these parameters as $\vec{\Pi}_{\Sigma}$.

The final value of $\Delta < .0001$ is very small, but in general the procedure converges after only a few iterations, and so there is no reason to allow a larger final value. We use the same $\approx 970,000$ Monte Carlo events as in Chapter 7, and the final results are

$$\vec{\Pi}_{\Sigma} = \begin{pmatrix} 2.76 \\ 0.0459 \\ 0.0462 \end{pmatrix} \tag{8.21}$$

These values are close to the original, uncorrected values of Equation 8.4. If we evaluate Δ of Equation 8.18, using $\delta = \vec{\Pi}_{\Sigma} - \vec{\Pi}_{\Sigma}^{data}$, we get $\Delta = 0.49$. This is a small change for a 3-parameter fit, and it indicates that the corrections are small relative to the statistical uncertainty on the parameters.

8.4.2 Correction to $\vec{U}$ Fits

We correct $\vec{\Pi}_U$ using the same procedure that was used in the previous section to correct $\vec{\Pi}_\Sigma$. The seven parameters of $\vec{\Pi}_U$ are used to generate $\vec{U}$ in the Monte Carlo. The $\vec{U}$ model is described above in Section 8.3.1.

We want to find parameters $\vec{\Pi}_U^{in}$ which we can use as the input to the Monte Carlo, and which are such that the Monte Carlo output looks like the data. To see how close the output is to the data, we fit the output as if it were real data. This gives us a set of fit parameters which we label $\vec{\Pi}_U^{out}$. The Monte Carlo input parameters are correct when $\vec{\Pi}_U^{out}$ is close to the original fits, $\vec{\Pi}_U^{data}$. The original fits are listed in Equation 8.17.

In the $\vec{U}$ fits of Section 8.3.2, we determined a set of seven $\vec{U}$ model parameters, $\vec{\Pi}_U^{data}$. We fit the data using the unbinned likelihood function of Equation 8.16. The function depends on the data quantities U_1, U_2, Z P_T, and $\sum E_T$. We run the $Z \rightarrow ee$ Monte Carlo with a first guess at $\vec{\Pi}_U^{in}$, which determine the Monte Carlo generated values for U_1 and U_2. We form the simulated values for U_1 and U_2, as well as Z P_T and $\sum E_T$. The simulated values of U_1 and U_2 include a rotation of U_1 into U_2 caused by measurement error on the direction of the Z boson. The simulated values also include corrections for the removal of the towers around the electron cluster and allow a contribution from bremsstrahlung photons that do not land in the electron cluster. We write out the simulated quantities, where the output of the Monte Carlo has all the $Z \rightarrow ee$ cuts applied. We fit the output of the Monte Carlo using the same procedure as was used to fit the data in Section 8.3.2.

The only difference between this fit and the original fit of Section 8.3.2 is that instead of minimizing Equation 8.16, we minimize a weighted unbinned likelihood

function

$$L = -2 \times \sum w_i \log P_i(U_1, U_2, Z P_T, \sum E_T) \tag{8.22}$$

where the sum is over all the Monte Carlo data, w_i is the event weight, and P_i is the Gaussian probability of Equation 8.15. The weighted likelihood function is necessary since the Monte Carlo produces weighted events. The output of the fitting procedure is the set of parameters $\vec{\Pi}_U^{out}$.

To determine how close the output parameters, $\vec{\Pi}_U^{out}$, are to the original data fit parameters, $\vec{\Pi}_U^{data}$, we define the variable $\vec{\delta} \equiv \vec{\Pi}_U^{out} - \vec{\Pi}_U^{data}$. We calculate the quantity $\Delta \equiv \vec{\delta} \cdot \tilde{C}_U^{-1} \cdot \vec{\delta}$, where $\tilde{C}_U$ is the covariance matrix associated with the original fits to the data. Δ is a measure of how close $\vec{\Pi}_U^{out}$ is to $\vec{\Pi}_U^{data}$ relative to the statistical uncertainty on $\vec{\Pi}_U^{data}$.

If Δ is greater than 0.0001, then we iterate $\vec{\Pi}_U^{in}$ as

$$\vec{\Pi}_U^{in} \rightarrow \vec{\Pi}_U^{in} + \vec{\delta} \tag{8.23}$$

We then repeat the fitting procedure, using the new $\vec{\Pi}_U^{in}$ in the Monte Carlo. When we iterate the procedure, we do not regenerate the Monte Carlo. Instead, we adjust the event weights. For every Monte Carlo event, we use the generated values for U_1, U_2, Z P_T, and $\sum E_T$, and we re-weight the event according to the Gaussian probability function $P_i(U_1, U_2, Z P_T, \sum E_T)$ of Equation 8.15.

If $\Delta < 0.0001$, then $\vec{\Pi}_U^{in}$ are the final, corrected fit parameters. We will refer to these parameters as $\vec{\Pi}_U$.

We use the same $\approx 970,000$ Monte Carlo events as in Chapter 7, and the final

results are

$$\vec{\Pi}_U = \begin{pmatrix} 3.07 \times 10^{-4} \\ 0.933 \times 10^{-4} \\ 1.20 \times 10^{-1} \\ -1.77 \times 10^{-1} \\ 2.97 \times 10^{-2} \\ -5.42 \times 10^{-3} \\ -6.62 \times 10^{-4} \end{pmatrix} \tag{8.24}$$

With $\vec{\delta} = \vec{\Pi}_U - \vec{\Pi}_U^{data}$, we calculate $\Delta = 22.3$. This is a large number for a 7−parameter fit, and this indicates that the corrections are significantly larger than the statistical uncertainty on the fits. The largest effect of the corrections is to make $\mu(ZP_T)$ less negative, where $\mu(ZP_T)$ is the mean of U_1 as a function of Z P_T. As discussed above, the electron resolution and the falling Z P_T spectrum have the effect of making this quantity less negative. The dashed curve of Figure 8.3 shows μ vs P_T^{boson} for the corrected parameters. The uncorrected fit from the data is less negative, as expected.

8.5 Summary

We have presented a model for the calorimeter response to the low energy particles that recoil against the boson P_T, and also to those which arise from the underlying event. The model is necessary to simulate the variable $\vec{U}$ and therefore $\vec{\not{E}}_T$.

The model is empirical in the sense that its form is justified by the data and its parameters determined from the data. The $\sum E_T$ shape determines the resolutions according to a form fit from minimum bias data, and we fit for $\vec{U}$ as a function of

P_T^{boson} using Z data. We have also discussed biases on the fits caused by resolution errors on the measured Z P_T, as well as other, smaller effects. We corrected for such a bias in Section 8.4, and the final fit parameters, $\vec{\Pi}_\Sigma$ and $\vec{\Pi}_U$, which we will use for the model, are defined by Equations 8.21 and 8.24.

Chapter 9

Comparison of W Data and Monte Carlo

In this chapter, we compare various distributions of the $W \rightarrow e\nu$ data with the Monte Carlo.

There are 14 Monte Carlo input parameters. They were determined from the Z data in previous chapters. The calorimeter response model depends on the 3 parameters of $\vec{\Pi}_\Sigma$ which determine the $\sum E_T$ shape, and also on the 7 parameters of $\vec{\Pi}_U$, which determine the $\vec{U}$ shape. These parameters were fit to the Z data in Chapter 8. In addition, there are 4 parameters in $\vec{\Pi}_x$ which determine the P_T^{boson} shape, and these were fit to the Z data in Chapter 7.

The s_1 and s_2 parameters of $\vec{\Pi}_U$ allow the resolution on $\vec{U}$ to vary with Z P_T. These parameters are correlated to the $\sum E_T$ parameters, since the $\sum E_T$ shape in the Monte Carlo also determines the $\vec{U}$ resolutions. In Chapter 13 we perturb the input parameters to better fit the W data, but we only vary the $\vec{\Pi}_U$ and $\vec{\Pi}_x$ parameters, and we keep the $\sum E_T$ parameters fixed.

We combine the 11 input parameters of $\vec{\Pi}_U$ and $\vec{\Pi}_x$ into the variable $\vec{\omega}$, defining

$$\vec{\omega} \equiv (\vec{\Pi}_x, \vec{\Pi}_U) \tag{9.1}$$

We refer to the results from the Z fits as $\vec{\omega}_Z$.

In Chapter 13 we find a set of parameters that are consistent with the Z fits, but that better fit the W data. We refer to this set of parameters as $\vec{\omega}_W$. We include the $|\vec{U}|$, $U_{||}$, E_T and M_T distributions in the fit for $\vec{\omega}_W$. Thus, the Monte Carlo for these distributions should agree better with the data when we use the $\vec{\omega}_W$ input parameters, than when we use the $\vec{\omega}_Z$ parameters. In this chapter we compare the W data with the W Monte Carlo using both $\vec{\omega}_Z$ and $\vec{\omega}_W$.

In Section 9.1, we compare the $\vec{U}$ distributions; in Section 9.2, we compare the E_T, $\not{E}_T$, and M_T distributions; and in Section 9.3 we compare the $U_{||}$ distributions in bins of M_T and $|\vec{U}|$. We conclude in Section 9.4.

9.1 $\vec{U}$ Distributions

The top plots of Figures 9.1, 9.2, and 9.3 show the distributions of $|\vec{U}|$, $U_{||}$, and $|U_\perp|$, respectively, of data and Monte Carlo. For each plot, two Monte Carlo distributions are shown: one with the input parameters $\vec{\omega}_Z$ and one with $\vec{\omega}_W$. For all the Monte Carlo plots the W mass is fixed at 80.443 GeV, and the W width is fixed at the Standard Model prediction. The $\vec{U}$ distributions are not sensitive to variations in the W mass or width.

The Monte Carlo includes the background distributions which were presented in Chapter 4. The $\tau \to e\nu\nu$ background is included as a subset of the Monte Carlo events. For the QCD, the lost Z, and the $\tau \to$ hadrons backgrounds, we make

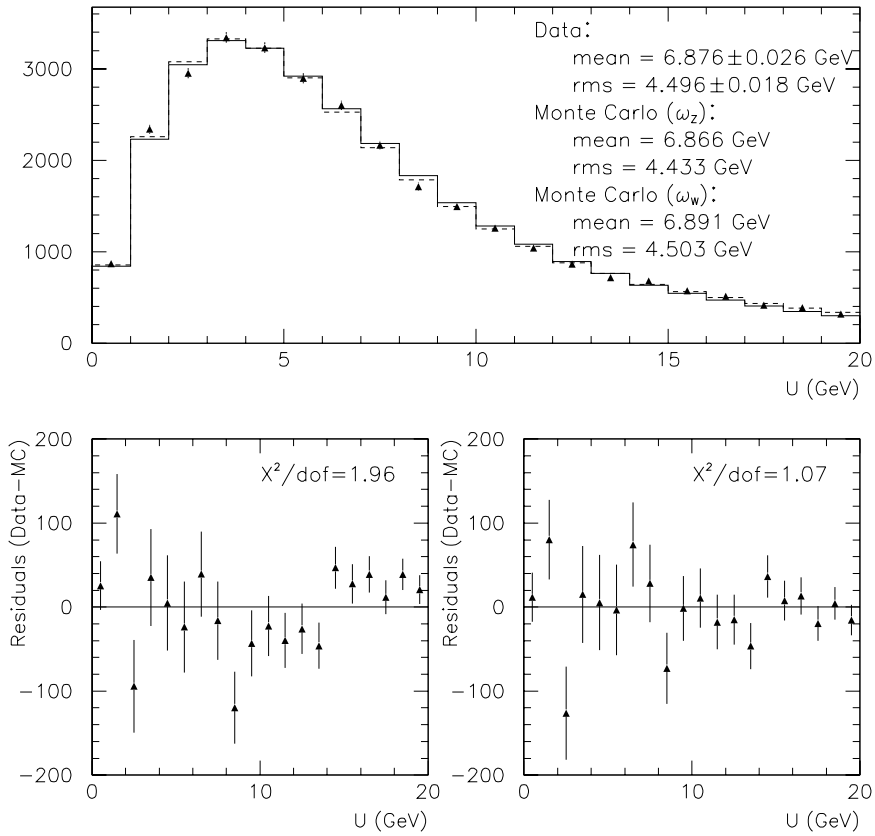

Figure 9.1: Top: $|\vec{U}|$ for $W \to e\nu$ data (triangles) and Monte Carlo (histograms). The solid histogram is for the case of using input parameters $\vec{\omega}_Z$, and the dashed is for $\vec{\omega}_W$. Bottom: difference between data and Monte Carlo distributions of the top plot. The bottom left plot is for the $\vec{\omega}_Z$ Monte Carlo, and the bottom right plot is for $\vec{\omega}_W$. The Monte Carlo is normalized to the data. The mean and rms for the data and Monte Carlo are shown on the top plot. The errors on the mean and rms for the data are taken to be rms$/\sqrt{N}$ and rms$/\sqrt{2N}$ respectively. The values shown for χ^2/dof are the sum of the squares of the residuals over their uncertainties, divided by the number of bins in the plot. The input parameters $\vec{\omega}_Z$ and $\vec{\omega}_W$ are discussed in the text.

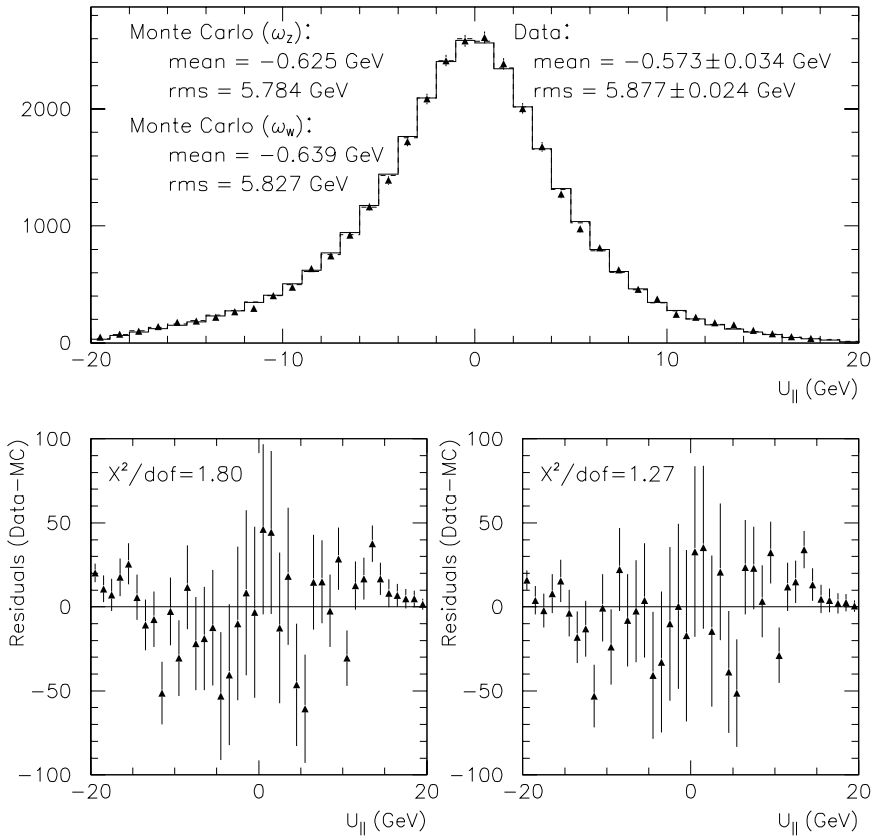

Figure 9.2: Top: $U_{||}$ for $W \rightarrow e\nu$ data (triangles) and Monte Carlo (histograms). Both a solid and dashed histogram are plotted although they are not easily distinguished. The solid histogram is for the case of using input parameters $\vec{\omega}_Z$, and the dashed is for $\vec{\omega}_W$. Bottom: difference between data and Monte Carlo distributions of the top plot. The bottom left plot is for the $\vec{\omega}_Z$ Monte Carlo, and the bottom right plot is for $\vec{\omega}_W$. The Monte Carlo is normalized to the data. The mean and rms for the data and Monte Carlo are shown on the top plot. The errors on the mean and rms for the data are taken to be rms/$\sqrt{N}$ and rms/$\sqrt{2N}$ respectively. The values shown for χ^2/dof are the sum of the squares of the residuals over their uncertainties, divided by the number of bins in the plot. The input parameters $\vec{\omega}_Z$ and $\vec{\omega}_W$ are discussed in the text.

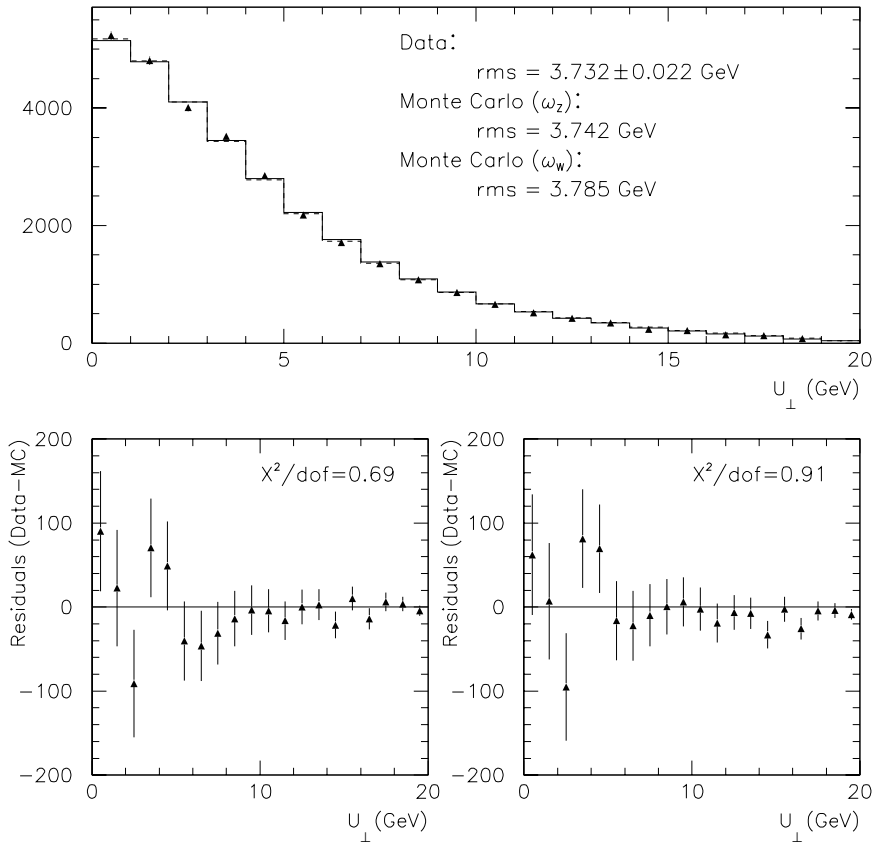

Figure 9.3: Top: $|U_\perp|$ for $W \to e\nu$ data (triangles) and Monte Carlo (histograms). The solid histogram is for the case of using input parameters $\vec{\omega}_Z$, and the dashed is for $\vec{\omega}_W$. The two histograms are not easily distinguished. Bottom: difference between data and Monte Carlo distributions of the top plot. The bottom left plot is for the $\vec{\omega}_Z$ Monte Carlo, and the bottom right plot is for $\vec{\omega}_W$. The Monte Carlo is normalized to the data. The rms of the data and Monte Carlo are shown on the top plot. The errors on the rms for the data are taken to be rms$/\sqrt{N}$. The values shown for χ^2/dof are the sum of the squares of the residuals over their uncertainties, divided by the number of bins in the plot. The input parameters $\vec{\omega}_Z$ and $\vec{\omega}_W$ are discussed in the text.

histograms of the $U_\perp$, $U_{||}$, $|\vec{U}|$, and E_T distributions. These histograms are added to the Monte Carlo histograms according to the fractions determined in Chapter 4. For the $U_{||}$ histogram, adding the background histograms makes the mean of $U_{||}$ lower by ≈ 15 MeV.

The bottom plots of Figures 9.1, 9.2, and 9.3 show the differences between the data and Monte Carlo, after normalizing the Monte Carlo to the data. The residuals for both the $\vec{\omega}_Z$ and $\vec{\omega}_W$ cases are shown.

When we run the Monte Carlo with the input parameters that were from the Z data, $\vec{\omega}_Z$, we produce distributions for $|\vec{U}|$ and $U_{||}$ which do not agree perfectly with the data. The value for χ^2/dof are 1.96 and 1.80 respectively, where the number of degrees of freedom is taken to be the number of bins in the plots. For the $|\vec{U}|$ shape, the data show a small excess in the tails, which is consistent with the data having a higher value for the rms than the Monte Carlo. Similarly, for the $U_{||}$ shape, the data has an excess in the positive and negative tails of $U_{||}$. This is also consistent with the data having a significantly larger rms.

The input parameters $\vec{\omega}_W$ produce better agreement between the data and Monte Carlo. For this case, the values for χ^2/dof for $|\vec{U}|$ and $U_{||}$ are 1.07 and 1.27, respectively. The tails for both shapes are better modelled, and the rms of the Monte Carlo agrees better with the data. Nevertheless, for $U_{||}$ shape, the rms of the Monte Carlo is still significantly lower than the data, and the mean is significantly too negative. However, the mean and rms are sensitive to the fluctuations in the tails. For example, the residuals show an excess in the data between $U_{||} = 12$ and 15 GeV. If the Monte Carlo reproduced this bump, then the Monte Carlo mean would be less negative by 30 MeV, and the rms would be larger by 30 MeV.

The $U_\perp$ distributions for the data and Monte Carlo are both symmetric around

zero. This is expected since $U_\perp$ is $\vec{U}$ projected along an axis perpendicular to the electron. Along that axis, neither the positive nor the negative direction is preferred. We fold the distributions around zero, making plots of the absolute value of $U_\perp$. For this variable, the Monte Carlo agrees well with the data for the $\vec{\omega}_Z$ and $\vec{\omega}_W$ case. The rms of the Monte Carlo for the $\vec{\omega}_W$ case is significantly higher than the rms of the data. The rms is sensitive to the tails of the distribution, and the high rms is consistent with fluctuations in the tails, which are visible in the residuals.

9.2 E_T, $\not{E}_T$, and M_T

The E_T, $\not{E}_T$, and M_T distributions are sensitive to the W mass and the energy scale. For these distributions we have applied the non-linearity corrections of Section 12, as well as the final scale factor. The E_T, $\not{E}_T$, and M_T distributions are shown in Figures 9.4, 9.5, and 9.6. The Monte Carlo is run with both sets of input parameters, $\vec{\omega}_Z$ and $\vec{\omega}_W$; and the Monte Carlo is run exactly as in the previous section, including all backgrounds.

The E_T shape of the data agrees well with the Monte Carlo. The variable E_T has a first order dependence on the W P_T. The goodness of the fits indicates that our boson P_T model works well. The data and Monte Carlo agree well for the input parameters which were fit to the Z data, $\vec{\omega}_Z$, as well as the input parameters which include constraints from the W data, $\vec{\omega}_W$.

The $\not{E}_T$ shape of the data also agrees with the Monte Carlo. This distribution is sensitive to modelling of $\vec{U}$ as a function of the boson P_T. A comparison of the data to the Monte Carlo gives values for χ^2/dof of 1.91 and 1.56 for the $\vec{\omega}_Z$ and $\vec{\omega}_W$ cases respectively. The bulk of the data distribution is reproduced well by the Monte Carlo,

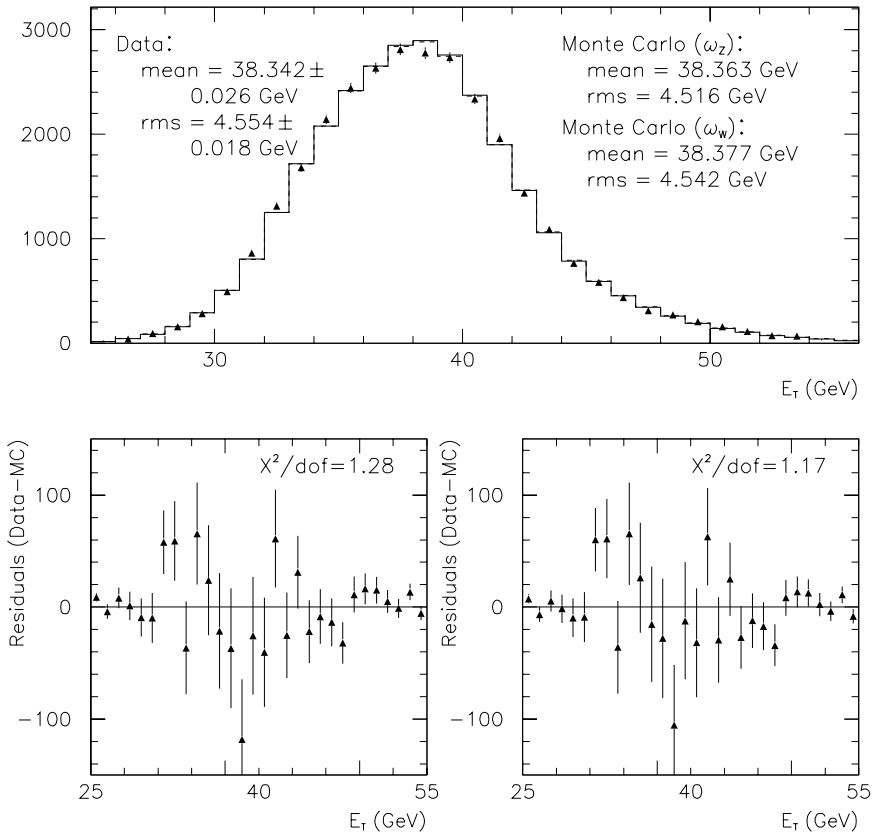

Figure 9.4: Top: E_T for $W \to e\nu$ data (triangles) and Monte Carlo (histograms). The solid histogram is for the case of using input parameters $\vec{\omega}_Z$, and the dashed is for $\vec{\omega}_W$. Bottom: difference between data and Monte Carlo distributions of the top plot. The bottom left plot is for the $\vec{\omega}_Z$ Monte Carlo, and the bottom right plot is for $\vec{\omega}_W$. The Monte Carlo is normalized to the data. The mean and rms for the data and Monte Carlo are shown on the top plot. The errors on the mean and rms for the data are taken to be rms/$\sqrt{N}$ and rms/$\sqrt{2N}$ respectively. The values shown for χ^2/dof are the sum of the squares of the residuals over their uncertainties, divided by the number of bins in the plot. The input parameters $\vec{\omega}_Z$ and $\vec{\omega}_W$ are discussed in the text.

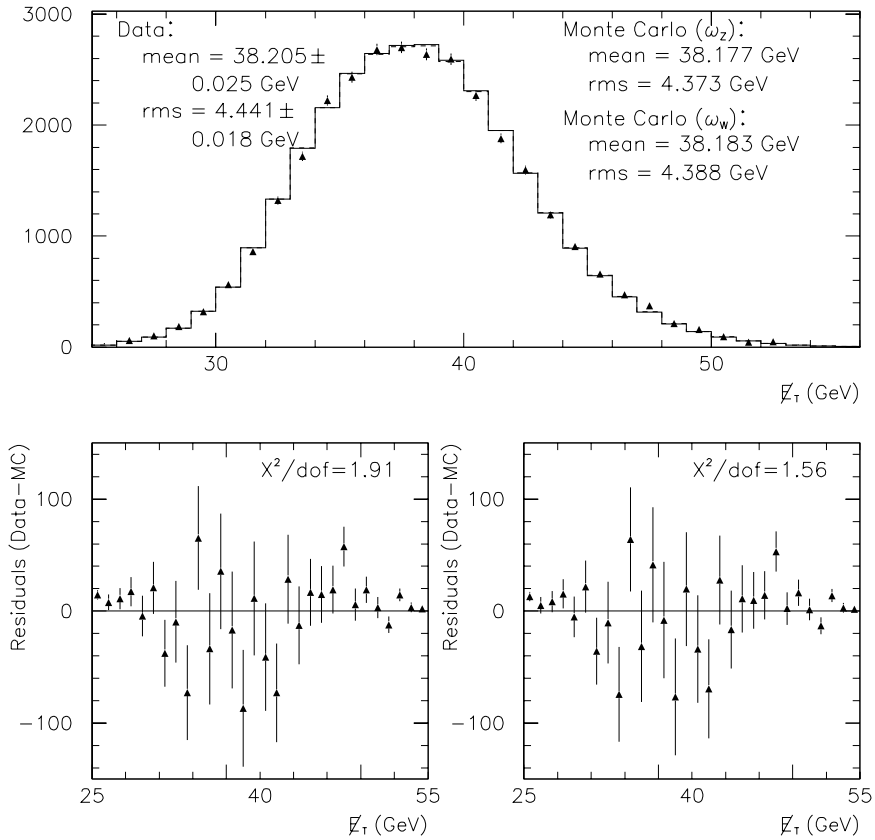

Figure 9.5: Top: $\not{E}_T$ for $W \to e\nu$ data (triangles) and Monte Carlo (histograms). The solid histogram is for the case of using input parameters $\vec{\omega}_Z$, and the dashed is for $\vec{\omega}_W$. Bottom: difference between data and Monte Carlo distributions of the top plot. The bottom left plot is for the $\vec{\omega}_Z$ Monte Carlo, and the bottom right plot is for $\vec{\omega}_W$. The Monte Carlo is normalized to the data. The mean and rms for the data and Monte Carlo are shown on the top plot. The errors on the mean and rms for the data are taken to be rms/$\sqrt{N}$ and rms/$\sqrt{2N}$ respectively. The values shown for χ^2/dof are the sum of the squares of the residuals over their uncertainties, divided by the number of bins in the plot. The input parameters $\vec{\omega}_Z$ and $\vec{\omega}_W$ are discussed in the text.

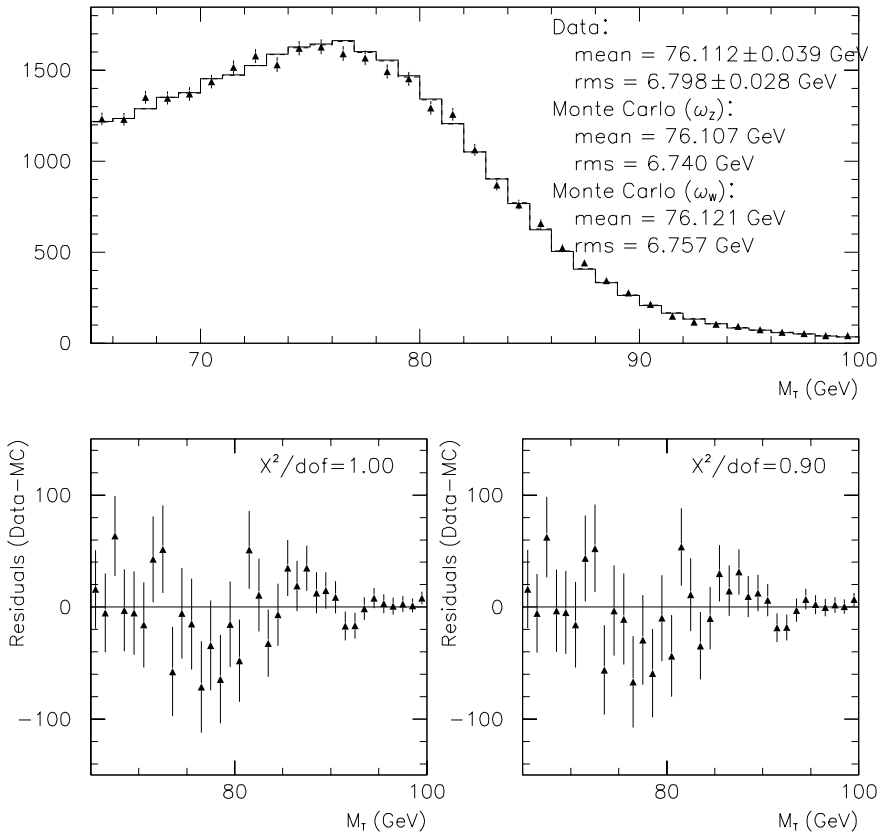

Figure 9.6: Top: M_T for $W \to e\nu$ data (triangles) and Monte Carlo (histograms). The solid histogram is for the case of using input parameters $\vec{\omega}_Z$, and the dashed is for $\vec{\omega}_W$. Bottom: difference between data and Monte Carlo distributions of the top plot. The bottom left plot is for the $\vec{\omega}_Z$ Monte Carlo, and the bottom right plot is for $\vec{\omega}_W$. The Monte Carlo is normalized to the data. The mean and rms for the data and Monte Carlo are shown on the top plot. The errors on the mean and rms for the data are taken to be rms/$\sqrt{N}$ and rms/$\sqrt{2N}$ respectively. The values shown for χ^2/dof are the sum of the squares of the residuals over their uncertainties, divided by the number of bins in the plot. The input parameters $\vec{\omega}_Z$ and $\vec{\omega}_W$ are discussed in the text.

but the tails show a few points which have large deviations relative to the statistical uncertainty on the points. For example, the first point in the distribution, at 25 GeV, shows a large disagreement between data and Monte Carlo relative to the statistical uncertainty on the data. If we drop this point in the calculation of χ^2/dof, we get values of $\chi^2/dof = 1.54$ and 1.32 for the $\vec{\omega}_Z$ and $\vec{\omega}_W$ cases, respectively.

For the transverse mass shape, the data agree reasonably well with the Monte Carlo. This distribution is sensitive to the W mass, as well as our model for the $\vec{U}$ response. There is also some dependence on the boson P_T distribution, as discussed in Chapter 1. The residuals show some structure, although this may be from random fluctuations. The M_T distribution is further discussed in Chapter 13.

9.3 $U_{||}$ as a Function of M_T, $|\vec{U}|$, and E_T

Figures 9.7, 9.8, and 9.9, show the $U_{||}$ distribution in bins of M_T. The Monte Carlo is shown only with the input parameters $\vec{\omega}_W$. All backgrounds are included in the Monte Carlo distributions.

As discussed in Chapter 1, the variable M_T partially corrects the electron E_T for the effect of the boson transverse momentum. If $\vec{U}$ were a perfect measurement of the boson P_T, then the M_T distribution would be twice the electron E_T distribution in the boson rest frame. Since the rest frame E_T is independent of the boson P_T, we would expect the $U_{||}$ distributions to look roughly the same for all bins in M_T. However, $\vec{U}$ is not a perfect measure of the boson P_T, and we expect some variation in the shape of $U_{||}$ when we bin the data in M_T.

Figures 9.7, 9.8, and 9.9, show $U_{||}$ distributions for $65 < M_T < 70$, $70 < M_T < 75$, $75 < M_T < 80$, $80 < M_T < 85$, $85 < M_T < 90$, and $90 < M_T < 100$ GeV. The data

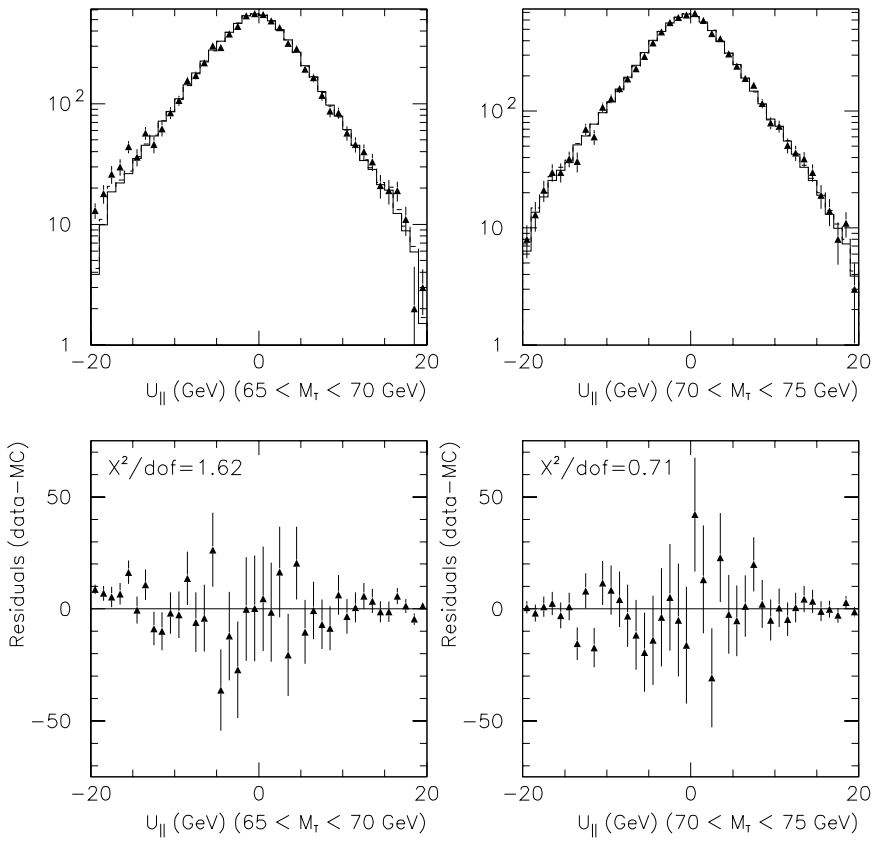

Figure 9.7: Top: $U_{||}$ in bins of M_T for data (triangles) and Monte Carlo (histograms). The top left distribution is for $65 < M_T < 70$ GeV, and the top right distribution is for $70 < M_T < 75$ GeV. Bottom: difference between data and Monte Carlo distributions for the top plots. The bottom left is for $65 < M_T < 70$ GeV, and the bottom right is for $70 < M_T < 75$ GeV. The Monte Carlo is normalized to the data. The values shown for χ^2/dof are the sum of the squares of the residuals over their uncertainties, divided by the number of bins in the plot. The Monte Carlo is run with input parameters $\vec{\omega}_W$, which are discussed in the text.

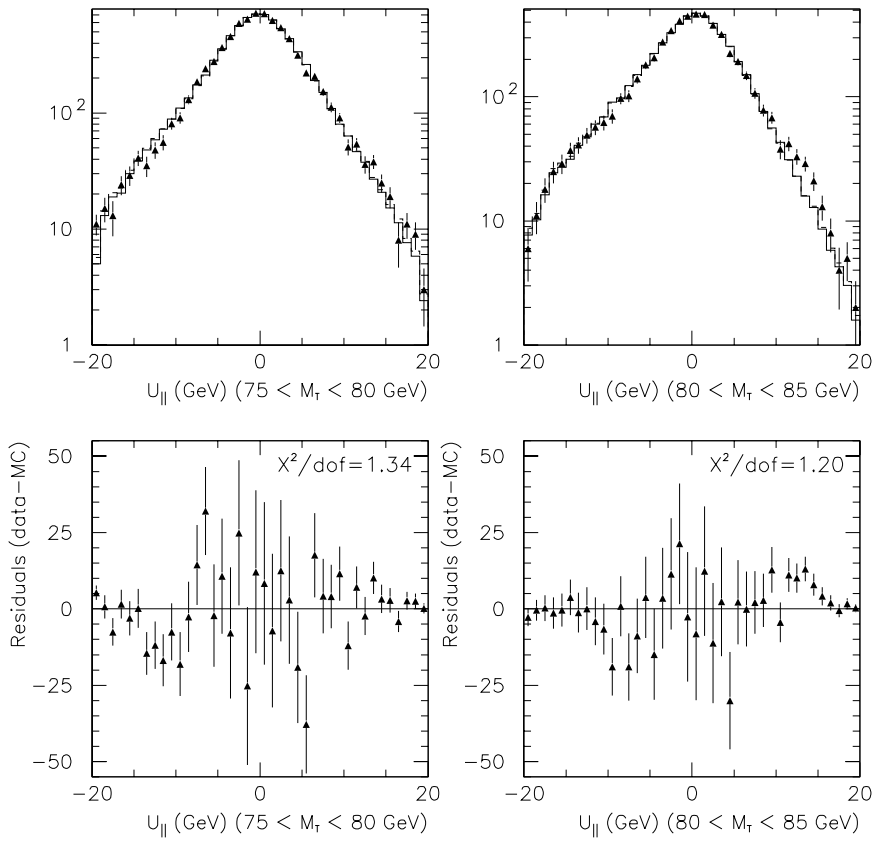

Figure 9.8: Top: $U_{||}$ in bins of M_T for data (triangles) and Monte Carlo (histograms). The top left distribution is for $75 < M_T < 80$ GeV, and the top right distribution is for $80 < M_T < 85$ GeV. Bottom: difference between data and Monte Carlo distributions for the top plots. The bottom left is for $75 < M_T < 80$ GeV, and the bottom right is for $80 < M_T < 85$ GeV. The Monte Carlo is normalized to the data. The values shown for χ^2/dof are the sum of the squares of the residuals over their uncertainties, divided by the number of bins in the plot. The Monte Carlo is run with input parameters $\vec{\omega}_W$, which are discussed in the text.

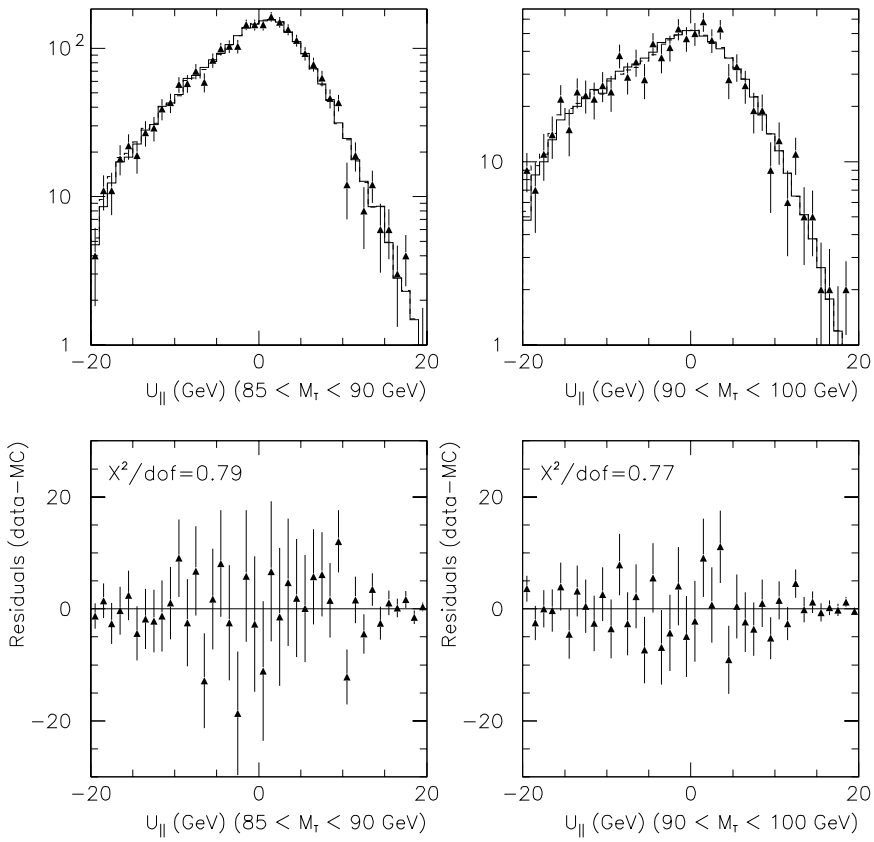

Figure 9.9: Top: $U_{||}$ in bins of M_T for data (triangles) and Monte Carlo (histograms). The top left distribution is for $85 < M_T < 90$ GeV, and the top right distribution is for $90 < M_T < 100$ GeV. Bottom: difference between data and Monte Carlo distributions for the top plots. The bottom left is for $85 < M_T < 90$ GeV, and the bottom right is for $90 < M_T < 100$ GeV. The Monte Carlo is normalized to the data. The values shown for χ^2/dof are the sum of the squares of the residuals over their uncertainties, divided by the number of bins in the plot. The Monte Carlo is run with input parameters $\vec{\omega}_W$, which are discussed in the text.

distributions show good agreement with the Monte Carlo for all the plots. The worst agreement is for $80 < M_T < 85$ GeV, which is shown in Figure 9.8. A small bump is visible in the data around $U_{||} = 12$ GeV which is not reproduced by the Monte Carlo.

The mean of $U_{||}$ as a function of M_T is shown in Figure 9.10. For this plot, the Monte Carlo follows the data, although the residuals show a possible slope with M_T. In Figure 9.10, we average $U_{||}$ between ± 20 GeV. The average is sensitive to the tails of the distribution. If we calculate the average of $U_{||}$ between ± 10 GeV, the Monte Carlo and data agree better. Figure 9.11 shows the mean of $U_{||}$ as a function of M_T where the mean is calculated between ± 10 GeV.

Figures 9.12 and 9.13 show the $U_{||}$ distribution in bins of $|\vec{U}|$. The plots show $U_{||}$ for $0 < |\vec{U}| < 5$, $5 < |\vec{U}| < 10$, $10 < |\vec{U}| < 15$, and $15 < |\vec{U}| < 20$ GeV.

The $U_{||}$ plots for $5 < |\vec{U}| < 10$, $10 < |\vec{U}| < 15$, and $15 < |\vec{U}| < 20$ GeV show a double peak structure. This structure is the result of the approximate azimuthal symmetry of the $\vec{U}$ distribution. We can write the vector $\vec{U}$ in cylindrical coordinates as $(|\vec{U}|, \Delta\phi)$, where $\Delta\phi$ is the angle between $\vec{U}$ and the electron $\vec{E}_T$. The "x"− and "y"−axes are then $U_{||} = |\vec{U}| \cos \Delta\phi$ and $U_{\perp} = |\vec{U}| \sin \Delta\phi$. Figures 9.12 and 9.13 are thus projections onto the x−axis, for different regions of the radial variable $|\vec{U}|$. A double peak structure is expected for any such projection where the azimuthal variable has an approximately flat distribution.

In Figures 9.12 and 9.13, the peaks at negative $U_{||}$ are larger than the peaks at positive $U_{||}$. This is the result of the E_T and M_T cut biases, which prefer larger values for E_T. Events with larger values for E_T tend to have been boosted by the W P_T and have more negative values for $U_{||}$. The bias on the data is reproduced in each plot by the Monte Carlo.

The mean of $U_{||}$ as a function of E_T is shown in Figure 9.14. The effect of the W

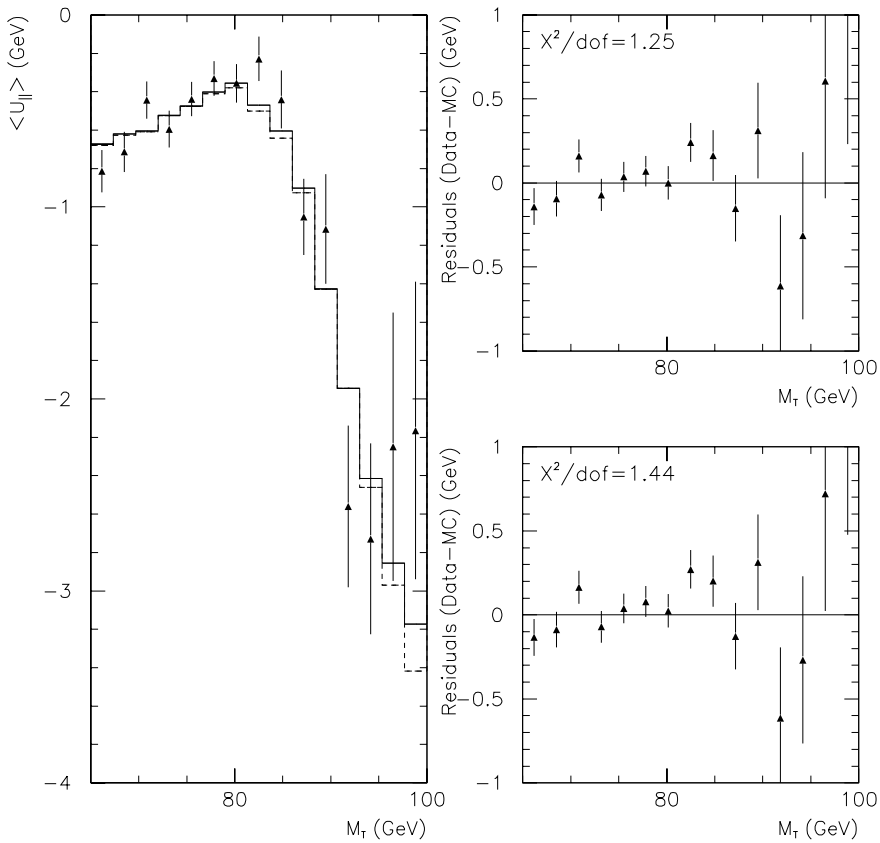

Figure 9.10: Left: Mean of $U_{||}$ in bins of M_T for data (triangles) and Monte Carlo (histograms). The mean of $U_{||}$ is calculated between ± 20 GeV. The solid histogram is for the case of using input parameters $\vec{\omega}_Z$, and the dashed is for $\vec{\omega}_W$. Right: the differences between the data and Monte Carlo of the left plot. The top right plot is for the Monte Carlo run with input parameters $\vec{\omega}_Z$, and the bottom right is for $\vec{\omega}_W$. The uncertainties on the means are rms/$\sqrt{N}$. The values shown for χ^2/dof are the sum of the squares of the residuals over their uncertainties, divided by the number of bins in the plot. The input parameters $\vec{\omega}_Z$ and $\vec{\omega}_W$ are discussed in the text.

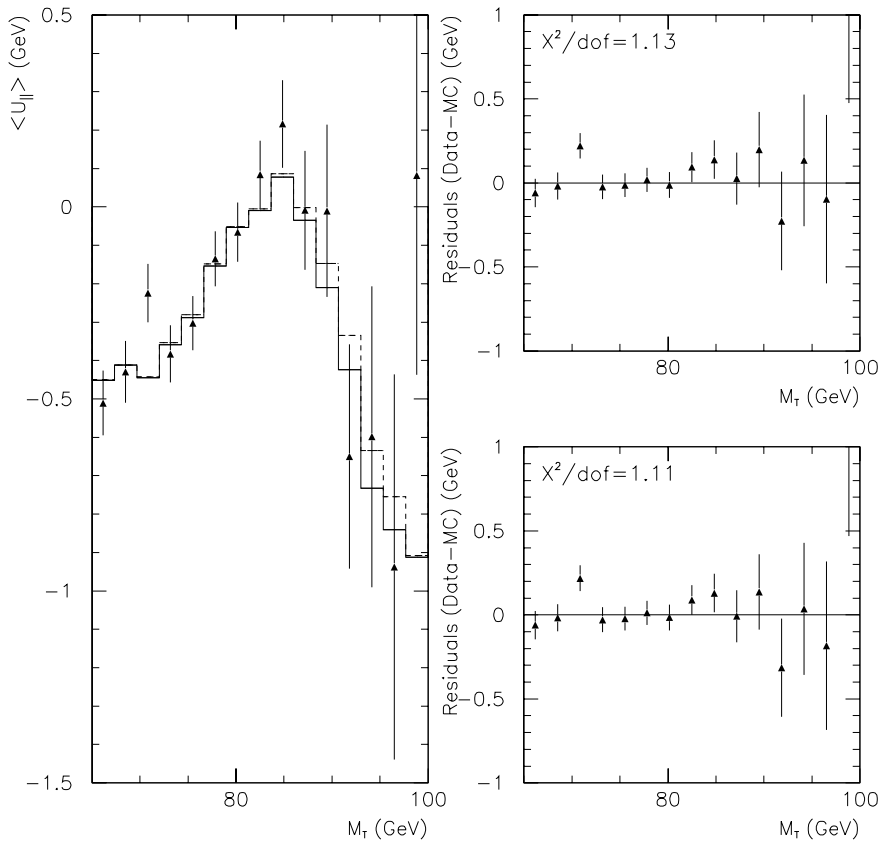

Figure 9.11: Left: Mean of $U_{||}$ in bins of M_T for data (triangles) and Monte Carlo (histograms). The mean of $U_{||}$ is calculated between ± 10 GeV. The solid histogram is for the case of using input parameters $\vec{\omega}_Z$, and the dashed is for $\vec{\omega}_W$. Right: the differences between the data and Monte Carlo of the left plot. The top right plot is for the Monte Carlo run with input parameters $\vec{\omega}_Z$, and the bottom right is for $\vec{\omega}_W$. The uncertainties on the means are rms$/\sqrt{N}$. The values shown for χ^2/dof are the sum of the squares of the residuals over their uncertainties, divided by the number of bins in the plot. The input parameters $\vec{\omega}_Z$ and $\vec{\omega}_W$ are discussed in the text.

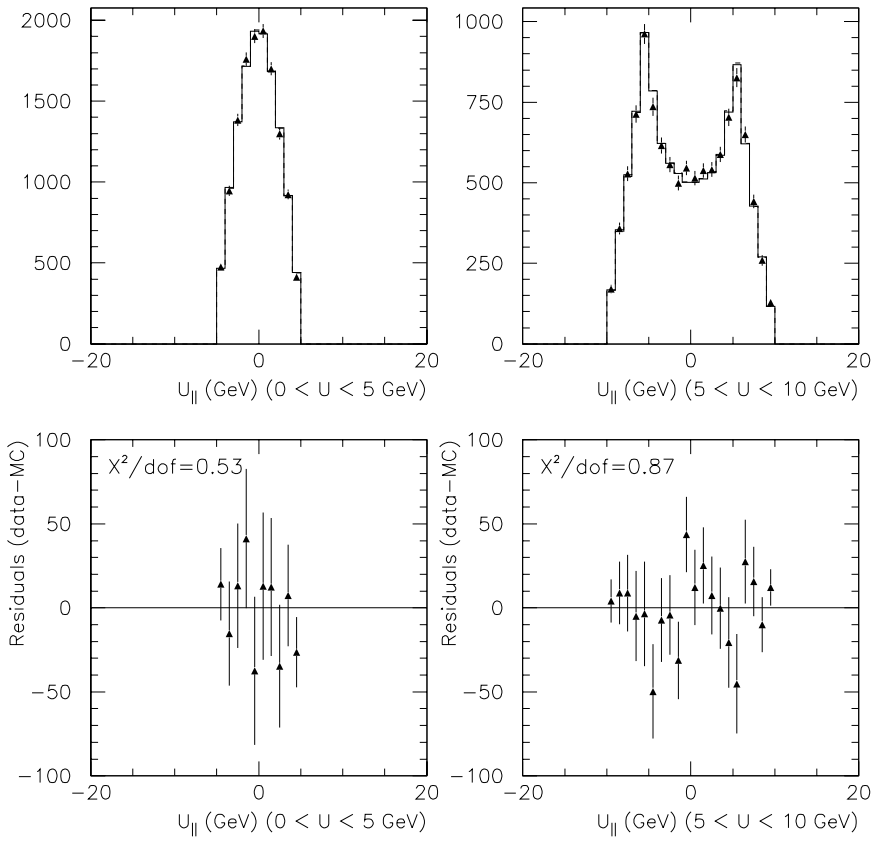

Figure 9.12: Top: $U_{||}$ in bins of $|\vec{U}|$ for data (triangles) and Monte Carlo (histograms). The top left distribution is for $0 < |\vec{U}| < 5$ GeV, and the top right distribution is for $5 < |\vec{U}| < 10$ GeV. Bottom: difference between data and Monte Carlo distributions for the top plots. The bottom left is for $0 < |\vec{U}| < 5$ GeV, and the bottom right is for $5 < |\vec{U}| < 10$ GeV. The Monte Carlo is normalized to the data. The values shown for χ^2/dof are the sum of the squares of the residuals over their uncertainties, divided by the number of bins in the plot. The Monte Carlo is run with input parameters $\vec{\omega}_W$, which are discussed in the text.

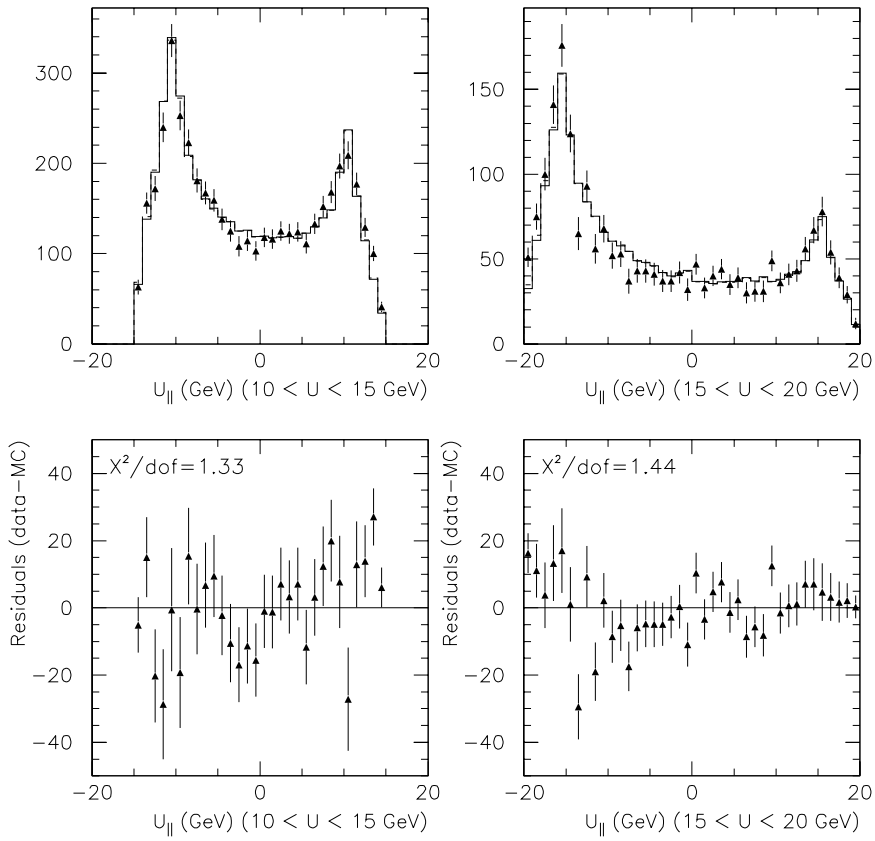

Figure 9.13: Top: $U_{||}$ in bins of $|\vec{U}|$ for data (triangles) and Monte Carlo (histograms). The top left distribution is for $10 < |\vec{U}| < 15$ GeV, and the top right distribution is for $15 < |\vec{U}| < 20$ GeV. Bottom: difference between data and Monte Carlo distributions for the top plots. The bottom left is for $10 < |\vec{U}| < 15$ GeV, and the bottom right is for $15 < |\vec{U}| < 20$ GeV. The Monte Carlo is normalized to the data. The values shown for χ^2/dof are the sum of the squares of the residuals over their uncertainties, divided by the number of bins in the plot. The Monte Carlo is run with input parameters $\vec{\omega}_W$, which are discussed in the text.

P_T on the electron E_T is visible in the plot. Events with negative $U_{||}$ tend to have the electron E_T increased by the W P_T, while the opposite is true for the positive $U_{||}$ events. There is roughly a 30 GeV variation in the mean of $U_{||}$ for E_T between 25 and 55 GeV. The Monte Carlo reproduces the data well for this distribution.

9.4 Conclusion

We have compared the W data and Monte Carlo, and we have seen good agreement between data and Monte Carlo. We have examined the Monte Carlo with the input parameters fit from the Z data, which we have called $\vec{\omega}_Z$, as well as with input parameters constrained with the W data, which we have called $\vec{\omega}_W$. The method we use to constrain the parameters with the W data is discussed in Chapter 13. In general, the $\vec{\omega}_W$ Monte Carlo agrees better with the data than the $\vec{\omega}_Z$ Monte Carlo. This is expected since the parameters $\vec{\omega}_Z$ were fit from the Z data, and the Z sample is significantly smaller than the W sample.

In Chapter 13 we fit for the W mass using different regions of $U_{||}$ and $|\vec{U}|$. This allows us to test the effect of differences in the $\vec{U}$ distributions between the data and the Monte Carlo.

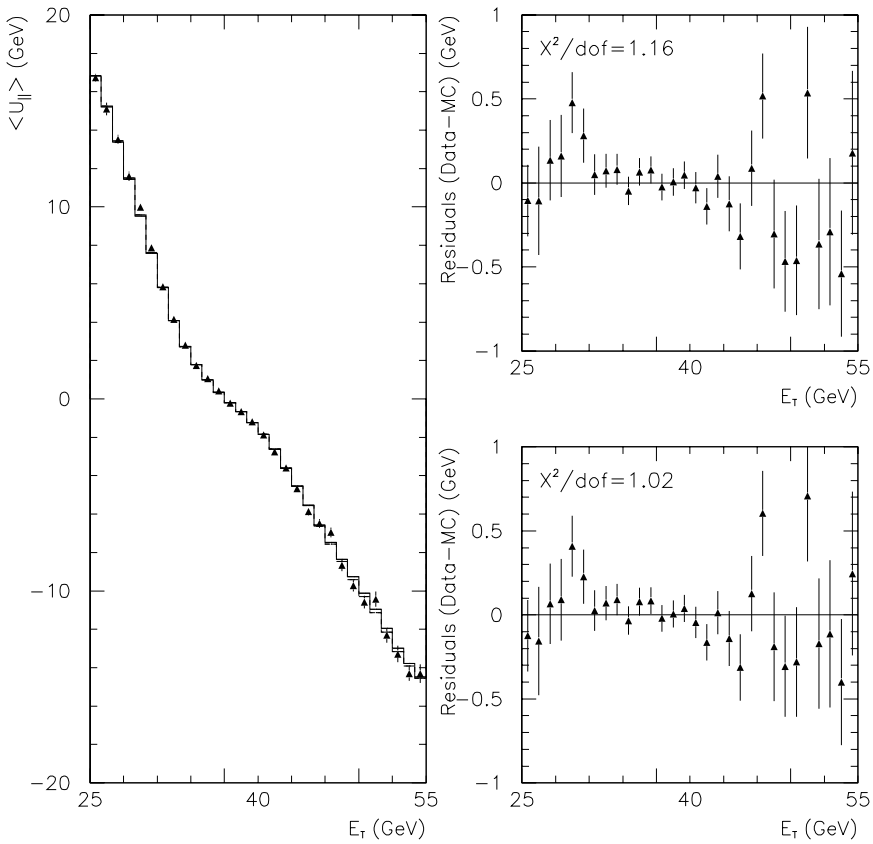

Figure 9.14: Left: Mean of $U_{||}$ in bins of E_T for data (triangles) and Monte Carlo (histograms). The mean of $U_{||}$ is calculated between ± 20 GeV. The solid histogram is for the case of using input parameters $\vec{\omega}_Z$, and the dashed is for $\vec{\omega}_W$. Right: the differences between the data and Monte Carlo of the left plot. The top right plot is for the Monte Carlo run with input parameters $\vec{\omega}_Z$, and the bottom right is for $\vec{\omega}_W$. The uncertainties on the means are rms$/\sqrt{N}$. The values shown for χ^2/dof are the sum of the squares of the residuals over their uncertainties, divided by the number of bins in the plot. The input parameters $\vec{\omega}_Z$ and $\vec{\omega}_W$ are discussed in the text.

Chapter 10

Energy Scale Determination with M_Z

We refer to the absolute calibration of the CEM as the energy scale determination. The scale is a factor which multiplies the energy measurement of the calorimeter, and we refer to the scale as S_E. In this chapter we determine S_E with the invariant mass of $Z \rightarrow ee$ events.

We run the Z Monte Carlo with the Z mass and width fixed at the world average values [5] of 91.187 and 2.490 GeV, respectively. We smear the simulated electron E_T measurement according to the E_T resolution of Equation 6.10. We allow the resolution constant term, κ, to vary. We also scale the Monte Carlo E_T. We compare M_Z of the data to the Monte Carlo and determine a best value for the Monte Carlo energy scale.

We try three fitting methods. In Section 10.1 we do a binned likelihood fit; in Section 10.2 we determine S_E using the mean of M_Z; and in Section 10.3 we compare the data and Monte Carlo with a Kolmogorov-Smirnov statistic. In Section 10.1 we

also fit for κ; and in Section 10.3 we also verify that our Monte Carlo sample is large enough.

10.1 Likelihood Fit

We bin M_Z for the Monte Carlo and data in 40 bins from 70 to 110 GeV. We minimize a binned likelihood function, L, defined as

$$L = -2 \times \sum_{M_Z \; bins} [-\lambda_i T + n_i \log(\lambda_i T)] \tag{10.1}$$

where n_i is the number of data points in bin i, and λ_i is the sum of the weights of the Monte Carlo events in bin i. The quantity T normalizes the Monte Carlo to the data. The Monte Carlo includes 1% QCD background. The magnitude of the QCD background and the background M_Z shape are determined from same sign events, as discussed in Chapter 4.

We vary κ in 7 steps from 1.0% to 2.2%, and we vary the Monte Carlo electron energy scale in 21 steps from 0.995 to 1.005. For each value of κ and the Monte Carlo energy scale, we evaluate L. To determine a minimum, we then fit L to a cubic polynomial in κ, where each of the coefficients is a cubic polynomial in the Monte Carlo energy scale.

This procedure determines a scale factor which should be applied to the Monte Carlo. The scale factor to apply to the data, S_E, is simply the inverse of this number. The results for the scale factor on the data and for κ are

$$\begin{aligned} S_E &= 1.0000 \pm 0.0009 \\ \kappa &= (1.53 \pm 0.27)\% \end{aligned} \tag{10.2}$$

κ is the constant term in the CEM resolution. The constant term in the resolution accounts for variations in the leakage energy, which does not get included in the electron cluster, and it also accounts for tower to tower variations as well as variations in the CEM response with time. The stochastic part of the fractional energy resolution is $13.5\%/\sqrt{E_T}$. For $Z \rightarrow ee$ events, the stochastic term contributes $\approx 2.0\%$. The constant term is thus comparable in size to the stochastic term, and the combined resolution is $\approx 2.6\%$.

The stochastic term, $13.5\%/\sqrt{E_T}$, is determined from test beam data. We do not consider any uncertainty on this term. The E_T distribution of Z events occurs over a relatively narrow range, and errors in the stochastic term can be absorbed into the fitted constant κ. However, the functional form for the CEM resolution, Equation 6.10, allows us to carry the fitted resolution from the Z events to the W events, and the W events have an average E_T which is roughly 5 GeV lower than Z events. It is possible that errors in the stochastic term will cause us to use the wrong resolution for the W events. We find that changes in the resolution at the W E_T scale which are caused by errors on the stochastic term are significantly smaller than the uncertainty on the resolution which comes from the statistical uncertainty on κ. We only consider the uncertainty on the resolution caused by the uncertainty on κ.

The value for S_E comes out to be 1.0 because the default scale, which has already been applied to the data, was fixed to get the correct Z mass.

We did a simultaneous fit for the two parameters κ and the Monte Carlo energy scale, but the fit results are mostly independent. Figure 10.1 shows the $1-\sigma$ contour of the fit results. The axes of the ellipsoid are nearly horizontal and vertical, indicating that the fit results for S_E and κ are not strongly correlated, and we neglect any possible correlation.

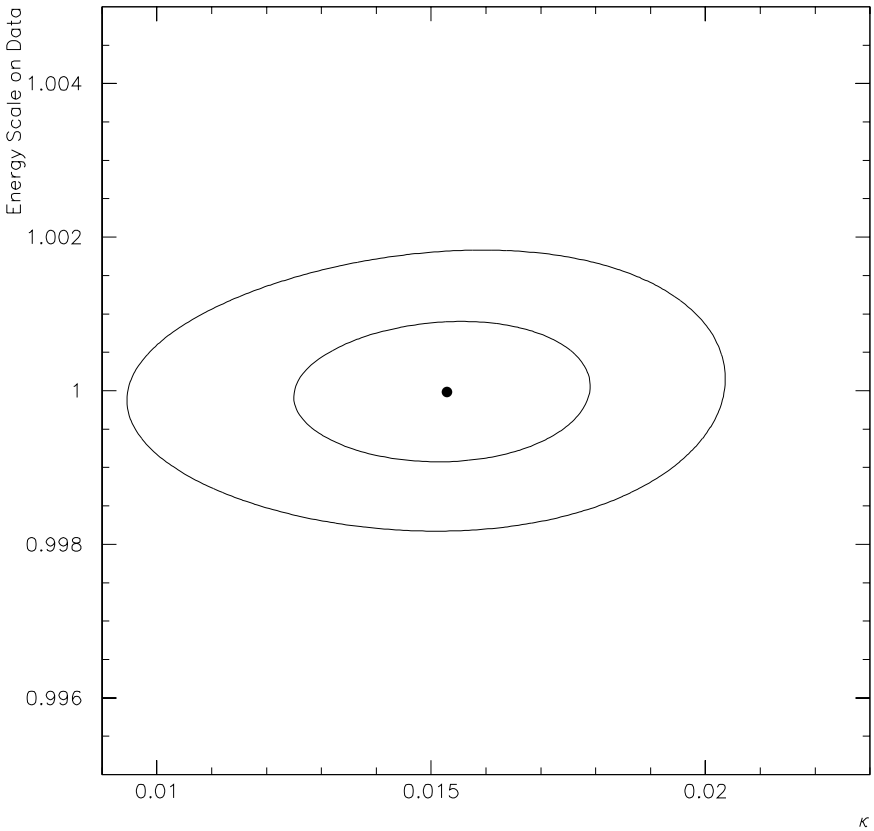

Figure 10.1: 1− and $2-\sigma$ contours for likelihood fit to the Z mass. On the $x-$axis is the fitted value for the constant term in the electron resolution, κ. The $y-$axis is the energy scale that should multiply the data. The likelihood function is actually a function of the energy scale that multiplies the Monte Carlo, and the $y-$axis is one over that value. The solid circle is the best fit value.

The top plot of Figure 10.2 shows the data with the best fit Monte Carlo overlaid, and the bottom plot shows the residuals of the top plot. The value for χ^2/dof is 1.3, where we take the number of degrees of freedom to be 40, which is the number of histogram bins.

As mentioned above, the Monte Carlo includes 1% QCD background. If we do not include the background, the fitted energy scale changes by less than 0.003%, and the fitted value for κ changes by 0.0005. Both these changes are negligible relative to the statistical uncertainties, and we conclude that uncertainties in the background have a negligible contribution to the uncertainties on the fit results.

We also check that the likelihood fitting procedure is unbiased. We draw randomly from a smoothed Monte Carlo histogram of M_Z and make 1000 subsamples of the same size as the data. The histogram which is smoothed has an energy scale of 1.0 and $\kappa = 1.6\%$. We fit the 1000 samples for an energy scale, and we hold κ fixed at 1.6% in the fit. The 1000 results have a Gaussian distribution with a mean of 0.99993 and a width of 0.0009. The mean is marginally below the expected value of 1.0, and this may indicate a flaw in the procedure we use to smooth the histogram we draw from. The width is the same as the uncertainty reported above, which was defined by a change in L of ± 0.5.

10.2 Fitting with the Mean of M_Z

As a check, we fit for the energy scale by comparing the mean of the Monte Carlo M_Z distribution with the mean of the data. To avoid fluctuations in the tails, we calculate the mean using events close to the peak. We bin the data and Monte Carlo in 1 GeV bins between 86 and 96 GeV, and we consider the mean of this histogram.

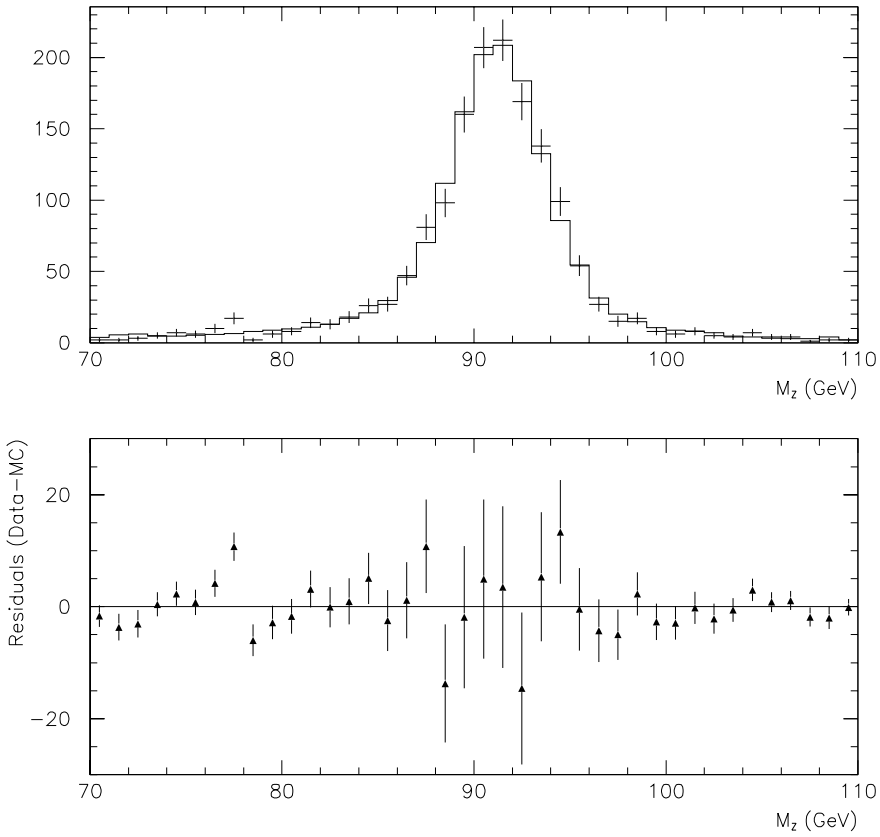

Figure 10.2: Top: Best fit Monte Carlo (histogram) overlaid with data (crosses). The Monte Carlo histogram is the weighted combination of two different Monte Carlo histograms, one with $\kappa = 1.4\%$, and one with $\kappa = 1.6\%$. The Monte Carlo is normalized to the data. Bottom: The residuals of the top plot, data minus Monte Carlo with the Monte Carlo normalized to the data.

We refer to this mean as $< M_Z >$.

Figure 10.3 shows $< M_Z >$ for the Monte Carlo as a function of the Monte Carlo energy scale S_E^{mc}. The mean of the data is also shown on the plot. The Monte Carlo was run with $\kappa = 1.6\%$ for this plot. The data mean and the Monte Carlo mean agree for $S_E^{mc} = 1.0004 \pm 0.0010$. The energy scale for the data is the inverse of this, or $S_E = 0.9996 \pm 0.0010$, which agrees with Equation 10.2.

The Monte Carlo points in Figure 10.3 use $\kappa = 1.6\%$. If we run the Monte Carlo with $\kappa = 1.4\%$, we get a fit value $S_E = 0.9997 \pm 0.0010$. To use the best fit value of $\kappa = 1.53\%$, we should average this result with the $\kappa = 1.6\%$ result, even though the two results agree within one tenth of the statistical uncertainty. We also vary κ within its uncertainties. This produces a variation in the fitted value for S_E of order ± 0.0001, which is a negligible variation.

As in Section 10.1, the Monte Carlo includes the effect of 1% QCD background. We vary the background between 0% and 2%, and the fitted value for S_E shows a variation of ± 0.00002. This is a negligible variation.

10.3 Kolmogorov-Smirnov Comparison

In this section, we use a Kolmogorov-Smirnov statistic (KS) to evaluate how well the Monte Carlo reproduces the data. We also check the fits of Sections 10.1 and 10.2 by minimizing KS with respect to variations in the energy scale. The KS statistic is calculated without binning the data or the Monte Carlo, and this allows us to check that binning the data in Sections 10.1 and 10.2 does not significantly increase the statistical uncertainties. Above we saw that the background has a negligible contribution to the fit results, and for this section it is not included in the Monte

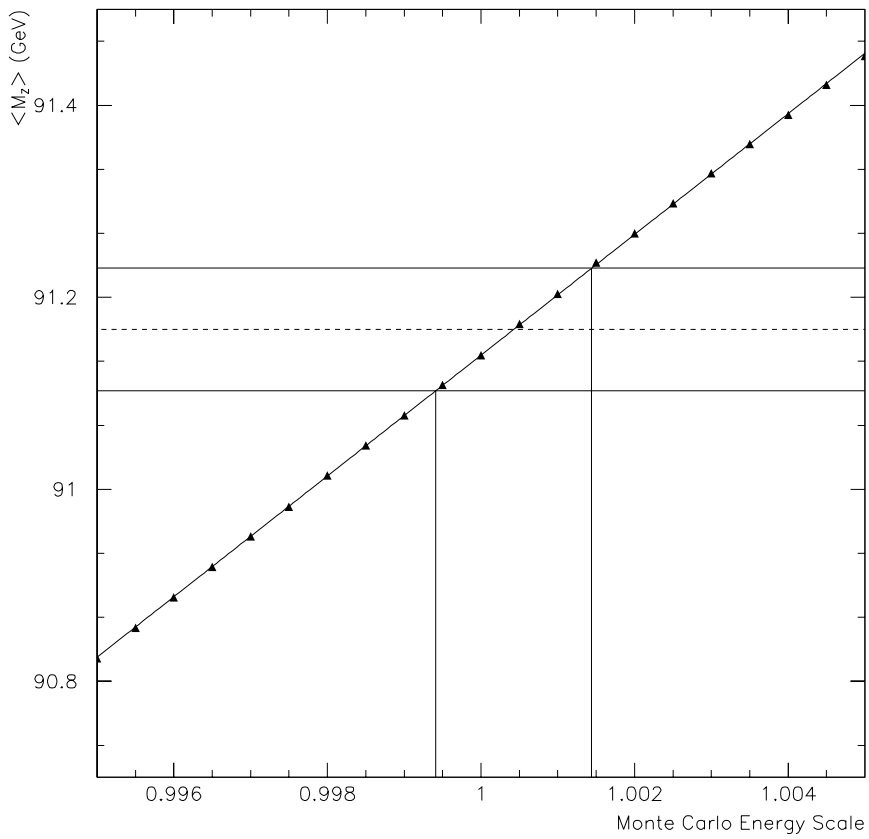

Figure 10.3: Mean of the Monte Carlo M_Z histogram as a function of the Monte Carlo energy scale (triangles). A fit line through the triangles is shown. The fit is $< M_Z >= S_E^{mc} \times 62.910 + 28.230$, where $< M_Z >$ is in GeV. The horizontal lines indicate the mean of the data and its $1 - \sigma$ uncertainties. The mean of the data histogram is 91.166 ± 0.064 GeV where the error is $\mathrm{rms}/\sqrt{N}$. The vertical lines indicate the predicted region for the Monte Carlo energy scale.

Carlo.

To calculate KS, we form the integrated distributions of M_Z for data and Monte Carlo. The integrated distribution is $I(x)$, where $I(x)$ is the fraction of the data which has $M_Z < x$. For the Monte Carlo, $I(x)$ is the fraction of the total Monte Carlo weight that is associated with events with $M_Z < x$. For both data and Monte Carlo, we only consider events with $70 < M_Z < 110$ GeV. Figure 10.4 shows the integrated distribution of data and Monte Carlo. The data is shown with the default scale of $S_E = 1.0$, and for comparison it is also shown with a CEM scale factor $S_E = 0.996$. We use 0.996 as a comparison, since in the next Chapter we determine the energy scale with the E/p distribution, and we get a result near $S_E = 0.996$. The Monte Carlo in this section uses $\kappa = 1.6\%$.

KS is defined to be the maximum vertical distance between the Monte Carlo integrated distribution and the data integrated distribution. A KS value of 0 would correspond to perfect agreement between the two distributions. The maximum vertical distance between data and Monte Carlo in Figure 10.4 is 0.0162 for the data with $S_E = 1.0$, and 0.0646 for the data with $S_E = 0.996$.

We can use the value for KS to calculate the probability that the parent distribution of the data is well described by the Monte Carlo. If we have N data points, then the probability, Pr, of observing a value worse than a given KS value is [41]

$$Pr = 2\sum_{j=1}^{\infty}(-1)^{j-1}\exp(-2j^2\lambda^2) \tag{10.3}$$

where $\lambda = \sqrt{N} \times KS$. For the data with $S_E = 1.0$, we get the values $\lambda = 0.64$ and $Pr = 81\%$. This value for Pr indicates excellent agreement between data and Monte Carlo. If we were to make many Monte Carlo samples of the same size as the data,

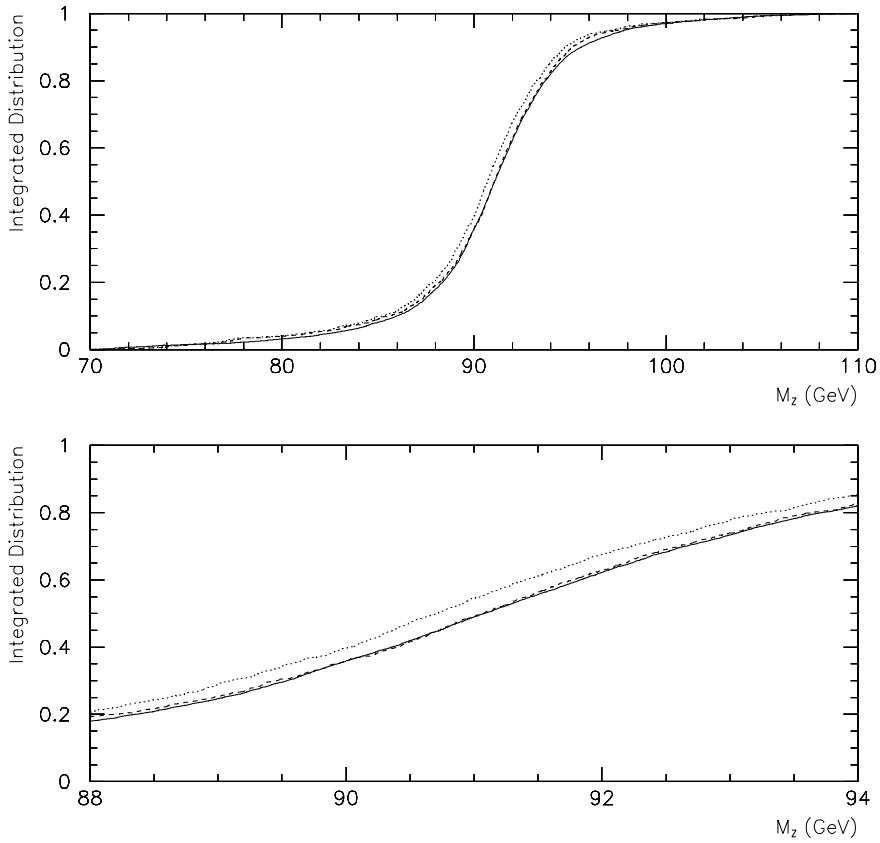

Figure 10.4: Integrated distribution of M_Z for $Z \to ee$ events between 70 and 110 GeV. Three curves are shown. The solid curve is the Monte Carlo; the dashed curve is the data with the default energy scale of 1.0; and the dotted curve is the data with E scaled by $S_E = 0.996$. The top plot shows the full range 70 to 110 GeV, and the bottom plot shows the region around the M_Z peak.

only 19% of them would have smaller values for KS. By comparison, when we scale the data by 0.996, we get $\lambda = 2.53$, and $Pr = 5.5 \times 10^{-6}$.

We check the fits of Sections 10.1 and 10.2 by minimizing KS with respect to variations in the energy scale. We change the energy scale on the data, and for each value of S_E, we recalculate the Kolmogorov-Smirnov statistic KS. The location of the minimum KS is the predicted scale. The energy scale is applied before the cuts on the data, and we choose κ in the Monte Carlo to be fixed at 1.6%.

Figure 10.5 shows KS as a function of S_E. The minimum occurs at $S_E = 1.0007$. The minimum value for KS is 0.0133, and Equation 10.3 gives a corresponding value for Pr of 95%.

The statistical uncertainty associated with this fit is determined by drawing randomly from a smoothed version of a Monte Carlo histogram, as was done above for the likelihood scale determination. We make 100 samples the same size as the data, and we fit each of them for an energy scale. The location of the minimum is distributed with a mean of 1.0, and an rms of 0.0010. The rms of the distribution is the statistical uncertainty.

We also use these Monte Carlo samples to check Equation 10.3. Equation 10.3 predicts that only 19% of the Monte Carlo samples which are the same size as the data will have KS smaller than 0.0162. 0.0162 is the KS value we found for the data with $S_E = 1.0$. We calculate KS for the Monte Carlo samples where we do not vary an energy scale on the samples, but keep the scale fixed at 1.0. We find that 26 of the 100 samples have $KS < 0.0162$. This agrees with the prediction from Equation 10.3.

The fitted scale is $S_E = 1.0007 \pm 0.0010$. This result agrees with the result in Equation 10.2, even though it is not identical. Some variation is expected from different fitting procedures, and these variations are accounted for in the statistical

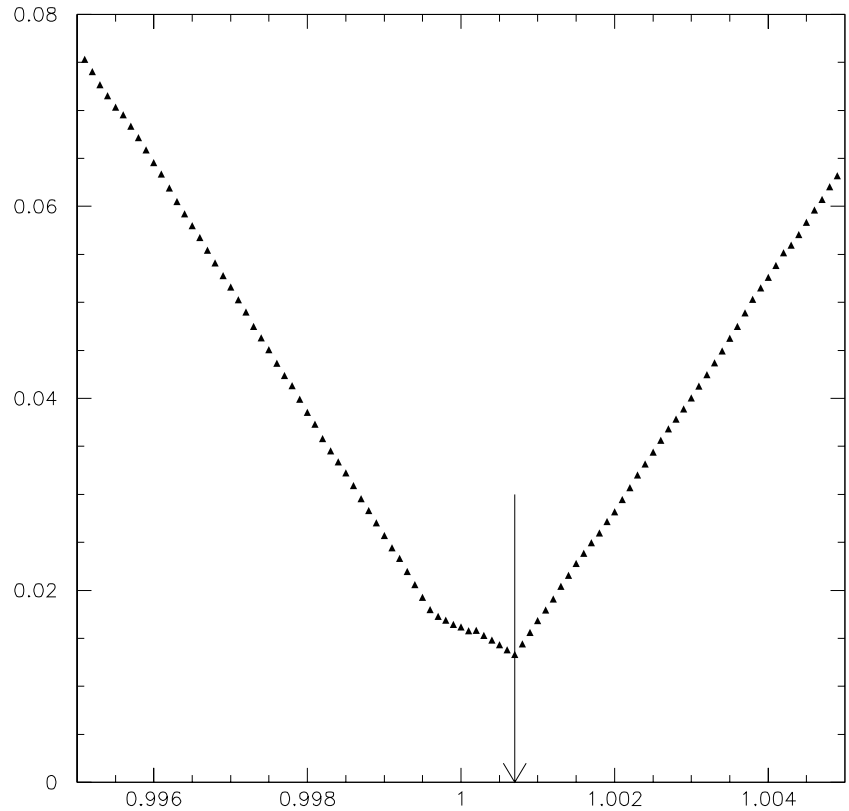

Figure 10.5: Kolmogorov-Smirnov statistic, KS, as a function of the CEM scale S_E for the comparisons of the data and Monte Carlo M_Z distributions. The Monte Carlo uses $\kappa = 1.6\%$. The minimum location is indicated by the arrow, and it occurs at $S_E = 1.0007$. The value of the minimum is $KS = 0.0133$.

uncertainty.

We also use the Kolmogorov-Smirnov fitting procedure to check that we have generated enough Monte Carlo. Our Monte Carlo includes slightly more than 980,000 weighted events. We split this into independent subsamples of 48,000 events each, and refit the data with each. The rms spread of the results is 0.0003. The full Monte Carlo is ≈ 20 times larger than each of the subsamples. The statistical error should scale as $1/\sqrt{N}$, and dividing 0.0003 by $\sqrt{20}$ gives a total Monte Carlo statistical uncertainty of less than 0.0001. This is negligible relative to the statistical uncertainty from the data.

10.4 Conclusion

We have fit for the energy scale on the data, S_E, using three different fitting methods: a likelihood fit, a mean fit, and a Kolmogorov-Smirnov fit. For the likelihood fit we also determined the constant term in the CEM resolution, κ. The best fit value is $\kappa = 1.6\%$. The Kolmogorov-Smirnov calculations of Section 10.3 indicate that there is good agreement in the M_Z shape between the data and Monte Carlo.

The three methods give consistent values for S_E, and some variation in fit results is expected from statistical fluctuations. The statistical uncertainties associated with the three methods are the same.

We use the result from the likelihood fit, which is Equation 10.2, for the CEM scale.

Chapter 11

Energy Scale Determination with E/p

In this chapter we determine the energy scale using the E/p distribution. The quantity E/p is the ratio of the electron energy as measured in the calorimeter to the track momentum, as determined by the CTC. The CTC scale is determined with J/ψ data, as discussed in Section 3.2 and also in Appendix B. The E/p result and the energy scale determined from M_Z in Chapter 10 differ by ~ 3.5 standard deviations. We choose to use the M_Z result since it sets the scale on the CEM directly, using CEM data. This separates our measurement from complications which may arise from tracking.

The difference in the E/p and M_Z results can be stated as follows. If we set the energy scale with E/p, then the Z mass comes out low by roughly 350 ± 100 MeV. Alternatively, when we set the energy scale with the Z mass, the E/p distribution of the data is visibly shifted to the right relative to the Monte Carlo. In Appendix B, we discuss checks which have been done on the E/p simulation, as well as the Z mass

simulation. We also discuss possible reasons for the discrepancy. This discrepancy is not understood and is interesting in its own right.

The CTC measures the track curvature and thus P_T. In practice E/p is defined as $E \sin\theta / P_T$. E/p can be different than 1 as a result of measurement resolution, and also as a result of bremsstrahlung in the material before and in the CTC. The fraction of the electron energy radiated by bremsstrahlung is independent of the electron energy. Uncertainties on the electron E_T distribution will produce negligible uncertainties on the E/p shape. E/p thus allows us to tie the CEM scale to the CTC scale in a way that is independent of the assumed W mass and other inputs which effect the E_T shape.

The amount of material in the simulation will effect the rate of bremsstrahlung and thus the E/p distribution. The tail of the E/p distribution is sensitive to the amount of material, and in Section 11.1 we verify that the tail of the E/p distribution in the data agrees with the Monte Carlo.

In Section 11.2, we use the E/p distribution to determine a resolution on $1/P_T$, $\sigma(1/P_T)$. We vary the resolution in the Monte Carlo by varying a scale factor on the CTC covariance matrix. Rather than report the result as a covariance matrix scale factor, we report the result as a resolution on $1/P_T$.

In Sections 11.3 and 11.4 we determine an energy scale on the CEM relative to the momentum scale of the CTC, using both W and Z events. We conclude in Section 11.5

When we fit for an electron energy scale, we vary the Monte Carlo scale factor, S_E^{MC}, between 0.9975 and 1.0025. We use S_E^{MC} to predict a value for the energy scale on the data, $S_E = 1/S_E^{MC}$. The E/p fits prefer an energy scale around $S_E = 0.996$. In this chapter, when we do the energy scale fits, we will already have applied a 0.996 scale factor to the data. Thus, in this chapter, since the data are already scaled by

0.996, we have the relationship, $S_E = 0.996/S_E^{MC}$.

11.1 Check on Amount of Material with E/p Tail

The amount of material in the detector is determined from a sample of photon conversions, as discussed in Section 6.1.2. With this amount of material, the Monte Carlo W decay electrons pass through 7.20 ± 0.38 percent of a radiation length on average.

We check this number with the W data. The top plot of Figure 6.2 shows the E/p distribution of the data. The extended high-end tail is the result of bremsstrahlung, both internal and external. External bremsstrahlung occurs in the material that the electrons pass through, while internal bremsstrahlung corresponds to the photons produced with the primary electron in radiative $W \rightarrow e\nu\gamma$ events.

We assume the internal bremsstrahlung rate is known, and we use the fraction of material in the tail to check the rate of external bremsstrahlung. The internal photons account for roughly $\sim 40\%$ of the shift in the E/p peak and similarly for the fraction of events in the tail.

We define the quantity f_{TAIL} to be the fraction of events with E/p between 1.4 and 1.8. We start at 1.4 so that we are away from the peak position and are not sensitive to the E or p resolutions.

In the next section we will discuss a non-Gaussian tail to the $1/P_T$ resolution. The contribution of this tail to low E/p does not extend significantly past 0.8. If we assume that there is an equivalent high end tail, then we do not expect any contribution from this tail beyond E/p of ~ 1.2. Nevertheless, to reduce the contribution from tracking problems, we require that more than half of the 24 stereo layers be used in the track reconstruction. This requirement is only used for the calculation of f_{TAIL}.

The value for f_{TAIL} in the data is 0.0520 ± 0.0014. This number must be corrected for the contribution of the QCD background. The QCD background is significant at high E/p. As an approximation to the E/p shape of the QCD background, we look at the E/p shape of electrons from $W \rightarrow e\nu$ events that fail cuts on electron identity variables. This shape is only approximate, since E/p for the QCD background is correlated to the identity variables. The shape predicts that $\sim 35\%$ of QCD events in the $W \rightarrow e\nu$ sample will have E/p between 1.4 and 1.8. Using the background rates of Chapter 4, this predicts a correction on f_{TAIL} of $\sim 4\%$. This number is only an approximation, and it is not the number we use to account for the QCD background. Instead, we apply a series of cuts to the data which should reduce the background but which should not bias the E/p shape of the signal.

Internal photons may be produced at a different polar angle than the primary electron, but external photons are produced at essentially the same polar angle. Since the magnetic field causes bremsstrahlung photons and electrons to be separated in the azimuthal direction, but not in the z direction, the external photons hit the calorimeter at the same z position as the primary electron. There are several electron identity variables which are independent of the rate of external bremsstrahlung since they only depend on the size of the electron shower in the z direction. We use two of them, χ^2_{strips} and L_{share}. χ^2_{strips} compares the strip chamber shower profile in the z-direction with the expectation from the test beam. This variable is discussed in Chapter 4. L_{share} compares the sharing of the electron energy among the calorimeter towers with the expectations from the test beam, where the comparison only includes the "seed" tower and the two neighboring towers in the z direction.

These two variables are shown in Figure 11.1 for Z data. Both plots show the Z data for E/p between 0.9 and 1.1 and also for E/p between 1.4 and 1.8. We use Z data

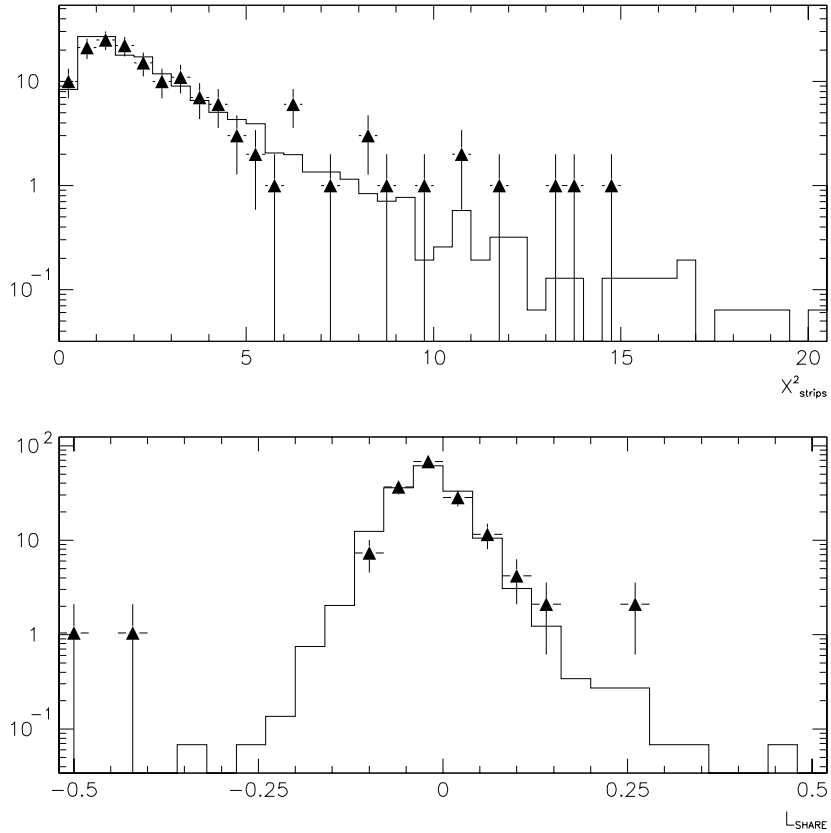

Figure 11.1: Top: χ^2_{strips} and bottom: L_{share} for Z data. The histograms are for E/p between 0.9 and 1.1 and the triangles are for E/p between 1.4 and 1.8. The histogram and the triangles for both plots are normalized to the total number of events between 1.4 and 1.8.

since the QCD background can be simply calculated from the number of same sign events. There is no visible difference between the two E/p regions for either variable. We might have expected to see some difference from internal photons, which are potentially produced at wide angles from the electron. If the internal photons were to significantly alter the L_{share} or χ^2_{strips} distributions, then cutting on those variables would bias the E/p shape of the signal.

We define f_{BACK} to be the fraction of events with M_T below 20 GeV when we

remove the $|\vec{U}|$ cut. As discussed in Chapter 4, we expect the QCD background to be proportional to f_{BACK}. To see how f_{TAIL} depends on f_{BACK}, we plot f_{TAIL} and f_{BACK} for different regions of χ^2_{strips} and L_{share}. These plots are shown in Figure 11.2.

We do not expect the L_{share} and χ^2_{strips} cuts to bias the signal, and variations in f_{TAIL} can be ascribed to variations in the total background. The $y-$axis intercept is our prediction of f_{TAIL} for 0% background. The three fits of Figure 11.2 (from left to right and top to bottom) have intercepts of 0.0494 ± 0.0014, 0.0487 ± 0.0014, and 0.0484 ± 0.0014, respectively. The intercepts change negligibly if we fit to a quadratic instead of a line, or if we include the $x-$axis errors in the fit. The intercepts are robust to the extrapolation method because the point with the smallest error bar is closest to $f_{BACK} = 0$. We average the three fits and conclude that

$$f_{TAIL} = 0.0488 \pm 0.0014(stat) \pm 0.0004(sys) \tag{11.1}$$

where the second error is simply the rms of the three extrapolations.

The top plot of Figure 11.3 shows f_{TAIL} as a function of $< X_0 >$, for the Monte Carlo. The error bars for both plots are the statistical uncertainty from the data and are included on the plots for reference only. From the linear fit shown, we conclude that the value for f_{TAIL} above corresponds to $< X_0 > = (7.55 \pm 0.37)\%$ of a radiation length. This is consistent with the result from the photon conversions above. To avoid questions related to the extrapolation procedure, and to be conservative, we do not combine the two numbers, but simply use the photon conversion result of Equation 6.5.

The bottom plot of Figure 11.3 shows the mean of E/p between 0.9 and 1.1, as a function of the amount of material $< X_0 >$. From the slope of the fitted line, we

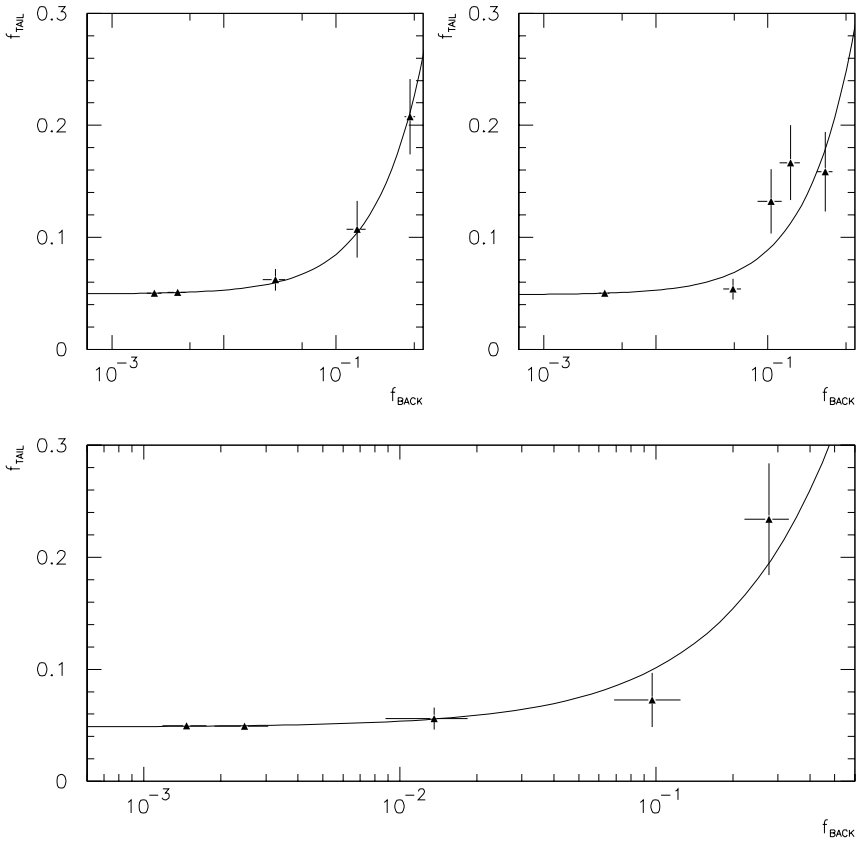

Figure 11.2: f_{TAIL} vs f_{BACK} for different regions of L_{share} and χ^2_{strips}. Top left: the 5 points from left to right are for L_{share} below 0, between 0 and 0.1, between 0.1 and 0.2, between 0.2 and 0.4, and above 0.4. Top right: the 5 points from left to right are for χ^2_{strips} below 10, between 10 and 20, between 20 and 30, between 30 and 50, and above 50. Bottom: same as top right plot, but with $L_{share} < 0.2$ cut applied. The $x-$axes are shown on a log-scale, and the curves shown are linear fits.

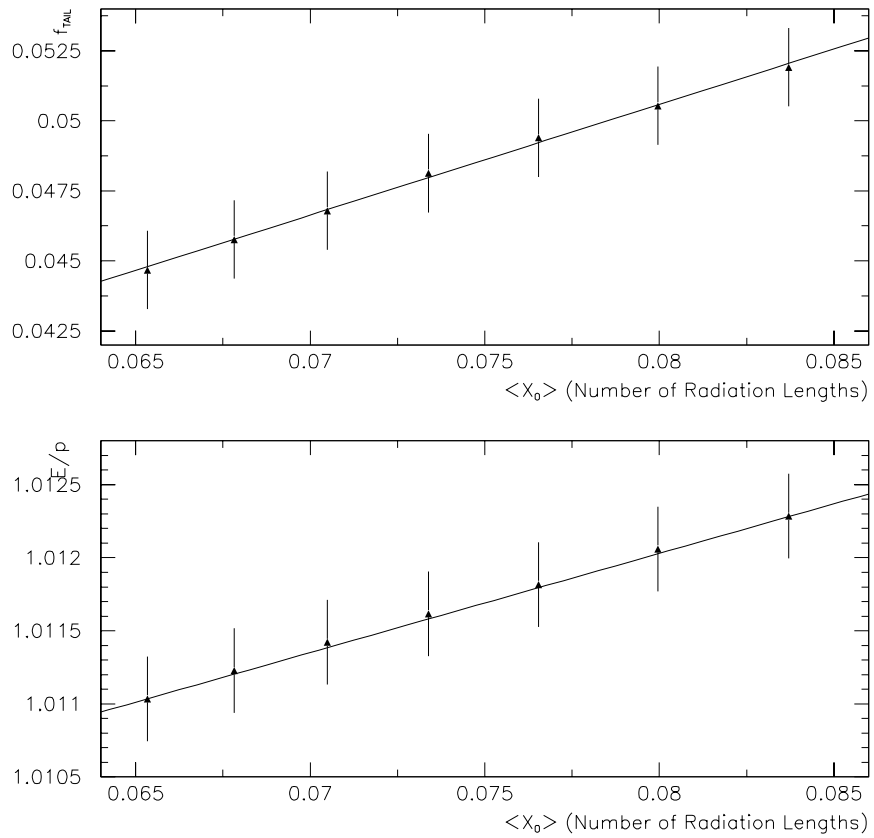

Figure 11.3: Top: f_{TAIL} as a function of $< X_0 >$ for Monte Carlo $W \rightarrow e\nu$ events. f_{TAIL} is defined as the fraction of events with E/p between 1.4 and 1.8. Bottom: Mean of E/p between 0.9 and 1.1 vs $< X_0 >$. The mean is calculated as in Figure 11.11 below. The fitted line for the top plot is $f_{TAIL} = 0.018965 + 0.39529 \times < X_0 >$, and for the bottom plot is $< E/p >= 1.0066 + 0.067867 \times < X_0 >$.

determine that an uncertainty on $< X_0 >$ of 0.0037 will produce an uncertainty on the mean of the E/p peak of 0.00025. Figure 11.11 below shows that a shift in the mean of 0.00025 corresponds to a shift in the energy scale of 0.00036. Thus, the uncertainty on the energy scale associated with the amount of material is 0.00035.

11.2 Momentum Resolution

The resolution on E/p is a convolution of a resolution on E_T and a resolution on $1/P_T$. Electrons from W decays have transverse energies around 40 GeV, and the fractional error on P_T is $\sigma(P_T)/P_T \approx .001 \times P_T = 4\%$. The fractional error on E_T is smaller, $\sigma_E/E \approx \sigma(E_T)/E_T = 2.7\%$, where we have used $\kappa = 1.6\%$. Both the E_T and P_T resolutions will contribute to the E/p width, but the P_T resolution will dominate.

11.2.1 Very Low E/p Tail

The E/p distribution is shown in the top plot of Figure 11.4 with a Gaussian fit superimposed. Bremsstrahlung radiation contributes to the distribution above 1.0, but events fall below 1.0 only because of resolution. If E_T and P_T have Gaussian resolutions, then the low-end tail should have a Gaussian distribution. A non-Gaussian tail, however, is clearly evident in the plot.

The bottom plot of Figure 11.4 shows the M_T distribution for events with $E/p <$ 0.85 superimposed on events with E/p in the peak. The similarity of the two histograms indicates that events in the low-end E/p tail are not backgrounds events. The similarity also indicates that the low-end E/p tail is not a result of E_T mismeasurement. Events below 0.85 would have E_T mismeasured low by at least $\approx 15\%$. This would shift the M_T distribution by ≈ 12 GeV or more. Such a shift is clearly

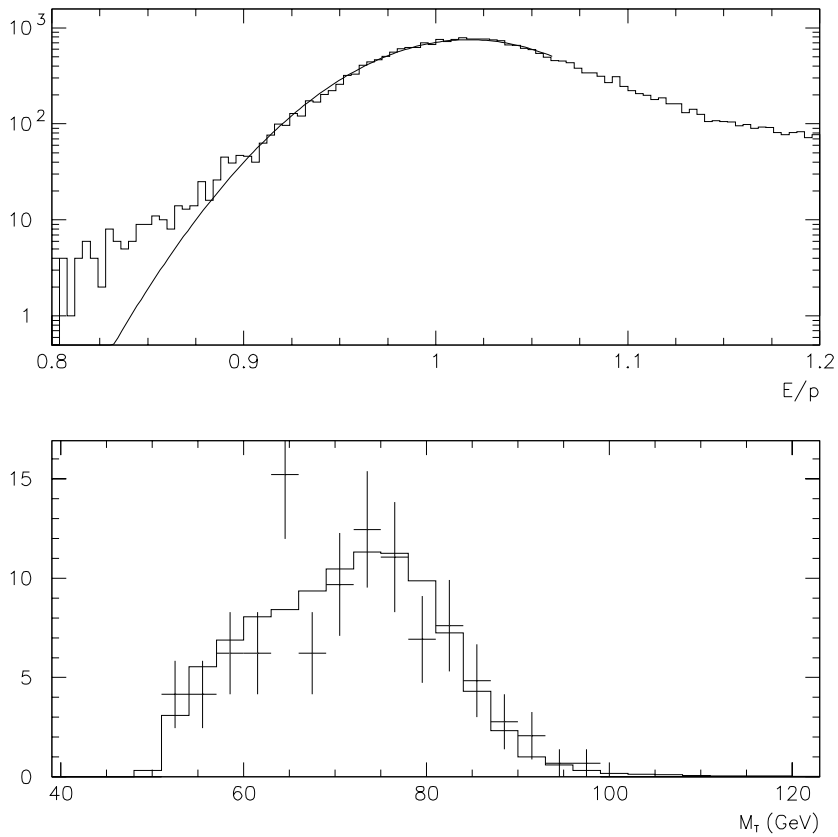

Figure 11.4: Top: E/p distribution of W events, on a log scale, with a Gaussian fit superimposed. The Gaussian fit is for $0.8 < E/p < 1.06$. Bottom: M_T distribution for W data without M_T cuts. The points with error bars are for events with $E/p < 0.85$, and the histogram is for events with $0.9 < E/p < 1.1$. The histogram is normalized to the number of events with $E/p < 0.85$.

inconsistent with the plot. The mean of the M_T distribution for the peak E/p region is 71.30 ± 0.06 GeV. This is consistent with 72.17 ± 1.0 GeV, which is the mean M_T for the low-end E/p tail.

We can also calculate M_T using P_T instead of E_T. We refer to this quantity as $M_T(track)$. The transverse mass depends on the calculation of $\not{E}_T$, and when calculating $M_T(track)$ we also use P_T for the $\not{E}_T$ calculation instead of E_T. Since M_T for the low E/p events is not shifted, we expect that $M_T(track)$ is. A comparison of $M_T(track)$ for events with E/p below 0.85 and for events with $0.9 < E/p < 1.1$ is shown in the top plot of Figure 11.5. The low-end events are clearly shifted towards higher $M_T(track)$. The mean of $M_T(track)$ for those events is higher than the peak E/p events by 21 ± 1 GeV. This indicates that the low E/p events are the result of P_T being mismeasured high.

The bottom plot of Figure 11.5 provides further evidence that the very low E/p events are not background. The plot shows the angle between the electron and the highest E_T jet in the event. The very low E/p events appear reasonably flat.

The distributions of N_{stereo} and N_{axial} are shown in Figure 11.6, for the low E/p events, and also for events with E/p in the peak. N_{stereo} is the number of CTC wires with stereo information that are used to reconstruct the track, and N_{axial} is the number of axial wires that are used. If all the stereo wires are used for a given track, then $N_{stereo} = 24$, and if all the axial wires are used then $N_{axial} = 60$. The plots show that the low E/p data use fewer stereo wires and also fewer axial wires than events with E/p in the peak. The majority of the low E/p data use less than half the stereo wires. These plots are consistent with the explanation that the low E/p events are the result of badly measured tracks.

We conclude that the low E/p tail consists of events with badly measured tracks

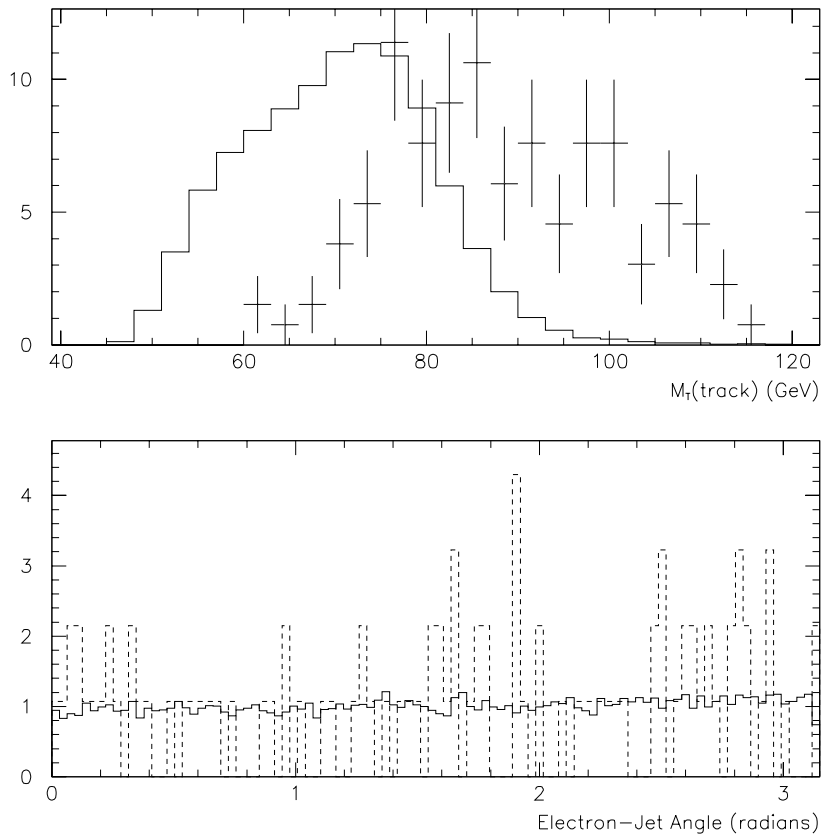

Figure 11.5: Top: $M_T(track)$ distribution for events with $E/p < 0.85$ (crosses) and events with $0.9 < E/p < 1.1$ (histogram). No M_T cut is applied to the top plot. Bottom: Angle between the electron and the highest jet in the event for $E/p < 0.85$ (dashed histogram), and for $0.9 < E/p < 1.1$ (solid histogram). All histograms are normalized to the number of events with E/p below 0.85.

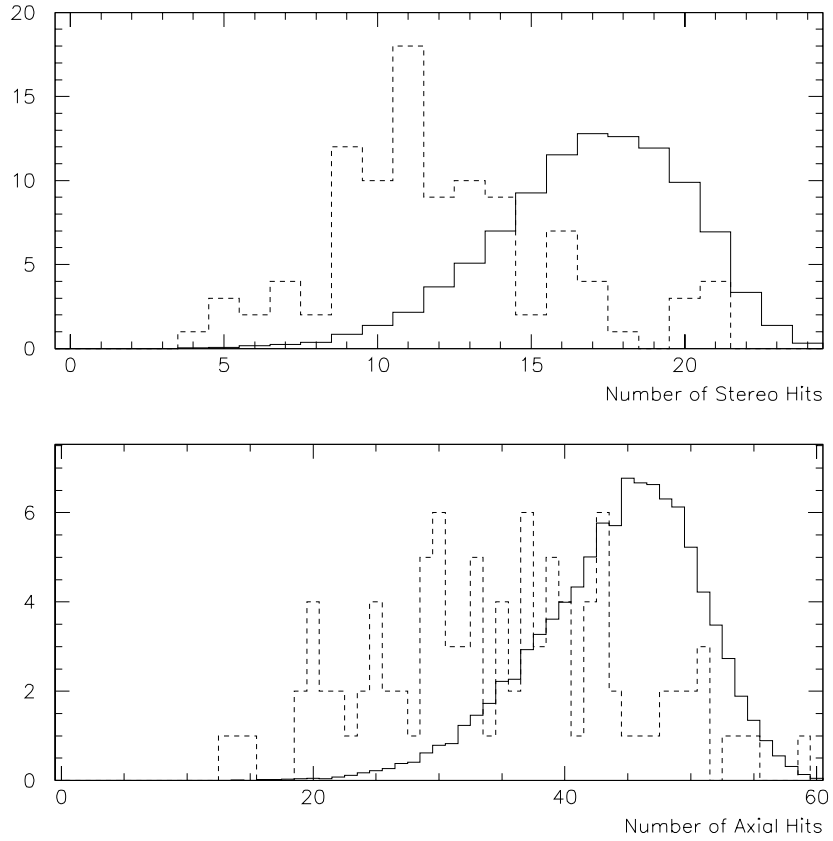

Figure 11.6: Top: N_{stereo} distribution for events with $E/p < 0.85$ (dashed histogram) and events with $0.9 < E/p < 1.1$ (solid histogram). Bottom: N_{axial} for $E/p < 0.85$ (dashed histogram), and for $0.9 < E/p < 1.1$ (solid histogram). N_{stereo} is the number of stereo wires used in the reconstruction of a given track, and N_{axial} is the number of axial wires. All histograms are normalized to the number of events with E/p below 0.85.

but which are otherwise good W events. We simulate these events by describing the $1/P_T$ resolution with two Gaussians. We find that simulating 8% of the events with $\sigma(1/P_T) = 0.0026$ GeV^{-1} allows us to adequately simulate the low E/p tail. We will use the peak region $0.9 < E/p < 1.1$ to determine the energy scale. The low E/p events will not significantly effect the scale.

11.2.2 Peak of E/p Distribution

We fit the E/p distribution of the data to the Monte Carlo and vary the three variables κ, $\sigma(1/P_T)$, and the Monte Carlo energy scale S_E^{MC}. We do not directly vary $\sigma(1/P_T)$, but instead we vary a scale factor on the calculated covariance matrix. There is a direct relationship between $\sigma(1/P_T)$ and the square root of the covariance scale, and below we will report a result for $\sigma(1/P_T)$, rather than the covariance scale.

To include the second Gaussian distribution discussed in Section 11.2.1, we run a mock-up Monte Carlo where E_T is chosen randomly from a Monte Carlo histogram, and P_T is chosen based on the distribution of radiated energy, also chosen from a Monte Carlo histogram. E_T is then smeared and scaled according to the different values for κ and S_E^{MC}, and $1/P_T$ is smeared according to the resolution discussed in Section 11.2.1. This mock-up Monte Carlo differs from the full Monte Carlo only slightly and is adequate for our purposes. We add this shape to the full Monte Carlo shape so that the final Monte Carlo shape contains an 8% contribution from the larger $1/P_T$ resolution.

We do a binned likelihood fit, minimizing the function

$$L = -2 \times \sum_{E/p\ bins} [-\lambda_i T + n_i \log(\lambda_i T)] \tag{11.2}$$

where n_i is the number of data points in bin i, and λ_i is the sum of the weights of the Monte Carlo events in bin i. The quantity T normalizes the Monte Carlo to the data. We include the QCD background at its predicted rate by adding an E/p histogram for the QCD background to the Monte Carlo histogram. We do not change the background shape as a function of the energy scale. The QCD background mostly occurs at high E/p, and it has a negligible effect on the peak fit. The E/p shape is binned in 50 bins from 0.8 to 1.2, and the likelihood calculation is a sum over the middle 25 bins, approximately from 0.9 to 1.1. There are $22,112$ events in this region.

We hold κ fixed at each of its input values, and we minimize L with respect to S_E^{MC} and $\sigma(1/P_T)$ simultaneously. The best fit values for $\sigma(1/P_T)$ as a function of the assumed value for κ are shown in Figure 11.7. The plot shows that if we assume a better E_T resolution in the Monte Carlo, then we have to increase the $1/P_T$ resolution to match the data.

The error bars shown in Figure 11.7 include a simple correction for correlations with S_E^{MC}. To calculate the errors, we hold κ fixed at 1.6% and fit for $\sigma(1/P_T)$ as a function of the Monte Carlo input values for S_E^{MC}. The results of these 1−dimensional fits are described by $\sigma(1/P_T)(\mathrm{GeV}^{-1}) = -0.00922 + 0.0101 \times S_E^{MC}$. The statistical uncertainty on S_E is ≈ 0.0004, and $0.0004 \times 0.0101 = 4.0 \times 10^{-6}$. This is approximately 1/3 of the statistical uncertainty of the 1-dimensional $\sigma(1/P_T)$ fits, which are done with S_E^{MC} and κ held fixed. The uncertainties plotted in Figure 11.7 are the uncertainties from these 1-dimensional fits added in quadrature to 4.0×10^{-6}.

The values for $\sigma(1/P_T)$ shown in Figure 11.7 were calculated assuming that 8% of the events had the larger resolution of Section 11.2.1. To see the effect of the second resolution, we try fitting without it and set the 8% value to 0%. We get values for $\sigma(1/P_T)$ which are $\approx 0.000\ 09\ \mathrm{GeV}^{-1}$ higher than the values calculated

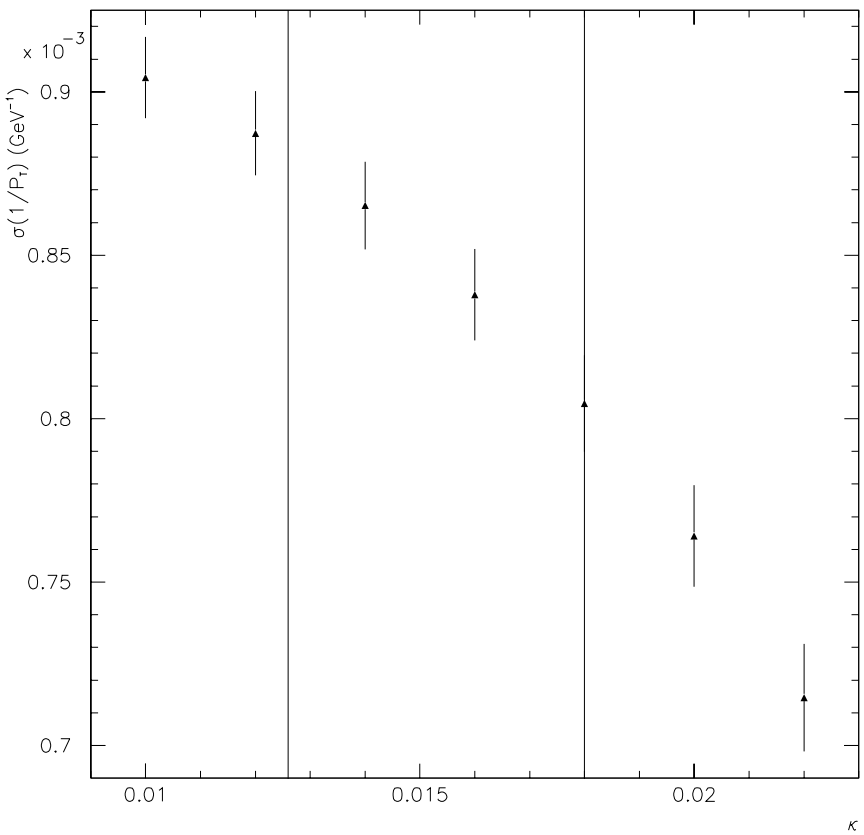

Figure 11.7: Fitted values for $\sigma(1/P_T)$ as a function of the assumed value for κ in the Monte Carlo. The points shown are the result of 2 -dimensional fits with κ held at the value shown and $\sigma(1/P_T)$ and both S_E^{MC} varied. The errors shown include a correction for correlations with the S_E^{MC}. The lines indicate the $1-\sigma$ bounds on κ as calculated from M_Z.

above, for all input values of κ. For example, in Figure 11.7, with $\kappa = 1.6\%$, we have $\sigma(1/P_T) = 0.000\ 837 \pm 0.000\ 013$ GeV^{-1}. If we do not include the second, larger resolution, we get $\sigma(1/P_T) = 0.000\ 925$ GeV^{-1}. This last value agrees better with values for $\sigma(1/P_T)$ which are calculated from $Z \rightarrow \mu\mu$ events, where for those calculations the second resolution is not included.

11.3 Scale Determination With W Events

Figure 11.8 shows the results for the fitted value of the energy scale, S_E, as a function of the Monte Carlo input value for κ. The fit procedure is the same as in Section 11.2.2, where we have allowed both the Monte Carlo energy scale as well as $\sigma(1/P_T)$ to vary in the fit. The y-axis of the plot is the energy scale which should multiply the data. These values are related to the Monte Carlo energy scale S_E^{MC} by $S_E = 0.996/S_E^{MC}$. The factor of 0.996 is needed since we have already scaled the data for the fit, as discussed above.

A quadratic fit is shown on the plot. In Chapter 10, we calculated that the $\kappa = (1.53 \pm 0.27)\%$. With this value and the quadratic fit, we get $S_E = 0.99613 \pm 0.00040(stat) \pm 0.00026(\kappa)$. Including the uncertainty from the amount of material, we get the result

$$S_E = 0.99613 \pm 0.00040(stat) \pm 0.00024(\kappa) \pm 0.00035(X_0) \tag{11.3}$$

where the X_0 uncertainty is from Section 11.1. This fit was done with the second Gaussian resolution of Section 11.2.1 contributing 8% of the time. If we ignore this contribution, the fitted energy scale changes by less than 0.00002 for $\kappa = 1.6\%$. This is a negligible shift for an extreme change in the contribution of the second resolution,

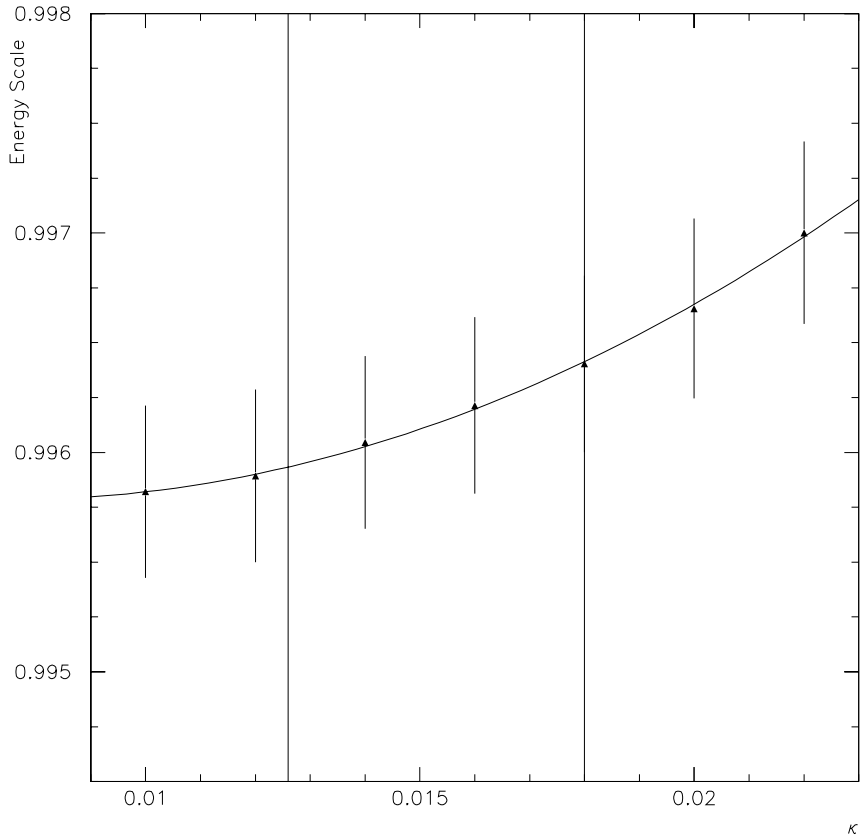

Figure 11.8: Fitted values for the energy scale on the data, S_E, as a function of the assumed value for κ in the Monte Carlo. The points shown are the result of 2 - dimensional fits with κ held at the value shown and both $\sigma(1/P_T)$ and S_E^{MC} varied. The errors shown are the statistical errors for a 1-dimensional fit with $\sigma(1/P_T)$ fixed near its final value and κ held at 1.6%. The contribution to the uncertainty from correlations with $\sigma(1/P_T)$ are found to be negligible. The curve shown is a quadratic fit and is $S_E = 0.99610 - 0.08468 \times \kappa + 5.6723 \times \kappa^2$. The vertical lines indicate the $1-\sigma$ bounds on κ as calculated from M_Z.

and we neglect any uncertainty associated with the second resolution.

Figure 11.9 shows the best fit Monte Carlo E/p distribution overlaid with the data. The Monte Carlo was run at discrete values for $\sigma(1/P_T)$, and to make this histogram we interpolated between two Monte Carlo histograms.

The top plot of Figure 11.10 is the same as Figure 11.9 but on a log scale. The bottom plot of Figure 11.10 shows the residuals of the top plot. Between 0.9 and 1.1, where the fit was performed, the residuals look flat, although there is a slight rise in the residuals around 0.9. This may indicates that we still have not perfectly modelled the resolution. Summing the squares of the residuals over their errors gives $\chi^2/dof = 0.86$, where the number of bins in the histogram is taken to be the number of degrees of freedom. There are 50 bins in the E/p histograms.

As a check on our fitting procedure, we fit for the energy scale using just the mean of the E/p distribution. Figure 11.11 shows the histogram average of the E/p distribution as a function of the input Monte Carlo energy scale. For this plot, the Monte Carlo has $\sigma(1/P_T) = 0.00085$ GeV^{-1}, which is close to the fitted value above, and $\kappa = 1.6\%$. The second resolution is included as above.

The average is calculated by assuming that the contents of each histogram bin occur at the center of the bin, and we only use the middle 25 bins of the histogram exactly as in Equation 11.2. A linear fit is also shown on the plot. The slope is less than 1 because we are calculating a truncated mean, and this slope increases the error on the fitted scale.

After scaling the data by 0.996, we calculate $< E/p >= 1.01254 \pm 0.00030$, and so the plot predicts $S_E^{MC} = 0.99989 \pm 0.00040$. If we repeat the procedure with $\sigma(1P_T) = 0.00079$ GeV^{-1} in the Monte Carlo, we get the result $S_E^{MC} = 0.99952$. The predicted value for $\sigma(1P_T)$ from the previous section, for $\kappa = 1.6\%$, is 0.000837

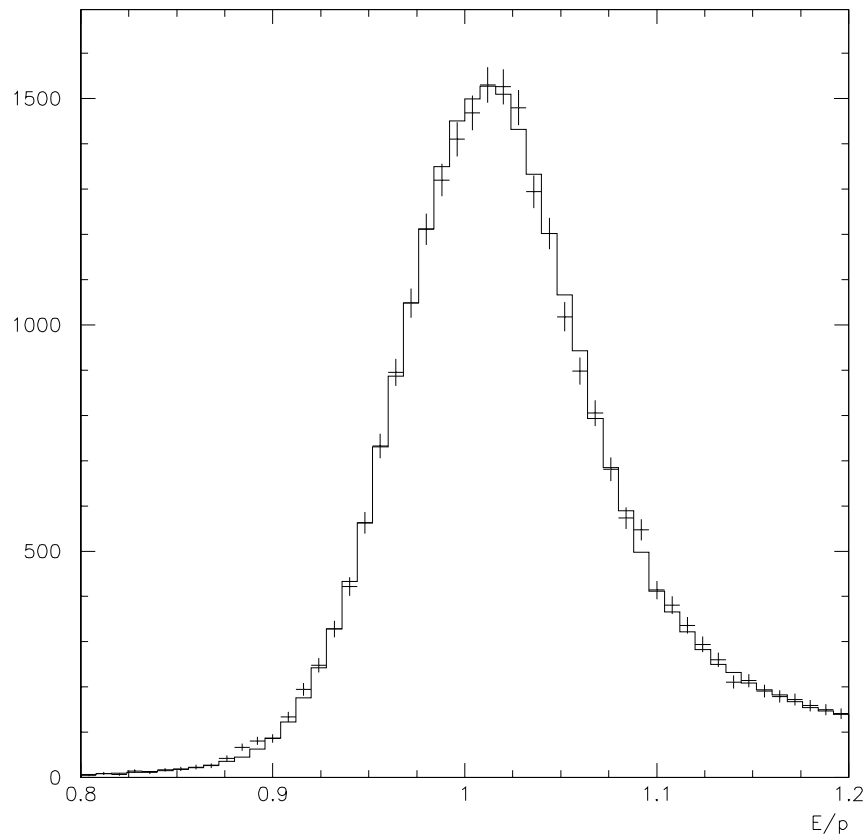

Figure 11.9: Best fit E/p distribution for $W \rightarrow e\nu$ Monte Carlo (histogram), with W data overlaid (crosses). The best fit plot was formed by interpolating between two Monte Carlo plots which were run with $\sigma(1/P_T)$ slightly higher and slightly lower than the best fit value. κ is taken to be 1.6%, and the energy scale is within 0.00002 of the best fit value for the energy scale. The Monte Carlo is normalized to the data.

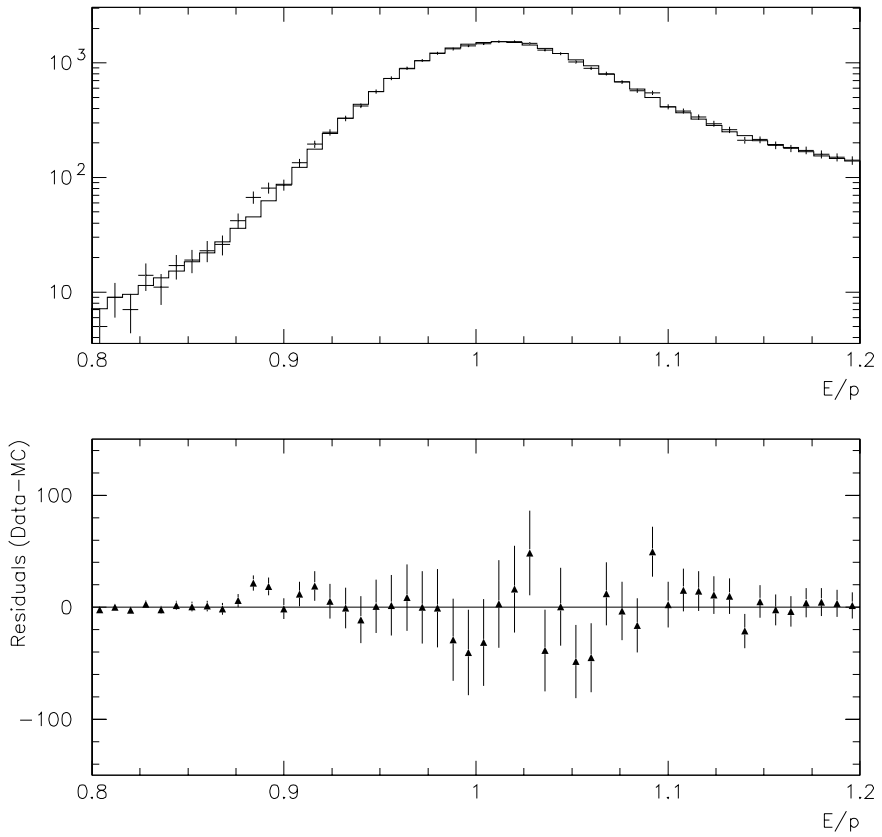

Figure 11.10: Best fit E/p distribution for W events. Top: Best fit E/p distribution for Monte Carlo (histogram) with data overlaid (crosses), on a log scale. Bottom: the residuals of the top plot, data minus Monte Carlo. The errors on the bottom points are the statistical errors associated with the data. Summing the squares over the points divided by their errors gives $\chi^2/dof = 0.86$. The best fit plot was formed by interpolating between two Monte Carlo plots which were run with $\sigma(1/P_T)$ slightly higher and slightly lower than the best fit value. κ is taken to be 1.6%, and the energy scale is within 0.00002 of the best fit value for the energy scale. The Monte Carlo is normalized to the data.

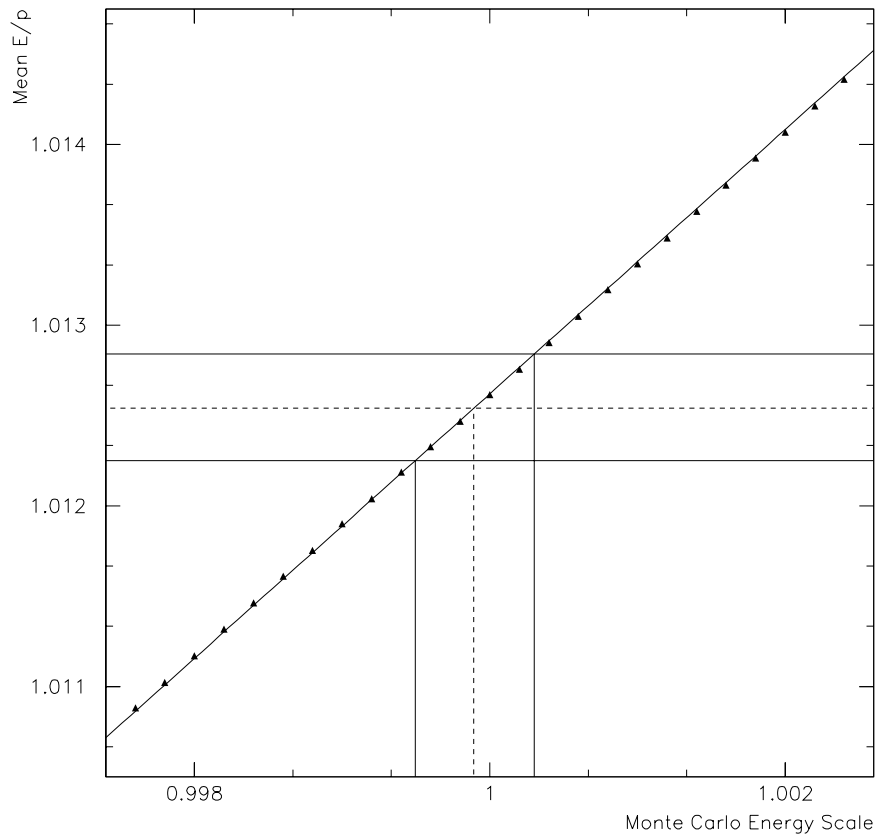

Figure 11.11: Mean of Monte Carlo E/p as a function of the input Monte Carlo energy scale. The linear fit shown is $< E/p >= 0.2807778 + 0.7318406 \times S_E^{MC}$. The slope of the line is less than 1 because we are calculating a truncated mean. The dashed horizontal line indicates the corresponding mean of the data, after scaling the data by 0.996. The solid horizontal lines indicate the $1-\sigma$ uncertainties on the mean. The solid vertical lines indicate the $1-\sigma$ region for predicted the Monte Carlo energy scale. The fit value for S_E^{MC} is the point where the dashed line intercepts the diagonal. The fit value is indicated by the dashed vertical line.

GeV^{-1}. Averaging the two values for S_E^{MC}, weighted by how close they are to the correct value for $\sigma(1P_T)$, we get $S_E^{MC} = 0.99981$. As discussed above the value for the energy scale on the data is $S_E = 0.996/S_E^{MC}$, where the 0.996 factor is needed since we have already scaled the data for this calculation. The fitted value for the scale is then

$$S_E = 0.99619 \pm 0.00040(stat) \quad (mean\ fit) \tag{11.4}$$

This result agrees well with Equation 11.3. The statistical errors of the two fits also agree, and this indicates that for purposes of setting the energy scale, the mean of E/p is as good a statistic as the likelihood.

11.4 Scale Determination With Z Events

We repeat the likelihood fitting procedure of Section 11.3 using the E/p distribution of Z events. The second resolution is included, as is the QCD background. As above, we find the background to have a negligible effect on the results. For both the Z simulation and the data, we include both decay electrons in the E/p histogram. There are 2,300 entries in the histogram bins used in the fit. This is approximately one tenth of the W statistics, and we expect the statistical uncertainties to be ≈ 3 times as large. As above, we initially scale the Z data by 0.996 so that the fit value for the Monte Carlo energy scale will be near 1.

Holding κ fixed at 1.6% we minimize Equation 11.2 with respect to the Monte Carlo energy scale and $\sigma(1/P_T)$ simultaneously, as in Section 11.3. The best fit value for the resolution is $\sigma(1/P_T) = 0.000\ 82 \pm 0.000\ 04$. This agrees with the results above for the fit to the W data. The best fit value for the Monte Carlo energy scale is 0.9990 ± 0.0013. We invert this to get an energy scale on the data, and then we

scale by the factor of 0.996 which has already been applied to the data. We get

$$S_E = 0.9970 \pm 0.0013(stat) \pm 0.00035(X_0) \quad (Z\ E/p\ data) \tag{11.5}$$

This agrees well with the W result of Section 11.3. The uncertainty on the amount of material is the same as for the W result.

We find that there is no dependence on the fitted energy scale as a function of the assumed values for κ. In the W data, the E_T resolution introduces a cut bias on the E/p shape since we cut on E_T and M_T. The M_T cut creates a "running" E_T cut that depends on other event variables. Events that have E_T smeared high tend to get kept and events with E_T smeared low tend to be thrown out. This can create a bias on E/p since the E_T cuts in the W data occur along a rising distribution. For the Z data, however, the E_T cut occurs lower on the E_T distribution.

The best histogram for the Monte Carlo is shown with the data overlaid in Figure 11.12. The residuals of the comparison are also shown. Summing the residuals over the errors squared gives $\chi^2/dof = 1.1$.

We also fit for an energy scale using the geometric mean of E/p of the two decay electrons. The geometric mean is $\sqrt{(E/p)_1(E/p)_2}$, where $(E/p)_1$ and $(E/p)_2$ are the values of E/p for the two electrons. We repeat the likelihood fitting procedure of the above sections, except comparing the geometric mean of the data to the Monte Carlo. We fit using the same E/p bins as above.

We keep κ fixed at 1.6% and minimize Equation 11.2 with respect to the Monte Carlo energy scale and $\sigma(1/P_T)$ simultaneously, as above. The best fit value for the resolution is $\sigma(1/P_T) = 0.000\ 96 \pm 0.000\ 06$. This is $\approx 2\sigma$ higher than the fit value above. It may be that there is a correlation between the resolutions of the two tracks

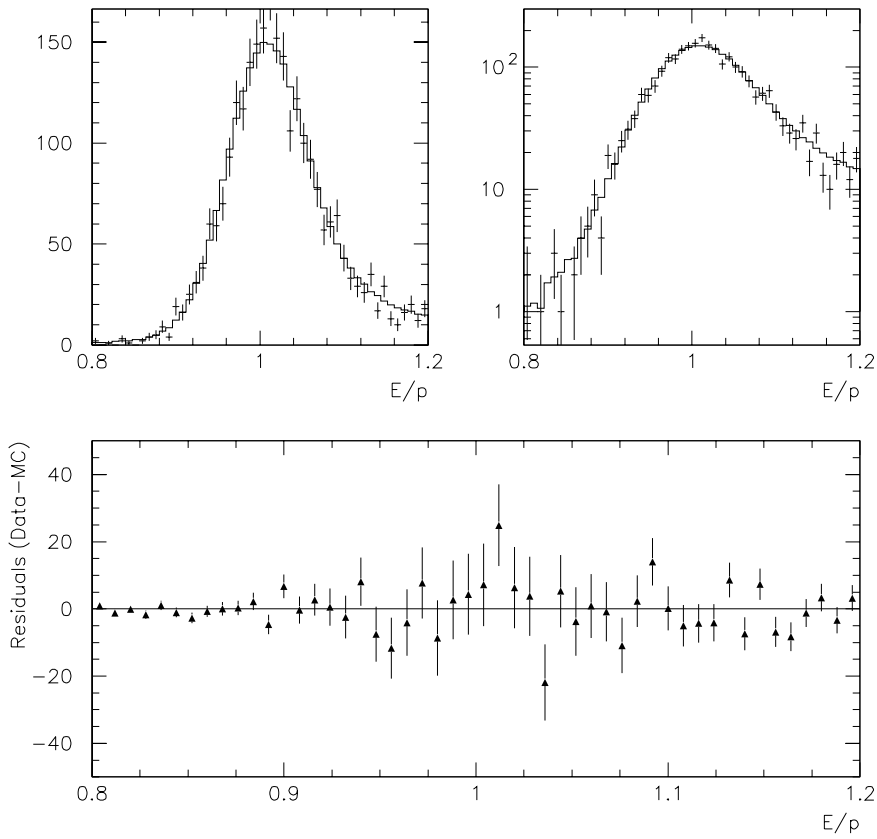

Figure 11.12: Best fit E/p distribution for Z events. Top left and right: Best fit E/p distribution for Monte Carlo (histogram) with data overlaid (crosses), on a linear and log scale. Bottom: the residuals of the top plot, data minus Monte Carlo. The errors on the bottom points are the statistical errors associated with the data. Summing the squares of the points divided by their errors gives $\chi^2/dof = 1.1$. For the Monte Carlo we interpolate between two histograms which have $\sigma(1/P_T)$ near the fitted value. κ is taken to be 1.6%. The data include a scale factor of 0.996, and the Monte Carlo energy scale is 0.9990. The Monte Carlo plots are normalized to the data.

that we are not accounting for in the Monte Carlo. For this fit, we are including the second P_T resolution at a rate of 8%. When we calculate the second resolution, we smear both tracks that are used in the geometric mean. If we only smear one of the tracks, the fit resolution becomes $\sigma(1/P_T) = 0.000\ 97 \pm 0.000\ 06$, which is only slightly higher.

The best fit value for the Monte Carlo energy scale is 0.9997 ± 0.0017, which agrees with the E/p fits above. This number does not change if we smear only one of the tracks with the second resolution. We invert this to get an energy scale on the data, and then we scale by the factor of 0.996 which has already been applied to the data. We get

$$S_E = 0.9963 \pm 0.0017(stat) \pm 0.00035(X_0) \quad (Z\ data) \tag{11.6}$$

The best histogram for the Monte Carlo is shown with the data overlaid in Figure 11.13. The residuals of the comparison are also shown. Summing the residuals over the errors squared gives $\chi^2/dof = 0.82$.

11.5 Conclusion

We have determined a CEM energy scale relative to the CTC scale. The W result is reported in Equation 11.3, and the Z result in Equation 11.5. The results for both the W data and Z data agree. The most significant sources of uncertainty arise from the finite statistics, the amount of material, and the E_T resolution term κ.

The best fit from the W data is Equation 11.3. The result is

$$S_E = 0.99613 \pm 0.00040(stat) \pm 0.00024(\kappa) \pm 0.00035(X_0) \quad (W\ data)$$

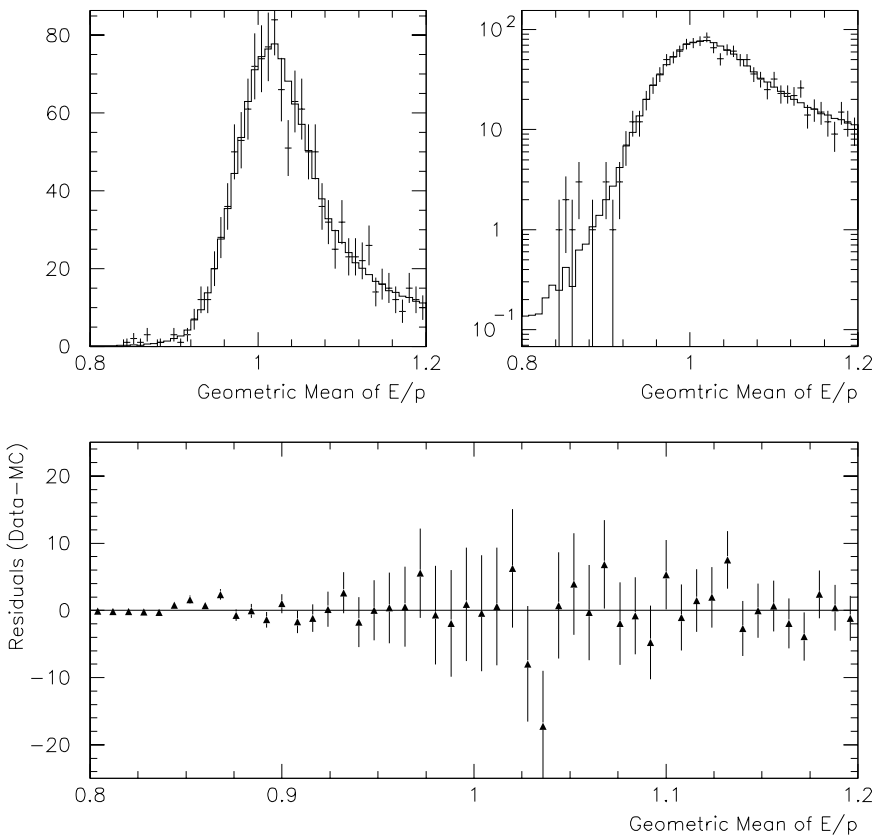

Figure 11.13: Best fit $\sqrt{(E/p)_1(E/p)_2}$ distribution for Z events. Top left and right: Best fit distribution for Monte Carlo (histogram) with data overlaid (crosses), on a linear and log scale. Bottom: the residuals of the top plot, data minus Monte Carlo. The errors on the bottom points are the statistical errors associated with the data. Summing the squares of the points divided by their errors gives $\chi^2/dof = 0.82$. The data include a scale factor of 0.996. The Monte Carlo plots are normalized to the data.

For the Z data we used both the E/p distribution of both legs and the geometric mean of the two values for E/p. The two results are listed in Equation 11.5 and Equation 11.6. The two results are

$$S_E = 0.9970 \pm 0.0013(stat) \pm 0.00035(X_0) \quad (all\ Z\ data)$$

and

$$S_E = 0.9963 \pm 0.0017(stat) \pm 0.00035(X_0) \quad (geometric\ mean\ of\ Z\ data)$$

respectively.

Chapter 12

Non-Linearity Between W and Z Energy Scales

Figure 12.1 shows the E_T distributions of electrons from W and Z decays. The average of the Z events is $\approx$ 4.5 GeV higher than the W events. To extrapolate the energy scale from the Z events to W events, we need to account for potential non-linearities in the CEM scale. We write the nonlinearity as

$$\frac{\Delta S_E}{S_E} = \xi \times E_T \tag{12.1}$$

where $\Delta S_E/S_E$ is the fractional change in the energy scale, and ξ is the slope as a function of E_T. If the CEM is perfectly linear, then ξ will be identically zero.

The calorimeter has several potential sources of non-linearities. For example, the CEM integrates the electron shower energy over 18 radiation lengths. This contains most of the energy from the electron shower, but a small percentage of the energy "leaks" out the back of the calorimeter. The leakage fraction varies with the energy of the electron, since higher E_T electrons deposit more of their energy farther back

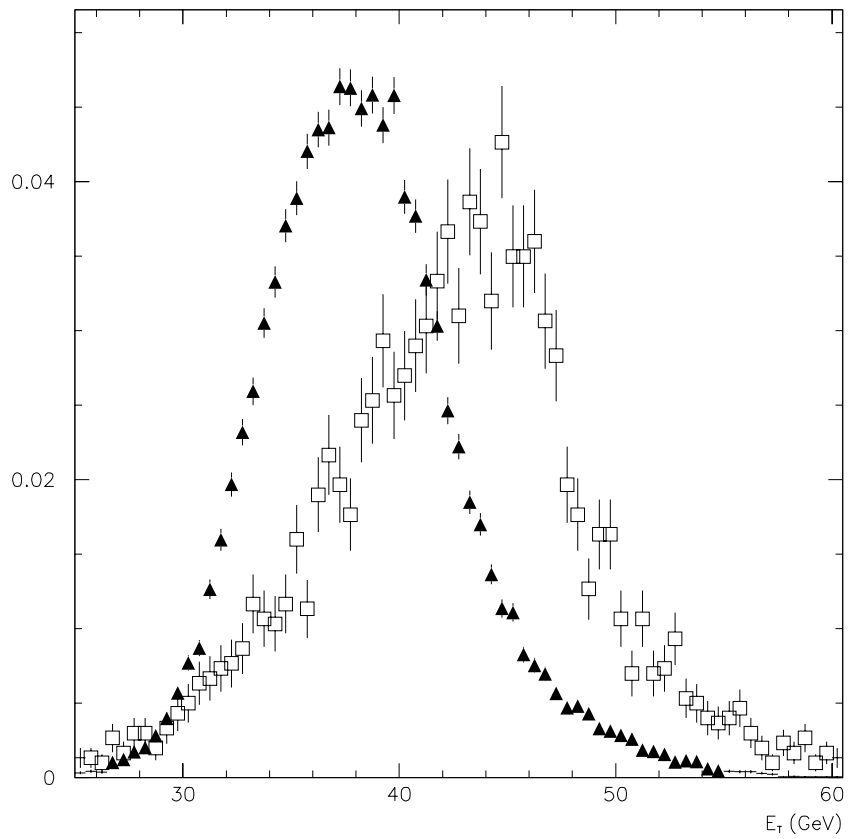

Figure 12.1: E_T distributions for electrons for $W \rightarrow e\nu$ and $Z \rightarrow ee$ data. The squares are for Z events, and the triangles are for W events. For Z decays both electrons are included in the plot. The distributions are normalized to unit area. The average E_T is 38.34 ± 0.03 and 42.7 ± 0.1 GeV for the W and Z data respectively.

in the calorimeter. An EGS study of the CEM predicts that the leakage fraction varies between roughly 2.5% and 3.5% as the electron E_T varies between 25 and 50 GeV [42]. This would produce values for ξ of $\sim 0.000\ 8$ GeV^{-1}.

This source of non-linearity is potentially offset by energy deposited in the solenoid. The solenoid presents ~ 1 radiation length to the electrons before they enter the CEM. The solenoid can reduce the measured CEM energy by several percent [43]. The energy loss before the solenoid will decrease as the electron E_T increases because the shower deposition profile changes with E_T.

Reference [42] further suggests that there is a higher efficiency to measure energy deposited in the back of the CEM since on average the light pulses from the scintillators in the back of the CEM travel a smaller distance to the phototubes. This also would produce a non-linearity which might offset the leakage energy non-linearity.

Another potential source of non-linearity arises from the decline in the CEM response. The CEM response has declined by roughly 10% over the course of Runs 1A and 1B. This decline is not well understood. It may introduce a non-linearity if the decline is not uniform in depth. For example, we have done a simple calculation where we assume that the total CEM decline is 10%, but that the decline occurs at different rates in the different CEM layers. If we assume that the longitudinal decline profile is proportional to the longitudinal energy deposition profile of electrons, then we calculate a change in CEM response of $\sim$ 0.15% over the 4.5 GeV difference between the average E_T of W and Z decay electrons.

There is a potential non-linearity between the E_T ranges of W and Z events on the order of tenths of a percent. This corresponds to $\xi \sim 0.000\ 2$ GeV^{-1}. We do not rely on a calculation of the non-linearity. Instead we use the E/p distribution of W and Z events, implicitly assuming that the CTC P_T measurement is linear over the

E_T range of W and Z events.

In Section 12.1 we measure ξ by comparing the W and Z CEM scales as determined from the E/p distributions. In Sections 12.2 and 12.3 we use the E_T spread of the data to measure ξ. We conclude in Section 12.4.

12.1 Comparison of W and Z E/p Fits

In Chapter 11 we determined an energy scale using the E/p distribution of both W and Z events. The largest systematic uncertainty on both numbers is the amount of material, but this is in common with both measurements and does not effect the difference of the results. For the Z result, we use the fit to the geometric mean of E/p of the two electrons. We use this result, rather than the fit result to E/p of both electrons combined, because the Z mass is proportional to the geometric mean of E_T of the two decay electrons.

The difference between the Z result of Equation 11.6 and the W result of Equation 11.3, relative to the W result, is

$$\frac{\Delta S_E}{S_E} = 0.00017 \pm 0.00177 \tag{12.2}$$

where the uncertainty includes the statistical uncertainties on both fits and the uncertainty on the W result associated with κ. The average value for the geometric mean of E_T for the two legs of $Z \rightarrow ee$ decays is 4.5 GeV higher than the average E_T of electrons in $W \rightarrow e\nu$ events. Dividing Equation 12.2 by 4.5 GeV, we get

$$\xi = 0.000\ 04 \pm 0.000\ 39\ \ GeV^{-1} \tag{12.3}$$

This number is consistent with zero.

12.2 E/p vs E_T for W Events

The E_T distributions of both W and Z events occur over a broad enough range that they overlap. In the sections below we consider different ways of using the E_T spreads to measure ξ.

The top plots of Figure 12.2 show the average of E/p between 0.9 and 1.1 in bins of E_T, for both W and Z events. The structure of the plots is mostly a result of the E_T resolution. Each E_T bin contains events which have E_T mismeasured high and E_T mismeasured low. Where the E_T shape is falling, there will be more events with E_T mismeasured high than low, and E/p will be biased high. The opposite effect occurs where the E_T shape is rising.

The structure of the plots is also effected by the boson recoil energy. The contribution to E_T from the boson recoil energy is not flat in E_T. Higher E_T events tend to be boosted and have the recoil energy directed opposite the electron, while the lower E_T events tend to have the recoil energy directed at the electron cluster. Not only do the higher E_T events have less recoil energy, but the recoil energy is smaller as a fraction of the electron energy. We calculate that the recoil energy decreases from $\approx 0.25\%$ of the electron energy to $\approx 0.15\%$ as the electron E_T varies between 25 and 50 GeV. These effects are included in the Monte Carlo.

The residuals, data minus Monte Carlo, of the top plots of Figure 12.2 are shown in the bottom plots. The slope of the residuals for the W fit is $(2.66 \pm 0.65) \times 10^{-4}$ GeV^{-1}, and the slope for the Z events is $(-1.8 \pm 1.6) \times 10^{-4}$ GeV^{-1} The fits to the residuals include all the points on the plots. If we only use the points with E_T between

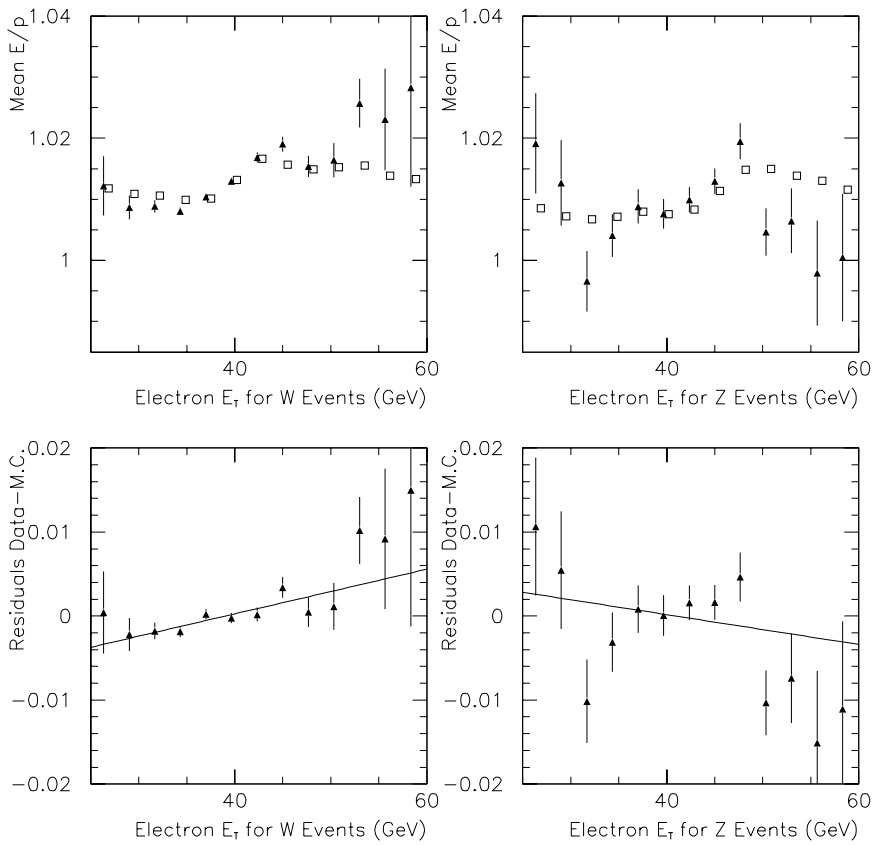

Figure 12.2: Top left and right: Mean E/p between 0.9 and 1.1 for W and Z events respectively. The triangles are data and squares Monte Carlo. The Monte Carlo was run $\kappa = 1.6\%$. The squares are offset slightly to the right to make the points easier to see. Bottom: Residuals of the top two plots, data minus Monte Carlo. The fitted slope for the W events is $(2.66 \pm 0.65) \times 10^{-4}$ GeV^{-1}. For the Z events it is $(-1.8 \pm 1.6) \times 10^{-4}$ GeV^{-1}.

30 and 50 GeV, the slope becomes smaller by 0.3×10^{-4} for the W events. This is not a large change compared to the statistical uncertainty. For the Z events, however, there is a larger change, and the slope becomes $(1.8 \pm 2.0) \times 10^{-4}$ GeV^{-1}.

We combine the W and Z residuals by calculating a weighted average at each point in E_T, weighting according to the statistical uncertainties on each point. This is shown in Figure 12.3. The plot is dominated by the W events, and the slope is $(1.91 \pm 0.58) \times 10^{-4}$ GeV^{-1}. If we just use the points between 30 and 50 GeV, we get a slope of $(2.24 \pm 0.66) \times 10^{-4}$ GeV^{-1}.

In addition to the statistical uncertainty on the slope, we must also consider the uncertainty associated with the electron resolution. We refit the slope using $\kappa = 1.2\%$ and $\kappa = 2.0\%$. We get the slopes 2.53×10^{-4} GeV^{-1} and 1.18×10^{-4} GeV^{-1} for these two values of κ, respectively. We average the magnitude of the difference between these results and the result above for $\kappa = 1.6\%$; and we scale by 0.0027/0.004 since we have varied κ by ± 0.004 but the uncertainty on κ from the Z fit is ± 0.0027. The uncertainty on the slope from the uncertainty on κ is then 0.46×10^{-4} GeV^{-1}.

We use the variations with κ to adjust the fitted slope. Figure 12.3 used the Monte Carlo with $\kappa = 1.6\%$, but the best fit value is $\kappa = 1.53\%$. This is a small correction, and the adjusted slope is $(2.03 \pm 0.58) \times 10^{-4}$ GeV^{-1}.

In Chapter 11, we saw that to convert from a change in the mean of E/p to a change in the fitted energy scale, we should divide by 0.7. We use the adjusted fit to Figure 12.3, and dividing by 0.7, we determine that the CEM response varies with E_T with a slope of

$$\xi = -0.000\,29 \pm 0.000\,08(stat) \pm 0.000\,07(\kappa) \;\; GeV^{-1} \tag{12.4}$$

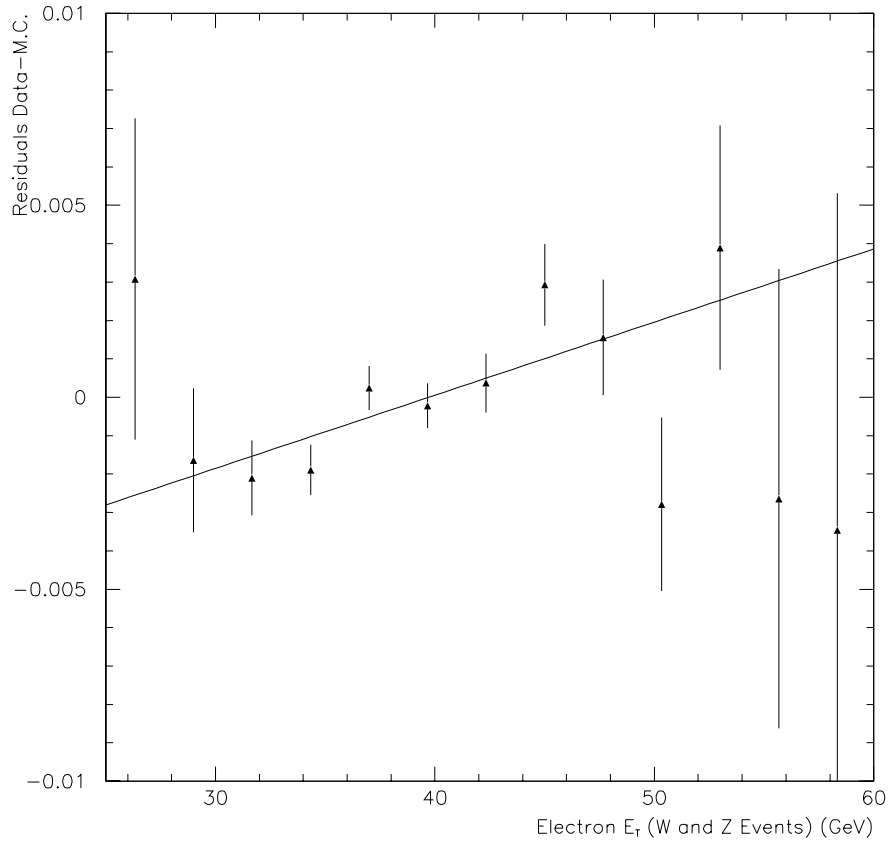

Figure 12.3: Weighted average of W and Z residuals plots of Figure 12.2. The fitted line has a slope of $(1.91 \pm 0.58) \times 10^{-4}$ GeV^{-1} The goodness of fit of the fitted line is $\chi^2/dof = 1.4$. If we fit to a line with no slope, we get $\chi^2/dof = 2.2$.

The minus sign indicates that E/p is growing with E_T and so the fitted energy scale becomes smaller. We multiply by 4.5 GeV to calculate the change in the CEM response between Z and W events. This value for ξ predicts that the response for energies associated with Z events is higher by $(0.13 \pm 0.05)\%$.

12.3 <E/p> vs $U_{||}$ for W Events

In the previous Section we plotted the average of E/p as a function of E_T. These plots are shown in Figure 12.2. One reason the plots are not flat is that we are binning in E_T, and the E_T resolution, in combination with a non-flat E_T distribution, will bias the E/p shape. This is discussed above. If we partition the data as a function of $U_{||}$ instead, we can reduce this effect.

The top plot of Figure 12.4 shows the average of the electron E_T as a function of $U_{||}$. Events with $U_{||}$ negative tend to have higher E_T because the W P_T adds to the electron E_T for those events; and events with $U_{||}$ positive tend to have lower E_T. For $U_{||}$ between ± 20 GeV, the average E_T varies between 30 and 50 GeV. By plotting the mean of E/p as a function of $U_{||}$, we are effectively plotting E/p over a range of values for E_T.

The bottom plot of Figure 12.4 shows the mean of E/p as a function of $U_{||}$. Both data and Monte Carlo are shown. The Monte Carlo shows a slight rise as a function of $U_{||}$. This is the effect of the recoil energy, as discussed in the previous section.

The top plot of Figure 12.5 shows the average E/p for each of the $U_{||}$ bins, as a function of the average E_T in each bin. The y-axis points are the same as the bottom plot of Figure 12.4, but we have plotted them as a function of the average E_T in each $U_{||}$ bin. Both the data and Monte Carlo are shown. The bottom plot shows the

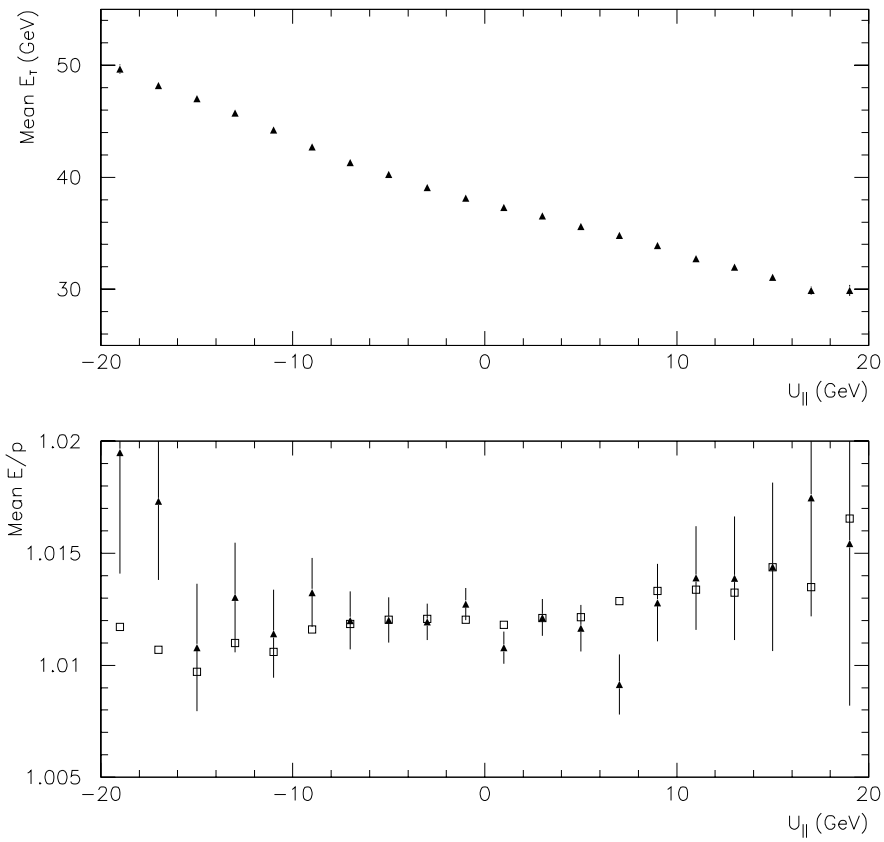

Figure 12.4: Top: Mean E_T vs $U_{||}$ for $W \to e\nu$ data. The E_T average is calculated between 25 and 60 GeV. Bottom: Mean of E/p between 0.9 and 1.1 vs $U_{||}$ for $W \to e\nu$ data (triangles) and Monte Carlo (squares).

residuals of the top plot, data minus Monte Carlo. Two linear fits are shown, one which allows a slope and one which has no slope. The value for χ^2/dof is marginally better for the fit with a slope. The value for the slope is $(2.0 \pm 1.1) \times 10^{-4}$ GeV^{-1}. We divide this by 0.7 to convert from a change in the mean of E/p to a change in the energy scale. We get the result

$$\xi = -0.000\ 29 \pm 0.000\ 15(stat)\ \ GeV^{-1} \tag{12.5}$$

As above, the minus sign indicates that E/p is growing with E_T and so the fitted energy scale becomes smaller.

This value agrees with the result of Equation 12.4. The two numbers are correlated although they have different systematic uncertainties.

To avoid fitting a line through the data of Figure 12.5, we compare the E/p distributions for events with positive $U_{||}$ and events with negative $U_{||}$. We calculate the mean of E/p between 0.9 and 1.1. For the Monte Carlo, events with positive $U_{||}$ have the mean of E/p higher by 0.00054. This is primarily the effect of the recoil energy having a larger percentage contribution for the positive $U_{||}$ events. For the data, the positive $U_{||}$ events have the mean of E/p lower by 0.00097 ± 0.00058. The shift of the data is lower than the shift of the Monte Carlo by $0.00097 + 0.00054 = 0.00151 \pm 0.00058$.

The average E_T for the positive $U_{||}$ events is lower by 4.3 GeV than the negative $U_{||}$ events. If we attribute the difference between the data and the Monte Carlo to a non-linearity, then we calculate ξ by dividing 0.00151 by 4.3 GeV, and also scaling by 1/0.7 to convert from a shift in the mean of E/p to a shift in energy scale. We get

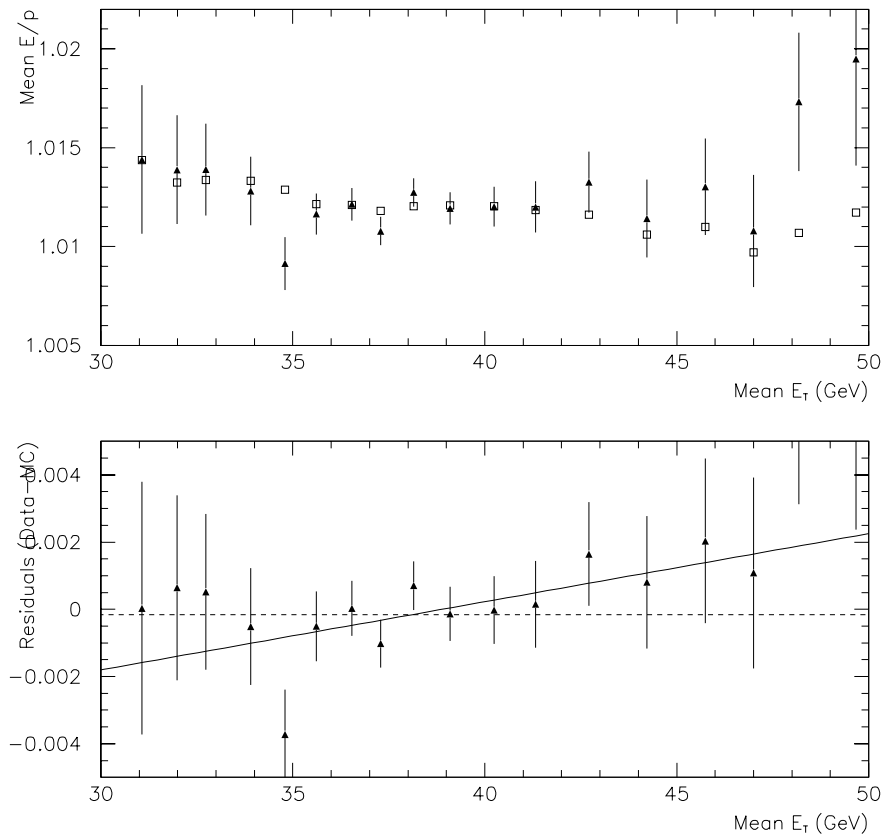

Figure 12.5: Top: <E/p> vs $< E_T >$ for bins of $U_{||}$, for $W \rightarrow e\nu$ events. The triangles are the data and the squares the Monte Carlo. Bottom: The residuals of the top plot. The solid is the result of a linear fit using the points with E_T between 30 and 48 GeV. The slope of the line is $(2.0 \pm 1.1) \times 10^{-4}$ GeV^{-1}. The dotted line is a fit to a line with no slope. The value for χ^2/dof is 0.68 for the fit with a slope, and 0.87 for the fit with no slope.

the result

$$\xi = -0.000\ 50 \pm 0.000\ 19(stat)\ \ GeV^{-1} \tag{12.6}$$

This slope is larger than the results listed in Equations 12.4 and 12.5.

12.4 Conclusion

We have three results which use only the W data to calculate ξ. These are listed in Equations 12.4, 12.5, and 12.6. To combine these numbers, we do a weighted average of the three results. The numbers are highly correlated, and combining the numbers does not improve the statistical uncertainty. They have different systematic uncertainties, but for all three numbers the statistical uncertainties are larger than the systematic uncertainties. We use the smallest uncertainty of the three for the combined uncertainty, and we add the rms of the three numbers as an additional systematic uncertainty. The combined result is

$$\xi = -0.000\ 33 \pm 0.000\ 14\ \ GeV^{-1}\ \ (W\ Data) \tag{12.7}$$

Equation 12.3 is the result for ξ which is calculated by comparing the E/p distributions of W and Z data. This number is independent of the result of Equation 12.7, and two numbers are consistent with each other. We do a weighted average of these two numbers to get the final result

$$\xi = -0.000\ 29 \pm 0.000\ 13\ \ GeV^{-1}\ \ (All\ Data) \tag{12.8}$$

For the W mass fits of the next section we apply a correction for the non-linearity.

We correct the electron energy according to

$$E \rightarrow E \times [1 - 0.00029 \times (E_T - 42.73)] \tag{12.9}$$

where E_T is measured in GeV. The average E_T for Z events is 42.73 GeV, and the correction is such that this average is not changed. We have verified that the energy scale as determined from the Z mass remains 1.0000 ± 0.0010 after the correction. The best fit for κ becomes slightly smaller after the correction. We get $\kappa = (1.50 \pm 0.027)\%$.

Chapter 13

W Mass Fit

In this chapter we fit for the W mass using the transverse mass distribution of the $W \rightarrow e\nu$ data.

The Monte Carlo M_T distribution depends on the W mass, M_W, and the W width, , $_W$, through the Breit-Wigner function of Equation 5.6. Each Monte Carlo event weight is scaled by this function. The Monte Carlo weight also depends on the 14 parameters that determine the $\sum E_T$ shape, the $\vec{U}$ model, and the boson P_T distribution. These parameters effect the event weight through the three probability distributions of Equation 8.1, 8.15, and 7.1. These distributions determine the $\sum E_T$ shape, the $\vec{U}$ distribution, and the boson P_T distribution, respectively.

In Section 13.1 we fit simultaneously for the W mass and width. In Section 13.2 we search for a perturbed set of input parameters, $\vec{\omega}_W$, which are consistent with the input parameters from the Z fits, $\vec{\omega}_Z$, but which better describe the W data. In Section 13.3, we use the parameters $\vec{\omega}_W$ to determine the W mass. We use these fits for the final W mass determination. We discuss systematic uncertainties in Section 13.4; and in Section 13.5 we perform several checks on the fits.

In Chapter 9 we compared the W data to the Monte Carlo using the input parameters $\vec{\omega}_Z$, as well as the perturbed parameters $\vec{\omega}_W$.

13.1 W Mass and Width Fits Using Inputs Parameters from Z Data, $\vec{\omega}_Z$

In this section, we determine the W mass using the simulation input parameters which were derived from the Z data. There are 14 Monte Carlo input parameters which have been determined from the Z data. The calorimeter response model depends on the 3 parameters of $\vec{\Pi}_\Sigma$ which determine the $\sum E_T$ shape, and also on the 7 parameters of $\vec{\Pi}_U$, which determine the $\vec{U}$ shape. These parameters were fit to the Z data in Chapter 8. In addition, there are 4 parameters in $\vec{\Pi}_x$ which determine the P_T^{boson} shape, and these were fit to the Z data in Chapter 7.

The input parameters are fixed at the values which were fit to the Z data, and we float the W mass and width. We find a minimum of the binned likelihood function

$$L = -2 \times \sum_{M_T\ bins} [-\lambda_i T + n_i \log(\lambda_i T)] \tag{13.1}$$

where M_T is binned in 35 bins from 65 to 100 GeV, n_i is the number of data points in bin i, and λ_i is the sum of the weights of the Monte Carlo events in bin i. The quantity T normalizes the Monte Carlo to the data and is the number of data points divided by the sum of all the Monte Carlo weights.

The fit results are $M_W = 80.438 \pm 0.073(stat)$ GeV, and $,_W = 2.41 \pm 0.16(stat)$ GeV. The uncertainties are the square roots of the diagonal part of the covariance matrix, and the off-diagonal element is -4.5×10^{-3} GeV^2. The 2×2 covariance

matrix represents the statistical uncertainty associated with the W statistics of the transverse mass fit.

The Standard Model predicts a value for $,_W$ that is proportional to M_W^3 [44]. We define the quantity R_Γ, where

$$R_\Gamma \equiv ,_W / M_W^3 \tag{13.2}$$

The Standard Model prediction for R_Γ is [44]

$$R_\Gamma(s.m.) = (4.022 \pm 0.008) \times 10^{-6}\ GeV^{-2} \tag{13.3}$$

QCD and QED radiative corrections are included in this number. The uncertainty is dominated by the uncertainty on α_s.

The fitted value for R_Γ is $R_\Gamma \equiv ,_W / M_W^3 = (4.63 \pm 0.31) \times 10^{-6}$ GeV^{-2}. This is higher than the Standard Model value by $(4.63 - 4.02)/0.31 = 2.0$ statistical standard deviations. Figure 13.1 shows the $1-$ and $2-\sigma$ contours of the fitted width vs the fitted W mass, as determined by the fit covariance matrix.

The parameter $,_W$ determines how quickly the M_T distribution drops off at its falling edge. The input Monte Carlo parameters, which determine the $\vec{U}$ model and the boson P_T distribution, also effect the sharpness of the falling edge. Thus we expect the fitted width and the input parameters to have a strong correlation. To plot the correlation we vary the input parameters according to their uncertainties, and we recalculate fit values for M_W and $,_W$.

We vary the 7 parameters of $\vec{\Pi}_U$ according to the covariance matrix $\tilde{C}_U$, which is discussed in Chapter 8. These parameters determine the $\vec{U}$ model. We then refit for the W mass and width using these new values for $\vec{\Pi}_U$. We do this 100 times. The 100 results are shown as the filled triangles in Figure 13.1. The 100 results form a

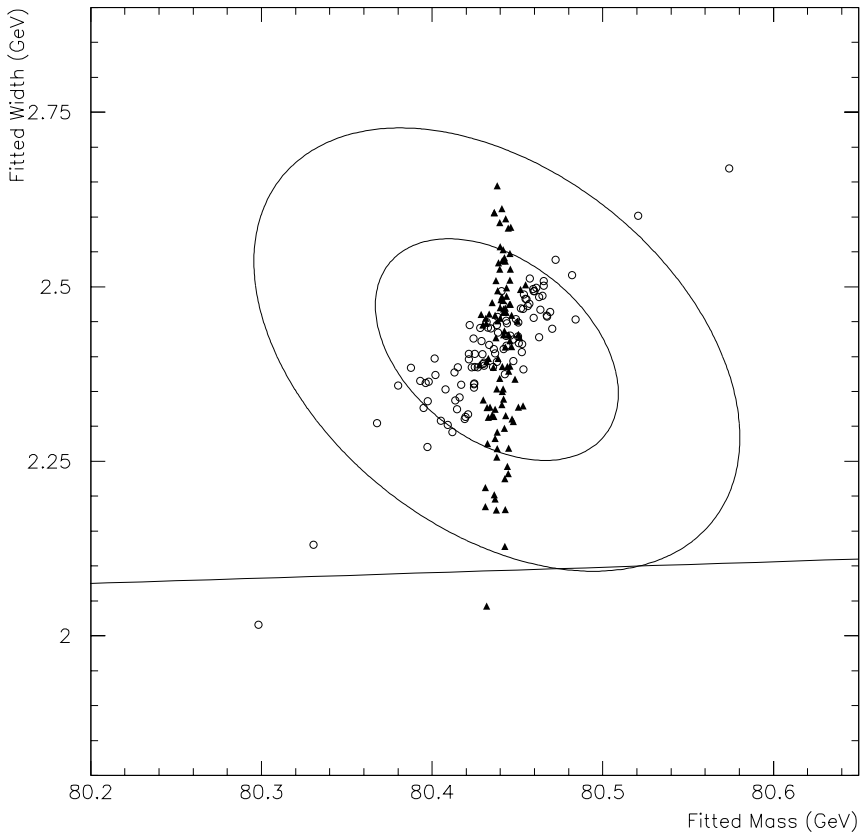

Figure 13.1: The fitted width as a function of the fitted mass, using the Monte Carlo inputs fixed at the fits to the Z data, $\vec{\omega}_Z$. The ovals are the $1-$ and $2-\sigma$ contours of the fit. The line represents the Standard Model prediction for the width, $,_W = R_\Gamma M_W^3$ where $R_\Gamma = (4.022 \pm 0.008) \times 10^{-6}$ GeV^{-2}. There are also 200 points shown. The 100 open circles are the results for the fitted mass and width after varying the Monte Carlo boson P_T input parameters, $\vec{\Pi}_x$, randomly according to their covariance matrix. The 100 filled triangles are the results after varying the $\vec{U}$ model parameters, $\vec{\Pi}_U$ according to their covariance matrix.

narrow vertical band, showing a strong correlation with the fitted width. Errors on the $\vec{U}$ model input parameters are compensated for by errors on the fitted width.

We also vary the 4 parameters of $\vec{\Pi}_x$, and keep the $\vec{U}$ model parameters fixed. We vary these 4 parameters according to their covariance matrix, which is discussed in Chapter 7. The 100 results for the fitted mass and width are shown as the open circles in Figure 13.1. The effect of errors on the boson P_T has a stronger effect on the fitted mass than the $\vec{U}$ model parameters.

Our fitted width may be high because of imperfections in the input parameters. The parameters were determined from the Z data, and may not perfectly describe the higher statistics of the W data. The spread of the points in Figure 13.1 indicates that there are regions of the input parameter space which are consistent with the Z fits and which give a fitted W width which is within one standard deviation of the expected value.

13.2 Perturbing the Input Parameters

In the previous section, we saw that the $\vec{U}$ model input parameters, $\vec{\Pi}_U$, were strongly correlated with the fitted width. The boson P_T parameters, $\vec{\Pi}_x$, were also correlated, although not as strongly. These parameters were determined from the Z data, and we do not necessarily expect them to perfectly describe the higher statistics W data. We wish to find a set of input parameters which are consistent with the Z data, and which better describe the W data.

We allow all 11 parameters of $\vec{\omega} \equiv (\vec{\Pi}_x, \vec{\Pi}_U)$ to vary. These 11 parameters determine the boson P_T distribution and the $\vec{U}$ model. We also allow the W mass to vary since the M_T and E_T distributions depend on the W mass, and we include both of

those variables in the minimization function below.

We keep the width fixed at the Standard Model prediction. Instead of fitting the M_T distribution, we include several other functions which provide constraints on the parameters. The function we minimize with respect to these 12 parameters is

$$L = L(M_T) + L(E_T) + L(|\vec{U}|) + L(U_{||}) + \Delta(\vec{\Pi}_U) + \Delta(\vec{\Pi}_x) \tag{13.4}$$

where $L(M_T)$ is exactly the binned log likelihood function of Equation 13.1; and $L(E_T)$, $L(|\vec{U}|)$, and $L(U_{||})$ are the corresponding binned log likelihood functions for the E_T, $|\vec{U}|$, and $U_{||}$ shapes, respectively. They are defined as in Equation 13.1 except that $L(E_T)$ uses the E_T distribution, binned in 30 bins between 25 and 55 GeV; $L(|\vec{U}|)$ uses the $|\vec{U}|$ distribution binned in 20 bins from 0 to 20 GeV, and $L(U_{||})$ uses the $U_{||}$ distribution, binned in 40 bins from -20 to 20 GeV. The functions $\Delta(\vec{\Pi}_U)$ and $\Delta(\vec{\Pi}_x)$ constrain the floated input parameters to remain near the original Z fits. They are defined as $\Delta(\vec{\Pi}_U) \equiv (\vec{\Pi}_U - \vec{\Pi}_U^Z) \cdot \tilde{C}_U^{-1} \cdot (\vec{\Pi}_U - \vec{\Pi}_U^Z)$, and $\Delta(\vec{\Pi}_x) \equiv (\vec{\Pi}_x - \vec{\Pi}_x^Z) \cdot \tilde{C}_x^{-1} \cdot (\vec{\Pi}_x - \vec{\Pi}_x^Z)$, where $\vec{\Pi}_U^Z$ and $\vec{\Pi}_x^Z$ are the original values for the parameters as determined from the Z data, and where $\tilde{C}_U$ and $\tilde{C}_x$ are the corresponding covariance matrices from the Z fits.

Figure 13.1 shows that there is a set of parameters which is consistent with the Z fits, and which produces a value for the W width which is consistent with the Standard Model prediction. However, these parameters may not produce good fits to all the W distributions, and may even produce worse fits. The four likelihood functions of Equation 13.4 include information from the W data and force the chosen set of parameters to produce reasonable fits for these distributions. The four functions are all correlated since $U_{||}$ depends on $|\vec{U}|$, and M_T depends on $\vec{U}$ and E_T. This will

not invalidate the fit results, but it will make the fitted uncertainty on the parameters difficult to interpret. We will not use the uncertainties from this fit.

We refer to the resulting parameters $\vec{\Pi}_x$ and $\vec{\Pi}_U$ as $\vec{\omega}_W \equiv (\vec{\Pi}_x, \vec{\Pi}_U)$. These parameters are listed in Table A.1 of Appendix A. The parameters $\vec{\omega}_W$ are consistent with the Z fit parameters $\vec{\omega}_Z$. Using the final fit results we get $\Delta(\vec{\Pi}_x) = 1.4$ and $\Delta(\vec{\Pi}_U) = 4.9$, which are small numbers for the 4−dimensional and 7−dimensional fits for $\vec{\Pi}_x$ and $\vec{\Pi}_U$ respectively. The fitted values for the mass is $M_W = 80.443$ GeV, which is close to the result of Section 13.1.

The W Monte Carlo using the fit results $\vec{\omega}_W$ are plotted in Chapter 9.

13.3 W Mass Fit Using Perturbed Input Parameters, $\vec{\omega}_W$

We fit for the W mass using just the M_T distribution. We keep the input parameters fixed at the new, perturbed values $\vec{\omega}_W$, and we let the W mass and width float. The W mass may be different from the previous section because we are only including the M_T distribution.

When we minimize Equation 13.1 with respect to the W mass and width, and we get the fit results $M_W = 80.426 \pm 0.073(stat)$ GeV, and , $_W = 2.33 \pm 0.16(stat)$ GeV. We compare this result to the Standard Model prediction of Equation 13.3. Our value for the width is higher than the Standard Model prediction by $(4.48 - 4.02)/0.31 = 1.5$ statistical standard deviations.

We fit for the W mass with the width fixed at the Standard Model prediction,

and M_W allowed to float. The fit result is

$$M_W = 80.473 \pm 0.65(stat)\ GeV \tag{13.5}$$

A plot of the binned likelihood function of Equation 13.1 is shown in Figure 13.2. In this plot, the input parameters are held fixed, and we calculate Equation 13.1 as a function of M_W.

For the fitted W mass we use the result with the width fixed and the parameters fixed at the floated values $\vec{\omega}_W$. This is the result of Equation 13.5 above.

13.4 Systematic Uncertainties on the W Mass

In this section we measure various contributions to the systematic uncertainty on M_W. For all the M_W fits which we do in this section we fix $,_W$ at the Standard Model prediction, and we fix the Monte Carlo input parameters at $\vec{\omega}_W$. Only the W mass is floated in the fits.

13.4.1 Energy Scale

We vary the energy scale on the data, S_E, between 0.995 and 1.005, before we apply any cuts, and we re-fit for the W mass. For each value of S_E, we calculate the ratio $M_W/M_W(S_E = 1)$, where $M_W(S_E = 1)$ is the result for $S_E = 1$. $M_W(S_E = 1)$ is the best fit result of Equation 13.5 above. Figure 13.3 shows this ratio as a function of S_E. The plot shows that a fractional change in the energy scale leads to the same fractional change in M_W.

We set the energy scale using $Z \rightarrow ee$ events. This is discussed in Chapter 10.

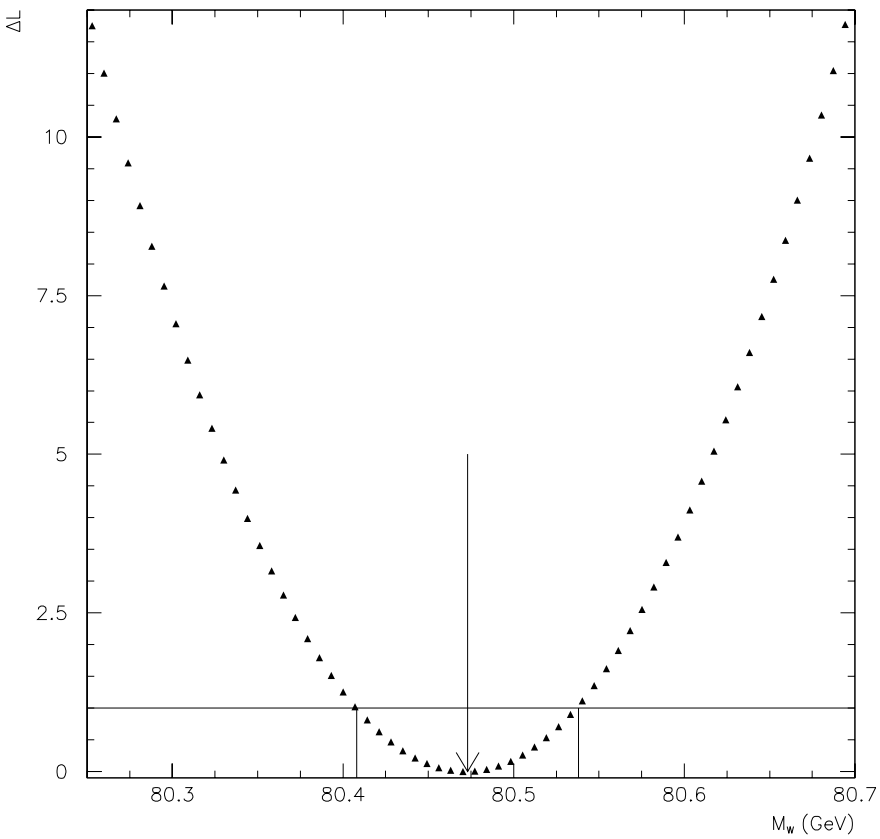

Figure 13.2: Binned likelihood for the M_T distribution as a function of M_W. The $y-$axis is L of Equation 13.1 with the value of the function at the minimum subtracted off. L is -2 times a binned likelihood function. The location of the minimum is indicated by the arrow. The horizontal line is a line at 1 and indicates the change in L that corresponds to a $1-\sigma$ variation on M_W. The two small vertical lines indicate the $1-\sigma$ bounds on the fitted value for M_W.

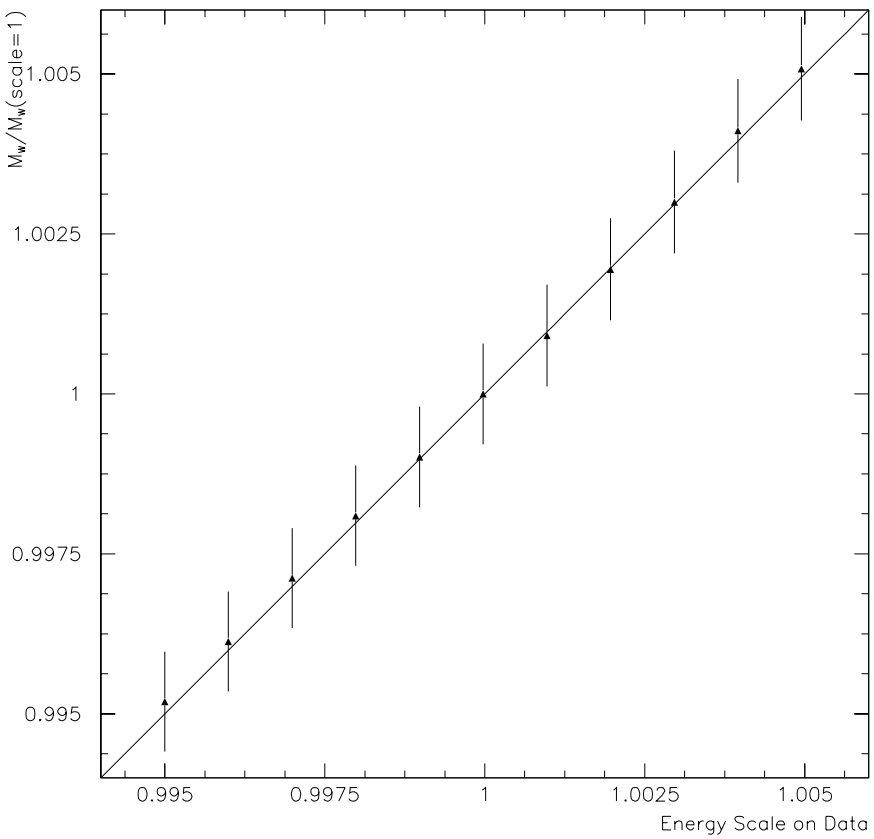

Figure 13.3: The fitted value for M_W relative to $M_W(S_E = 1)$ as a function of the energy scale on the data, S_E. $M_W(S_E = 1)$ is the W mass result for an energy scale of 1.0. A line with a slope of 1 is also shown.

The uncertainty on the energy scale is 0.1%, and, therefore, the fractional uncertainty on the W mass from the energy scale is 0.1%. The contribution to the uncertainty on M_W is

$$\sigma = 0.080\ GeV\ (scale) \tag{13.6}$$

13.4.2 Energy Scale Non-linearity

The energy scale is determined from the invariant mass of $Z \rightarrow ee$ events. To apply this scale to W events, we considered the possibility that there is a non-linearity in the CEM energy response. The non-linearity is measured in Chapter 12. The data has the non-linearity correction of Equation 12.9 applied. This correction increases the E_T of electrons which have $E_T < 42.73$ GeV, and decreases E_T for $E_T > 42.73$ GeV. The number 42.73 GeV is near the average E_T of electrons from $Z \rightarrow ee$ events, and it is such that the measured energy scale from Z events is unchanged. The average E_T from $W \rightarrow e\nu$ events is 38.34 GeV, and the E_T of these events is increased on average by 0.13%. This is an increase of ~ 50 MeV.

However, even though the E_T of each W decay electron is increased by ~ 50 MeV on average, the average of the E_T distribution is observed to increase by less than 5 MeV. The reason for this is that by increasing the E_T of the events, we increase the number of events that pass the E_T and M_T cuts. These new events appear at lower E_T, and they lower the average of the E_T distribution. For the average of the E_T distribution, this effect compensates for the non-linearity correction.

Similarly, the percentage change in the average of the M_T distribution is smaller than 0.13%. We find that the non-linearity correction causes the mean of M_T to increase by 17 MeV, where the mean is calculated between 65 and 100 GeV.

To measure the effect of the non-linearity correction on the W mass, we fit for

M_W without applying it the data. Without the correction, there 253 fewer events that pass all the cuts. We fit for the W mass with the width fixed at the Standard Model value, and we hold the Monte Carlo input parameters fixed at $\vec{\omega}_W$. We get a result that is 34 MeV lower than the best fit result of Equation 13.5 above, which has the non-linearity correction applied. 34 MeV is 0.04% of the W mass, roughly a third the size of the average non-linearity correction that is applied to the $W \rightarrow e\nu$ events.

The uncertainty on the non-linearity correction, from Equation 12.8, is slightly less than 50% of the correction itself. The entire correction changes the measured mass by 34 MeV. We take the uncertainty on M_W from the non-linearity to be 50% of this change. The contribution to the uncertainty on M_W is therefore

$$\sigma = 0.017\ GeV\ (CEM\ non-linearity) \tag{13.7}$$

The non-linearity correction also has an effect on the measured W width. Since lower E_T electrons get more of an increase on average than higher E_T electrons, the correction tends to make the E_T shape narrower. The rms of the E_T shape is reduced by $\sim 0.5\%$ by the correction. The change in the M_T shape is more noticeable. The non-linearity correction makes the falling edge of the M_T distribution sharper. If we float the W width in the M_W fit, we find that the fitted value for , $_W$ is increased by 0.14 GeV if we do not apply non-linearity correction. The uncertainty on , $_W$ from the uncertainty on the non-linearity is $\sim 50\%$ of this shift, or 0.070 GeV. This large change in the fitted width may indicate that our fitted width comes out high because we have not applied a large enough non-linearity correction.

13.4.3 Monte Carlo Input Parameters

The Monte Carlo input parameters determine the boson P_T shape and the $\vec{U}$ model. To determine the effect of the input parameters on the W mass, we allow all 11 parameters to float, as well as the W mass, and we minimize the function

$$L = L(M_T) + \Delta(\vec{\Pi}_U) + \Delta(\vec{\Pi}_x) \tag{13.8}$$

where $L(M_T)$, $\Delta(\vec{\Pi}_U)$, and $\Delta(\vec{\Pi}_x)$ are as defined in Equation 13.4 above. The functions $\Delta(\vec{\Pi}_U)$ and $\Delta(\vec{\Pi}_x)$ constrain the parameters to be near the original Z fit values, relative to the statistical uncertainties on those fits.

The uncertainty on M_W from this fit includes the effect of allowing the parameters to vary within their uncertainties. The resulting value for M_W is $M_W = 80.476 \pm 0.075(stat + inputs)$ GeV. When we fix the parameters in the fit and only allow M_W to vary, the uncertainty on M_W is 0.065 GeV. The uncertainty with the parameters allowed to float is 0.075 GeV. Therefore Monte Carlo input parameters contribute

$$\sigma = \sqrt{0.075^2 - 0.065^2} = 0.037 GeV \tag{13.9}$$

to the total uncertainty on M_W.

When we determined $\vec{\omega}_W$, we used the W data to constrain the allowed parameters, and not just the Z data. The uncertainty calculated above assumes that we are only using the Z data to constrain the input parameters, and therefore is an overestimate of the uncertainty. To be conservative, we quote this overestimate for the systematic uncertainty from the input parameters.

13.4.4 Backgrounds

The Monte Carlo includes backgrounds from QCD events, $Z \rightarrow ee$ events, and $W \rightarrow \tau\nu$ events. These backgrounds are discussed in Chapter 4. The $W \rightarrow \tau\nu \rightarrow e\nu\nu\nu$ background is well known, and we do not consider a contribution to the uncertainty from this background. To measure the effect of the other backgrounds, we fit for the W mass without them. These backgrounds are the QCD background, the lost Z background, and the $W \rightarrow \tau\nu \rightarrow$hadrons$+\nu$ background.

The fitted W mass comes out 12 MeV lower than the W mass which includes these backgrounds in the Monte Carlo. This is a small change for a large change in the background rate. We therefore do not attribute any uncertainty on M_W to the backgrounds.

13.4.5 Electron Resolution

The E_T resolution consists of a stochastic term added in quadrature with a constant term. The constant term, κ, was determined in Chapter 10. The best fit is $\kappa = 0.0153 \pm 0.0027$, as listed in Equation 10.2. To determine the uncertainty on the fitted W mass from the uncertainty on κ, we use a Monte Carlo histogram that has $\kappa = 1.6\%$. We fit this histogram as if it were real data.

The Monte Carlo that we use to fit this histogram is run with several different values of κ. We find that if we change κ by $\Delta\kappa$, the fitted value for M_W changes by $10 \times \Delta\kappa$ GeV. The uncertainty on κ is 0.0027, and therefore the uncertainty on M_W is 10 GeV times 0.0027. This number is

$$\sigma = 0.027\ GeV\ (\kappa) \tag{13.10}$$

13.4.6 Parton Distribution Functions

The measured W mass is effected by the parton distribution functions (PDFs) in two ways. The distribution functions determine the parton luminosities. Since the parton luminosities are falling distributions, they will create a bias towards the production of W events at lower $\sqrt{\hat{s}}$. The PDFs also determine the longitudinal momentum distribution of the W.

Since E_T and M_T are transverse quantities, they are not changed by the longitudinal boost of the event. However, by requiring that the electrons land in the central calorimeter, we introduce a dependence on the longitudinal boost. A longitudinal boost will cause some central electrons to land in the plug region, and some plug electrons to land in the central; and the plug electrons have lower E_T than the central on average.

Figure 13.4 shows the variation on M_W for 12 recent parton distribution functions[45]. The fit values for M_W for each of the distributions was determined by comparing the mean of the M_T distributions. For this comparison the Monte Carlo only uses generated quantities, rather than measured quantities. It requires only that the electron is central, and that the electron and neutrino both have E_T above 25 GeV. It is also required that M_T fall between 65 and 100 GeV. This simpler Monte Carlo should be adequate since we are only interested in the variation in the fit results among the PDFs, and not the absolute value of M_W.

The results are plotted relative to the MRSD-′ result. We compare to MRSD-′ since that was the PDF used for the Run 1A W mass measurement. We are using the MRS-R2 PDFs. If we were to use MRSD-′ our result on M_W would come out $\sim$ 30 MeV higher. The 12 PDFs in Figure 13.4 have an rms on M_W of 6 MeV.

In the Run 1A analysis, the CDF W asymmetry data was used to constrain

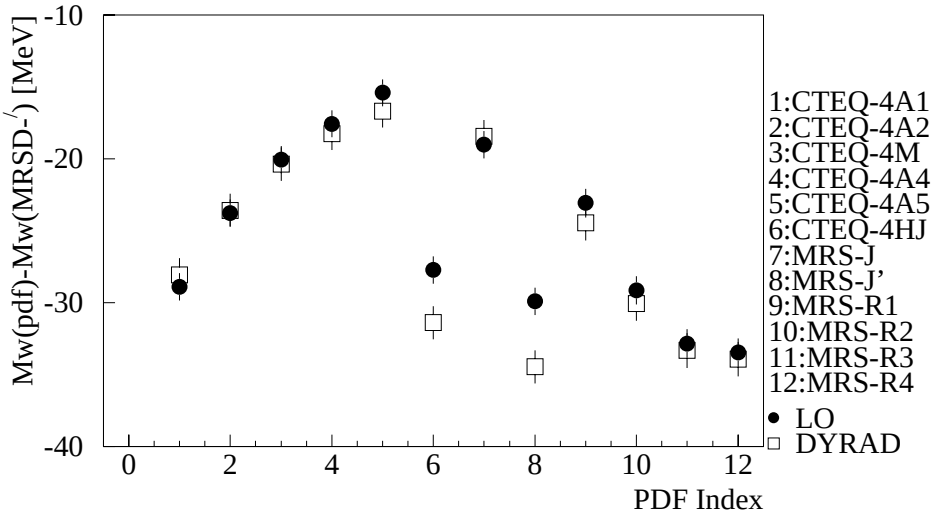

Figure 13.4: Shift in the fitted mass M_W for 12 different parton distribution functions, relative to the 1A default distribution function, MRSD-′. The 12 functions are listed on the right side of the plot. For this plot, the Monte Carlo only used generated quantities. The solid circles are generator with a leading order matrix element, and the open circles are for the DYRAD generator, which uses a next to leading order calculation. The rms of the 12 results is 6 MeV. This figure is taken from [45].

acceptable PDFs. The asymmetry is the difference in the number of positive and negative electrons as a function of pseudorapidity. This quantity is sensitive to the ratio of the u and d quark momentum distributions. The 1A asymmetry analysis only used electrons in the central regions. Recent PDFs include the results of the 1A data, and these distributions produce the same asymmetry as the CDF data, in the central region.

We calculate the quantity ΔA to be the difference between the average asymmetry of the data and the average of the Monte Carlo, relative to the uncertainty on the data. If we only use the central region in the average, the values for ΔA from the PDFs in Figure 13.4 are all between 0 and 1.

The 1B asymmetry measurement has been extended to pseudorapidities of nearly 2. In the region above ~ 1.2 the asymmetry of the data is significantly closer to 0

than the value predicted by any of the PDFs we examine. If we include all rapidity in the calculation of ΔA, then the PDFs in Figure 13.4 all produce values around -2.

In the 1A analysis a correlation was observed between ΔA and the fitted value for M_W for the different PDFs. A similar correlation is observed for the recent PDFs, although the variation in ΔA among the recent PDFs is significantly smaller. This correlation is used to estimate that a change in ΔA of 2 would produce a 25 MeV change in the mass.

This is likely an overestimate because we do not expect that changes in the asymmetry at high values of pseudorapidity will have as strong an effect on the mass as changes as lower values of pseudorapidity. On the other hand, the rms of the points shown in Figure 13.4 is an underestimate of the uncertainty from the PDFs because the PDFs were determined from mostly the same data. To be conservative we assign an uncertainty on M_W of

$$\sigma = 0.025\ GeV\ (PDF) \tag{13.11}$$

from the parton distribution functions.

13.4.7 Monte Carlo Statistical Uncertainty

The fits are done with slightly more than 1.8 million weighted Monte Carlo events. To determine the statistical uncertainty associated with this number of weighted events, we divide the Monte Carlo into 10 independent samples of 180,000 events each. We fit for the W mass with each of the 10 samples. The 10 results have an rms of 0.055 GeV. The statistical uncertainty on the full sample is $0.055/\sqrt{10} = 0.017$ GeV.

If we add this in quadrature to the statistical uncertainty from the data, we can calculate a combined statistical uncertainty of the data and the Monte Carlo.

This value is $\sqrt{0.065^2 + 0.017^2} = 0.067$ GeV. This is a small increase relative to the statistical uncertainty on the data. We conclude that the uncertainty associated with the Monte Carlo statistics is small relative to the statistical uncertainty on the data. We include a statistical uncertainty of

$$\sigma = 0.017\ GeV\ (Monte\ Carlo) \tag{13.12}$$

to account for the finite Monte Carlo statistics.

13.5 Checks on the W Mass Fits

In this section we look for systematic biases on the W mass fit by making various cuts on the data and Monte Carlo and refitting for the W mass. For all the fits below we fix , $_W$ at the Standard Model prediction, and the we fix the Monte Carlo input parameters at $\vec{\omega}_W$. Only the W mass is floated in the fits.

13.5.1 M_W in Bins of $|\vec{U}|$ and $U_{||}$

$\vec{U}$ is our measure of the boson P_T. We partition the data and Monte Carlo into four bins of $|\vec{U}|$, and also four bins of $U_{||}$. We then fit for M_W using the transverse mass shape for each of the $|\vec{U}|$ and $U_{||}$ bins. This is a check that our model reproduces the M_T shape of the data as a function of the boson P_T. It is also a check that errors in the $\vec{U}$ modelling are not significantly biasing the fitted value for M_W. Moreover, since $M_T \approx 2E_T + U_{||}$, partitioning the data in $U_{||}$ allows a check that we are correctly simulating the correlation between E_T and $U_{||}$. E_T and $U_{||}$ are correlated because both variables are strongly effected by the W P_T.

First we divide the data and Monte Carlo into four bins in $|\vec{U}|$: $0 < |\vec{U}| < 5$, $5 < |\vec{U}| < 10$, $10 < |\vec{U}| < 15$, and $15 < |\vec{U}| < 20$ GeV. We fit for M_W in each bin. We define ΔM_W to be the difference between the fit results in each of the four bins, and the fit result of Equation 13.5 above. We get $\Delta M_W = -1 \pm 86$, $\Delta M_W = -36 \pm 110$, $\Delta M_W = 161 \pm 204$, and $\Delta M_W = -348 \pm 385$ MeV, respectively, for each of the four bins. The uncertainties are the statistical uncertainties on the fits in each of the $|\vec{U}|$ regions. The results are plotted in Figure 13.7 below.

Figure 13.5 shows the M_T distributions for data and Monte Carlo for each of the four $|\vec{U}|$ regions. The Monte Carlo distributions use the best fit value for M_W in each region. The M_T shape changes significantly among the four different $|\vec{U}|$ bins, and the changes in the data are tracked by changes in the Monte Carlo.

Instead of binning according to $|\vec{U}|$, we also try dividing the data and Monte Carlo into four bins of $U_{||}$. The bins are $-20 < U_{||} < -10$, $-10 < U_{||} < 0$, $0 < U_{||} < 10$, and $10 < U_{||} < 20$ GeV. We fit for M_W in each bin, and we get the results $\Delta M_W = 152 \pm 370$, $\Delta M_W = 16 \pm 90$, $\Delta M_W = -3 \pm 92$, and $\Delta M_W = 443 \pm 394$ MeV, respectively, for each of the four bins. The uncertainties are the statistical uncertainties on the fits in each of the $U_{||}$ regions. The results are plotted in Figure 13.7 below.

Figure 13.6 shows the M_T distributions for data and Monte Carlo for each of the four $U_{||}$ regions. The Monte Carlo distributions use the best fit value for M_W in each region. As for $|\vec{U}|$ bins above, the M_T shape changes significantly among the four different $U_{||}$ bins, and the changes in the data are tracked by changes in the Monte Carlo.

The results of the four M_W fits in $|\vec{U}|$ bins and the four in $U_{||}$ bins are plotted in Figure 13.7. The numbers are consistent with each other and with the best fit value for M_W from Equation 13.5 above. This indicates that our Monte Carlo reproduces

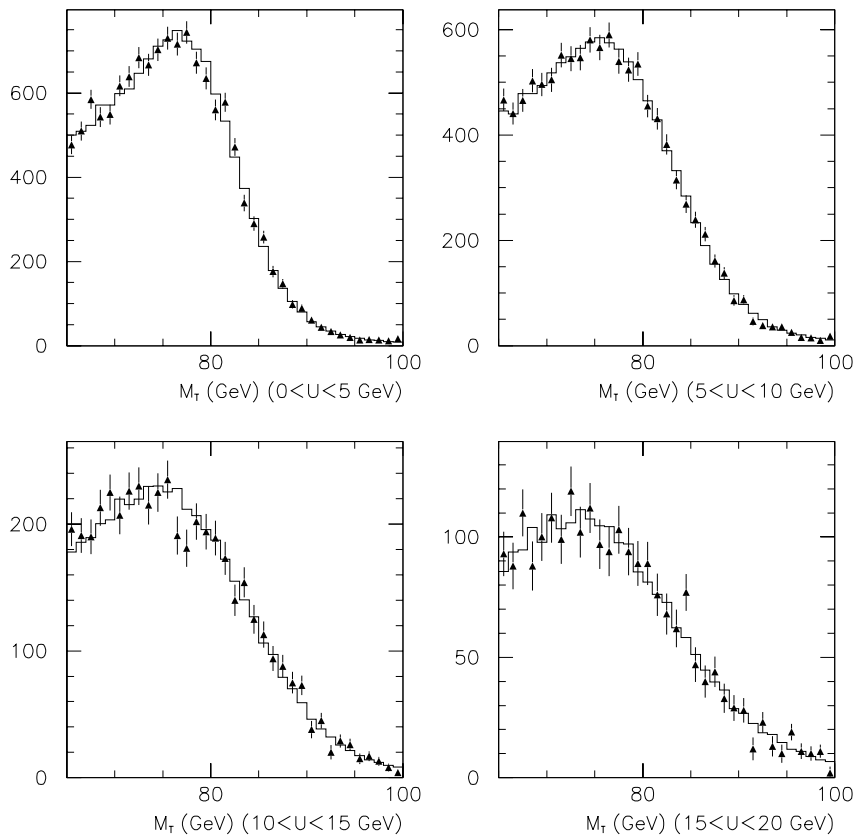

Figure 13.5: M_T distributions in bins of $|\vec{U}|$, for $W \to e\nu$ data and Monte Carlo. The four $|\vec{U}|$ bins are $0 < |\vec{U}| < 5$ (upper left), $5 < |\vec{U}| < 10$ (upper right), $10 < |\vec{U}| < 15$ (lower left), and $15 < |\vec{U}| < 20$ (lower right) GeV. The data are the triangles and the Monte Carlo are the histograms. The four Monte Carlo plots use slightly different values for M_W: they each use the best fit value for M_W in each of the regions. The comparison of data to Monte Carlo in each of the four regions gives $\chi^2/dof = 1.4$ (upper left), 0.92 (upper right), 1.1 (lower left), and 1.1 (lower right), where we simply take the number of M_T bins to be the number of degrees of freedom.

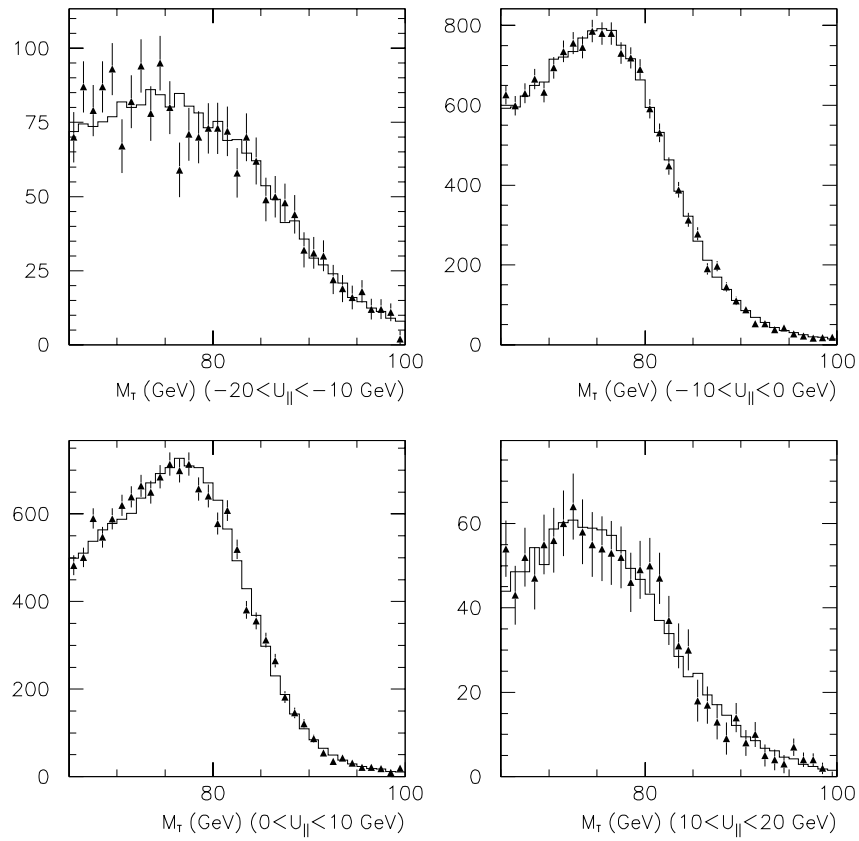

Figure 13.6: M_T distributions in bins of $U_{||}$, for $W \to e\nu$ data and Monte Carlo. The four $U_{||}$ bins are $-20 < U_{||} < -10$ (upper left), $-10 < U_{||} < 0$ (upper right), $0 < U_{||} < 10$ (lower left), and $10 < U_{||} < 20$ (lower right) GeV. The data are the triangles and the Monte Carlo are the histograms. The four Monte Carlo plots use slightly different values for M_W, since they each use the best fit value for M_W in each of the regions. The comparison of data to Monte Carlo in each of the four regions gives $\chi^2/dof = 1.0$ (upper left), $\chi^2/dof = 0.71$ (upper right), $\chi^2/dof = 1.6$ (lower left), and $\chi^2/dof = 0.70$ (lower right), where we simply take the number of M_T bins to be the number of degrees of freedom.

well the M_T shape of the data as a function of the boson P_T. As mentioned above, the consistency of the M_W results in $U_{||}$ bins indicates that the Monte Carlo is correctly simulating the correlations between E_T and $U_{||}$, since $M_T \approx 2E_T + U_{||}$. E_T and $U_{||}$ are correlated because both variables are strongly effected by the W P_T.

13.5.2 M_W Fit Using E_T and $\not{E}_T$ Distributions

Instead of fitting for M_W with the transverse mass distribution, we fit with the E_T and $\not{E}_T$ distribution.

We fit for the W mass with the Monte Carlo input parameters fixed at $\vec{\omega}_W$, and with the W width fixed at the Standard Model prediction. Only M_W is allowed to float in the fit. We minimize a binned likelihood function which is defined exactly as in Equation 13.1 above, except we use E_T histograms for the E_T fit, and $\not{E}_T$ histograms for the $\not{E}_T$ fit. The E_T and $\not{E}_T$ histograms are divided into 30 bins between 25 and 55 GeV.

The fit results are

$$\begin{aligned} \Delta M_W &= -81 \pm 60(stat)\,(MeV) \quad (E_T\ fit) \\ \Delta M_W &= 76 \pm 60(stat)\,(MeV) \quad (\not{E}_T\ fit) \end{aligned} \tag{13.13}$$

where ΔM_W is the difference between these fits and the M_T fit of Equation 13.5 above. The statistical uncertainties on the E_T and $\not{E}_T$ fits are 82 MeV, and the uncertainties quoted in Equation 13.13 are the uncertainties on ΔM_W. The two values for ΔM_W differ from zero by slightly more than one standard deviation. The uncertainties on ΔM_W are calculated using many fake data samples of the same size as the real data.

The splitting between the E_T fit and the M_T fit is correlated to the $U_{||}$ distribution since $M_T \approx 2E_T + U_{||}$. The $\not{E}_T$ fit has the opposite correlation since $M_T \approx 2\not{E}_T - U_{||}$.

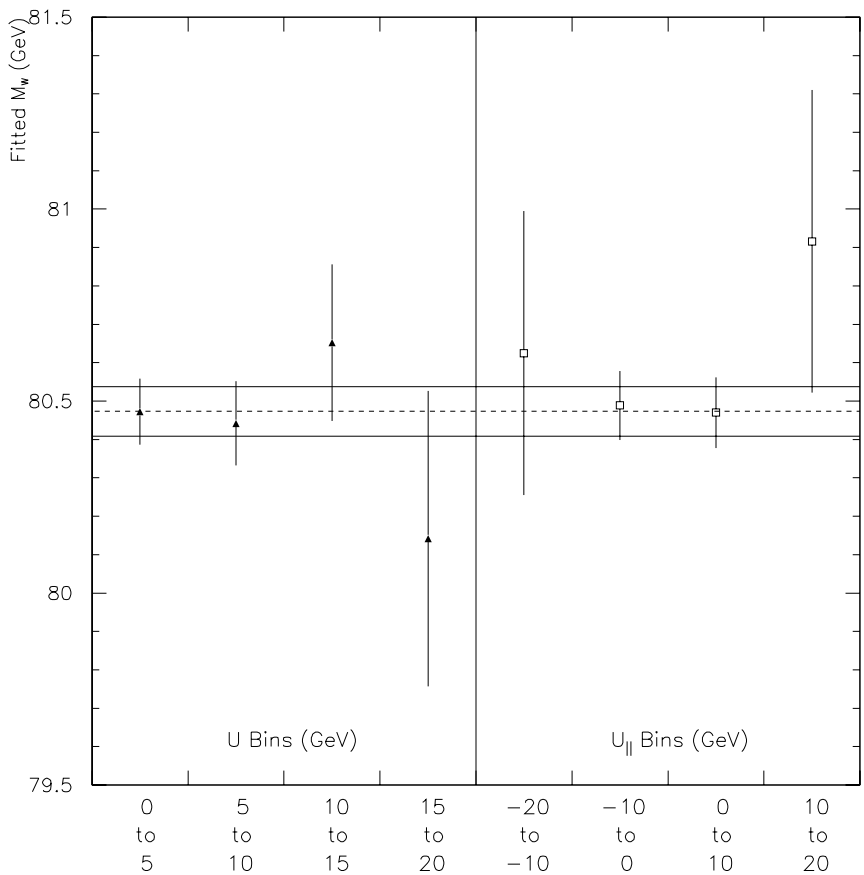

Figure 13.7: Fit results for M_W in bins of $|\vec{U}|$ and $U_{||}$. The triangles are the fit results for the data and Monte Carlo partitioned in $|\vec{U}|$ bins, and the squares are for the $U_{||}$ bins. The four $|\vec{U}|$ bins are $0 < |\vec{U}| < 5$, $5 < |\vec{U}| < 10$, $10 < |\vec{U}| < 15$, and $15 < |\vec{U}| < 20$ GeV. The four $U_{||}$ bins are $-20 < U_{||} < -10$, $-10 < U_{||} < 0$, $0 < U_{||} < 10$, and $10 < U_{||} < 20$ GeV. The dashed horizontal line is the fit result for M_W using the full data sample, and the solid horizontal lines represent its $1-\sigma$ statistical uncertainty.

We expect the two values for ΔM_W from the E_T and $\not{E}_T$ fits to have roughly equal magnitudes and opposite signs.

13.5.3 M_W Fit with Higher E_T and $\not{E}_T$ Cuts

We raise the E_T and $\not{E}_T$ cuts to 30 GeV on both the data and the Monte Carlo, and we refit for the W mass, using the M_T distribution. The difference between this fit and the fit result of Equation 13.5 is

$$\Delta M_W = 17 \pm 18(stat)\ MeV \quad (E_T > 30, \not{E}_T > 30) \tag{13.14}$$

The only difference between this result and Equation 13.5 is the change in the E_T and $\not{E}_T$ cuts from 25 to 30 GeV. The uncertainty on ΔM_W is calculated using fake data samples.

The change in the fitted W mass is consistent with zero, indicating that small discrepancies between the data and Monte Carlo for the low E_T and $\not{E}_T$ bins do not strongly bias the W mass fit.

13.5.4 M_W Fit for Different M_T Boundaries

We vary the upper and lower bounds of the M_T fit region and recalculate the W mass. We write the difference between the recalculated W mass and the fit result of Equation 13.5 as ΔM_W. We use the three regions $65 < M_T < 95$, $65 < M_T < 90$,

and $70 < M_T < 100$. We get the results

$$\begin{aligned} \Delta M_W &= -7 \pm 20(stat)\ MeV \quad (65 < M_T < 95) \\ \Delta M_W &= 22 \pm 32(stat)\ MeV \quad (65 < M_T < 90) \\ \Delta M_W &= 27 \pm 50(stat)\ MeV \quad (70 < M_T < 100) \end{aligned} \tag{13.15}$$

The uncertainties are the statistical uncertainties on the difference between these fits and the result of Equation 13.5. We calculate the uncertainties using fake data samples. The fit results are all consistent with the result of Equation 13.5.

We also use the fake data to calculate the uncertainties on the differences among the three fits. The three fit results are all consistent with each other although the difference between the result for $65 < M_T < 95$ and the result for $65 < M_T < 90$ is slightly high. These two numbers differ by approximately 1.1 statistical standard deviations.

The consistency in the W mass fit for the different M_T regions indicates that small discrepancies between data and Monte Carlo in the tails of the M_T distribution are not strongly effecting the W mass fit.

13.5.5 Check of Bias from the Fitting Procedure

We check that the fitter is not producing a biased result for M_W. We make a Monte Carlo M_T distribution with $M_W = 80.35$ GeV and , $_W$ fixed at the Standard Model prediction. We use all the Monte Carlo data, and we smooth the resulting histogram. We then fit this distribution as if it were the real data. We do not include the backgrounds in the distribution, or in the fit to the distribution. We get the result $M_W = 80.350$ GeV, as expected. This does not test that the Monte Carlo distribution is unbiased, but it does verify that the fitting procedure does not produce a biased

value M_W.

13.5.6 Check of Monte Carlo Calculation of Statistical Uncertainty

The fitting program calculates a $1-\sigma$ uncertainty by varying the fit parameters until the function it is minimizing changes by 1, relative to the minimum. Since we are minimizing a likelihood function scaled by -2, this corresponds to a change in likelihood of 0.5. To verify that this produces the correct statistical uncertainty, we use a Monte Carlo M_T histogram that is run with $M_W = 80.35$ GeV. We smooth this histogram with a spline function, and we then choose random values for M_T according to the smoothed function. We make many fake data distributions of the same size of the real data, and we fit them for M_W.

We fit 100 fake data samples. For each sample we calculate an uncertainty based on a change in likelihood of 0.5. The 100 values for this quantity have a mean of 0.063 GeV and an rms of 0.0003 GeV. The mean of this distribution agrees with the uncertainty calculated for the real data in Section 13.3 above, which is 0.065 GeV.

The rms of fitted value for M_W for the 100 samples is 0.057 GeV. This value is a better measure of the statistical uncertainty than the value calculated by a change in likelihood of 0.5. The two results are reasonably close, however. To be conservative we use 0.065 GeV for the statistical uncertainty of the data.

Chapter 14

Conclusion

We have determined the W mass to be

$$80.473 \pm 0.067(stat) \pm 0.097(sys)\ GeV \tag{14.1}$$

The measurement uncertainties are summarized in Table 14.1.

Source of Uncertainty	Size of Uncertainty (MeV)	
Statistical		67
Data Statistics	65	
Monte Carlo Statistics	17	
Systematic		97
Energy Scale	80	
Non-Linearity	17	
$\vec{U}$ and P_T^{boson}	37	
Backgrounds	< 10	
Electron E_T Resolution	27	
Parton Distribution Functions	25	
Total Uncertainty		120

Table 14.1: Measurement Uncertainties on the W mass.

A comparison of this measurement to previously published measurements is shown

in Chapter 1 in Table 1.1. We have plotted the predicted value for M_W as a function of the Higgs mass in Figure 1.3. Our measurement does not exclude any value for the Higgs mass, but it prefers lower values to higher.

We have set the calorimeter energy scale for this measurement using the invariant mass of $Z \rightarrow ee$ events. Ideally, the E/p distribution also can be used to set the energy scale. The E/p distribution ties the calorimeter energy scale to the tracking chamber scale. It has a smaller statistical uncertainty than the method of using the $Z \rightarrow ee$ mass because it makes use of the higher statistics of the W sample. The E/p method, however, gives a significantly different result than the $Z \rightarrow ee$ mass method. We use the $Z \rightarrow ee$ mass to set the energy scale to avoid any questions associated with the tracking chamber measurement. The discrepancy between E/p and the $Z \rightarrow ee$ mass is discussed further in Appendix B.

The uncertainty on the measured W mass is slightly higher than the current world average. All the systematic uncertainties in Table 14.1 are constrained by CDF data. For example, the largest uncertainty is the uncertainty on the calorimeter energy scale, which is set with the M_Z distribution. The uncertainty should scale as one over the square root of the number of $Z \rightarrow ee$ events. Run 2 at Fermilab is expected to produce 2 fb^{-1} of data. This would represent a 20-fold increase in statistics over Run 1. If all the uncertainties scale with the statistics, then the Run 2 W mass measurement with electons should be able to achieve an uncertainty $\sim$ 25 MeV.

On the other hand, a number of systematic effects will need to be calculated more carefully. For example, the E_T dependence of the CEM resolution may need to be accounted for more carefully. In this paper, we did not include any uncertainty on the stochastic term, since the effect of variations were small compared to the uncertainty on the constant term κ. This will probably not be the case for Run 2. It is also

possible that the calorimeter measurement will have to be simulated more carefully. For example, with the higher statistics, the absorption of soft photons in the solenoid may have a noticeable effect on the M_Z and E/p shapes.

Finally, it will be interesting to see if the discrepancy between E/p and M_Z persists in the next run. This discrepancy is not understood and is interesting in its own right.

Appendix A

Summary of Monte Carlo Input Parameter Results

Description	Parameter	Value from Z Data	Value from W and Z Data
$\vec{\Pi}_x$: Boson P_T Shape	a	54.8	43.9
	b	18.2	15.2
	f	0.642	0.594
	p	1.40	1.22
$\vec{\Pi}_\Sigma$: $\sum E_T$ Shape	α_0	2.76	(Not Changed)
	α_1	$0.0459\ GeV^{-1}$	
	β_0	$0.0462\ GeV^{-1}$	
$\vec{\Pi}_U$: $\vec{U}$ Distribution	s_1	$3.07 \times 10^{-4}\ GeV^{-2}$	$3.30 \times 10^{-4}\ GeV^{-2}$
	s_2	$0.933 \times 10^{-4}\ GeV^{-2}$	$1.41 \times 10^{-4}\ GeV^{-2}$
	b_0	1.20×10^{-1}	1.68×10^{-1}
	c_0	$-1.77 \times 10^{-1}\ GeV^{-1}$	$-1.83 \times 10^{-1}\ GeV^{-1}$
	c_1	$2.97 \times 10^{-2}\ GeV^{-1}$	$3.24 \times 10^{-2}\ GeV^{-1}$
	c_2	$-5.42 \times 10^{-3}\ GeV^{-1}$	$-10.9 \times 10^{-3}\ GeV^{-1}$
	c_3	$-6.62 \times 10^{-4}\ GeV^{-1}$	$38.9 \times 10^{-4}\ GeV^{-1}$

Table A.1: Summary of Monte Carlo input parameters. The three sets of parameters shown describe the boson P_T shape, the $\sum E_T$ shape, and the $\vec{U}$ distribution. The parameters are defined in Chapters 7 and 8. The parameters are initially determined from the Z data. In Chapter 9 we describe a procedure to include the W data in the parameter determination. These fits are listed in the fourth column of the table.

$\widetilde{C}_x$: Boson P_T Fit Covariance Matrix

	a	b	f	p
a	279	56.9	0.324	6.26
b		12.5	$7.63 \cdot 10^{-2}$	1.29
f			$4.65 \cdot 10^{-3}$	$-2.15 \cdot 10^{-3}$
p				0.166

$\widetilde{C}_\Sigma$: $\sum E_T$ Fit Covariance Matrix

	α_0	α_1	β_0
α_0	$1.16 \cdot 10^{-2}$	$-1.14 \cdot 10^{-4}$	$1.50 \cdot 10^{-4}$
α_1		$3.12 \cdot 10^{-5}$	$2.94 \cdot 10^{-6}$
β_0			$3.05 \cdot 10^{-6}$

$\widetilde{C}_U$: $\vec{U}$ Fit Covariance Matrix

	s_1	s_2	b_0	c_0	c_1	c_2	c_3
s_1	$5.98 \cdot 10^{-9}$	$2.60 \cdot 10^{-17}$	$6.63 \cdot 10^{-8}$	$-2.90 \cdot 10^{-8}$	$2.97 \cdot 10^{-8}$	$-7.98 \cdot 10^{-9}$	$7.14 \cdot 10^{-9}$
s_2		$3.57 \cdot 10^{-9}$	$2.48 \cdot 10^{-13}$	$-8.17 \cdot 10^{-14}$	$3.70 \cdot 10^{-14}$	$-1.65 \cdot 10^{-15}$	$3.67 \cdot 10^{-16}$
b_0			$6.74 \cdot 10^{-2}$	$-2.22 \cdot 10^{-2}$	$1.00 \cdot 10^{-2}$	$-4.44 \cdot 10^{-4}$	$1.04 \cdot 10^{-4}$
c_0				$7.52 \cdot 10^{-3}$	$-3.65 \cdot 10^{-3}$	$1.93 \cdot 10^{-4}$	$-4.57 \cdot 10^{-5}$
c_1					$2.13 \cdot 10^{-3}$	$-1.72 \cdot 10^{-4}$	$4.67 \cdot 10^{-5}$
c_2						$2.89 \cdot 10^{-5}$	$-1.22 \cdot 10^{-5}$
c_3							$1.02 \cdot 10^{-5}$

Table A.2: Covariance matrices from the determination of the input parameters with the Z data. Only the upper triangular part of the matrices are shown, and all numbers are rounded off to three digits. For these numbers, the parameters are measured in the same units as in Table A.1. The fits are described in Chapter 7 and 8.

	M_W	a	b	f	p
M_W	$3.13\cdot10^{-3}$	$7.90\cdot10^{-2}$	$1.49\cdot10^{-2}$	$3.08\cdot10^{-5}$	$1.66\cdot10^{-3}$
a		69.7	15.4	$4.28\cdot10^{-2}$	1.95
b			3.83	$1.80\cdot10^{-2}$	0.434
f				$2.75\cdot10^{-3}$	$-4.99\cdot10^{-3}$
p					$7.05\cdot10^{-2}$

	s_1	s_2	b_0	c_0	c_1	c_2	c_3
M_W	$-3.65\cdot10^{-7}$	$-4.16\cdot10^{-8}$	$-2.44\cdot10^{-4}$	$9.81\cdot10^{-6}$	$9.72\cdot10^{-7}$	$1.45\cdot10^{-5}$	$-3.59\cdot10^{-6}$
a	$-7.60\cdot10^{-6}$	$5.54\cdot10^{-7}$	$-4.84\cdot10^{-2}$	$-2.57\cdot10^{-3}$	$1.12\cdot10^{-2}$	$2.52\cdot10^{-3}$	$-1.28\cdot10^{-3}$
b	$-3.07\cdot10^{-6}$	$-1.02\cdot10^{-6}$	$-1.07\cdot10^{-2}$	$7.55\cdot10^{-4}$	$1.41\cdot10^{-3}$	$4.12\cdot10^{-5}$	$5.87\cdot10^{-4}$
f	$3.98\cdot10^{-8}$	$-5.04\cdot10^{-8}$	$-6.48\cdot10^{-5}$	$-1.63\cdot10^{-4}$	$3.58\cdot10^{-4}$	$-6.98\cdot10^{-5}$	$2.52\cdot10^{-5}$
p	$-2.57\cdot10^{-7}$	$6.91\cdot10^{-8}$	$-1.27\cdot10^{-3}$	$4.34\cdot10^{-4}$	$-6.08\cdot10^{-4}$	$2.05\cdot10^{-4}$	$-6.74\cdot10^{-5}$
s_1	$5.013\cdot10^{-9}$	$-3.89\cdot10^{-11}$	$-3.19\cdot10^{-8}$	$1.16\cdot10^{-9}$	$-8.16\cdot10^{-9}$	$-3.63\cdot10^{-9}$	$-3.43\cdot10^{-9}$
s_2		$3.20\cdot10^{-9}$	$-4.97\cdot10^{-8}$	$1.27\cdot10^{-8}$	$1.12\cdot10^{-8}$	$-1.80\cdot10^{-9}$	$1.33\cdot10^{-9}$
b_0			$1.62\cdot10^{-2}$	$-5.06\cdot10^{-3}$	$1.95\cdot10^{-3}$	$-4.04\cdot10^{-5}$	$8.44\cdot10^{-6}$
c_0				$1.69\cdot10^{-3}$	$-7.89\cdot10^{-4}$	$3.59\cdot10^{-5}$	$-7.64\cdot10^{-6}$
c_1					$5.55\cdot10^{-4}$	$-5.50\cdot10^{-5}$	$1.40\cdot10^{-5}$
c_2						$1.15\cdot10^{-5}$	$-4.69\cdot10^{-6}$
c_3							$4.80\cdot10^{-6}$

Table A.3: Covariance matrix from the W and Z combined fit. The matrix is a 12×12 matrix. This includes M_W, the 4 parameters of $\vec{\Pi}_x$, and the 7 parameters of $\vec{\Pi}_U$. The matrix is shown physically in two parts to fit it on the page. Only the upper triangular part of the matrix is shown. All numbers are rounded off to three digits. For these numbers, the parameters are measured in the same units as in Table A.1, and M_W is measured in GeV.

Appendix B

Discussion of Discrepancy Between E/p and M_Z

In Chapter 10 we used the invariant mass of $Z \rightarrow ee$ events to determine an energy scale of

$$S_E(M_Z) = 1.0000 \pm 0.0009$$

In Chapter 11 we used the E/p distribution to tie the calorimeter energy scale to the CTC scale. We determined $S_E(E/p) = 0.99613$. If we include the non-linearity correction of Chapter 12, then the energy scale becomes

$$\begin{aligned} S_E(E/p) = 0.9946 \quad &\pm \quad 0.00040(stat) \\ &\pm \quad 0.00024(\kappa) \\ &\pm \quad 0.00035(X_0) \\ &\pm \quad 0.00048(P_T\ scale) \\ &\pm \quad 0.00075(CEM\ Non-linearity) \end{aligned}$$

where we have included the uncertainty on the P_T scale as determined from the J/ψ mass [27]. We have also included an uncertainty on the CEM non-linearity correction. The energy scale as determined from E/p is 0.9946 ± 0.0011. The difference between the M_Z result and the E/p result is

$$\frac{1.0000 - 0.9946}{\sqrt{0.0009^2 + 0.0011^2}} = 3.8 \tag{B.1}$$

standard deviations. This is unlikely to be a statistical fluctuation. The integrated M_Z distributions of Figure 10.4 show the extent to which a scale factor of 0.996 disagrees with the Z data. 0.996 is the E/p result without the non-linearity correction. We calculate a Kolmogorov-Smirnov statistic for the comparison of the data to the Monte Carlo, where we scale the data by 0.996. The probability that a statistical fluctuation would produce a worse agreement in the integrated distributions is 5.5×10^{-6}.

Figure B.1 shows the value for M_Z that we would obtain if we set the energy scale according to the E/p distribution. Also shown are the results from the $Z \rightarrow \mu\mu$ data, as well as the Run 1A data. For the Run 1A electron result, the energy scale is set with the E/p distribution. The Run 1B Z mass with electrons is consistent with the Run 1A result, although the 1B result is significantly lower than the world average value.

In this Appendix we discuss possible explanations of the discrepancy between E/p and M_Z. We divide the explanations into three sections. In Section B.1 we discuss the hypothesis that there is a tracking problem, either because the P_T scale is incorrect, or other reasons. In Section B.2 we discuss the possibility that there is a flaw in our method of setting the energy scale with E/p. In Section B.3, we discuss the possibility

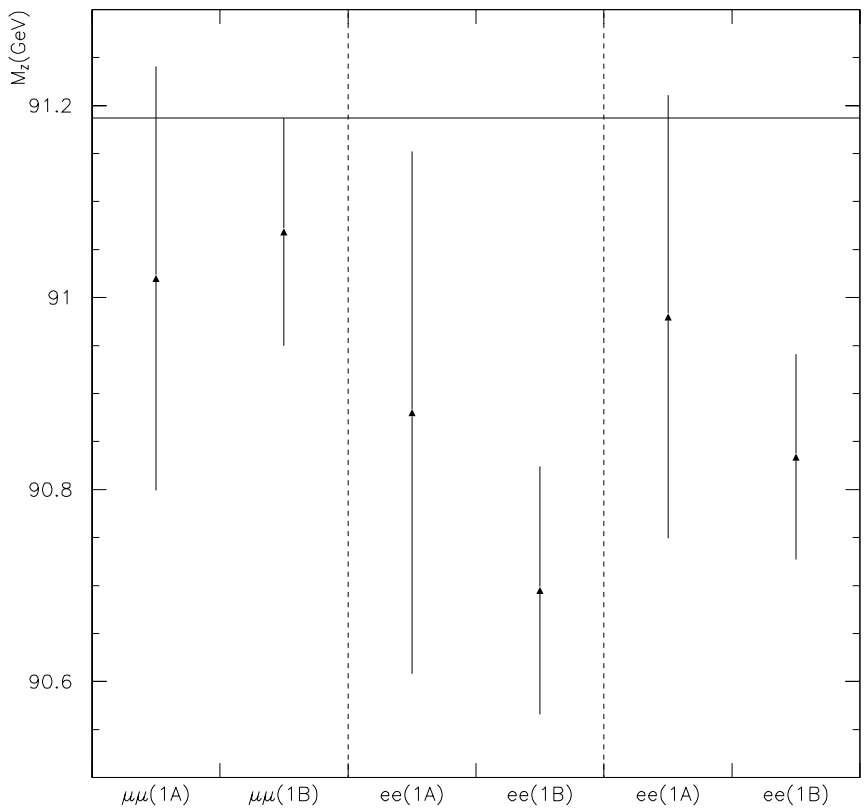

Figure B.1: The results for M_Z with CDF data. The left two points are calculated with $Z \to \mu\mu$ data. Both the Run 1A and 1B data are shown. The next two points are the results from the $Z \to ee$ data for the Run 1A and Run 1B data. For these two points, we apply the measured non-linearity correction, and the Run 1A result also has a non-linearity correction applied. The last two points are the $Z \to ee$ data also, but no non-linearity correction is applied. The 1A results are from [5], and the 1B $Z \to \mu\mu$ result is from [46]. The horizontal line represents the world average value for M_Z.

that some theoretical inputs into our simulation are not correct. We have labelled that section "New Physics." Most of the possibilities we discuss have been checked, or can otherwise be excluded, but it is worthwhile to present them here.

B.1 Is the Discrepancy Caused by Tracking?

In this section we consider possible explanations that are related to tracking problems.

The Momentum Scale is Incorrect. If the P_T scale is too low, we will measure E/p too high.

- From $J/\psi \rightarrow \mu\mu$ decays it is determined that P_T needs to be scaled upwards by 1.00023 ± 0.00048 [27]. For all the data in this paper, we have included this scaling factor. For the P_T scale to be off by 0.4%, this scale factor would have to be significantly wrong compared to its quoted uncertainty. The statistical uncertainty on the P_T scale is negligible, and the total uncertainty is dominated by systematic effects. The two largest effects are an unexpected variation in the fitted J/ψ mass as a function of the amount of material traversed by the decay muons, and a variation in the P_T scale as a function of muon momentum. The second effect is discussed below.
- The J/ψ mass calculation of reference [27] was done before the final CTC calibration and alignment. However, for this paper, we are using the final CTC calibration and alignment for our W decay electron tracks. Reference [47] has repeated the analysis of the J/ψ data of Reference [27], using the final CTC calibration and alignment. The P_T scale changes to 1.00035 from 1.00023. This change is small compared to the systematic uncertainty on the P_T scale.

- There may be a non-linearity in the P_T measurement, so that the extrapolation to the high P_T of W and Z events introduces an error of $\approx 0.4\%$. The average P_T of J/ψ decay muons is ~ 3.5 GeV, while the average P_T of W and Z decay electrons is ~ 40 GeV. Figure B.2 shows the difference between the measured J/ψ mass and the expected mass as a function of the sum of $1/P_T$ of the two decay muons. To extrapolate to the high P_T range of W and Z events, we want to calculate the J/ψ mass for the sum of $1/P_T$ of the muons around 0.05 GeV^{-1}, which occurs on the far left of the plot. Before the final CTC calibration and alignment, the plot shows a clear slope, approaching lower values of the J/ψ mass near the left side of the plot. After the final CTC calibration and alignment, the plot is significantly flatter. This change is not understood. The measured $Z \rightarrow \mu\mu$ mass did not change after the final alignment and calibration.

- An argument against the momentum scale being wrong is that the Z mass measured with muons comes out correct, although slightly low. The measured value for the $Z \rightarrow \mu\mu$ mass is shown in the bottom plot of Figure B.2. The Z mass with muons has been measured to be 0.9987 ± 0.0013 relative to the expected value of 91.187 GeV [46]. If we apply the energy scale from E/p, then our Z mass with electrons will come out low by 0.9946 ± 0.0013, where we have not included the uncertainty from the J/ψ mass determination of the P_T scale. The splitting between our measurement and the Z mass with muons is then

$$\frac{0.9987 - 0.9946}{\sqrt{.0013^2 + .0013^2}} = 2.2$$

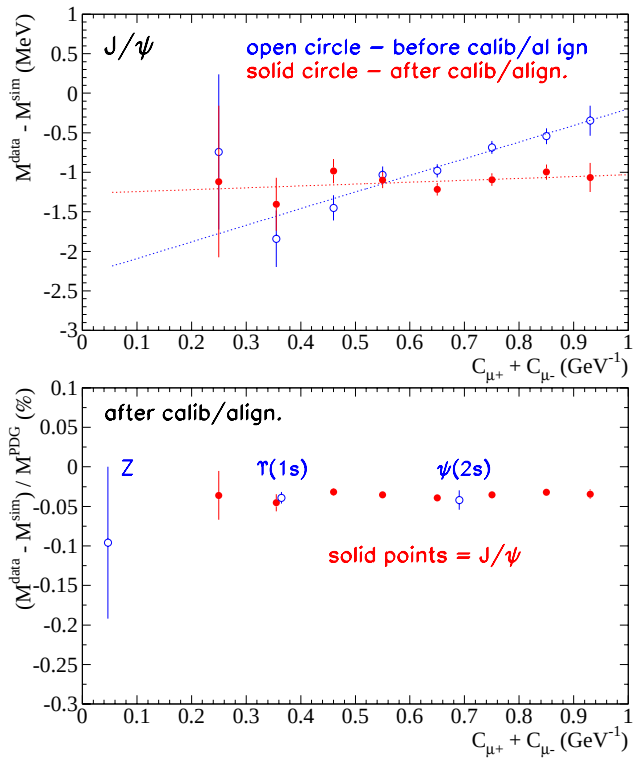

Figure B.2: The results of Gaussian fits to the $J/\psi \rightarrow \mu\mu$ mass peak with a linear background, as a function of the sum of $1/P_T$ of the two decay muons. The label "$C_{\mu+} + C_{\mu-}$" is the sum of $1/P_T$ of the two muons. Top: The difference between data and Monte Carlo. The open circles are before the final CTC calibration and alignment, and the filled circles are after. Bottom: The fractional difference between data and Monte Carlo after the final CTC calibration and alignment. The closed circles are for the $J/\psi(1S)$ data; and the open circles are for the $J/\psi(2S)$ mass peak, as well as the $\Upsilon \rightarrow \mu\mu$ and $Z \rightarrow \mu\mu$ mass peaks. The $J/\psi(2S)$, Υ, and Z data are shown at the location of the average value of $C_{\mu+} + C_{\mu-}$. This plot is taken from Reference [47].

standard deviations. The splitting is reduced because the invariant mass from $Z \rightarrow \mu\mu$ decays is slightly low, and also because it produces a significantly larger uncertainty on the P_T scale than the uncertainties calculated with the J/ψ data. If we do not include the non-linearity on the CEM energy scale, the splitting becomes 1.5 standard deviations.

- We can also check the momentum scale by calculating the invariant mass of $Z \rightarrow ee$ events using the P_T of the electron tracks, rather than their calorimeter energy, E_T. We refer to this quantity as the "track-track" mass, $M_Z(pp)$. We compare the $M_Z(pp)$ distribution of the data to the Monte Carlo to determine that we need a P_T scale factor on the data of 1.0015 ± 0.0024. Our fit value is consistent with a scale factor of 1.0, but because it has a large uncertainty, it is also consistent with P_T in the data being low by up to $\sim 0.4\%$.

The Invariant Mass Measurement is Incorrect. Calculating the invariant mass of $Z \rightarrow ee$ events makes use of a different set of track parameters than calculating E/p, and one could hypothesize errors in the angular variables causing errors in the invariant mass. We would not necessarily expect the electron and muon invariant masses to look the same since one uses E_T and the other P_T. One could also imagine measurement correlations between the different tracking parameters which have the net effect of shifting the measured mass. The two tracks themselves could also be correlated since for Z events they are largely back-to-back. For example, if one track enters a superlayer on the right side of a cell, the other track will be biased to do the same. However, we have not been able to see any such effect in the data.

The Inner Superlayers are Causing Problems. To check this we refit the Z electron tracks with superlayers 0 and 1 removed. While the resolution got worse, we did not see any significant change in the means of E/p of the electrons or M_Z or $M_Z(pp)$. We also tried refitting the same tracks but removing superlayer 5 instead of 0 and 1. Again no significant change was observed in the means of E/p, M_Z, or $M_Z(pp)$. We have also checked that the mean of the E/p distribution of W data is insensitive to the number of stereo or axial wires used in the track reconstruction.

B.2 Is the Problem the E/p Fitting Procedure?

In this section we will discuss possible explanations that are in some way related to the E/p measurement which we have performed in this paper.

Coding Errors. The E/p code from the Run 1A W mass analysis [48] was used as a starting point for our E/p simulation. However, this code was significantly modified, and it is possible that a bug has been introduced. We have run our code on the 1A data and reproduced the 1A result, implying that if there is a bug, it was also in the 1A code. Moreover, other people have run Monte Carlos with independent code and have obtained similar answers.

CEM Non-Linearity. When we applied the non-linearity correction of Chapter 12, the CEM energy scale factor as determined from E/p moved from 0.9961 to 0.9946, which makes the discrepancy between E/p and M_Z worse. The uncertainty on the energy scale was also significantly increased by the uncertainty on the non-linearity. If we do not consider a non-linearity correction, then the discrepancy between the Z mass energy scale and the E/p energy scale is closer

to 3.3 standard deviations. The data, however, support a CEM non-linearity. Moreover, they do not support a non-linearity which has the opposite sign of the value derived in Chapter 12, which would be needed to account for the discrepancy.

Amount of Material is Incorrect. From the slope of the bottom plot of Figure 11.3, we can determine that to increase the fitted energy scale by 0.4%, we would have to increase the amount of material in the Monte Carlo by $\sim 4.5\%$ of a radiation length. However, the tail of the E/p distribution of the W data is not consistent with such an increase. Moreover, the tail of the invariant mass distribution of $J/\psi \rightarrow ee$ decays has been examined, and such an increase in the amount of material would significantly contradict the data [49].

Backgrounds are Biasing the Result. It is possible that our estimate of the E/p shape of the background is flawed, and that there is a significant source of non-electron background in the E/p peak region that is biasing our energy scale fit. We consider the worst case possibility that all the background is located at one of the edges of the E/p fit region. To increase the mean by 0.002, we would need to have 2% background piled up at E/p= 1.1. This is more QCD background than we have measured above, and since we expect the QCD background to be largely flat in E/p, we do not expect that backgrounds are significantly biasing our result. The agreement of the Z E/p fit with the W fit also indicates that the backgrounds are not a significant effect in the W fit. An E/p plot of the electrons from the same sign Z events shows that the QCD background is largely flat in E/p and is spread out from E/p$\approx$ 0.8 to $\approx$ 3.0, indicating that this background is also not a significant source of error in the Z E/p fit.

Beam Constraint is Biasing E/p. In Section 3.1.2 we discussed how the beam constraint can bias tracks that have undergone bremsstrahlung before the CTC active volume. Bremmsstrahlung causes the tracks to have a non-zero impact parameter, as described by Equation 3.3; and this non-zero impact parameter creates a bias on the beam constrained momentum, as described by Equation 3.2. We consider two possibilities:

- The Radial Distribution of Material May Be Wrong. The average radius of brems (including half the CTC gas) occurs at 22.21 cm in the simulation. Equation 3.3 shows that the bias depends on r^2, and so we might be sensitive to the location of the material. As a check we rerun the simulation but with all the material before the CTC gas placed in the beampipe, and then again but with all placed in the CTC inner can. We scale the material so $< X_0 >$ is the same for both cases. We find that f_{TAIL} for the beampipe case is higher than the CTC case by about 1% of itself. We also find that the average E/p from 0.9 to 1.1 is higher in the beampipe case than the CTC case by 0.0003. Both of these changes are small, and they are negligibly small when we consider that these are extreme cases for variations in the possible distributions of the material.

- In the Simulation, the Correlation Between Curvature and Impact Parameter Mismeasurements May Not Be Correct. This would cause the Monte Carlo to produce the wrong bias from the beam constraint. However, in the Monte Carlo, we use CTC wire hit patterns from the real W data to determine a covariance matrix to use in the beam constraint. We use the identical procedure that is used to beam constraint the real data.

We also try setting the energy scale with the E/p distribution before the beam constraint. We compare the Monte Carlo distribution to the data distribution. We get a result for the energy scale which is consistent with the beam constrained E/p result. This is more evidence that we are accounting for the beam constraint bias correctly.

Tracking Resolutions are Not Being Simulated Correctly. For the Monte Carlo, we smear the track parameters according to the calculated covariance matrix, and we then beam constraint according to this same covariance matrix. Thus, in the Monte Carlo, the covariance matrix used in the beam constraint describes the correlations and resolutions of the track parameters exactly. On the other hand, it is not necessarily the case for the data that the correlations and resolutions are described correctly by the covariance matrix.

We can measure the correlation between impact parameter and curvature by plotting the average of qD_0 as a function of E/p. The slope of this plot for the data is slightly different than for the Monte Carlo. Since the Monte Carlo covariance matrix is the same matrix that is used to beam constrain the data, we conclude that the beam constraint covariance matrix does not perfectly describe the underlying measurement correlations of the data.

To see how much of an effect this has on E/p we run the Monte Carlo as follows: We smear the Monte Carlo according to an adjusted covariance matrix, where all the off-diagonal terms are set to 0 except for $\sigma^2(crv, D_0)$, and where we fix $\sigma^2(crv, D_0)$ according to the W data. When we apply the beam constraint, however, we use the same covariance matrices that are used by the data to do the beam constraint. In this way, we simulate the data more closely: smearing

according to one matrix, and beam constraining according to a slightly different matrix. We find no effect on the average E/p between 0.9 and 1.1.

Low Energy Bremsstrahlung Cutoff Is Not Low Enough. Since the number of external photons diverges as 1/E, we only consider external photons above a certain energy. In particular, we only simulate photons above $y = 0.1\%$, where y is the fraction of the electron energy taken up by the photon. However, we can integrate the total fraction of the electron energy that is carried by photons below the cutoff. The total fraction is $y = 0.1\% \times 0.085$, where 0.085 is an approximation of the effective number of radiation lengths seen by the electrons, including the CTC gas and wires. We expect this to effect the energy scale by less than 0.0001, which is a negligible amount. As a simple check we have increased the cutoff and we do not see any significant change in the fitted energy scale. A similar argument should hold for the internal photons.

Solenoid May Cause Non-Linearity in Photon Response. The solenoid presents ~ 1 radiation length for electrons in W and Z events, and also for any associated soft photons. Electron energy losses in the solenoid are not expected to effect our results since they are part of the CEM scale, which we are fitting for. However, it is possible that the soft photons are not making it through the solenoid and that this is distorting the E/p shape. As a simple check, we use a formula from the PDG Full Listings [5] which describes the energy loss profile of a particle as a function of its depth in radiation lengths. We apply this formula to all the photons created in the Monte Carlo and reduce their energy accordingly. This is not a rigorous check since we are applying the formula to low energy photons, which are in an energy region where the formula is not necessarily

accurate. We rerun the Z Monte Carlo with this effect put in, and we treat this new Monte Carlo as "data" and fit it with the default Monte Carlo. Fitting E/p gives a Monte Carlo energy scale of 0.99960 (the "solenoid-corrected" Monte Carlo is lower by 0.99960), and fitting M_Z gives a scale of 0.99935. We are interested in M_Z relative to E/p, and $0.99960 - 0.99935 = 0.00025$. This is a small difference although not totally insignificant. The two Monte Carlo samples were not entirely correlated, and we have not necessarily run enough Monte Carlo statistics. The estimated Monte Carlo statistical error on this calculation is 0.00015.

Landau-Pomeranchuk-Migdal Effect. Multiple scattering of the electron can suppress the production of bremsstrahlung at low photon energies [50]. Qualitatively, if the electron is disturbed while in the "formation zone" of the photon, the bremsstrahlung will be suppressed. The "formation zone" is appreciable for the low energy brems. (Similarly, the electron bending in a magnetic field can also suppress low energy photons, but the CDF magnet isn't strong enough for this to be significant.) SLAC has measured this effect for 25 GeV electrons. The suppression of bremsstrahlung depends on the density of the material and occurs below around $y = 0.01$ for gold and $y = 0.001$ for carbon, where y is the fraction of the electron energy taken up by the photon. The average density of material in the CDF detector before the CTC is closer to carbon than gold, and since we have a cutoff at $y = 0.001$, we are in effect simulating 100% suppression for the carbon case. Above we argued that this had a negligible effect on E/p. We note that the SLAC experiment provides a significant check of the formula we are using for the external brems, since their experiment agrees with that formula above the energies that are suppressed.

Synchrotron Radiation. The electron is being accelerated in a circle by the magnetic field, and we are not simulating the resulting synchrotron radiation. The standard calculation predicts the effect to be a few MeV, and this can be safely neglected.

Significant Energy Loss in Silicon Crystals. An electron moving through the material before the CTC will pass through $\approx 400\mu$ of aligned silicon crystals. If it travels through the crystal along a major axis of symmetry, it can potentially lose significantly more energy than is lost through bremsstrahlung [51, 52]. However, in the data we do not see any significant difference between electrons that pass through the SVX and those that do not, relative to the Monte Carlo. This indicates that this is not a significant effect.

B.3 New Physics?

It is possible that some of our theoretical assumptions about the observed events are incorrect. The 1A result does not preclude this possibility since the 1A Z mass is not inconsistent with the current measurement. Here are some possibilities.

The External Bremsstrahlung Distribution is Incorrect. The formula we are using for the photon energy distribution was calculated in 1974 [39]. This formula is still referenced in papers written today, but it is possible that the formula is unexpectedly breaking down at high energies. Evidence that it is not is given by the SLAC measurement of the Landau-Pomeranchuk-Migdal effect described above [50]. They measured the rate and energy distribution of bremsstrahlung of 25 GeV electrons incident on different targets. For all the targets, they measured some level of bremsstrahlung suppression at low

photon energies, as expected, but at higher photon energies, their measured distributions agreed well with the expectation from [39]. CERN data perhaps could also be used to check this formula, and it would be interesting to see if LEP experiments measure E/p to be consistent with their M_Z measurements.

Internal Bremsstrahlung Distribution is Incorrect. "Internal" photons are photons which are produced at the vertex in a radiative $W \to e\nu\gamma$ event (or $Z \to ee\gamma$ event). For Monte Carlo events with no external photons, we find that the average E/p between 0.9 and 1.1 is 1.00386. Part of this shift above 1 is from cut biases (≈ 0.0014), and so the internal brems shift the peak by ≈ 0.0025. If the distribution we are using is significantly ($\approx 100\%$) wrong, then our fitted energy scale might come out wrong enough to account for the discrepancy between the energy scale from M_Z and E/p.

- The generator that is used in this paper (PHOTOS in two-photon mode) has been compared to the calculation by Berends and Kleiss of Reference [53], and the two generators give similar energy-angle distributions [54]. Moreover, since [53] was used in the 1A W mass measurement [13], and our Monte Carlo reproduces the 1A result, we conclude that the PHOTOS generator is reproducing the Berends and Kleiss formula.
- Laporta and Odorico [55] argue that inclusion of multiple photon radiation from the final state electron may change the energy loss distribution of the electron relative to a single photon calculation, such as Berends and Kleiss. Reference [55] contains an algorithm to calculate the effect of a cascade of final state photons. By construction, this algorithm reduces to Berends and Kleiss for the case of single photon emission. We implemented their

algorithm for W decays and interfaced it to Bob Wagner's generator [53]. These events were generated with no W P_T but that should not significantly alter the E/p shape. We find that the Laporta and Odorico case has the mean E/p between 0.9 and 1.1 lower by 0.00033. This is not insignificant, but it is not large enough to significantly account for the discrepancy between M_Z and E/p. The statistical error on the Monte Carlo for this calculation was ≈ 0.00015.

- Baur, Keller, and Wackeroth [56] have done a calculation of the $W \to e\nu\gamma$ process which includes radiation from the W propagator. We have received their calculation in the form of a Monte Carlo [57]. The Monte Carlo can implement their calculation, and it can also implement Berends and Kleiss. We run separately in each mode and implement some simple CEM clustering of the photons and measurement resolutions. We find that [56] produces a value for the mean of E/p between 0.9 and 1.1 that is 0.00023 lower than the Berends and Kleiss result. While we generated more than 12 million events, it is hard to determine a statistical error since the events are weighted; nevertheless, it is doubtful that this is the size of effect we are looking for.

- If there were a new physics process that would significantly increase the rate of internal bremsstrahlung (for both $W \to e\nu\gamma$ and $Z \to ee\gamma$ events) and not be inconsistent with other measurements, this would explain the deviation we are seeing.

Any other new physics. This remains an open forum.

B.4 Conclusion

We have measured the energy scale using the peak of the E/p distribution of W data. The E/p distribution of Z events gives consistent results for the E/p distribution of W events. However, if we set the energy scale with E/p, then the invariant mass distribution of the Z events comes out significantly low. As a check we have refit the 1A data with the 1B Monte Carlo, and have gotten excellent agreement. It is possible that whatever problem we are seeing was also in the 1A data since the 1A Z mass measurement is not inconsistent with ours.

We have discussed several possible reasons that the Z mass comes out wrong. The problem could be a momentum scale problem or otherwise a tracking problem; it could be related to our simulation of E/p as presented in this paper; or it could be something theoretically unexpected. In any case, there is no clear solution, and it remains an open question.

For the final W mass measurement reported in this paper, we have used the invariant mass of the $Z \rightarrow ee$ events. In this way, we have separated our energy scale measurement from almost all questions associated with tracking.

Bibliography

[1] Sheldon L. Glashow. Partial-Symmetries of Weak Interactions. *Nuclear Physics*, 22:579–588, 1961.

[2] Steven Weinberg. A Model of Leptons. *Physical Review Letters*, 19(21):1264–1266, November 1967.

[3] N. Svartholm, editor. *A. Salam, Elementary Particle Theory: Relativistic Groups and Analyticity (Nobel Symposium No. 8)*. Almqvist and Wiksell, Stockholm, 1968.

[4] Peter W. Higgs. Broken Symmetries and the Masses of Gauge Bosons. *Physical Review Letters*, 13:508–509, 1964.

[5] C. Caso et al. 1998 Review of Particle Physics. *The European Physical Journal*, C3, 1998.

[6] Wolfgang F. L. Hollik. Radiative Corrections in the Standard Model and Their Role for Precision Tests of the Electroweak Theory. *Fortschritte Der Physik*, 38:165–260, 1990.

[7] A. Sirlin. Radiative Corrections in the $SU(2)_L \times U(1)$ Theory: A Simple Renormalization Framework. *Physical Review*, D22:971–981, 1980.

[8] G. Degrassi, P. Gambino, M. Passera, and A. Sirlin. The Role of M_W in Precision Studies of the Standard Model. *Physics Letters*, B418:209–213, 1998.

[9] G. Arnison et al. Experimental Observation of Isolated Large Transverse Energy Electrons with Associated Missing Energy at $\sqrt{s} = 540$ GeV. *Physics Letters*, B122:103–116, 1983.

[10] G. Arnison et al. Experimental Observation of Lepton Pairs of Invariant Mass Around 95 GeV/c^2 at the CERN SPS Collider. *Physics Letters*, B126:398–410, 1983.

[11] F. Abe et al. A Measurement of the W Boson Mass. *Physical Review Letters*, 65:2243–2246, 1990.

[12] J. Alitti et al. An Improved Determination of the Ratio of the W and Z Masses at the CERN $\overline{p}p$ Collider. *Physics Letters*, B276:354–364, 1992.

[13] F. Abe et al. Measurement of the W Boson Mass. *Physical Review*, D52:4784–4827, 1995.

[14] S. Abachi et al. Measurement of the W Boson Mass. *Physical Review Letters*, 77:3309–3314, 1996.

[15] B. Abbott et al. A Measurement of the W Boson Mass, December 1997. Preprint hep-ex/9712028, submitted to Physical Review Letters; see also hep-ex/9712029, submitted to Physical Review.

[16] K. Ackerstaff et al. Measurement of the Mass of the W Boson in e^+e^- Collisions at $\sqrt{s} = 161$ GeV. *Physics Letters*, B389:416–428, 1996.

[17] R. Barate et al. Measurement of the W Mass in e^+e^- Collisions at Production Threshold. *Physics Letters*, B401:347–362, 1997.

[18] M. Acciarri et al. Pair Production of W Bosons in e^+e^- Interactions at $\sqrt{s} = 161$ GeV. *Physics Letters*, B398:222–238, 1997.

[19] P. Abreu et al. Measurement and Interpretation of the W Pair Cross-Section in e^+e^- Interactions at 161 GeV. *Physics Letters*, B397:158–170, 1997.

[20] M. Acciarri et al. Measurements of Mass, Width, and Gauge Couplings of the W Boson at LEP. *Physics Letters*, B413:176–190, 1997.

[21] R. Barate et al. Measurement of the W Mass by Direct Reconstruction in e^+e^- Collisions at 172 GeV. *Physics Letters*, B422:384–398, 1998.

[22] K. Ackerstaff et al. Measurement of the W Boson Mass and W^+W^- Production and Decay Properties in e^+e^- Collisions at $\sqrt{s} = 172$ GeV. *European Physical Journal*, 1:395–424, 1998.

[23] P. Abreu et al. Measurement of the W-Pair Cross Section and of the W Mass in e^+e^- Interactions at 172 GeV. *European Physical Journal*, 2:581–595, 1998.

[24] J. Smith, W. L. van Neerven, and J. A. M Vermaseren. Transverse Mass and Width of the W Boson. *Physical Review Letters*, 50:1738–1740, 1983.

[25] V. Barger, A. D. Martin, and R. J. N. Phillips. Perpendicular $e\nu$ Mass from W Decay. *Zeitschrift für Physik*, C21:99–101, 1983.

[26] Bill Ashmanskas. CTC Alignment for Run 1B. CDF Internal Document: CDFNOTE 4456, May 1998.

[27] Young-Kee Kim. A Determination of the Momentum Scale for the Run 1B W Mass Measurement. CDF Internal Document: CDFNOTE 3972, February 1997.

[28] Larry Nodulman and Karen Byrum. Calibration of CEM for Run 1B. CDF Internal Document: CDFNOTE 3477, March 1996.

[29] K. Yasuoka, S. Mikamo, T. Kamon, A. Yamashita, et al. Response Maps of the CDF Central Electromagnetic Calorimeter with Electrons. *Nuclear Instruments and Methods in Physics Research*, A267:315–329, 1988.

[30] Larry Nodulman, Willis Sakamoto, and John Wahl. A Further Tweak to CEM Response for Incidence Angle. CDF Internal Document: CDFNOTE 3896, September 1996.

[31] Richard Field. *Applications of Perturbative QCD.* Addison-Wesley, Redwood City, California, 1989.

[32] John C. Collins and Davison E. Soper. Angular Distribution of Dileptons in High-Energy Hadron Collisions. *Physical Review*, D16:2219–2225, 1977.

[33] W. T. Giele and S. Keller. Determination of W Boson Properties at Hadron Colliders. *Physical Review*, D57:4433–4440, 1998.

[34] Peter B. Arnold and Russel P. Kauffman. W and Z Production at Next-to-Leading Order: From Large q_T to Small. *Nuclear Physics*, B349:381–413, 1991.

[35] G. A. Ladinsky and C. P. Yuan. The Nonperturbative Regime in QCD Resummation for Gauge Boson Production at Hadron Colliders. *Physical Review*, D50:4239, 1994.

[36] M. H. Reno. Relative Distributions of W's and Z's at Low Transverse Momenta. *Physical Review*, D49:4326–4330, 1994.

[37] A. B. Wicklund. Determination of CDF Inner Detector Materials Using Conversion Electrons. CDF Internal Document: CDFNOTE 2899, December 1994.

[38] R. W. Kadel. On the Thickness of the CTC Inner Support Cylinder. CDF Internal Document: CDFNOTE 2804, September 1994.

[39] Yung-Su Tsai. Pair Production and Bremsstrahlung of Charged Leptons. *Review of Modern Physics*, 46(4):815–851, October 1974. (See also Erratum, *Review of Modern Physics*, 49(2):421, April 1977).

[40] Mark Lancaster. A Recoil Model for the Run 1B W Mass Analysis. CDF Internal Document: CDFNOTE 4048, January 1997.

[41] M. G. Kendall and A. Stuart. *The Advanced Theory of Statistics, 2 (Inference and Relationships)*. Griffin, London, 1967.

[42] E. N. May. An EGS3 Simulation of the CDF Central Calorimeter. CDF Internal Document: CDFNOTE 121, April 1982.

[43] A. B. Wicklund. EGS4 Studies of CDF Preshower Response: B-field Effects and "Massless Gap" Resolution Response. CDF Internal Document: CDFNOTE 1639, December 1991.

[44] Jonathan L. Rosner and Mihir P. Worah. Oblique Corrections to the W Width. *Physical Review*, D49:1363–1369, 1994.

[45] Mark Lancaster. Parton Distributions and the Run 1B W Mass Analysis. CDF Internal Document: CDFNOTE 4047, February 1997.

[46] Mark Lancaster. Lepton Resolutions for the Run 1B W Mass Analysis. CDF Internal Document: CDFNOTE 4046, February 1997.

[47] Young-Kee Kim. Update on the Momentum Scale Determination for the Run 1B W Mass Measurement. CDF Internal Document: CDFNOTE 4757, September 1998.

[48] David Saltzberg. Personal communication.

[49] A. B. Wicklund. Personal communication.

[50] P. L. Anthony et al. An Accurate Measurement of the Landau-Pomeranchuk-Migdal Effect. *Physical Review Letters*, 75:1949, 1995.

[51] V. N. Baier, V. M. Katkov, and V. M. Strakhovenko. Theory of Pair Creation in Aligned Single Crystals. *Nuclear Instruments and Methods in Physics Research*, B16:5, 1986.

[52] V. N. Baier, V. M. Katkov, and V. M. Strakhovenko. Emission of Radiation by High-Energy Particles in Oriented Single Crystals. *Sov.Phys.JETP 65(4)*, April 1987.

[53] F. A. Berends and R. Kleiss. Hard Photon Effects in $W^{\pm}$ and Z^0 Decay. *Zeitschrift für Physik*, C27:365, 1985. The generator that was used in the 1A W mass analysis was based on this reference. The generator was written by Bob Wagner and is described in R.G. Wagner, Comput. Phys. Commun. 70, 15 (1992).

[54] Mark Lancaster. Personal communication.

[55] S. Laporta and R. Odorico. Effects from Multiple QED Radiation in Z^0 and $W^{\pm}$ Leptonic Decays. *Nuclear Physics*, B266:633, 1986.

[56] U. Baur, S. Keller, and D. Wackeroth. Electroweak Radiative Corrections to W Production at the Tevatron. FERMILAB-CONF-96/424-T, UB-HET-96-04, hep-ph/9611332, November 1996.

[57] U. Baur. Personal communication.